FORMULATION, DEVELOPMENT, AND ASSESSMENT OF A PAEDIATRIC AZITHROMYCIN NANOSUSPENSION

by

Sonal Bhana

ORCID: 0009-0003-5942-795X

A thesis submitted to Rhodes University in fulfilment of the requirements for the degree of

MASTER OF SCIENCES (PHARMACY)

in

PHARMACEUTICS

June 2025

Supervisor: Prof SMM Khamanga

Co-supervisor: Greg Purcell

Faculty of Pharmacy, Divisions of Pharmaceutics

Rhodes University, Makhanda 6139, South Africa

ABSTRACT

Palatability of paediatric medications is a core determinant of adherence and therapeutic success. Azithromycin (AZI), a macrolide antibiotic widely used to treat upper and lower respiratory tract infections in children, poses formulation challenges due to its bitterness, poor aqueous solubility, and instability under acidic conditions. This study focused on designing and evaluating a stable, palatable nanosuspension of AZI suitable for paediatric oral administration.

A validated reverse phase high performance liquid chromatography method was developed for quantification of AZI in formulation matrices. Critical method parameters including acetonitrile content, phosphate buffer pH, phosphate buffer molarity, and column temperature were optimised through a Central Composite Design, enabling evaluation of linear, interaction, and quadratic effects on retention time, resolution, and peak symmetry. The optimised method achieved excellent linearity (0.5–150 µg/mL; $R^2 > 0.999$), low limits of detection (0.9 µg/mL) and quantification (3 µg/mL), and inter/intra-day precision below 2% relative standard deviation. This ensured the method's suitability for analytical validation in line with ICH Q2(R1) guidelines and assisted in assessing the formulation.

Pre-formulation studies provided an insight into the physicochemical properties of AZI. Fourier transform infrared spectroscopy and differential scanning calorimetry were employed to assess the compatibility of AZI with excipients, identifying Tween®80 and PVP K30 as ideal and compatible stabilisers. Tween®80 served as a non-ionic surfactant to reduce interfacial tension and enhance dispersion, while PVP K30 provided steric stabilization to maintain nanoparticle integrity. Ethanol was selected as the solvent based on its high solubilising capacity for AZI (38.44 mg/mL at 37°C). This selection was based on quantitative solvent screening studies, which ruled out acetone, aqueous buffer, and deionized water due to insufficient solubilization.

The nanosuspension was formulated via a liquid antisolvent precipitation method, employing bottom-up nanocrystallisation with ultrasonication. This method offers advantages in reducing particle size through controlled nucleation while minimising energy consumption compared to top-down techniques like high pressure homogenisation. A Box Behnken design was employed to statistically model the influence of formulation and process variables, which include, PVP

K30 concentration, Tween®80 concentration, solvent: antisolvent ratio, and sonication time on critical quality attributes: particle size, polydispersity index, zeta potential, and initial drug release rate. Model adequacy was confirmed via analysis of variance tables, perturbation plots, and 3D surface analysis, which indicates significant quadratic and interaction terms in the formulation model.

The optimised nanosuspension demonstrated a mean particle size of 134.3 ± 26.6 nm, a narrow polydispersity index of 0.298 ± 0.092, and a zeta potential of -28.3 ± 5.6 mV, indicating sufficient repulsion for colloidal stability. Transmission electron microscopy revealed discrete, spherical particles without agglomeration, while Fourier transform infrared spectroscopy and X-ray diffraction analyses confirmed the retention of chemical integrity of the API. *In vitro* dissolution testing revealed significantly faster release of azithromycin from the nanosuspension within the first 10 minutes compared to the commercial suspension, pinpointing the improved biopharmaceutical profile achieved through nanosizing.

To address the challenge of palatability, taste masking efficiency was quantitatively assessed using the Alpha-MOS ASTREE electronic tongue. This advanced instrument mimics human gustatory perception using sensor arrays responsive to bitterness, sweetness, sourness, umami and saltiness. Nanosuspensions prepared at pH values ranging from 5 to 7.5 were compared to commercial AZI suspensions, pure drug, and placebo formulations. Principal component analysis, radar plots, and distance matrix analysis were used to interpret the sensor data. At pH 5, the optimised nanosuspension achieved the greatest sensory divergence from the pure drug and commercial formulation on bitterness sensor. The radar plots revealed a flattened response profile for the nanosuspension compared to the spiked sensor responses seen with the commercial AZI sample. This suggests that the physical entrapment of the azithromycin within a stabiliser matrix, along with pH buffering significantly diminishes the bitterness. This is further supported by the distance plots, where the optimised nanosuspension at pH 5 showed a greater than 95% discrimination.

Stability studies (physical and chemical) were conducted at 25°C/60% RH and 40°C/75% RH over eight weeks. Particle size, zeta potential, and drug content were monitored to assess colloidal and chemical stability. The nanosuspension remained physically stable with minimal growth in particle size and no signs of sedimentation or aggregation. Drug content remained within 95–105% of initial values, indicating chemical stability. Zeta potential also remained

negative, suggesting that the stabilisers retained their surface activity over time. This demonstrates the successful formulation and characterisation of an AZI nanosuspension with significant advantages in taste masking, dissolution enhancement, and predicted paediatric acceptability.

ACKNOWLEDGEMENTS

First and foremost, I express my deepest gratitude to God (Brahma, Vishnu, Maheshwara) for granting me the strength, perseverance, and wisdom to navigate this journey. Without His guidance, none of this would have been possible.

I would like to extend my heartfelt appreciation to my supervisor, Prof. S.M.M. Khamanga, for his invaluable support, mentorship, and guidance throughout my research and the writing of this thesis. His insights, encouragement, and belief in my work have been instrumental in shaping this project.

I am also grateful to my co-supervisor, Mr. Greg Purcell, for his unwavering support, ensuring the smooth procurement of essential materials.

A special note of thanks to Prof. Walker for granting me access to the BRG Laboratory, providing me with the necessary resources to carry out my experimental work effectively.
I also extend my appreciation to the staff at Rhodes University for their assistance and support during my academic journey.

To my incredible colleagues and friends, Handsome Ndlovu, Nyasha, and Anele Makhanjana, thank you for your camaraderie, motivation, and the many moments of encouragement that made this journey more manageable and memorable.

To my parents, Mr. Viresh Bhana and Mrs. Shanitha Bhana, words cannot express my gratitude for your unwavering love, sacrifices, and belief in my dreams. Your constant support and encouragement have been the foundation of my success. To my brother, Pranav Bhana, thank you for always being there, offering your support and understanding.

This thesis is the culmination of the collective support, guidance, and encouragement of many, and I am truly grateful to each and every one of you.

STUDY OBJECTIVES

Paediatric oral drug delivery remains a complex challenge due to the combined demands of accurate dosing, palatability, and bioavailability. AZI is effective in treating respiratory, skin, and soft tissue infections in children but suffers from poor aqueous solubility, degradation in acidic environments, and a strongly bitter taste, which collectively limit its clinical utility in paediatric formulations. This study aimed to develop a stable, taste masked azithromycin nanosuspension suitable for paediatric use by employing modern formulation science principles such as quality by design, liquid antisolvent nanoprecipitation, and electronic tongue evaluation.

1. To develop and validate a reversed-phase high-performance liquid chromatographic (RP-HPLC) method with adequate sensitivity and selectivity to quantify AZI accurately and precisely in the presence of excipients in pharmaceutical dosage forms.
2. To conduct pre-formulation studies to determine the compatibility between AZI and excipients used to manufacture a nanosuspension.
3. To conduct preliminary formulation studies to identify a suitable formulation in terms of stability and appearance for optimisation studies to be conducted using a central composite design and response surface methodology approaches.
4. To manufacture and assess the nanosuspension (solvent-antisolvent method) and optimised suspension formulation.
5. To evaluate the taste masking efficiency of nanosuspension through use of an electronic tongue.

Table of Contents

LIST OF FIGURES

LIST OF TABLES

LIST OF ABBREVIATIONS

ACN	Acetonitrile
AGP	Alpha-1 acid glycoprotein
ANOVA	Analysis of Variance
API	Active pharmaceutical ingredient
ATR	Attenuated total reflectance
AUC	Area Under the Curve
AZI	Azithromycin
BBD	Box-behnken design
CCD	Central composite design
CNT	Classical nucleation theory
DLS	Dynamic light scattering
DOE	Design of Experiments
DSC	Differential scanning calorimetry
FDA	Food and Drug Administration
FT-IR	Fourier transform infrared spectroscopy
GC	Gas chromatography
HILIC	Hydrophilic interaction liquid chromatography
HLB	Hydrophilic-lipophilic balance
HPLC-UV	High-Performance Liquid Chromatography with Ultraviolet Detection
HPH	High-pressure homogenisation
ICH	International Council for Harmonisation
IEC	Ion exchange chromatography
IUPAC	International Union of Pure and Applied Chemistry
LAS	Liquid antisolvent precipitation

LC	Liquid chromatography
LOD	Limit of Detection
LogP	Partition coefficient
LOQ	Limit of Quantification
MeOH	Methanol
mM	Millimolar
NLCs	Nanostructured lipid carriers
NMR	Nuclear magnetic resonance
nm	Nanometer
PDA	Photodiode array
PEGylated	Polyethylene glycol conjugated
XRD	X-ray diffraction
pKa	Acid dissociation constant
Pt	Peak tailing
PTF	Peak tailing factor
PVP K30	Polyvinylpyrrolidone K30
RSD	Relative standard deviation
Rf	Retention factor
RP-HPLC	Reverse phase high performance liquid chromatography
Rs	Resolution factor
RSM	Response surface methodology
S/N	Signal to Noise Ratio
SLNs	Solid lipid nanoparticles
TEM	Transmission electron microscopy
USP	United states pharmacopeia
UV/VIS	Ultraviolet visible spectrophotometry
VIF	Variance inflation factor

CHAPTER ONE

AZITHROMYCIN DIHYDRATE

1.1. INTRODUCTION

AZI is a derivative of erythromycin A, is characterised by its sizeable macrocyclic lactone rings classified as azalides [1,2]. Azalides contain a 15-member ring structure modified to enhance its antimicrobial effectiveness and pharmacokinetic properties [1,2]. This antibiotic integrates two sugar molecules, D-desosamine and L-cladinose, enhancing its binding capabilities and spectrum of activity against various bacteria [1,2].

The journey of AZI began in the early 1980s when it was first synthesized by researchers at Pliva, Croatia [1,2]. This innovation led to its patent in 1981 and introduction to the global market through a partnership with Pfizer under the brand names Sumamed® and Zithromax® [1,2]. Following FDA's approval in 1992, AZI became a preferred choice for treating numerous infections, ranging from respiratory tract to sexually transmitted diseases, due to its improved gastrointestinal tolerability and once daily dosing convenience [1,2].

1.2. PHYSICO-CHEMICAL PROPERTIES

1.2.1. Description

The International Union of Pure and Applied Chemistry (IUPAC) name of AZI dihydrate is (2*R*,3*S*,4*R*,5*R*,8*R*,10*R*,11*R*,12*S*,13*S*,14*R*)-13[(2,6-Dideoxy-3-*C*-methyl-3-*O*-methyl-α-L-*ribo*-hexopyranosyl) oxy]-2-ethyl-3,4,10-trihydroxy-3,5,6,8,10,12,14-heptamethyl-11-[[3,4,6-trideoxy-3-(dimethylamino)-β-D-*xylo*-hexopyranosyl]oxy]-1-oxa-6-azacyclopentadecan-15-one [3,4]. AZI is a white powder with a molecular formula $C_{38}H_{72}N_2O_{12}\cdot 2H_2O$ [3–5]. AZI dihydrate has a molecular weight of 785g/mol [3,6]. The chemical structure of AZI dihydrate is depicted in Figure 1.1.

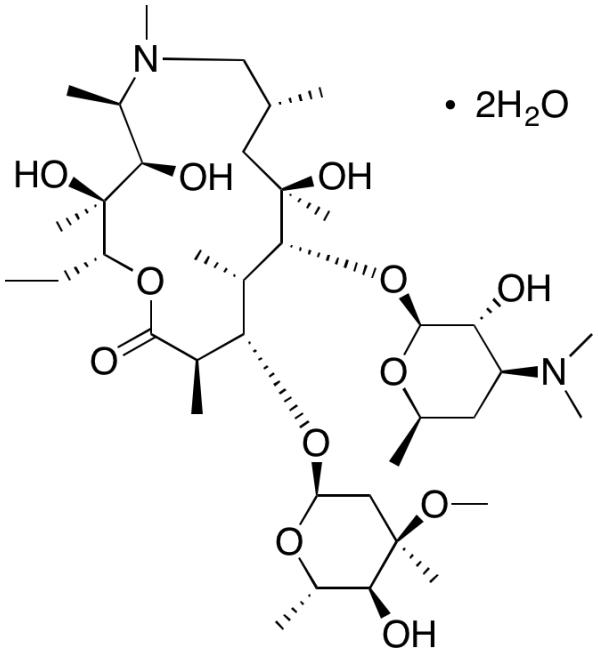

Figure 1.1. Chemical structure of AZI dihydrate

1.2.2. Solubility

According to the British Pharmacopoeia, AZI is practically insoluble in water and freely soluble in ethanol and methylene chloride (dichloromethane) [3,7]. AZI dihydrate solubility has been reported by Gandhi et al. to be 1.98 ± 0.11 mg/ml in water at 37°C [8].

1.2.3. Dissociation constant (pKa)

AZI dihydrate contains two tertiary amines at positions $C_{3'}$ (pKa_1) and C_{9a} (pKa_2), classifying it as a dibasic azalide. Various studies have reported the pKa value of AZI dihydrate (Table 1.1). pKa_1 and pKa_2 represent the ionization of AZI dihydrate on the $C_{3'}$ and $C_{9a,}$ respectively.

Table 1.1. pKa values for AZI

pKa1 ; pKa2	Source
8.75; 9.45	[9]
7.63; 8.72	[10]
8.85	[11]
8.5	[12]
8.6; 9.5	[13]

1.2.4. Partition coefficient (LogP)

Lipophilicity is a critical characteristic of active pharmaceutical ingredients (APIs), influencing their ability to distribute between aqueous environments and lipid-like media [14,15]. This characteristic is essential for predicting the absorption and distribution of drugs across biological membranes [14,15]. The lipophilicity of a compound is quantified using the logarithmic partition coefficient between octanol and water ($LogP_{o/w}$) [14,15]. The $LogP_{o/w}$ value for AZI was recorded at 4.02 by McFarland et al., closely aligning with the value of 4.04 reported by Chanteux et al. [9,16].

1.2.5. Infrared absorption (IR) spectrum

Fourier transform infrared spectroscopy is a technique used to obtain a compound's infrared spectrum of absorption [17]. It measures the wavelength and intensity of the absorption of IR radiation by the sample to identify compounds via a unique fingerprint based on their chemical composition [17].

The attenuated total reflectance (ATR) method was used to obtain the IR spectrum of AZI in the range of 4000 - 400cm^{-1} using a Perkin-Elmer FTIR spectrum two spectrophotometer (Perkin-Elmer® LTD, Beaconsfield, England). IR spectrum of AZI dihydrate is shown in Figure 1.2. The band assignments are shown in Table 1.2 using guidelines set by Silverstein [18].

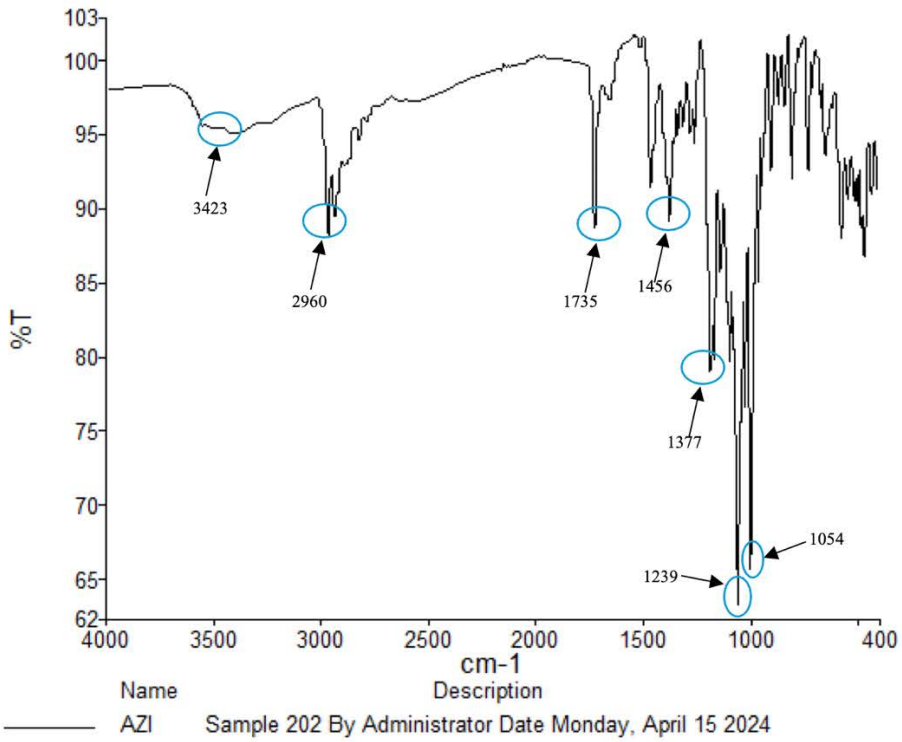

Figure 1.2. Infrared structure of AZI

Table 1.2. IR frequency bands of AZI

cm	Assignment
3423	O-H Stretching (hydroxyl groups)
2960	C-H Stretching (alkanes)
1735	C=O Stretching (ketones)
1456	C-H Bending (alkanes)
1377	C-H Bending (alkanes)
1239	C-N Stretching (amines)
1054	C-O Stretching (alcohols, ethers)

1.2.6. Ultraviolet (UV) absorption spectrum

The UV spectrum of AZI dihydrate was obtained in the presence of acetonitrile to phosphate buffer 20 mM, pH 7.5, 75:25v/v as discovered in Chapter 2. Spectrum were obtained using a Model UVmini-1240 UV-VIS spectrophotometer (Shimadzu Corp.®, Kyoto, Japan). The spectra obtained showed one shoulder at 206 nm as depicted in Figure 1.3. UV spectral studies

were performed to obtain the λ_{max} for AZI, which can be used in high-performance chromatographic method development to quantify AZI in pharmaceutical dosage forms using UV detection.

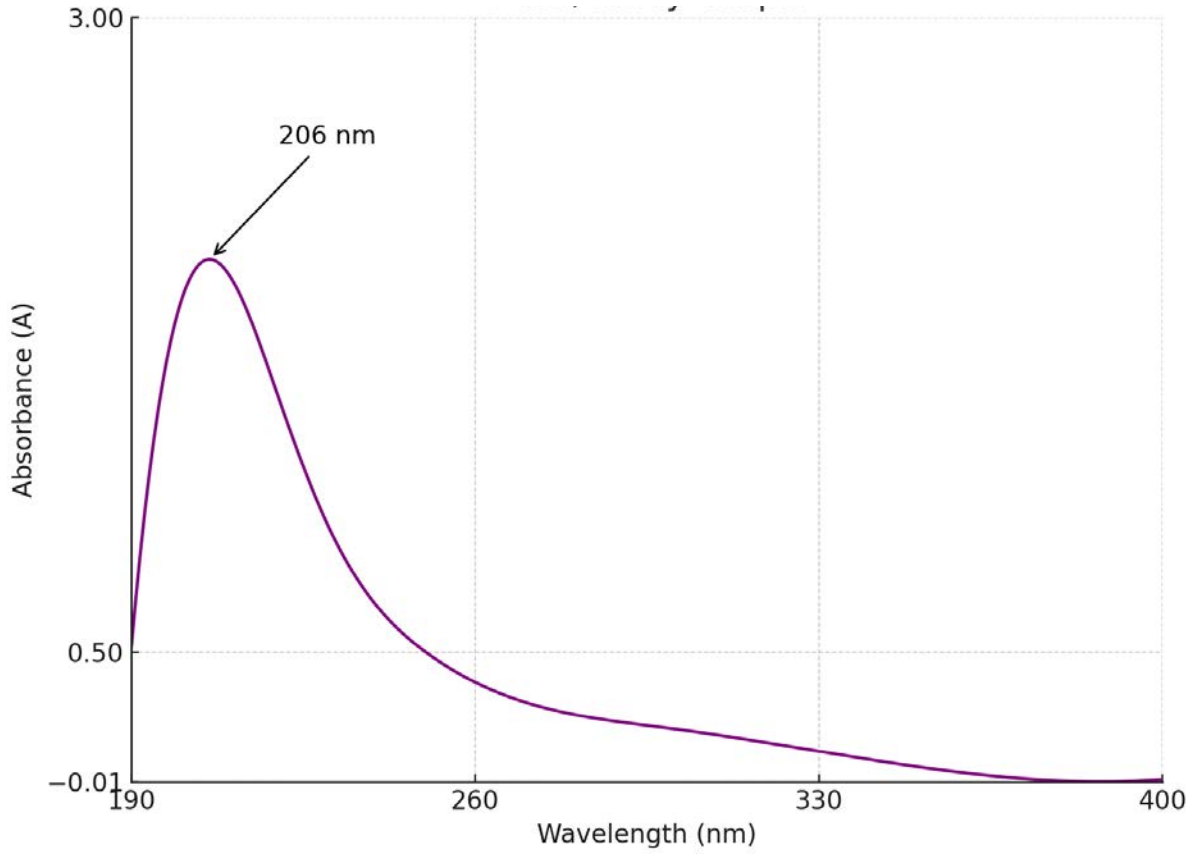

Figure 1.3. Ultraviolet Absorption spectrum of AZI

1.2.7. Differential scanning calorimetry (DSC) and melting range

In sealed aluminium pans, DSC thermograms of AZI dihydrate (Figure 1.4) were analysed using a Model DSC 6 (TA instruments, Lukens Drive, New Castle, DE, USA). Each pan containing a sample and an empty reference pan were placed on a disc inside the DSC standard cell. The melting point range of AZI dihydrate, measured over a heating range of 30°C to 135°C at a heating rate of 10°C/min, was found to be 119.15°C to 131.84°C. The melting endotherm occurred at 126.93°C. These results shown are consistent with those reported by Gandhi et al. [8,19,20].

.

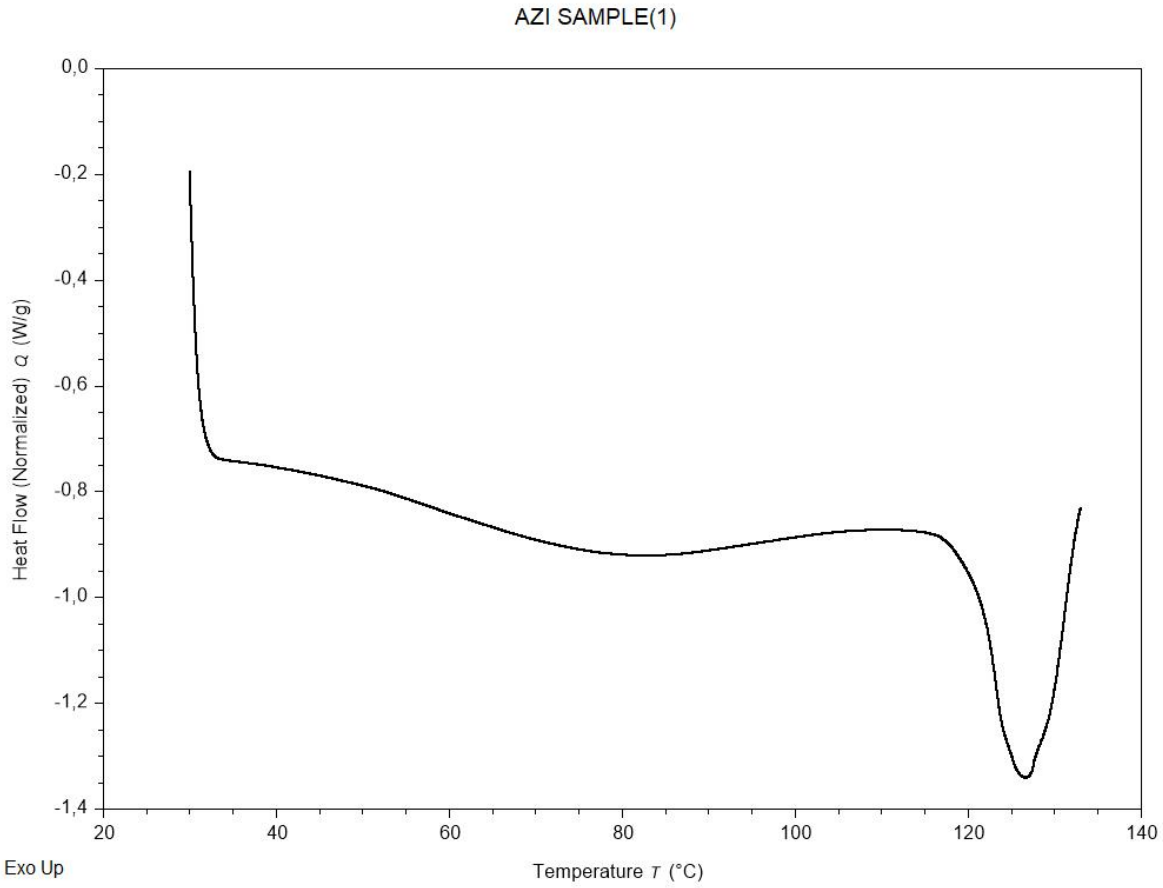

Figure 1.4. DSC thermogram of AZI dihydrate

1.3. SYNTHESIS OF AZI

AZI is synthesized through a semi-synthetic method by adding a nitrogen atom into the macrolide ring of Erythromycin A (Figure 1.5) [21,22]. The process forms 9-(E)-Erythromycin A oxime by reacting Erythromycin A with hydroxylamine hydrochloride [21,22]. This oxime produced undergoes a Beckmann rearrangement to form iminoether compounds. The intermediates are processed through hydrogenation to produce azathromycin [21,22]. This azathromycin undergoes N-methylation, leading to AZI formation [21,22]. This creates a unique azalide structure of AZI.

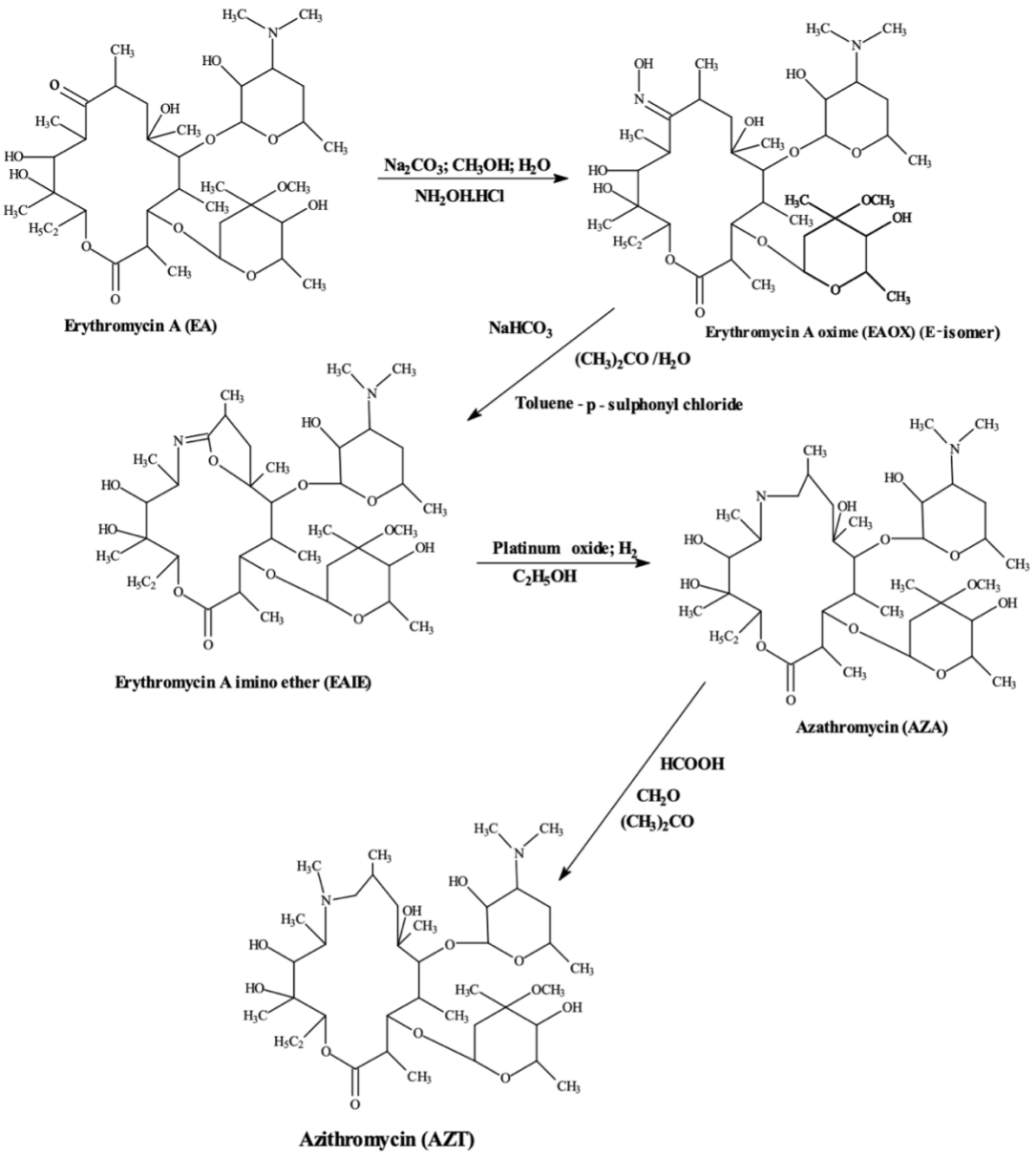

Figure 1.5. The synthesis of AZI

1.4. STABILITY OF AZI

The stability of AZI has drastically improved compared to erythromycin [23,24]. This is due to the structural modifications to improve its resistance to acidic conditions [23,24]. Fiese and Steffen reported that AZI is over 300 times more stable than erythromycin under highly acidic conditions (pH 2.0 at 37°C), with AZI degrading in 20.1 minutes and erythromycin in just 3.7 seconds [25]. These results correspond with those of Gandhi et al., where erythromycin begins to degrade within just 3.5 seconds in gastric conditions, whereas AZI remains stable for up to 20 minutes [8]. Inserting a 9a methyl-amino group at position C_{9a} prevents the formation of a

hemiketal (degradant found in erythromycin) [23,24]. This modification blocks acid hydrolysis at position C_9 [23,24]. AZI's degradation pathway involves acid hydrolysis of the ether bond at position C_3 [23,24]. This results in the production of a pseudo-aglycone degradation product (Figure 1.6).

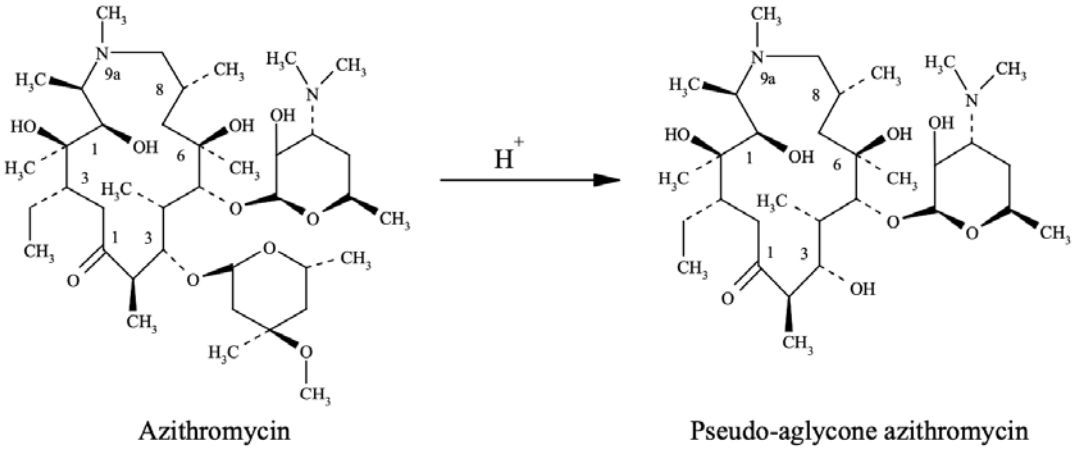

Figure 1.6. Decomposition of AZI in an acidic medium

AZI also undergoes oxidation when exposed to higher temperatures at the $C_{3'}$ position [26]. Degradation studies of AZI were performed by Michael et al. for three months at 55°C [26]. This paper identified major degradants using HPLC, NMR, and UV spectrophotometry [26]. These major degradants included AZI-N-oxide (Figure 1.7) and N-Formyl-N-di(dimethyl)-AZI (Figure 1.8) at 200.1nm [26].

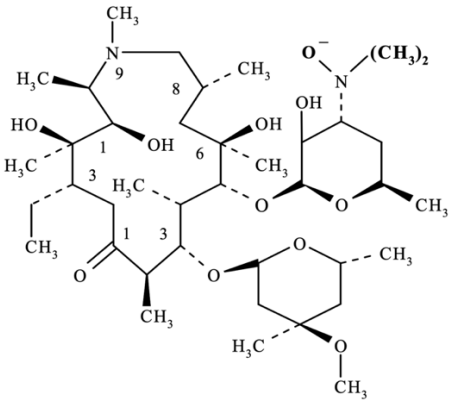

Azithromycin-N-oxide
Mwt = 765.5, λ_{max} = 200.1nm

Figure 1.7. Degradation product 1

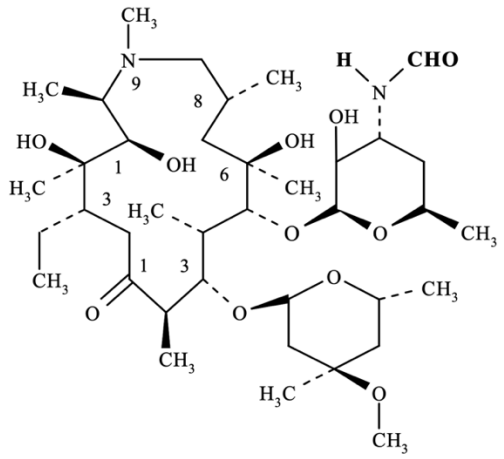

N-Formyl-N-di(dimethyl)-
Azithromycin
Mwt = 749.5, λ_{max} = 200.1nm

Figure 1.8. Degradation product 2

The stability of AZI dihydrate observed from literature when heating it to 80°C, and the compound transitions from its dihydrate to the anhydrous form without significant alterations to its crystalline lattice (isomorphic desolvation) [20]. This imparts the importance of temperature control during the manufacturing and storage processes to preserve the dihydrate form, as AZI dihydrate is more stable and less susceptible to rapid changes than the anhydrous state [20]. These stability stipulations are vital for maintaining AZI's therapeutic efficacy and shelf-life in pharmaceutical preparations.

1.5. CLINICAL PHARMACOLOGY OF AZI

1.5.1. Mechanism of action

AZI is a second-generation macrolide antibiotic with a large lactone ring, which prevents bacterial cells from synthesizing essential proteins [27]. AZI reversibly binds to the 2058 – 2062 region 23S ribosomal RNA of the bacterial 50S ribosomal subunit as shown in Figure 1.9, preventing transpeptidation and translocation by inhibiting peptidyl transferase, thereby blocking amino acid sequencing and, therefore, inhibition of protein synthesis [24,28,29]. AZI regulates inflammatory cytokines (activator protein 1, nuclear factor kappa B) and reduces inflammatory cell infiltration [28,29]. These processes suppress dividing bacterial organisms.

AZI are bacteriostatic agents as they only inhibit protein synthesis but can be bactericidal at high doses [28,29].

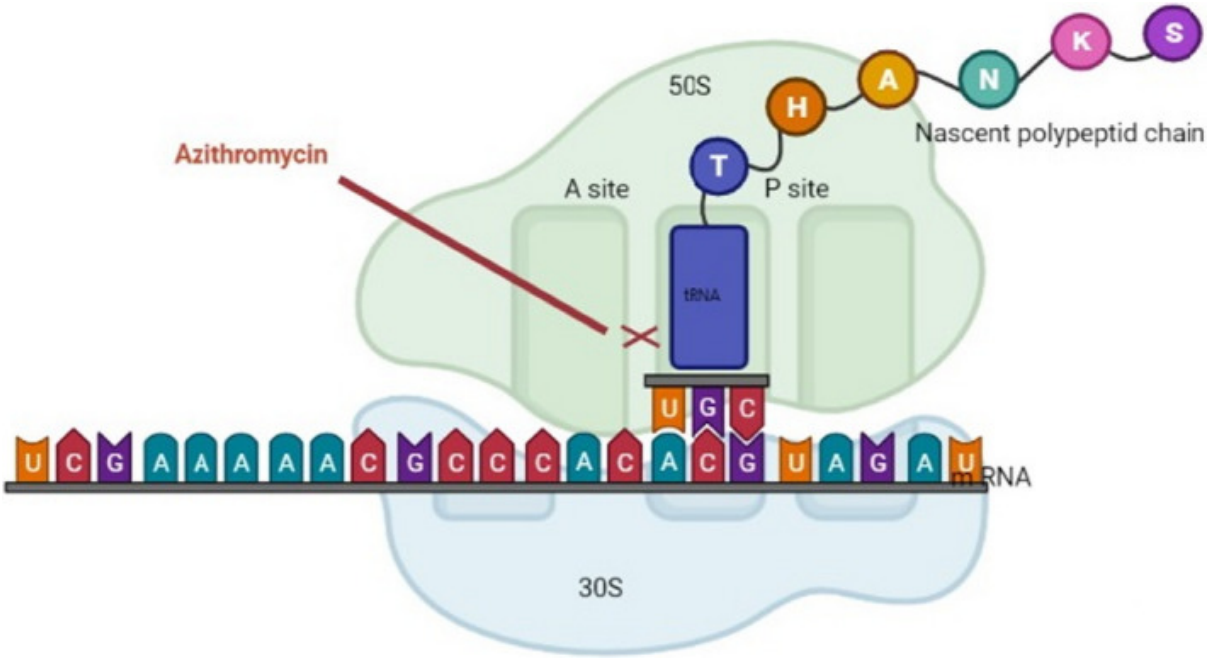

Figure 1.9. Schematic representation of AZI mode of action (Adapted from [30]).

1.5.2. Antimicrobial activity

AZI is a broad-spectrum antibiotic effective against various pathogens [1,31,32]. Table 1.3 describes AZI antimicrobial activity. The categories are divided into Gram-positive aerobes, Gram-negative aerobes, and other pathogens.

Table 1.3. The spectrum of activity of AZI [1,31,32]

Category	Organisms
Gram-positive aerobes	*Streptococcus pyogenes, Streptococcus pneumoniae, Streptococcus agalactiae, Streptococcus aureus, Viridans group streptococci, Neisseria gonorrhoeae*
Gram-negative aerobes	*Bordetella pertussis, Haemophilus influenzae, Moraxella catarrhalis, Legionella pneumophila. Chlamydia trachomatis, Chlamydia pneumoniae, Mycoplasma pneumoniae, Borrelia burgdorferi, Treponema pallidum, Campylobacter jejuni, MAC (Mycobacterium avium complex), Toxoplasma gondii, Prevotella bivia, Escherichia coli, Salmonella*
Other pathogens	*Yersinia enterocolitica, Shigella*

1.5.3. Indications

Table 1.4 provides an overview of the AZI indications when prescribed. It details the specific conditions treated within categories. This highlights AZI's broad spectrum application, from common respiratory pathogens to more complex infections in immunocompromised patients.

Table 1.4. Clinical indications for AZI use [33,29,34,35]

Indication	Specific condition treated
Respiratory infections	Acute bronchitis, community-acquired pneumonia, sinusitis, pharyngitis/tonsillitis, otitis media, chronic obstructive pulmonary disease exacerbations
Skin and soft tissue infections	Infections caused by Streptococcus pyogenes, Staphylococcus aureus, bite organisms
Sexually transmitted infections	Diseases caused by Chlamydia trachomatis, Neisseria gonorrhoeae
Other bacterial infections	Legionnaires' disease, Mycobacterium avium complex (MAC) in HIV patients, typhoid fever, trachoma
Infections caused by protozoa	Diseases such as cryptosporidiosis and toxoplasmosis

1.5.4. Resistance

AZI resistance presents a significant challenge [36–41]. Inappropriate prescriptions for viral infections, incorrect selection of antimicrobial spectrum, extended or missed doses or treatment durations, and patient non-compliance lead to a misuse of antimicrobial agents [36–41]. These misuse mechanisms allow insufficient drug concentrations that do not suppress bacterial colonies, allowing resistant strains to be developed [36–41]. AZI's resistance mechanism is facilitated by altering the ribosomal binding sites [36–41]. This occurs via the methyltransferase enzymes encoded by erm genes at the 23S rRNA of the 50S ribosomal subunit [36–41]. AZI resistance can also be developed by bacterial cells expelling drug contents via efflux pumps encoded by mef genes from the cell [36–41]. Streptococcus pneumoniae carries the ermB gene, and Staphylococcus aureus carries the ermA and ermC genes. They are bacterial strains that exhibits resistance against AZI [36–41]. These genes allow bacterial cells to methylate ribosomal binding sites, reducing AZI efficacy [36–41]. Streptococcus pyogenes encodes the mefA gene, demonstrating resistance through efflux pump mechanisms [36–41].

1.5.5. Dosage

AZI is an effective monotherapy in treating various infections, demonstrating its versatility in different treatment options. AZI is currently administered as a 500 mg daily dose for three days, proving as effective as longer courses of erythromycin and amoxicillin/clavulanic acid for respiratory and ear infections [41–43]. This dosage requirement necessitates a formulation that can deliver a high drug load in a small volume, while maintaining stability and palatability. Table 1.5 outlines the recommended dosages for AZI for various conditions for adult and paediatric patients [46].

Table 1.5. AZI dosage recommendations for adults and children [2,1,42,31,43–45]

Condition	Dosage and Administration
General infections	Adults: 500 mg daily for three days Children: 10 mg/kg daily
Sexually transmitted infections	1g as a single dose, 2g for gonorrhoea
Mycobacterium avium complex	1.2 g weekly
Community-acquired pneumonia	IV: 500 mg daily, followed by oral 500 mg daily to complete 7-10 days
Pelvic inflammatory disease	IV: 500 mg daily for 1-2 days followed by oral 250 mg daily for up to 7 days
Acute otitis media (Children)	30 mg/kg total, 10 mg/kg once daily for three days
Pharyngitis (Children)	12 mg/kg once daily for five days
Intravenous administration	500 mg as a bolus over 60 minutes

1.5.6. Drug Interactions

AZI is not a cytochrome P450 enzyme inhibitor or inducer [47]. Table 1.6 summarizes the potential drug interactions that can occur with co-administration with AZI.

Table 1.6. Drug interactions with AZI [1,2,45,46,48]

Drug	Interaction	Implication
Antacids	Reduced peak serum concentrations of AZI when taken simultaneously with antacids.	Drugs should not be taken concomitantly
Digoxin and colchicine	Increased serum levels of digoxin and colchicine	Clinical monitoring and serum digoxin level adjustments are necessary.
Ergot derivatives	Theoretical risk of ergotism.	Concurrent use is not recommended.
Coumarin-type oral anticoagulants	No alteration of anticoagulant effect was observed, but reports of potentiated anticoagulation exist.	Monitor prothrombin time when used concomitantly
Ciclosporin	Elevated ciclosporin Cmax and AUC	Monitor ciclosporin levels and adjust the dose
Hydroxychloroquine or chloroquine	Increased risk of cardiovascular events	Balance benefits and risks carefully before prescribing.

1.5.7. Adverse effects

AZI is well-tolerated but can manifest a spectrum of adverse effects ranging from mild to severe. Commonly reported side effects include gastrointestinal disturbances such as nausea, vomiting, abdominal pain, and diarrhoea [1,45]. These symptoms occur due to a disruption of the equilibrium of intestinal flora [1,45]. AZI has the potential to induce QT prolongation and arrhythmias [45,49]. Cases of sensorineural hearing loss associated with macrolides have been documented, with most incidents resolving after cessation of the drug [44,50]. These adverse effects highlight the importance of improving AZI's pharmacokinetic profile. The formulation strategy employed in this aims to enhance bioavailability and allow for lower dosing volumes, which may help reduce the incidence and severity of such side effects, while also improving patient adherence.

1.5.8. Precautions/contraindications

AZI is considered a generally safe macrolide antibiotic but comes with several cautions due to its potential adverse effects and interactions with other drugs. AZI must be administered with caution due to its potential to prolong the QT interval, which can trigger cardiac severe arrhythmias [9,44,51]. This risk is heightened in patients with pre-existing heart conditions or those on other QT-prolonging medications [9,44,51]. AZI may exacerbate liver dysfunction in patients with liver [44,45]. AZI can also provoke allergic severe reactions and exacerbate symptoms in patients with myasthenia gravis [44,45]. Their long-term use may result in superinfections such as Clostridium difficile-associated diarrhoea [44,45]. Hydroxychloroquine and AZI concomitant use may increase cardiovascular risk [44,45].

1.5.8.1. Geriatric patients

No difference exists between older and younger people unless hepatic dysfunction or cardiac arrhythmias exist [44,45].

1.5.8.2. Pregnancy

AZI is classified as a pregnancy category B drug (no risk in animal studies) [44,45,52,53]. AZI has undergone extensive evaluation through animal experiments and observational human research to determine its safety during pregnancy. In these animal tests involving rats and mice, high doses up to 200 mg/kg/day, above the typical usual human dosage, demonstrated no foetal harm [44,45,52,53].

Human observational studies, which have included over 7300 first-trimester exposures to AZI, do not associate the drug with congenital or cardiovascular malformations [44,45,52,53]. There is an indication of an increase in miscarriage risk when AZI is used early in pregnancy [44,45,52,53]. Due to the insufficient evidence, a cautious approach must be undertaken. AZI should only be administered during pregnancy when the potential health benefits surpass the possible risks [44,45,52,53].

1.5.8.3. Lactation

According to Elif et al., AZI has been detected in breast milk in minimal quantities. Pharmacokinetic studies suggest that an infant would be exposed to approximately 0.1-1.2 mg/kg/day of AZI [52]. This exposure level is considered relatively harmless as the relative

infant dose (RID) is significantly below 10% [52]. RID is commonly used to assess the safety of medications during breastfeeding [52]. There have been no severe adverse reactions reported in infants who are breastfed by mothers taking AZI [44,45,52].

The decision to continue with breastfeeding or AZI must be carefully weighed, taking into consideration the health benefits and risks to the child and the mother [44,45,52]. This recommendation is consistent with other sources that advise caution as AZI has a long half-life and, therefore, has the potential to accumulate in breast milk [44,45,52].

1.6. CLINICAL PHARMACOKINETICS OF AZI

1.6.1. Absorption

AZI is quickly absorbed after oral intake, achieving peak plasma levels around 2 to 3 hours later. AZI is stable in acidic conditions (such as the stomach), which helps extend AZI's concentration in the blood and increases concentrations within bodily tissues compared to erythromycin [54–56]. When a 500 mg dose of AZI is administered to healthy male volunteers in a fasted state, its oral bioavailability is approximately 37% [54–56]. This is based on the area under the plasma concentration-time curve (AUC) up to 24, 48, and 72 hours post-dosing [54–56]. The intestinal absorption of AZI is moderated by P-glycoprotein (ABCB1) efflux transporters, encoded by the ABCB1 gene [54–56]. These transporters play a crucial role in limiting the absorption of macrolides by transporting them back into the intestinal lumen, reducing their bioavailability [54–56].

Food intake affects the absorption of AZI, specifically with capsule dosage forms [54–56]. Eating a meal before taking AZI can decrease the peak serum concentration by as much as 50% and lower the AUC by 43% [54–56]. Taking AZI capsules one hour before or two hours after a meal is advisable to ensure absorption occurs on an empty stomach [54–56]. The bioavailability of AZI in tablet and oral suspension form is not markedly affected by food [1,2,32,54–57].

1.6.2. Distribution

Oral administered AZI is a lipophilic API widely distributed throughout the body in blood and tissues [1,2,58]. It bind to α-1-acid glycoprotein (AGP), with AZI being 93% unbound (free drug) in plasma but only 16% unbound in liver tissue [32,54,55,59,60]. AZI is absorbed into

tissues such as the tonsils, and gynaecological regions, where it achieves concentrations 10 to 100 times greater than in serum [61]. After a single oral dose of 500 mg, the concentration of AZI can range from 1 mg/kg to 9 mg/kg within 12 to 24 hours, exceeding the minimum inhibitory concentration for pathogens [32,54,55,59,60]. AZI's amphiphilic nature facilitates this extensive tissue distribution to penetrate cellular membranes efficiently via both passive and active transport into cells [31].

AZI is effective against intracellular pathogens due to its accumulation within leukocytes, monocytes, and macrophages [32,54,55,59,60]. This accumulation enables the sustained release of the drug at infection sites, enhancing its antimicrobial efficacy. The drug demonstrates minimal binding to serum albumin and instead binds to α- and β-globulins [60]. The levels of AGP further influence this process in the plasma, where higher levels lead to increased protein binding of the drug. AZI has a long half-life, exceeding 60 hours, which supports a once-daily dosing schedule [32,54,55,59,60]. This long half-life allows therapeutic levels of the drug to be maintained for 3 to 5 days. The extensive volume of distribution of 31.1 L/kg at a steady state and the slow release from cells contribute to this prolonged action, reducing the need for frequent dosing and minimising systemic side effects [32,54,55,59,60,62].

1.6.3. Metabolism

AZI is primarily metabolized in the liver. Its primary metabolic process is N-demethylation at two sites: the desosamine sugar and the macrolide ring at the 9a position, leading to the formation of N-desmethylazithromycin and 9a-N-desmethylazithromycin, respectively [1,63–65]. Both metabolites maintain antimicrobial activity against various bacteria. Other metabolic reactions include O-demethylation at the C3″-OCH3 of cladinose, decladinosylation, and hydroxylation of the desosamine or lactone ring [1,63–65]. Studies in animals like rats have shown significant hepatic accumulation with high doses, without evidence of cytochrome P450 enzyme induction or inactivation. A study by Hunter et al., using the ball python snake model, identified fifteen metabolites illustrating the AZI metabolism [63]. Given its stable metabolic profile, AZI is effective for patients with different renal and hepatic functions but requires careful dose management [1,63–65]. This pharmacokinetic characteristic contributes to AZI’s long half-life and widespread use in treating bacterial infections.

1.6.4. Elimination

The elimination process of AZI from plasma is biphasic [1,46]. There is a rapid decline in AZI concentration due to the redistribution into body tissues [1,46]. This is followed by a slower phase where biliary excretion is the primary removal route. Upon intravenous administration, about 12% of AZI is excreted unchanged in the urine within three days, and significant amounts have been found in human bile [1,46,54,55,65]. The liver eliminates AZI via enterohepatic recycling. A portion of the drug is excreted unchanged through the bile, facilitated by liver transporters such as MRP2 (ABCC2) and ABCB1 [1,46,54,55,65]. The drug demonstrates a prolonged half-life of around 68 hours, which correlates with its slow elimination from tissue stores that typically last two to four days [44,45]. The kidneys role in AZI's elimination is reported to be between 100 ml/min and 189 ml/min [65]. Both oral and intravenous doses reveal that a small fraction of AZI, ranging from 4.5% to 12.2%, appears unchanged in the urine [1,46,54,55,65].

1.7. CONCLUSION

AZI's advancement from its predecessor, erythromycin, offers a wider spectrum of antibacterial activity and enhanced pharmacokinetic attributes. These improvements are primarily due to structural modifications that not only increase its effectiveness but also enhance its stability, making it a vital option for various treatments.

The development of AZI into a paediatric-friendly formulation through complexation and encapsulation not only addresses the practical challenges (taste, dosage form, dosing accuracy) of paediatric medicine delivery but also leverages the unique pharmacokinetic and physicochemical properties of AZI. Such innovations are set to significantly enhance the clinical outcomes for paediatric patients, fulfilling the urgent need for more effective and child-friendly antibiotic treatments. This will help develop stable pharmaceutical formulation of AZI, ensuring safety and efficacy in its final dosage forms.

CHAPTER 2

DEVELOPMENT AND VALIDATION OF A RP-HPLC METHOD WITH UV DETECTION FOR THE ANALYSIS OF AZITHROMYCIN DIHYDRATE

2.1. INTRODUCTION

HPLC techniques are performed on a large scale today and are applied in the biotechnology, pharmaceutical, dermatology, environmental and food industries [66,67]. This technique is able to separate, quantify and identify complex substances [66,67]. HPLC was developed in the 1960s from older liquid chromatography (LC) and gas chromatography (GC) methods. LC is an analytical technique which describes how a liquid phase moves through and interacts with a stationary phase. There are multiple types of LC: liquid-solid, liquid-liquid, ion exchange, thin layer, and size exclusion [66,67]. HPLC is suitable for macromolecules and has a higher throughput and power efficiency with great accuracy, precision and reproducibility [66]. The degree of separation depends on the type of column packing (solid, liquid, ion exchange or porous polymer), mobile phase composition and the functional groups of the target analyte [66].

2.2. PRINCIPLES OF HPLC

This method uses the interactions between a mobile phase and a stationary phase, which facilitate the separation process [66,67]. Chromatography works by partitioning of analytes between the mobile phase (liquid) and stationary phase (solid) [66,67]. Separation arises from the physicochemical properties of each analyte, such as polarity, size, or charge, which determine their behaviour in both phases [66,67]. As components move through the column, they separate based on their retention times. The effectiveness of separation depends on the strength of interactions between analytes and the stationary phase relative to their solubility in the mobile phase [66,67]. The extent of this partitioning is determined by the equilibrium constant K, which is the ratio of an analyte's concentration in the stationary phase (C_s) to its concentration in the mobile phase (C_m) as defined in Equation 2.1 [66]:

$$K = \frac{C_s}{C_m} \qquad \textit{Equation 2.1}.$$

Where:

K = the distribution co-efficient of solute molecules between both phases

C_s = the concentration of the solute is the stationary phase

C_m = the concentration of the solute in the mobile phase

These interactions with the stationary phase cause a difference in retention times. Stronger interactions with the stationary phase lead to longer retention times, while weaker interactions allow analytes to elute faster. These interactions can include hydrophobic forces, hydrogen bonding, van der Waals forces, and ionic interactions, depending on the nature of the stationary phase and the analyte.

The fundamental components of an HPLC system (Figure 2.1) work to achieve these separations. The solvent delivery system, or pump, is crucial for maintaining a high consistent and precise flow of the mobile phase [66]. Injectors introduce the sample into the mobile phase with minimal dispersion, ensuring accurate and repeatable sample volumes [66]. The column, packed with stationary phase material, acts as the core where the separation occurs [66]. Its chemical properties, such as polarity or hydrophobicity, govern the interactions with analytes [66]. Detectors identify and quantify eluted components, with common types including UV-Vis, fluorescence, and mass spectrometry detectors, each offering unique advantages for specific applications [66]. Data analysis software processes detector signals into chromatograms, providing quantitative insights and system monitoring [66].

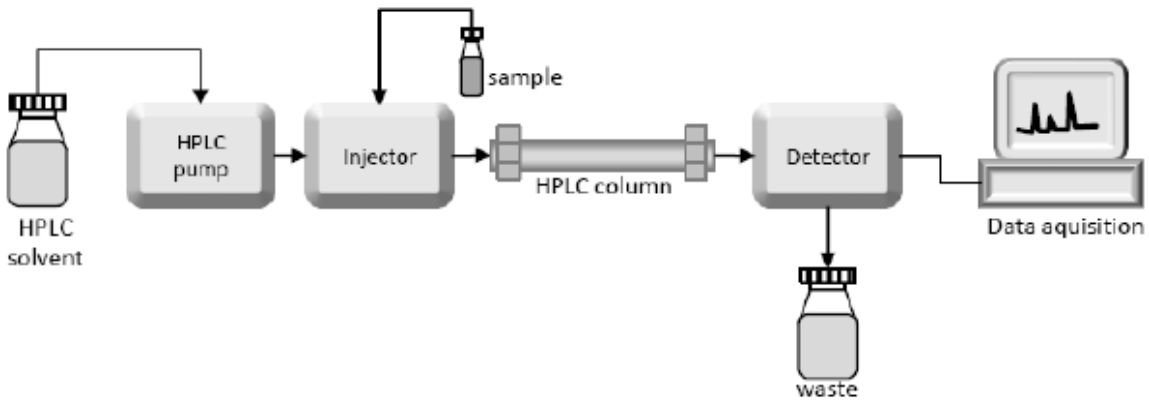

Figure 2.1. Schematic representation of the HPLC system.

Normal phase HPLC utilizes a non-polar mobile phase and a polar stationary which aids separation, whereas in reverse phase HPLC, the mobile phase is polar and the stationary phase

is non-polar [66,67]. The use of RP-HPLC is commonly utilized for hydrophobic API's as it interacts strongly with the non-polar stationary phase therefore increasing retention times with better separation [66,67]. Non-polar stationary phases include silica-based columns which comprises of C_4 (Butyldimethyl), C_8(Octyl), C_{18} (Octyldecyl – commonly used for antibiotic API), CN (Cyanopropyl), DPA-6S (Polymeric hexamide), Ph (Phenyl) alkyl chains with a silica end cap [66,67].

The mobile phase contains organic modifier solvents, acetonitrile (ACN) or methanol (MeOH) and buffers, potassium dihydrogen phosphate, to achieve good separation. ACN and MeOH which are less polar than water reduce the polarity of the mobile phase therefore reducing the retention time of the analyte [66,67]. The buffer maintains the pH of the mobile phase which prevents ionisation of the API [66,67]. The API passes through the column, is separated and eluted from the column. These elutions are picked up by the detector as electrical signals that are processed for analysis. The degree of separation and elution will depend on the integrations between the target analyte, mobile phase and stationary phase.

2.3. METHOD DEVELOPMENT

2.3.1. Background

Parameters like stationary-phase chemistry, mobile-phase composition, isocratic versus gradient design, column temperature, and choice of detector can be altered to maximize desired and reproducible results [68,69]. The choice between methanol (MeOH) or acetonitrile (ACN) as the organic modifier can noticeably affect chromatographic efficiency and selectivity [68,69]. By adjusting the mobile phase or the buffer pH help stabilize analytes, optimise ionization, and maintain consistent retention times [68,69].

A practical starting point often involves performing preliminary studies as shown in Table 2.1. to observe retention behaviours across a broad range of solvent compositions and previous studies done. This initial experimentation guides the refining of buffer strength, buffer pH, and adjusting temperature conditions [68,69]. Once a suitably consistent method emerges, its performance is typically subjected to optimisation using response surface methodology within a software (such as Design Expert® or, Stat-Ease®) to help reduce the retention time for analysis, increase resolution and minimize peak tailing [68,69]. These optimised chromatographical conditions are subjected to validation criteria under the ICH guidelines [67–70].

Table 2.1. Summary of HPLC methods for the analysis of AZI

Column	Mobile Phase Composition	Detection	Retention Time	Flow Rate	Sample injection	Reference
LiChroCART® C18, 5µm, 125x4.6mm	60:20:20 (v/v/v) 50mM Phosphate buffer , pH=8: acetonitrile: methanol	UV – 215nm	5mins	1.0mL/min	20µL	[71]
XTerra RP C18, 5µm, 250x4.6mm	35:10:55 (v/v/v) 0.2M Phosphate buffer , pH=6.5: water: acetonitrile	UV-215nm	30mins	1.0mL/min	100µL	[72]
Phenomenex Synergi® C18, 4µm, 250x4.6mm	Gradient elution 47:53 – 28:72 (v/v) 10mM phosphate buffer, pH=7: acetonitrile and methanol 1:1 (v/v)	UV-210nm	45mins	1.2mL/min	70µL	[73]
C18 column, 5µm, 250x4.6 mm (Published 2013)	10:90 (v/v) 20mM Phosphate buffer, pH=8: methanol	UV – 210nm	7.23mins	1.5mL/min	20µL	[74]
OSD C18 column, 5µm, 250x4.6 mm (Published 2019)	10:90 (v/v) 0.2M Phosphate buffer, pH=8: methanol	UV – 210nm	5.8mins	1.2mL/min	50µL	[75]
C8 column, 5µm, 250x4.6 mm (Published 2013)	20:80 (v/v) 0.2M Phosphate buffer, pH=7.5: methanol	UV – 210nm	8.35mins	1.2mL/min	20µL	[69]
XTerra RP C18, 5µm, 250x4.6mm (Published 2017)	15:1:59:25 (v/v/v/v) 0.1M Phosphate buffer , pH=6.5: tetrabutyl ammonium hydroxide pH=6.5: water: acetonitrile	UV-215nm	6mins	1.0mL/min	20µL	[76]
Hypersil Gold C18, 5µm, 250x4.6mm (Published 2017)	18:82 (v/v) 30mM Ammonium acetate buffer, pH=6.8: acetonitrile	UV-210nm	7.95mins	0.7mL/min	20µL	[77]
C18, 5µm, 250x4.6mm (Published 2010)	20:80 (v/v) 30mM Phosphate buffer pH=7.5: methanol	UV-210nm	6.8mins	2mL/min	20µL	[78]

2.3.2. Response surface methodology (RSM)

RSM is a powerful statistical and mathematical framework designed to model and optimise processes influenced by multiple variables [68]. It is useful in instances where responses are affected by various factors, such as in HPLC. By developing mathematical models, RSM establishes the relationship between input variables, such as buffer molarity, pH, temperature, and organic solvent content *($x_1, x_2, \ldots, x_k$)*, and a desired response (*Y*), such as retention time, resolution, or peak tailing [68,79,80]. RSM facilitates process optimisation by systematically exploring how these factors influence the response and determining optimal conditions for achieving specific objectives. This ensures better accuracy, efficiency, and reproducibility in analytical processes [68,79,80]. The methodology consists of three main components: creating a statistical model, designing experiments to test this model, and analyzing results to identify optimal conditions. By visualizing the response as a surface that evolves with changes in the factors, RSM allows researchers to select where the desired outcome is maximized or minimized [68,79,80].

The methodology is especially suited for systems where multiple variables interact non-linearly. For example, in HPLC, increasing the proportion of organic solvent in the mobile phase may decrease retention time, but the extent of this effect could depend on the pH of the buffer or the column temperature. RSM captures such intricate relationships, making it invaluable. The mathematical modelling makes use of polynomial regression between input and output variables. The general model in RSM is expressed in Equation 2.2 [68,79,80]:

$$Y = f'(x)\beta + \epsilon \qquad \textbf{\textit{Equation 2.2}}.$$

Where:

Y = represents the response

x = (*x1, x2…,xk*) are the input variables or independent factors

f'(*x*) = is a function comprising linear or quadratic terms

β = coefficients showing the effects of these terms

ϵ = a constant that accounts for experimental error

The response *(Y)* can be represented as 3D and/or contour plots to aid visualization of the shape of the response surface. There are two models commonly used in RSM include first order (*d*=1) and second order models (*d*=2), given in Equations 2.3. and 2.4.

The first order linear model is expressed as [68,79,80]:

$$Y = \beta_0 + \sum_{i=1}^{k} \beta_i x_i + \epsilon$$ ***Equation 2.3***.

Where:

Y = response surface

βo and βi = constant coefficients

xi = independent factor

ε = a constant that accounts for experimental error

This model assumes a proportional relationship between each factor and the response. In the context of HPLC, increasing the pH of the buffer might linearly improve analyte resolution, while raising the organic solvent content might linearly reduce retention times for non-polar compounds.

The second order quadratic model is expressed as [68,79,80]:

$$Y = \beta_0 + \sum_{i=1}^{k} \beta_i x_i + \beta_0 + \sum_{i=1}^{k} \beta_{ii} x_i^2 + \sum_{i<j} \beta_{ij} x_i x_j + \epsilon$$ ***Equation 2.4***.

Where:

βo ,βi ,βij = constant coefficients

xi and xj = independent factors

ε = a constant that accounts for experimental error

This model introduces quadratic (x_i^2) and interaction ($x_i x_j$) terms, therefore including non-linear relationships. For example, while increasing buffer molarity may initially improve retention times, excessive concentrations could negatively affect peak shapes, creating a curved relationship.

Choosing a model design in Response Surface Methodology (RSM) involves carefully considering the study's objectives, the complexity of the system, the number of variables, and the expected relationships between factors [68,79,80].

The selection begins with defining the study's purpose: for screening factors to identify those significantly influencing the response, simple designs like the Plackett-Burman Design (PBD)

are preferred, as they focus on main effects and minimize the number of experiments. Each factor is tested at two levels (−1,+1), and the total number of experiments is expressed in Equation 2.5 [68,79,80].

$$N = 4m \qquad \textbf{\textit{Equation 2.5}}.$$

Where:

m = is an integer, and N > k

For optimizing processes where both linear and quadratic effects are expected, designs such as Central Composite Design (CCD), Box-Behnken Design (BBD), or Doehlert Design are appropriate [68,79,80]. These designs are capable of capturing curvature and interaction effects in the response. CCD is often chosen when exploring wide experimental ranges and modelling complex systems, as it includes factorial points, axial points, and centre points, but it may require experiments beyond the natural range of variables [81]. CCD was the choice of design for this study. CCD is a second-order design that combines factorial points (−1,+1), axial points (±α), and centre points. It efficiently captures linear, quadratic, and interaction effects [68,79–81]. The total number of experiments is expressed in Equation 2.6.

$$N = 2^k + 2k + n_0 \qquad \textbf{\textit{Equation 2.6}}.$$

Where:

k = number of factors

n_o = number of centre points

Figure 2.2. and Figure 2.3. represents a two and three-factor CCD [81]. The designs are built around two (in the case of Figure 2.2) and three (in the case of Figure 2.3) factors, labelled as Factor A and Factor B and Factor C, which are plotted along the x- and y-axes, respectively. The factorial points (red circles) form the vertices of a square, representing combinations of the high (+1) and low (−1) levels of both factors. These points capture the linear effects and the primary interactions between the factors. The axial points (green circles) are positioned along the axes at a distance of ±α from the centre, extending the experimental range beyond the factorial points. These points are critical for detecting curvature in the response, which enables the modelling of quadratic effects. The centre point (blue circle) is located at the intersection of the axes, where both factors are at their midpoint. This point is typically

replicated to estimate experimental error and improve the model's reliability [81]. The dashed circle boundary indicates the rotatable nature of the design, where all points are equidistant from the centre, ensuring consistent prediction accuracy throughout the experimental space.

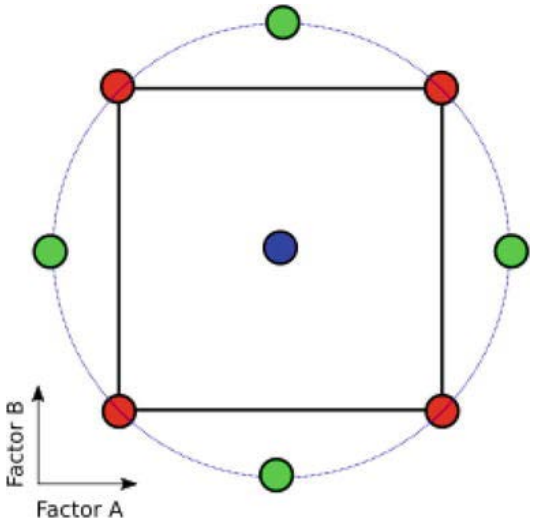

Figure 2.2. Schematic representation for a CCD with two design variables. Adapted from [81].

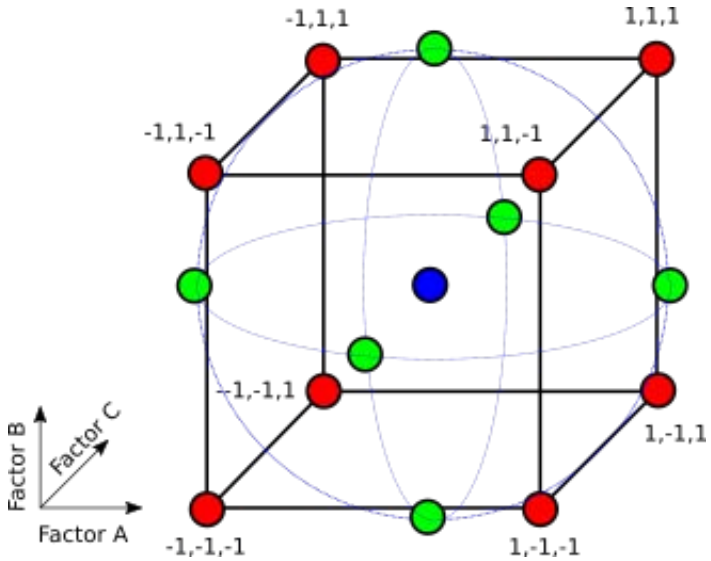

Figure 2.3. Schematic representation for a CCD with three design variables. Adapted from [81].

BBD is a more resource-efficient option, avoiding extreme factor levels while requiring fewer experiments than CCD, making it ideal for moderately complex systems [82]. The number of experiments is:

$$N = 2k(k-1) + C_0 \qquad \textbf{\textit{Equation 2.7}}.$$

Where:

k = number of factors

The 3^k factorial design, which evaluates all combinations of three levels for each variable, is detailed but becomes impractical with more than four variables due to its exponential growth in experimental runs [68].

$$N = 3^k \qquad \textbf{\textit{Equation 2.8}}.$$

Where:

k = number of factors

Doehlert Design offers flexibility by unevenly spacing levels of factors, which is useful for adjusting specific variables in narrow ranges while maintaining a uniform distribution of experimental points [68].

$$N = k^2 + k + 1 \qquad \textbf{\textit{Equation 2.9}}.$$

Where:

k = number of factors

2.3.3. Experimental and analysis of AZI

Prior to developing a method for the analysis of AZI using RSM, an extensive review of the literature was conducted to guide the preliminary experimental design. A summary of methods employing RP-HPLC with UV detection for the quantitative determination of AZI in pharmaceutical formulations is presented in Table 2.1. The analysis of AZI has been predominantly achieved using silica-based columns, particularly C_{18} and C_8 stationary phases, due to their compatibility with hydrophobic molecules [69,71,74,75,77]. The mobile phases commonly reported consist of binary or ternary mixtures, often incorporating acetonitrile, methanol, or water combined with phosphate buffer [69,71,74,75,77]. The addition of ion-pairing agents also been explored to enhance peak sharpness and retention [76]. The focus is the development and validation of a rapid, accurate, precise, and selective RP-HPLC method for the analysis of AZI in pharmaceutical dosage forms.

2.3.3.1. Chemicals and reagents

All reagents were of analytical reagent grade. AZI was procured from Skyrun® Inc. (Nanjing, Jiangsu, China) and the internal standard, Clarithromycin (CLA) was procured from Zhejiang botai® Inc. (Zhejiang, China). HPLC-grade water was prepared by reverse osmosis using a Direct Pure UP 10 UV with TOC water purification system by Microsep® (Port Elizabeth, Eastern Cape, South Africa). The water was pre-filtered through 3 stage stack filter kit (RephiLe® Inc., Boston, Massachusetts, USA). This purified water was used to prepare all buffer solutions. HPLC UV grade acetonitrile (ACN) was purchased from Microsep® (Port Elizabeth, Eastern Cape, South Africa). Potassium dihydrogen orthophosphate, and sodium hydroxide pellets were purchased from Associated Chemical Enterprises (Pty) Ltd Laboratories (Johannesburg, Gauteng, South Africa).

2.3.3.2. Instrumentation

The HPLC system consisted of a Waters® Alliance Model e2695 separation module equipped with a solvent delivery module, an autosampler, a degasser and a Waters® (Milford, MA, USA) Model 2996 Photodiode Array Detector set at a λ_{max} of 206nm (§ 1.2.6.). Data collection, processing and reporting were attained using Waters® (Milford, MA, USA) Empower 3 software. The separation between the internal standard CLA and AZI was achieved under isocratic conditions using a Phenomenex® (Torrance, CA, USA) C18, 5 µm (150 mm x 4.6 mm i.d column with a mobile phase consisting of ACN and 20 mM potassium phosphate buffer pH 7.5 in a 75:25 v/v ratio. The flow rate of the mobile phase and the injection volume were 0.6 mL/min and 100 µL respectively. The analytical column was maintained at 37.6 °C using a Waters® (Milford, MA, USA) temperature controller.

2.3.3.3. Preparation of stock solutions and calibration standards

Standard stock solutions of AZI (150 µg/mL) and CLA (75 µg/mL) were prepared by accurately weighing 15 mg and 7.5 mg of each API using a Model Pioneer PA214 Ohaus® analytical balance (Ohaus® Corp., Pine brook, New Jersey, USA), transferring into 100 ml A-grade volumetric flasks and diluting with 70 ml of mobile phase (diluent). The stock solutions were sonicated using a Model B12 Branson® ultrasonic bath (Branson® Inc., Shelton, Conn, USA) until a clear solution was observed. The resultant solutions were made to volume using the diluent. Calibration standards of AZI over the concentration range 0.5-150 µg/mL were prepared by serial dilution of the standard stock solution on the day of analysis using mobile

phase (diluent). A concentration of 75 µg/mL CLA was added to all calibration standards and test samples prior to analysis. The stock solutions were used within three days of preparation.

2.3.3.4. Preparation of buffer and mobile phase

20 mM pH 7.5 phosphate buffer solutions were prepared by accurately weighing 0.92g of potassium dihydrogen orthophosphate into a 1 L A-grade volumetric flask. The volume was made up to using HPLC grade water. The pH of the buffers was monitored at 25°C using a Model pH 8 Accsen pH-meter (Barcelona, Spain) and was adjusted to pH 7.5 using sodium hydroxide. The diluent was prepared by mixing specific volumes of the buffer and HPLC-grade ACN in A-grade measuring cylinders. The buffer mixture was transferred into a 1 L Schott® Duran bottle (Wertheim, Germany). This was sonicated using a Model B12 Branson® ultrasonic bath (Branson® Inc., Shelton, Conn, USA) until a clear solution was observed. The resultant buffer solution was filtered through a Millipore® (Bedford, MA, USA) 0.45 µm HVLP membrane filter under a Labotec® vacuum pump Model N820 Laboport prior to use.

2.3.3.5. Column selection

AZI's amphiphilic structure, combining a hydrophobic macrocyclic core with hydrophilic glycosidic groups, poses challenges for chromatographic separation, therefore careful column selection is crucial [1,2]. Silica remains the support material in RP-HPLC due to its high surface area, and modifiable surface chemistry [83].

There are different column chemistries: Phenyl-hexyl phases leverage π-π interactions with aromatic or conjugated systems [84]. While AZI's lactone ring is partially conjugated, its bulky structure impedes effective π-π bonding, resulting in inconsistent retention [84]. Polar embedded columns incorporate hydrophilic groups (amides) into C_{18} chains to stabilize basic analytes [85]. While beneficial for small basic molecules, azithromycin's retention primarily depends on hydrophobic interactions with the lactone ring. The embedded polar groups may reduce overall hydrophobicity, leading to weaker retention. Hydrophilic interaction liquid chromatography (HILIC) excels for polar analytes but struggles with amphiphilic molecules like AZI [83]. Traditional C_{18} columns without advanced end-capping (e.g., Hypersil® ODS) often retain residual acidic silanols, which interact with AZI's protonated amines (at acidic pH), causing peak tailing [83].

The Phenomenex® Luna C_{18} 150 x 4.6mm, 5µm column addresses the limitations. The 150 mm column length provides sufficient theoretical plates to resolve AZI from impurities or degradation products, balancing resolution and run time) [83]. Shorter columns (50–100 mm) reduce retention time but risk co-elution due to fewer plates, while longer columns (250 mm) increase resolution at the cost of higher backpressure and solvent consumption. The 100 Å pore size is critical for AZI's molecular weight [83]. Smaller pores (60 Å) restrict access to the hydrophobic stationary phase, reducing retention and efficiency, while larger pores (>120 Å) may diminish surface area and retention for mid-sized molecules. Particle size (5 µm) balances efficiency and practicality [83]. Smaller particles (3 µm) enhance efficiency but require ultra performance liquid chromatography (UPLC) systems to manage high backpressure. The 5 µm particles in the Phenomenex® Luna C_{18} ensure compatibility with standard HPLC instrumentation while maintaining robust separation.

2.3.3.6. Column suitability testing

Column suitability testing is a foundational practice in chromatographic analysis. By evaluating theoretical plates (*N*) for efficiency, asymmetry factor (A_s) for peak symmetry, retention factor (*k'*) for elution consistency, and resolution (R_s) for peak separation. This process ensures the reliability and reproducibility of experimental data.

2.3.3.6.1. Theoretical plate number

The theoretical plate number (*N*) is a measure of chromatographic column efficiency, reflecting the column's ability to separate analytes into sharp, well-resolved peaks [66,86,87]. It is derived from the concept of a theoretical plate, a band/zone where equilibrium between the mobile and stationary phases occurs [66,86,87]. A higher N value indicates greater efficiency, as more theoretical plates enhance peak resolution and minimize band broadening [66,86,87]. The *N* is calculated in Equations 2.10 or 2.11 [66,86,87].

$$N = 16 \left(\frac{t_r}{w_b}\right)^2 \qquad \textit{Equation 2.10}.$$

$$N = 5.54 \left(\frac{t_r}{w_{\frac{1}{2}}}\right)^2 \qquad \textit{Equation 2.11}.$$

Where:

N = number of theoretical plates of a column

t_r = the retention time of the molecule

w_b = the width of the peak at the baseline

$w_{½}$ = the width of the peak at one half the maximum height

The suitability of the column was evaluated using a test solution mixture of uracil, naphthalene, acetophenone, benzene and toluene in ACN. Separation was achieved using a mobile phase of ACN:H_2O 65:35 v/v ratio and was performed at ambient temperature (25°C) with an injection volume of 20 µL. The flow rate and detection wavelength were 1.0 mL/min and 254 nm respectively. A column may be considered suitable for routine HPLC analysis if a theoretical plate number is > 2000 [88]. The average theoretical plate number of the column was 5256 ± 0.312. Since the N was above 2000, the column was used for the development and validation of a RP-HPLC method for the analysis AZI.

2.3.3.6.2. Resolution factor

The resolution factor (R_s) quantifies the degree of separation between two adjacent chromatographic peaks, ensuring distinct analyte identification and accurate quantification [66,86,87]. The R_s is calculated in Equations 2.12 [66,86,87].

$$R_s = \frac{t_{R_2} - t_{R_1}}{0.5\left(t_{w_1} + t_{w_2}\right)} \qquad \textit{Equation 2.12}.$$

Where:

t_{R_1} = retention time of first peak

t_{R_2} = retention time of second pea

t_{w_1} = width of first peak at baseline

t_{w_2} = width of second peak at baseline

A resolution value ≥1.5 indicates baseline separation, ensuring peaks are fully resolved for reliable integration [66,86,87]. The Rs between AZI and CLA was 2.71 (0.21% RSD), indicating that the peaks were well-resolved and the column was suitable.

2.3.3.6.3. Asymmetry factor

The asymmetry factor (A_s) or peak tailing factor (*PTF*) is used to estimate peak symmetry and tailing. A_s or *PTF* is evaluated at 10% and 5% of peak height, making it sensitive to subtle fronting or tailing caused by column overload, poor packing, or secondary interactions [66,86,87]. The A_s and *PTF* is calculated in Equations 2.13 and 2.14 respectively [66,86,87].

$$As = \frac{B}{A} \qquad \textbf{\textit{Equation 2.13}}.$$

$$PTF = \frac{A + B}{2A} \qquad \textbf{\textit{Equation 2.14}}.$$

Where:

A = Distance between the middle point and the left side of the peak

B = Distance between the middle point and the right side of the peak

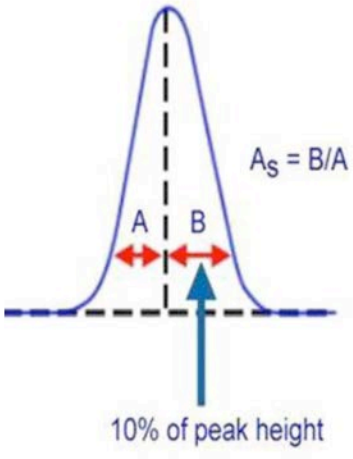

Figure 2.4. Peak asymmetry determination. Adapted from [87].

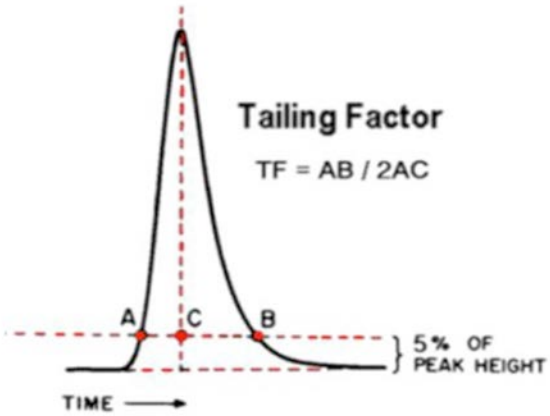

Figure 2.5. Peak tailing factor determination. Adapted from [87].

Columns that are efficient produce an A_s values ranging between 0.95 and 1.1. Ideally the A_s and *PTF* value should be ≤ 2 according to FDA guidelines [88].

2.3.3.6.4. Capacity factor

The capacity factor (k') is a parameter that quantifies the retention of an analyte on a column relative to an unretained compound [66,86,87]. It provides insights into the interaction between analytes and the stationary phase [66,86,87]. The ideal range is between 2 and 10 [66,86,87]. The *k'* is calculated in Equations 2.15 [66,86,87].

$$k' = \frac{t_R - t_M}{t_M} \qquad \textit{Equation 2.15}.$$

Where:

t_R = Retention time of the analyte

t_M = Void time of the column

The *k'* value for AZI was 6.91 (0.14% RSD) using CLA as an un-retained compound and on this basis the column was appropriate for use.

2.3.3.7. Method of detection

Ultraviolet-visible (UV-vis) detection is a widely utilized technique for the analysis of AZI and requires careful optimisation due to the compound's limited UV absorption properties [18,89]. AZI lacks a strong conjugated chromophore, resulting in weak absorption in the UV region. However, its detection is feasible at lower wavelengths 210-220 nm [18,89]. UV detection is a practical choice for analysing AZI due to its low cost, as it is cheaper to run and maintain than advanced techniques like LC-MS [90]. It is simple to use, requiring no complex chemical steps

or extra reagents, which speeds up testing. UV detection meets FDA and USP guidelines for checking AZI in medicines, ensuring quality and safety. UV-vis spectrophotometry is represented in Equation 2.16.

$$I_T = I_0 e^{-kLc} \qquad \textit{Equation 2.16}.$$

Where:

I_T = intensity of the transmitted light

I_o = intensity of light entering the cell

L = optical path length

c = solute concentration

k = constant

The λ_{max} of AZI was 206 nm (Figure 1.3, §1.2.6). This wavelength was used for the quantitation of AZI in subsequent studies.

2.4. METHOD OPTIMISATION

A computer-generated rotatable CCD design consisting of 30 experiments, 6 centre, 8 axial, and 16 factorial points was generated using Version 13.0.5 Design Expert® statistical software (Stat-Ease Inc., Minneapolis, MN, USA). The design parameters and experimental configuration are comprehensively outlined in Table 2.2. The minimum and maximum values for buffer molarity (X_1) were maintained at 20 mM and 40 mM, with the lower and upper axial points at 10 mM and 50 mM. Similarly, pH 6.5 and pH 7.5 were the minimum and maximum values for buffer pH (X_2), with the lower and upper axial values maintained at pH 6 and pH 8. The ACN concentration (X_3) was kept at minimum and maximum values of 65% v/v and 75% v/v with respect to buffer concentration, with the lower and upper axial levels of 60% v/v and 80% v/v. Temperature (X_4) was kept at a minimum and maximum values of 30°C and 50°C, with a lower and upper axial level of 20°C and 60°C. The independent input variables and ranges were selected based on preliminary studies, and the retention time (Y_1) of AZI peak, peak resolution (Y_2) and peak symmetry (Y_3) were the dependent output responses monitored. The data generated from the responses monitored were analysed using Design Expert® version 13.0.5 statistical software (Stat-Ease Inc., Minneapolis, MN, USA). Fisher's test for analysis of variance (ANOVA) was used to establish whether significant differences existed between the mean of the factors investigated.

Table 2.2. Randomised experimental runs conducted to assess the impact of method parameters on the analysis of AZI

Run	Factor 1 A: Acetonitrile %	Factor 2 B: pH	Factor 3 C: Buffer Molarity mM	Factor 4 D: Temperature Degree Celsius
1	70	7	10	40
2	70	7	30	60
3	70	6	30	40
4	70	7	30	40
5	75	6.5	40	50
6	65	7.5	40	30
7	75	6.5	40	30
8	65	6.5	40	30
9	70	7	50	40
10	70	7	30	20
11	65	6.5	40	50
12	65	6.5	20	30
13	70	7	30	40
14	60	7	30	40
15	65	6.5	20	50
16	70	8	30	40
17	70	7	30	40
18	65	7.5	20	30
19	65	7.5	20	50
20	75	7.5	40	50
21	75	6.5	20	30
22	65	7.5	40	50
23	80	7	30	40
24	70	7	30	40
25	75	6.5	20	50
26	70	7	30	40
27	75	7.5	20	50
28	75	7.5	20	30
29	75	7.5	40	30
30	70	7	30	40

All runs were randomized to minimize bias, ensuring the validity and reproducibility of the findings. The four independent variables buffer molarity, buffer pH, acetonitrile concentration, and column temperature were adjusted to analyse their effects on the chromatographic performance. The output responses, retention time, peak resolution, and peak tailing, were optimised to enhance separation quality and method reliability. The data was visualized using of 2D contour and one-factor effect plots.

The responses, which encompass the retention times (Y_1) for AZI, resolution factor (Y_2), along with the peak tailing (Y_3) are compiled in Table 2.3. The responses were analysed using Version 13.0.5 Design Expert® statistical software (Stat-Ease Inc., Minneapolis, MN, USA). The software fitted mathematical models between independent variables and responses as well as using ANOVA to identify the significance of each variable [91]. The software also estimated model coefficients using regression analysis, and assessed model adequacy through R^2, Adjusted R^2, and Predicted R^2 values [91]. The software also performed residual analysis and lack-of-fit tests to ensure model accuracy [91].

Table 2.3. Responses observed for CCD input variables.

Run	Response 1 (Y_1) Retention Time Minutes	Response 2 (Y_2) Resolution	Response 3 (Y_3) Peak Tailing
1	6.013	2.4302	1.2733
2	6.933	3.9190	1.2933
3	5.712	1.2620	1.3225
4	7.022	3.4871	1.3115
5	4.214	0	8.5239
6	9.098	3.3238	1.4725
7	2.750	1.1309	1.9163
8	2.407	1.4105	1.6682
9	6.465	2.6541	1.3214
10	4.279	0	1.1750
11	10.040	3.6669	1.4185
12	2.406	2.4880	1.6041
13	6.997	3.5219	1.2122
14	7.164	1.2795	1.3083
15	5.285	0	1.1760
16	8.640	5.1103	1.4826
17	6.403	2.7667	1.3347
18	9.634	4.0303	1.4533
19	10.788	6.1517	1.4371
20	6.605	4.1959	1.3358
21	2.813	1.0149	8.4170
22	10.298	4.9690	1.3562
23	5.132	2.7203	1.3958
24	5.890	2.1642	1.2674
25	4.876	1.4276	1.1267
26	5.872	2.1787	1.2730
27	6.708	4.5568	1.5230
28	5.013	1.9672	1.2665
29	6.459	3.1334	1.3876
30	5.911	2.2189	1.2812

2.4.1. Retention time (R_t) of AZI

The data was fitted to a linear regression model, and ANOVA was employed to assess the significance of the model and its individual factors. The results summarized in Table 2.4 indicate that the model is statistically significant, with an F-value of 14.21 and a p-value < 0.0001, demonstrating that at least one of the factors significantly influences retention time. pH (B) had the strongest effect on retention time (F = 29.41, p < 0.0001), followed by acetonitrile content (A) (F = 13.97, p = 0.0010) and column temperature (D) (F = 12.81, p = 0.0014), all of which were statistically significant. Buffer molarity (C) was not significant (F = 0.6376, p = 0.4321), suggesting that changes in buffer concentration do not strongly impact retention time within the tested design space.

The residual sum of squares of 45.06 with 25 degrees of freedom, and a lack of fit was found to be significant (F = 7.23, p = 0.0187). A significant lack of fit suggests that the model may not fully capture all systematic variations in retention time, potentially due to missing interaction terms or nonlinear effects. The pure error sum of squares was minimal (1.51, df = 5), indicating that experimental replicates were consistent.

Table 2.4. ANOVA data table for R_t of AZI

Source	Sum of Squares	df	Mean Square	F-value	p-value	
Model	102.43	4	25.61	14.21	< 0.0001	significant
A-Acetonitrile	25.18	1	25.18	13.97	0.0010	
B-pH	53.01	1	53.01	29.41	< 0.0001	
C-Buffer Molarity	1.15	1	1.15	0.6376	0.4321	
D- Column Temperature	23.09	1	23.09	12.81	0.0014	
Residual	45.06	25	1.80			
Lack of Fit	43.56	20	2.18	7.23	0.0187	significant
Pure Error	1.51	5	0.3012			
Correction Total	147.49	29				

The adequacy of the model was assessed as presented in Table 2.5. The $R^2 = 0.6945$ indicates that 69.45% of the variability in retention time is explained by the model, which is acceptable but suggests room for improvement. The adjusted R^2 (0.6456) is slightly lower, indicating potential overfitting due to the inclusion of a non-significant term (buffer molarity), but since

the difference is less than 0.2 shows reasonable agreement. The predicted R^2 (0.5278) is substantially lower than the adjusted R^2, implying that the model has limited predictive power and may not generalise well to unseen data. Adequate precision (13.5384), a measure of the signal-to-noise ratio, exceeds the recommended threshold of 4, confirming that the model is suitable for optimisation purposes. However, the coefficient of variation (C.V. = 21.44%) is relatively high. Despite these limitations, the model is still suitable for optimisation within the tested design space, but further refinement would enhance its reliability. To further assess the adequacy of the model and its sufficiency for continued optimisation, other diagnostic plots will be analysed, which include the Box-Cox plot (Figure 2.6), the normal probability plot of residuals (Figure 2.7), the Pareto plot of residuals versus experimental runs (Figure 2.8), and the observed versus predicted response plot (Figure 2.9).

Table 2.5. Statistical measures of model adequacy

Statistic	Values
R^2	0.6945
Adjusted R^2	0.6456
Predicted R^2	0.5278
Adequate Precision	13.5384
SD	1.34
Mean	6.26
Coefficient of variation %	21.44

The regression coefficients shown in Equation 2.17 reveal that an increase in ACN concentration results in a decrease in R_t, where higher organic content reduces analyte interaction with the stationary phase. Conversely, an increase in pH significantly increases R_t, due to changes in the ionization state of AZI, which in turn affects its interaction with the column. AZI contains tertiary amines that can participate in ionization (§ 1.2.3). At lower pH, AZI is protonated, causing repulsion with silanol groups on the stationary phase, which reduces hydrophobic interactions and shortens R_t. As pH increases, AZI becomes deprotonated, allowing stronger hydrophobic interactions with the stationary phase, leading to longer R_t. This aligns with the observed strong positive coefficient for pH (+2.97233), confirming that AZI retention is highly pH dependent. Buffer molarity had a negligible impact on R_t, as indicated by the near-zero coefficient (0.021883) and non-significant p-value. Temperature showed a slight positive effect on R_t, which could be attributed to viscosity changes in the mobile phase

at elevated temperatures. Higher temperatures make the mobile phase less viscous, allowing AZI to move more easily. While this usually speeds up elution, the slight increase in R_t suggests AZI may interact more with the stationary phase. The model's variance inflation factors (VIFs) were all 1, indicating no multi-collinearity among the independent variables.

$$AZI\ R_t = -4.78610 - 0.204850(A) + 2.97233(B) + 0.021883(C) + 0.098092(D) \quad \textbf{Equation 2.17.}$$

Where:

A = Acetonitrile content as a %,

B = pH

C = buffer molarity (mM), and

D = column temperature as °C

2.4.1.1. Box-Cox plot evaluation of model adequacy for R_t of AZI

The Box-Cox plot was generated to assess whether a transformation of R_t variable is required to meet the assumptions of normality and homoscedasticity in the regression model. The Box-Cox lambda (λ) determines the optimal transformation that should be applied to the response variable to improve model performance. From Figure 2.6, the current λ value (green line) is 1, lies within the 95% confidence interval for λ (0.12 to 1.56), indicating that the data do not require transformation, as the response variable already follows a normal distribution with stable variance.

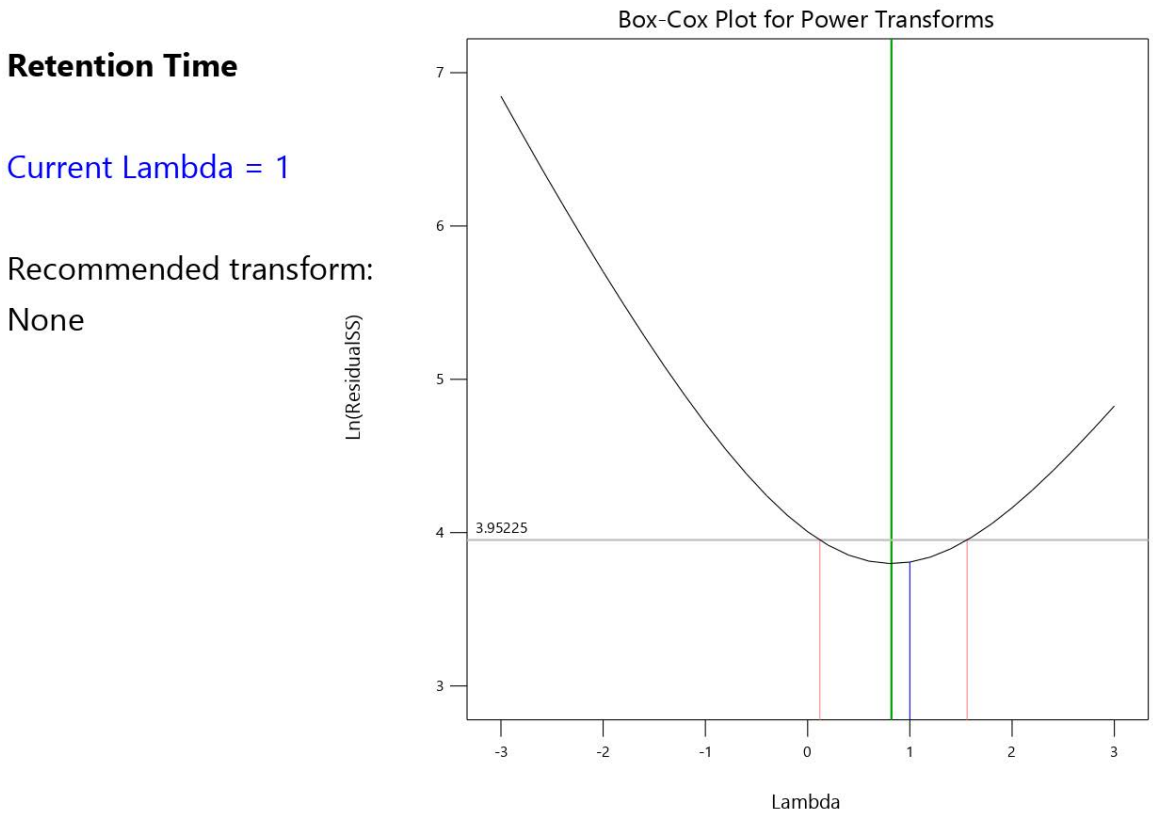

Figure 2.6. Box-Cox plot for the impact of solvent content on Rt analysis.

2.4.1.2. Evaluation of model fit for R_t of AZI

The normal plot of residuals is used to assess whether the residuals of the regression model follow a normal distribution. If the data points closely follow the reference straight line, it suggests that the residuals are normally distributed, ensuring the validity of ANOVA. In Figure 2.7, the residuals exhibit an approximately linear trend along the red reference line, indicating that the assumption of normality is met. There are minor deviations at the extremes, but these do not indicate major violations of normality. The colour points represent different column temperatures (30°C to 50°C), suggests that temperature does not introduce bias.

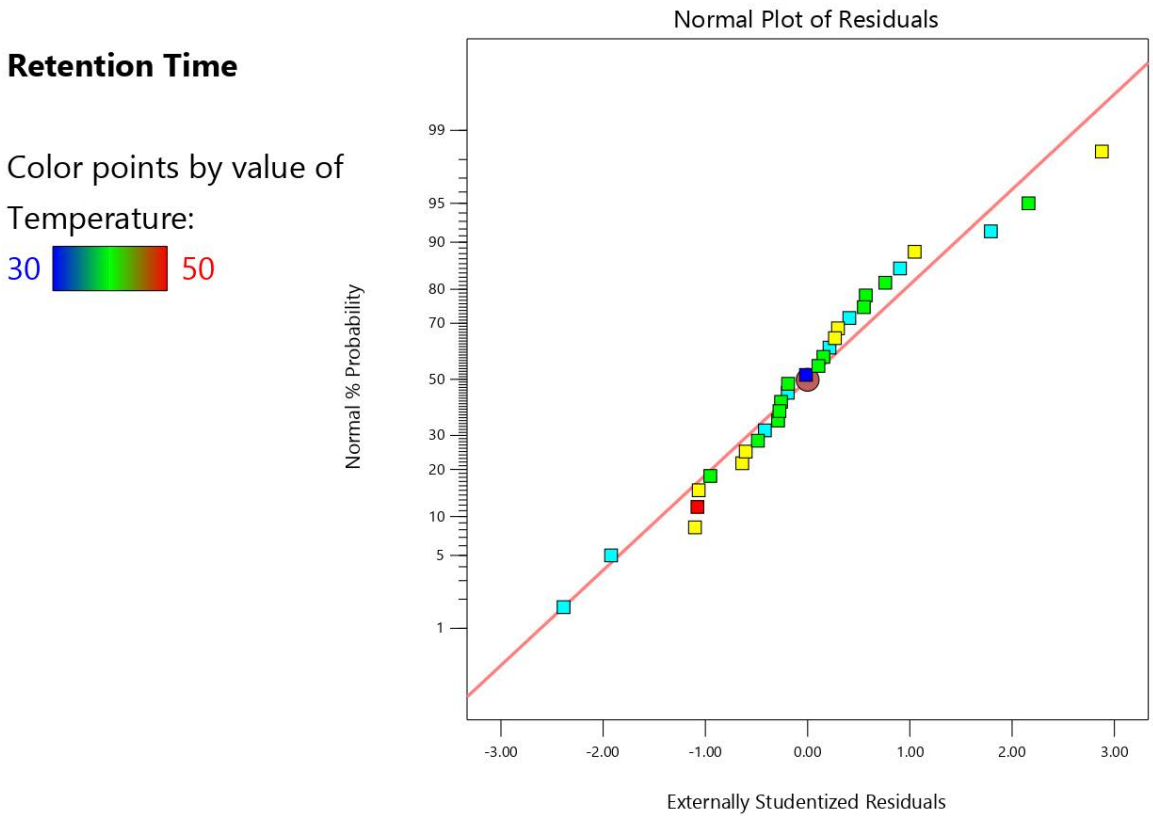

Figure 2.7. Normal plot of residuals depicting the impact of model terms on the Rt of AZI.

The residuals vs. run plot shows the randomness of residuals across experimental runs. The residuals should be randomly scattered around zero, without clear patterns, indicating that the model does not suffer from bias or systematic errors. In Figure 2.8, the residuals appear randomly distributed around the zero line, with no clear increasing or decreasing trend over the experimental runs. This confirms that there is no bias in the experimental design.

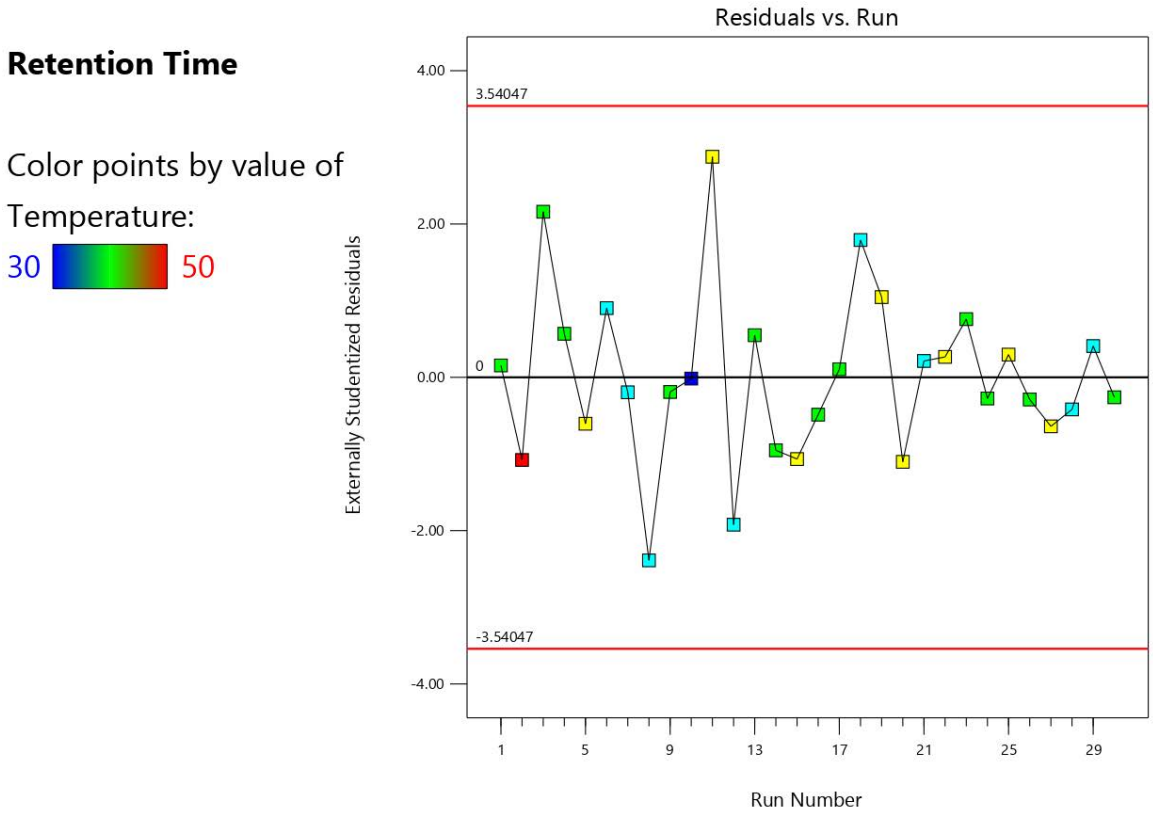

Figure 2.8. Pareto plot of residuals versus experimental runs.

The predicted vs. observed plot evaluates how well the model predictions align with the actual experimental data. The data points should be closely aligned along the reference line, indicating a strong correlation between observed and predicted R_t. In Figure 2.9, most data points fall near the reference line, indicating a reasonable fit between experimental results and model predictions. However, some deviations are noticeable at higher retention times, suggesting minor prediction errors. The colour distribution along the reference line suggests that temperature does not significantly impact model prediction accuracy. Despite some variation, the overall trend follows the expected reference line, confirming that the model has acceptable predictive accuracy.

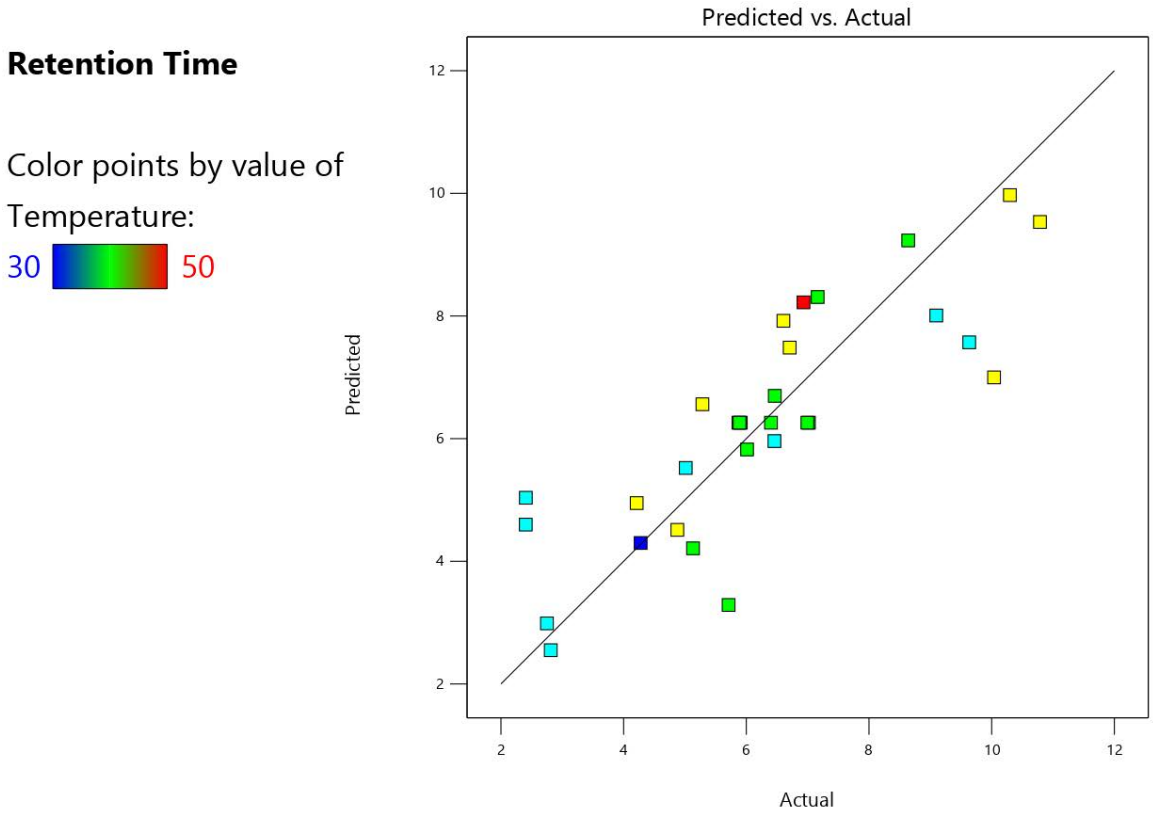

Figure 2.9. Observed versus predicted response plot for Rt of AZI.

2.4.1.3. Graphical interpretation and evaluation of the model for R_t of AZI

The perturbation plot (Figure 2.10) provides a graphical representation of how each independent variable influences the R_t of AZI while keeping all other factors constant. This allows for a direct comparison of the sensitivity of the response to each factor. The steepness of each line indicates the strength of the variable's effect on R_t, with steeper slopes suggesting a more significant influence. In Figure 2.10, the perturbation plot shows the impact of ACN content (A), pH (B), buffer molarity (C), and temperature (D) on R_t. The lines representing factors A and B show the most pronounced slopes, confirming that these variables have the strongest influence on R_t which aligns with § 2.4.1. The negative slope of A indicates that an increase in ACN content decreases R_t. Slope B shows a positive slope, stating the trend that higher pH leads to longer R_t. Slope C and D show minimal influence, as indicated by the near horizontal nature of their lines. This supports previous findings from ANOVA, where buffer molarity was statistically insignificant.

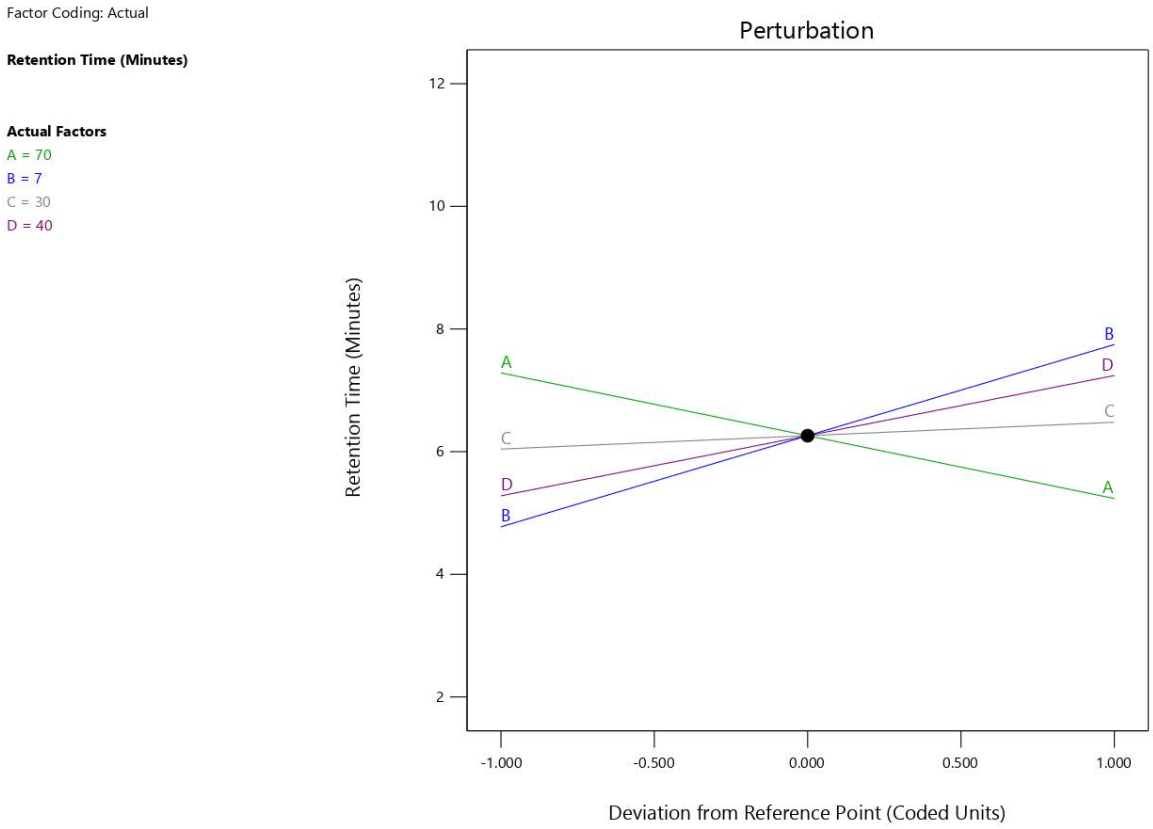

Figure 2.10. Perturbation plot demonstrating the impact of input variables on Rt of AZI.

2.4.1.4. Response surface model plots for Rt of AZI.

The contour plot (Figure 2.11) and the 3D surface plot (Figure 2.12) are graphical representations used in RSM to analyse and visualize the effect of independent variables on a response. Figure 2.11 shows how ACN and pH affect R_t. The colour gradient represents changes in R_t. Lower R_t values are represented in the blue region and higher R_t values in the green and yellow regions. The diagonal pattern of the contour lines indicates that both ACN and pH influence R_t. As ACN increases, R_t decreases, which aligns with § 2.4.1. Figure 2.12 provides a three-dimensional representation of the same relationship, illustrating the combined effect of ACN and pH on R_t. The surface slopes downward along the ACN axis, confirming that increasing ACN leads to faster elution. Along the pH axis, the surface rises, reinforcing that higher pH results in longer R_t. The smooth nature of the surface suggests a predictable interaction between these two factors without changes.

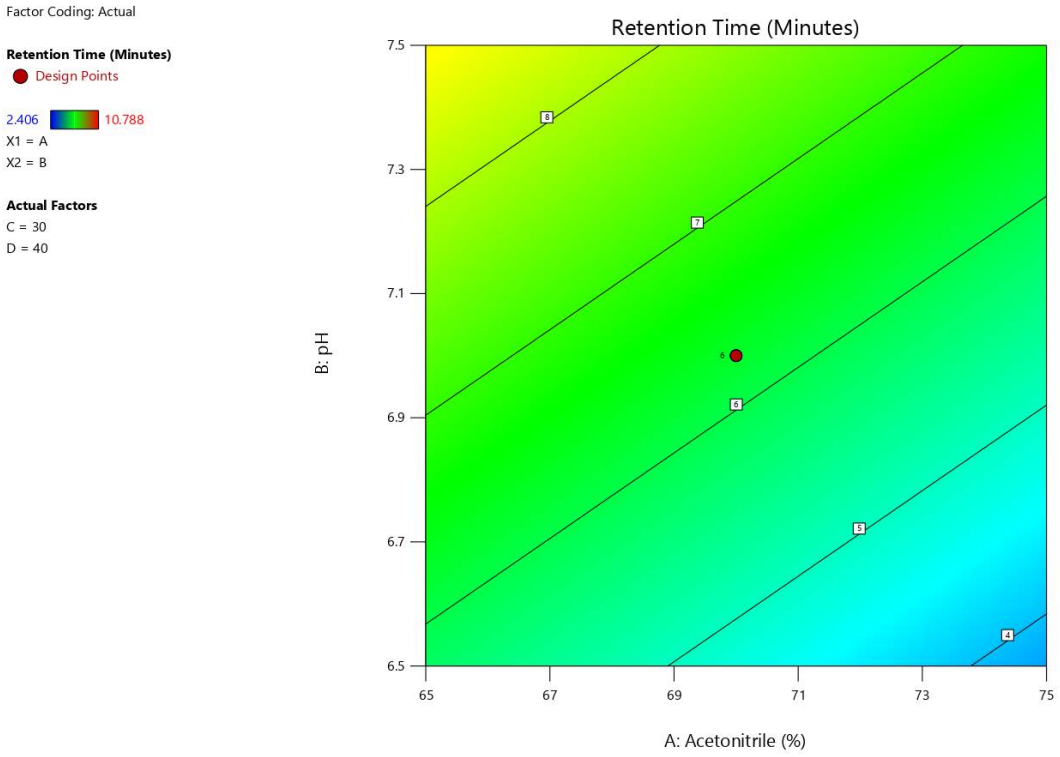

Figure 2.11. Contour plot depicting the impact of ACN content and pH on Rt of AZI.

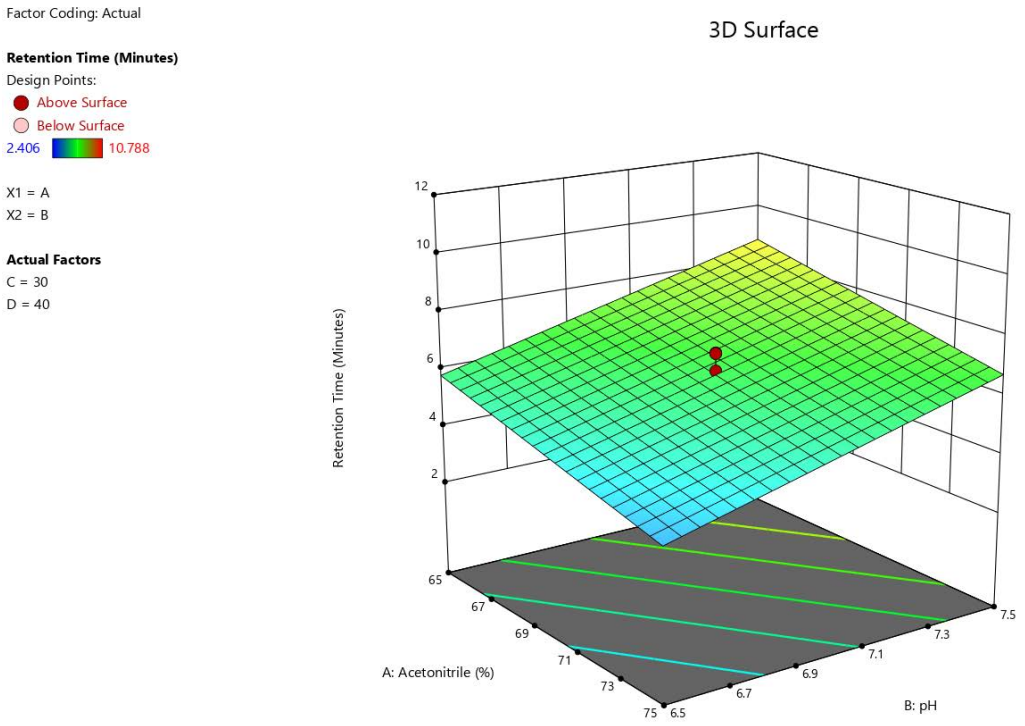

Figure 2.12. 3D response surface plot depicting the impact of ACN content and pH on Rt of AZI.

The contour plot (Figure 2.13) illustrates the effect of ACN and buffer molarity on R_t. The colour gradient remains uniform, indicating minimal variation in R_t across different buffer molarity concentrations. The parallel contour lines suggest that ACN has a stronger influence on R_t. Increasing ACN leading to shorter R_t, as explained in § 2.4.1. In contrast, changes in buffer molarity show little to no effect on R_t, aligning with previous findings. The 3D response surface plot (Figure 2.14) shows a flat surface along the buffer molarity axis, reinforcing its minimal effect on R_t. The surface slopes downward with increasing ACN, confirming that higher organic content accelerates elution. The absence of significant curvature suggests a linear relationship, with no strong interactions between ACN and buffer molarity.

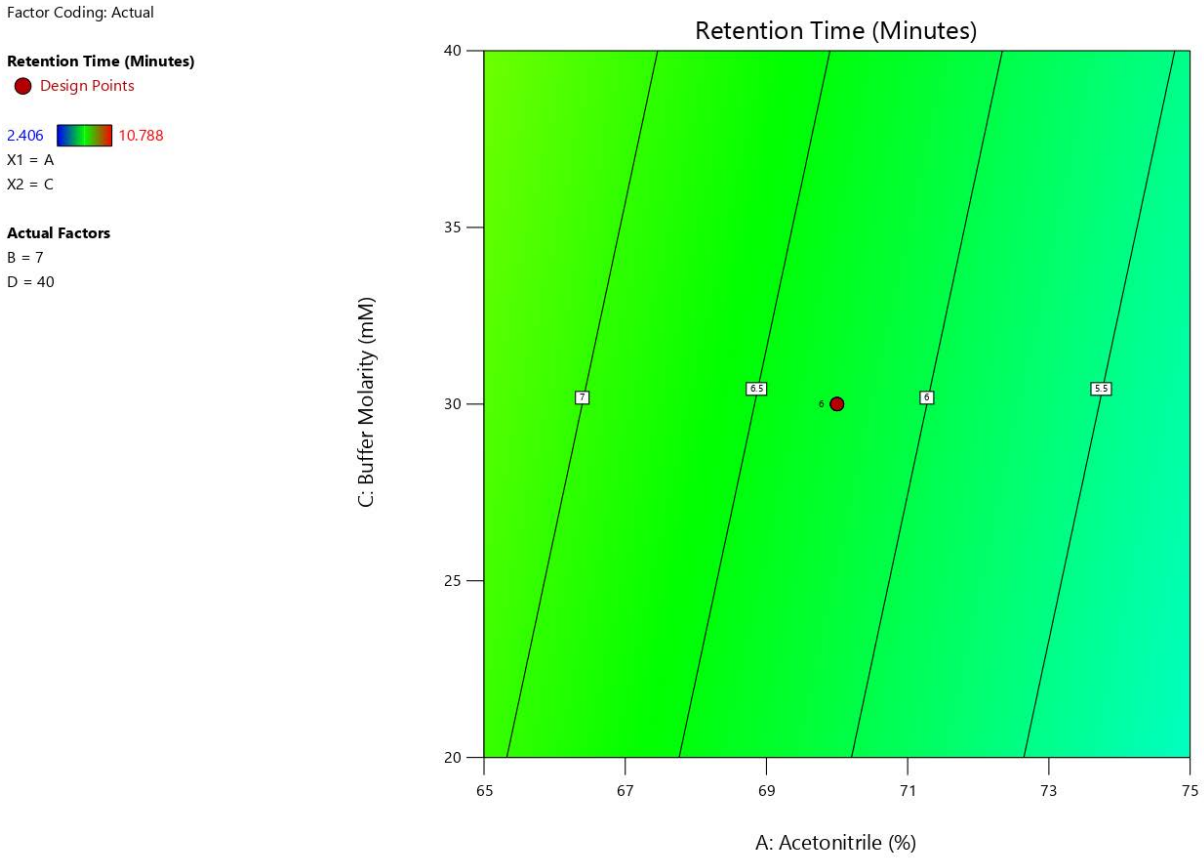

Figure 2.13. Contour plot depicting the impact of ACN content and buffer molarity on Rt of AZI

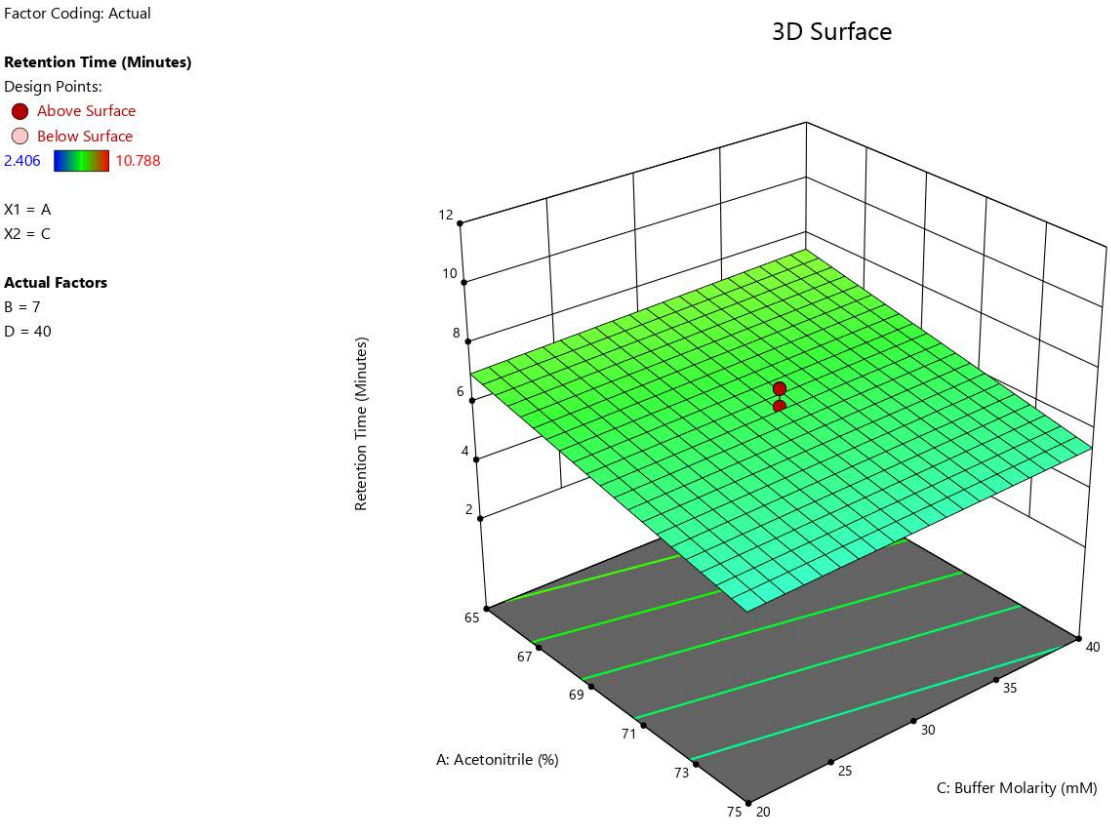

Figure 2.14. 3D response surface plot depicting the impact of ACN content and buffer molarity on Rt of AZI.

The contour plot (Figure 2.15) shows the effect of ACN and column temperature on R_t. The diagonal contour lines suggest that ACN has a stronger influence than temperature, with higher ACN content leading to shorter R_t, as explained in § 2.4.1. The uniform green shading across the temperature axis indicates that temperature has only a slight effect on R_t, confirming its lower effect compared to ACN. The 3D response surface plot (Figure 2.16) shows these trends, with a slope along the ACN axis, reinforcing its role in reducing R_t. The nearly flat surface along the temperature axis suggests minimal influence.

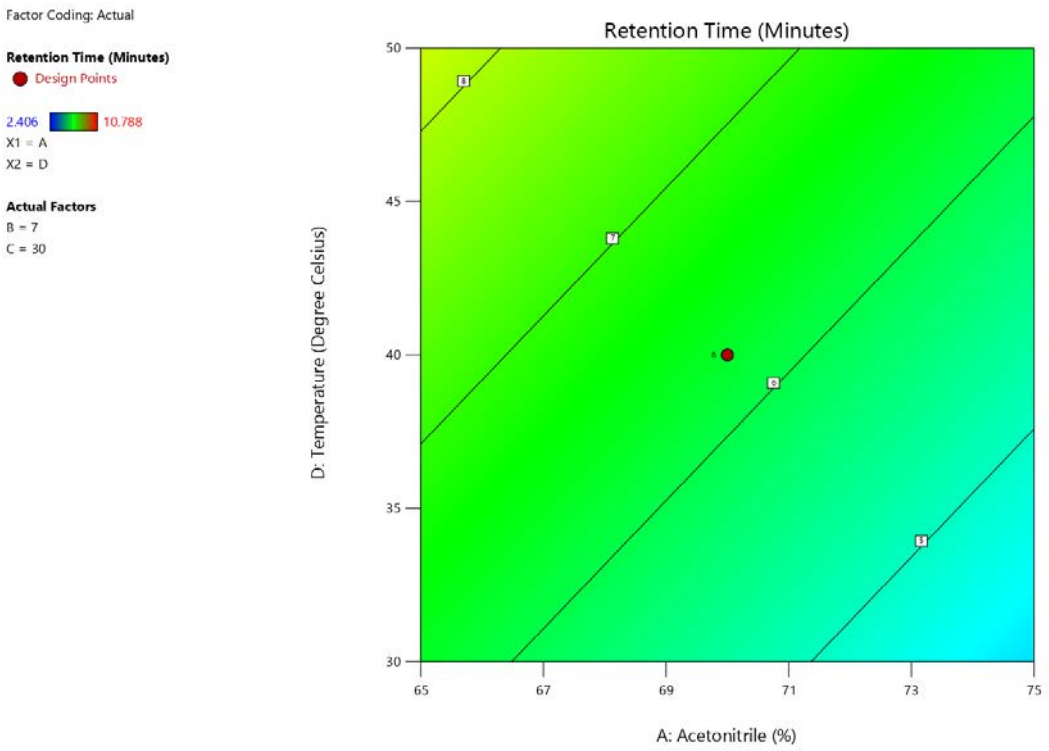

Figure 2.15.Contour plot depicting the impact of ACN content and column temperature on Rt of AZI.

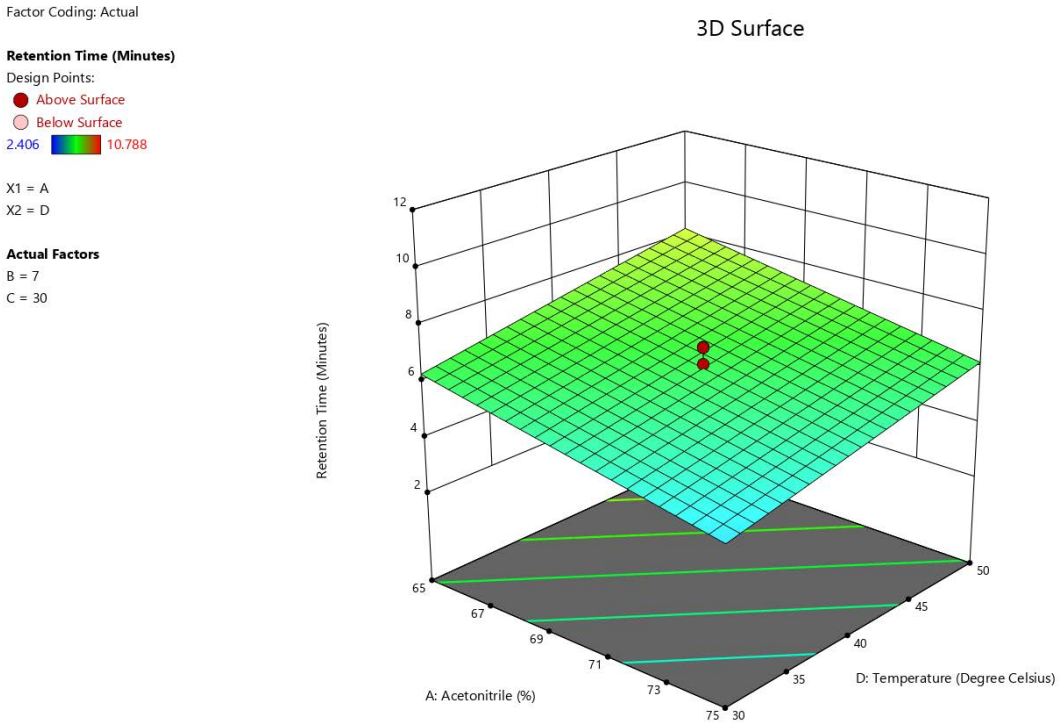

Figure 2.16. 3D response surface plot depicting the impact of ACN content and column temperature on Rt of AZI.

The contour plot (Figure 2.17) shows the effect of pH and buffer molarity on R_t. The nearly vertical contour lines indicate that pH has an impact on R_t, with higher pH leading to longer R_t. This is expected as explained in § 2.4.1. Buffer molarity has little to no effect, as seen from the minimal colour changes in R_t across different molarities. The 3D response surface plot (Figure 2.18) reinforces these findings, showing an upward slope along the pH axis, indicating an increase in R_t with higher pH. The nearly flat surface along the buffer molarity axis further confirms its minimal effect.

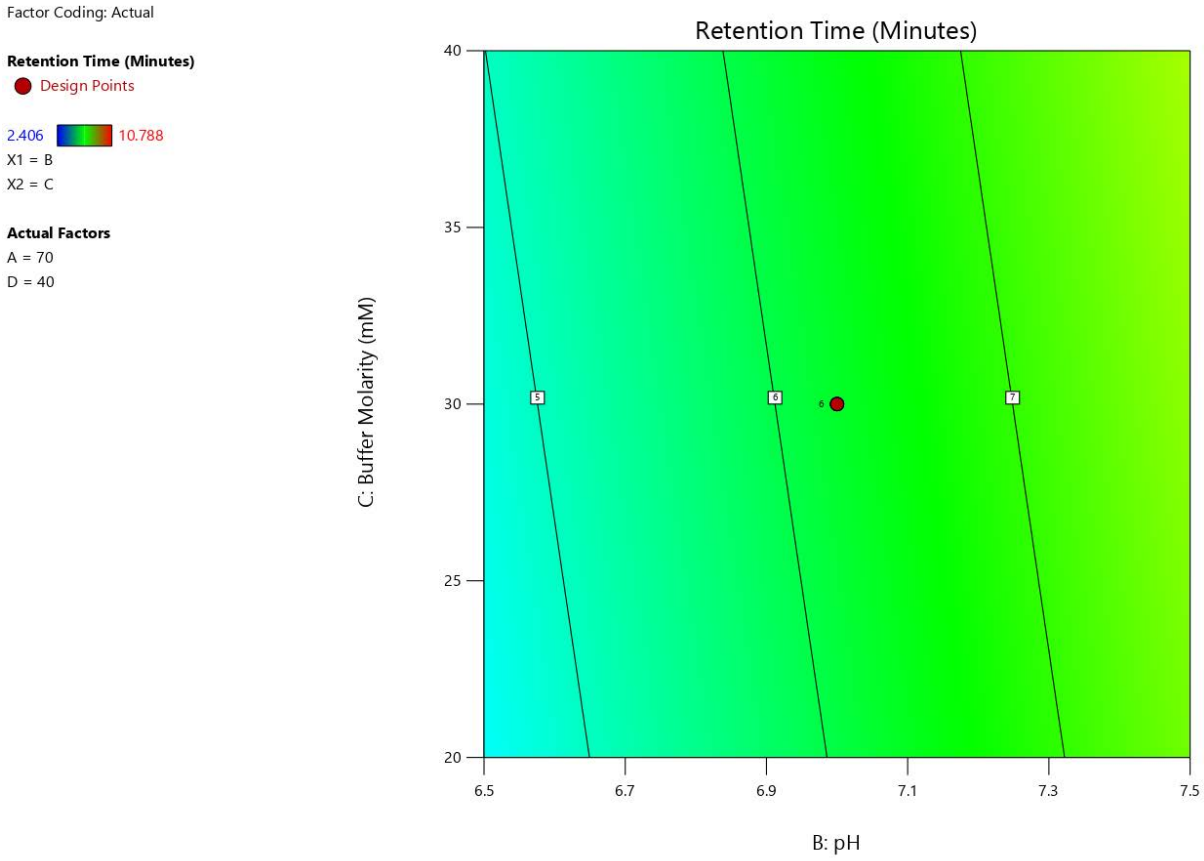

Figure 2.17. Contour plot depicting the impact of pH and buffer molarity on Rt of AZI.

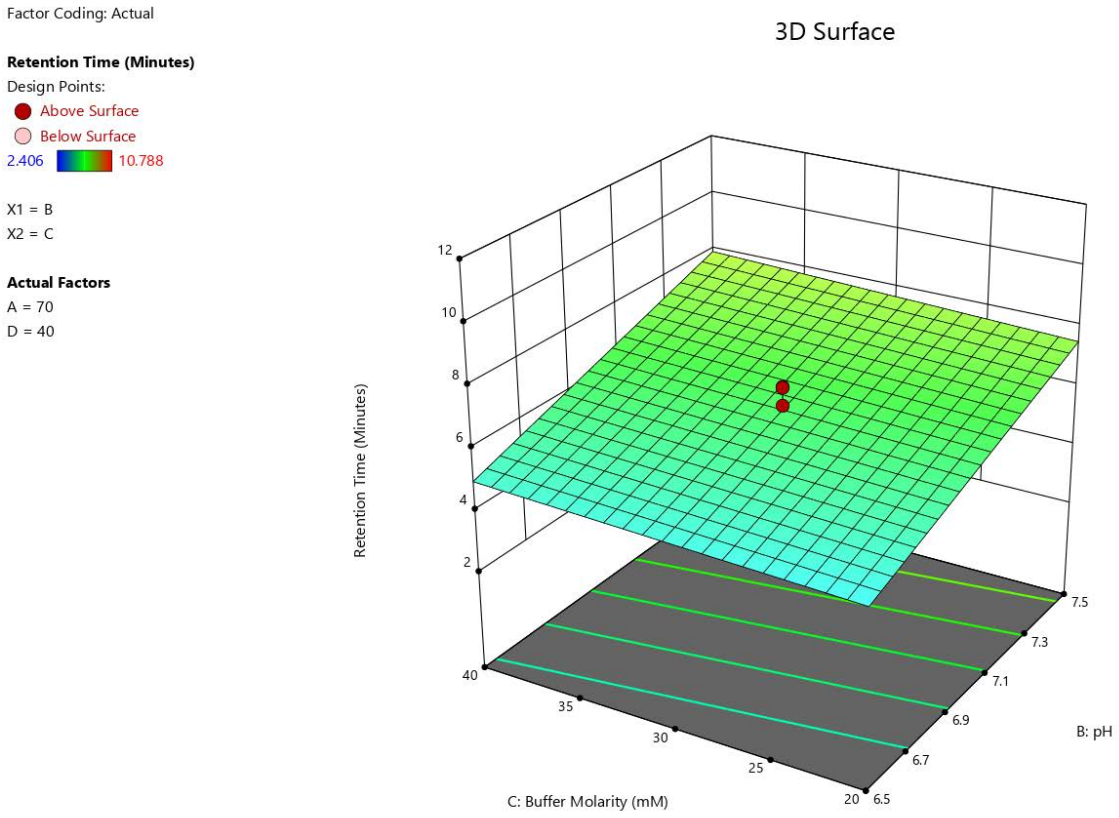

Figure 2.18. 3D response surface plot depicting the impact of pH and buffer molarity on Rt of AZI.

The contour plot (Figure 2.19) illustrates the effect of pH and column temperature on R_t. The diagonal contour lines indicate that both variables have an influence, with pH showing a stronger effect. As pH increases, R_t also increases. Temperature has a smaller effect, but a slight decrease in R_t is observed at higher temperatures. This is expected as explained in § 2.4.1. The 3D response surface plot (Figure 2.20) further confirms these trends. The surface slopes upward along the pH axis, reinforcing that increasing pH leads to longer R_t. Along the temperature axis, the slope is mild, indicating a minor effect, with higher temperatures slightly decreasing R_t. The smooth surface suggests that the interaction between pH and temperature is not significant.

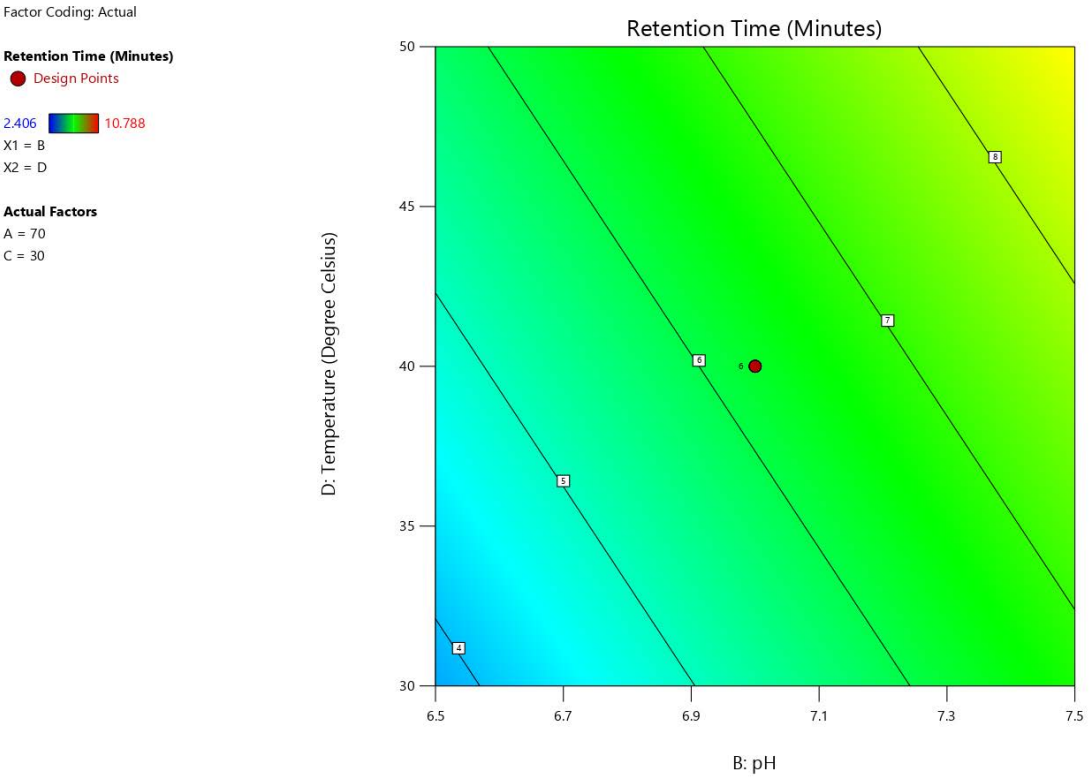

Figure 2.19. Contour plot depicting the impact of pH and column temperature on Rt of AZI.

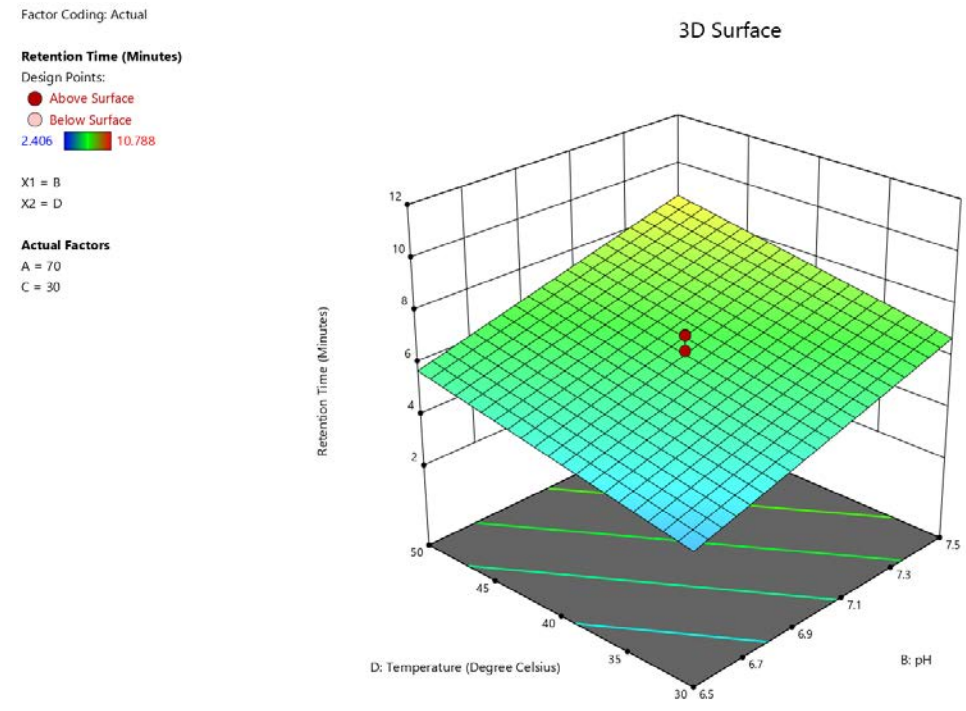

=

Figure 2.20. 3D response surface plot depicting the impact of pH and column temperature on Rt of AZI.

The contour plot (Figure 2.21) illustrates the effect of buffer molarity and column temperature on R_t. The nearly horizontal contour lines suggest that buffer molarity has little to no significant impact on R_t, as the colour gradient remains uniform across different molarities. The slight diagonal trend indicates that temperature has a minor effect, with higher temperatures leading to a slight decrease in R_t. This is expected as explained in § 2.4.1. The 3D response surface plot (Figure 2.22) further confirms these findings, with a nearly flat surface along the buffer molarity axis, reinforcing its negligible effect. The surface slopes slightly downward along the temperature axis, suggesting that higher temperatures lead to shorter R_t, though the effect is minimal.

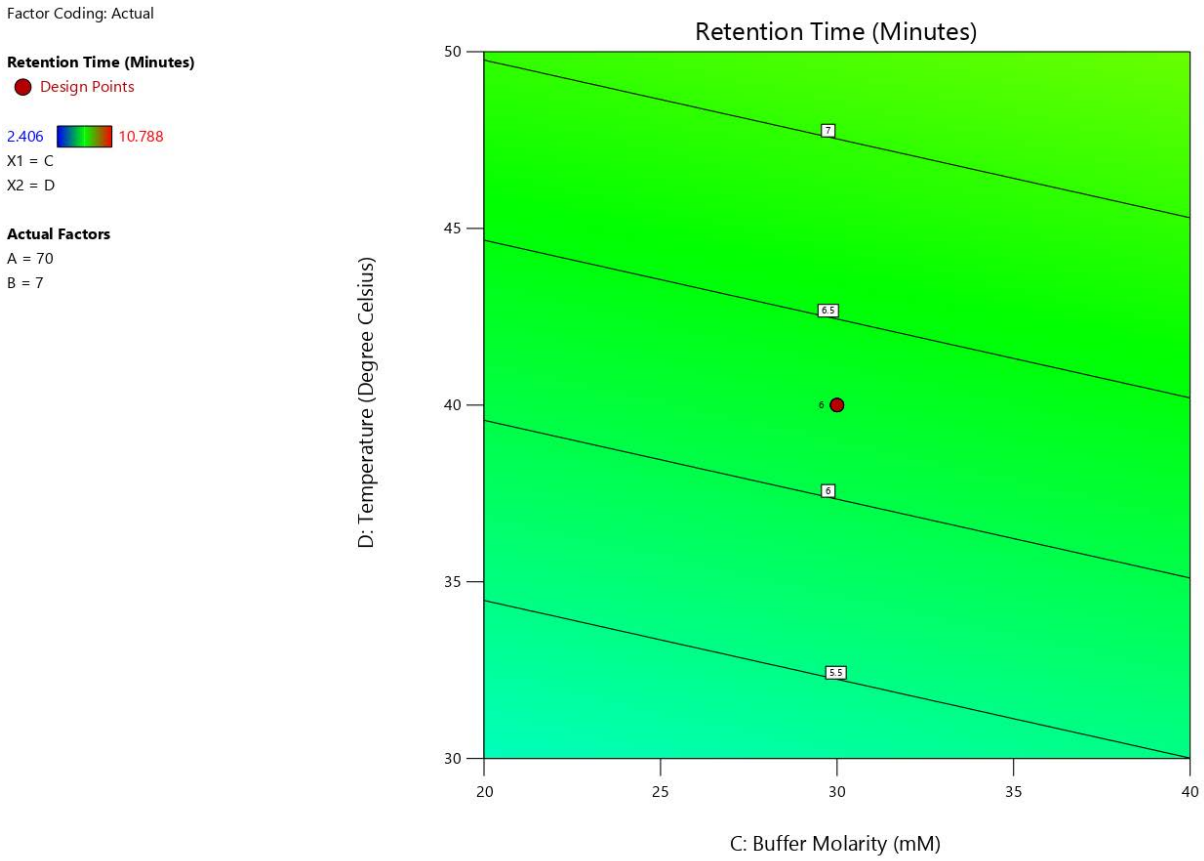

Figure 2.21. Contour plot depicting the impact of buffer molarity and column temperature on Rt of AZI.

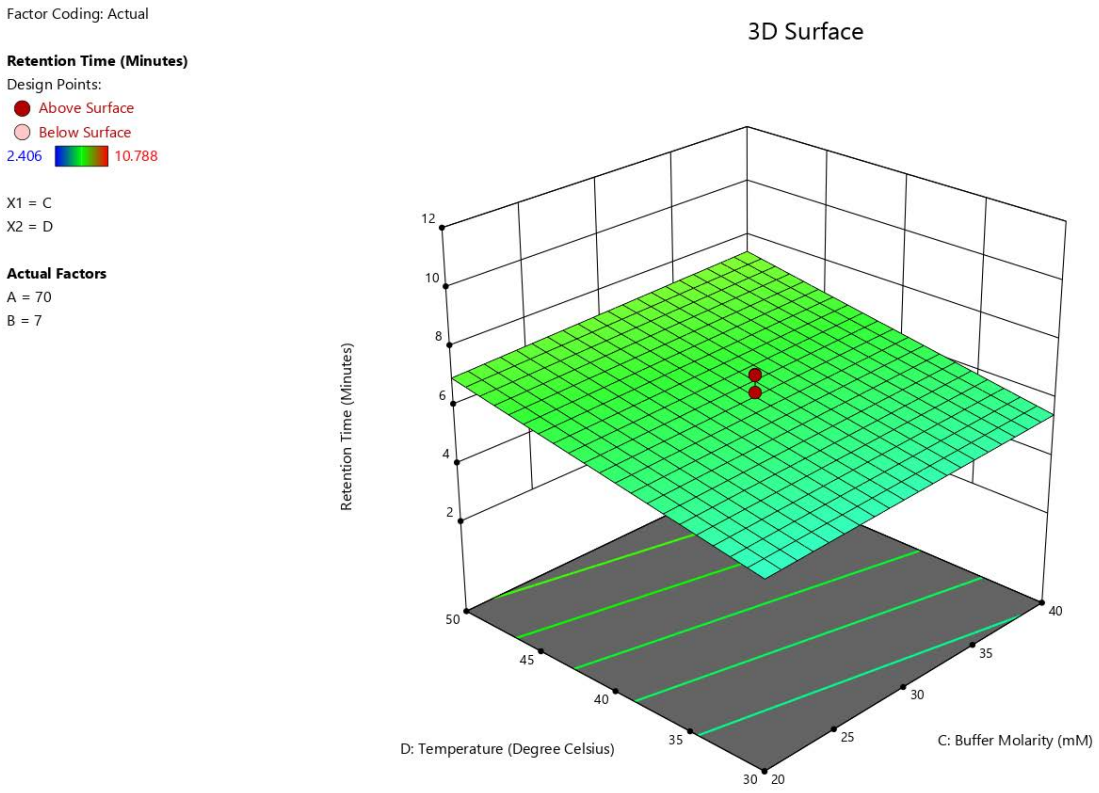

Figure 2.22. 3D response surface plot depicting the impact of buffer molarity and column temperature on Rt of AZI.

2.4.2. Peak resolution (R_s)

The R_s between AZI and CLA was an essential HPLC response and was therefore, also investigated during the optimisation stage of method development. A peak R_s greater than 2 is considered acceptable. The ANOVA analysis presented in Table 2.6 evaluates the peak R_s between AZI and IS. The statistical results indicate that the overall model is significant, with an F-value of 10.82 and a p-value of less than 0.0001, confirming that the selected factors influence R_s. pH had the most impact, with a high F-value of 33.66 and a highly significant p-value of less than 0.0001, demonstrating that even small changes in pH significantly affect the separation between peaks. Temperature also plays a role, with an F-value of 8.26 and a p-value of 0.0082, indicating that fluctuations in temperature influence R_s. In contrast, ACN concentration does not show statistical significance, as evidenced by its F-value of 1.33 and a p-value of 0.2605, suggesting it had little impact. Similarly, the impact of changes to buffer molarity is not significant, with an F-value of 0.0166 and a p-value of 0.8984. The lack of fit

is not significant, with a p-value of 0.1249, indicating that the model accurately fits the experimental data.

Table 2.6. ANOVA data table for R_s of AZI.

Source	**Sum of Squares**	**df**	**Mean Square**	**F-value**	**p-value**	
Model	44.68	4	11.17	10.82	< 0.0001	significant
A-Acetonitrile	1.37	1	1.37	1.33	0.2605	
B-pH	34.77	1	34.77	33.66	< 0.0001	
C-Buffer Molarity	0.0172	1	0.0172	0.0166	0.8984	
D-Temperature	8.53	1	8.53	8.26	0.0082	
Residual	25.82	25	1.03			
Lack of Fit	23.73	20	1.19	2.84	0.1249	not significant
Pure Error	2.09	5	0.4173			
Correction Total	70.50	29				

In Table 2.7, the R^2 value of 0.6338 indicates that 63.38% of the variation is explained by the model, with an adjusted R^2 of 0.5752. The predicted R^2 of 0.4426 suggests moderate predictive capability. Adequate precision of 11.6038 confirms a strong signal-to-noise ratio. The standard deviation is 1.02, with a mean R_s of 2.64 and a coefficient of variation of 38.50%, indicating variability in the response. The model is reasonably adequate for describing R_s trends but has room for predictive improvement.

Table 2.7. Statistical measures of model adequacy.

Statistic	**Value**
R^2	0.6338
Adjusted R^2	0.5752
Predicted R^2	0.4426
Adequate Precision	11.6038
SD	1.02
Mean	2.64
C.V. %	38.50

Equation 2.18 describes the mathematical relationship between peak R_s of AZI and other chromatographic variables. The negative intercept -13.33181 suggests that without the variables, R_s would be very low. The coefficient for pH (B) is 2.40714, showing that pH has the most significant positive effect on R_s, meaning an increase in pH greatly enhances peak separation. Temperature (D) also has a positive impact, with a coefficient of 0.059612, indicating that higher temperatures slightly improve R_s, whereas ACN content (A) had a small negative effect, with a coefficient of -0.047766, suggesting that increasing ACN decreases R_s. Buffer molarity (C) has the smallest effect, with a coefficient of 0.002675, showing minimal impact on separation.

$$AZI\ R_s = -13.33181 - 0.047766(A) + 2.40714(B) + 0.002675(C) + 0.059612(D)$$ ***Equation 2.18***.

Where:

A = Acetonitrile content as a %,

B = pH

C = buffer molarity (mM), and

D = column temperature as °C

2.4.2.1. Graphical interpretation and evaluation of the model for R_s of AZI

The perturbation plot in Figure 2.23 shows the effect of input variables (A,B,C,D) on the peak R_s. The most significant impact is observed with pH, which has the steepest slope, indicating that even small changes in pH result in changes in R_s. The positive slope suggests that increasing pH improves separation, aligning with the ANOVA table where pH had the highest F-value and the lowest p-value. Temperature also has a positive effect, lesser than pH, confirming that higher temperatures enhance R_s. ACN shows a slight negative trend, suggesting that increasing its percentage reduces resolution, which corresponds with its non-significant p-value in the ANOVA results. Buffer molarity has an almost negligible impact, as indicated by its nearly horizontal line, further supported by the statistical analysis showing no significant effect.

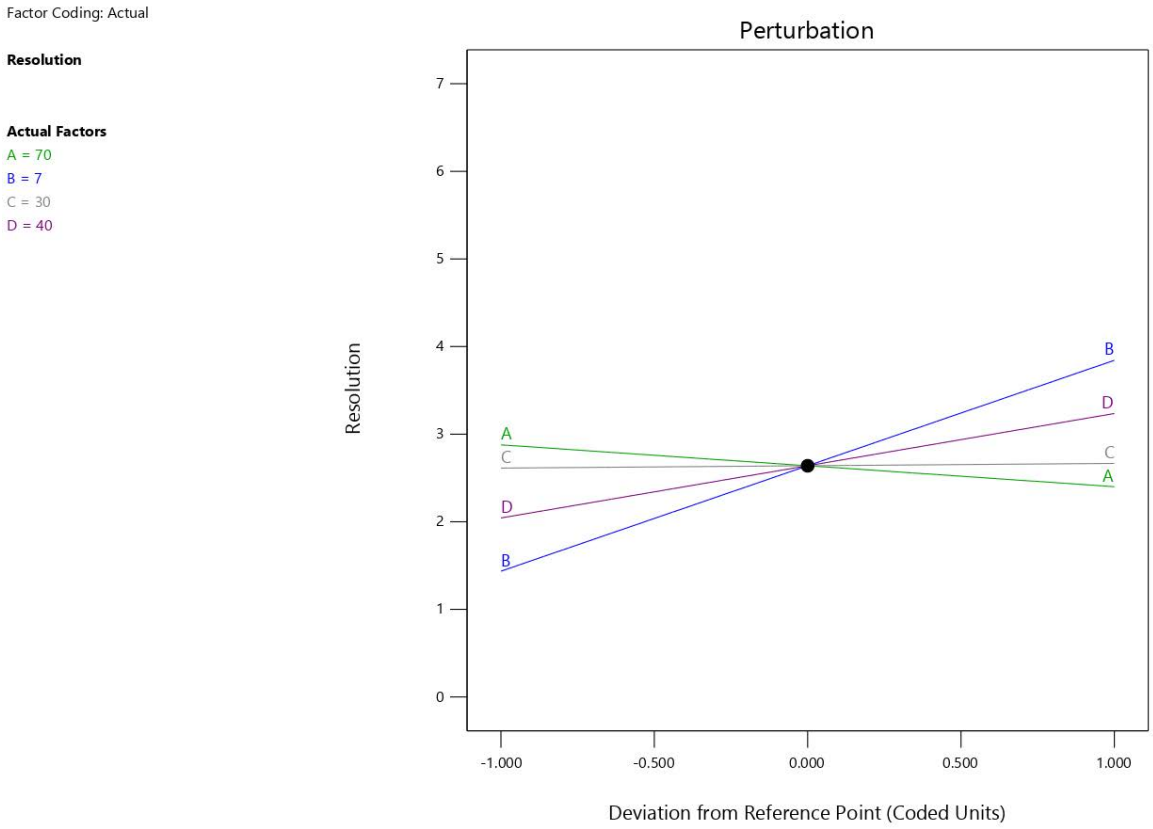

Figure 2.23. Perturbation plot demonstrating the impact of input variables on Rs of AZI.

The contour plot in Figure 2.24 illustrates the combined effect of pH (B) and column temperature (D) on the peak R_s of AZI. The x-axis represents pH, while the y-axis represents temperature. The colour gradient indicates R_s levels, with blue representing lower R_s and green to yellow indicating higher R_s. The plot shows that higher pH and increased temperature lead to improved R_s, as seen from the shift toward the green and yellow regions. This trend aligns with in Table 2.6, where pH had the most significant effect on resolution (F-value = 33.66, p-value < 0.0001), followed by temperature (F-value = 8.26, p-value = 0.0082). The contour lines are nearly parallel, indicating a more dominant influence of pH over temperature, which is consistent with the perturbation plot findings. Regions with lower pH and lower temperatures result in poor R_s, as shown in the blue-shaded areas.

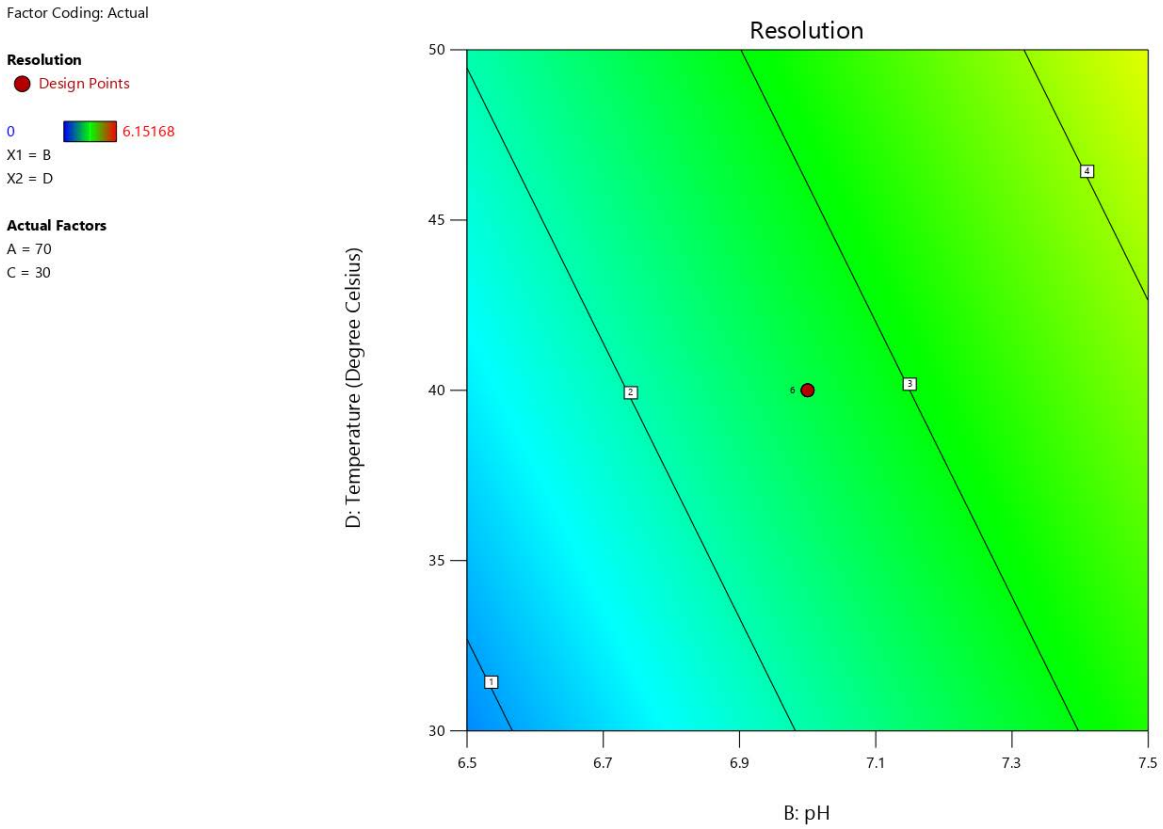

Figure 2.24. Contour plot depicting the impact of pH and column temperature on Rs of AZI.

2.4.3. Peak tailing (P_t) of AZI

P_t is a critical parameter in chromatographic analysis as it affects peak symmetry and resolution. The impact of ACN content, pH, buffer molarity, and column temperature on P_t was evaluated using a Two-Factor Interaction (2FI) model, which considers both individual effects and interaction terms. The ANOVA results indicate that the model is not statistically significant, with an F-value of 1.49 and a p-value of 0.2184. This suggests that the factors do not strongly influence P_t. pH had the highest effect, with an F-value of 3.04 and a p-value of 0.0972, though it did not reach significance, while ACN showed a moderate influence (F-value = 2.19, p-value = 0.1519). Buffer molarity and temperature exhibited minimal effects, with p-values of 0.8972 and 0.8992, respectively.

Interaction effects, such as pH × Acetonitrile (AB) and Buffer Molarity × Temperature (CD), were also found to be insignificant, indicating that these variables do not interact to affect P_t. The lack of fit F-value of 2159.50 (p-value < 0.0001) confirms that the model does not

adequately describe the data, and a higher-order model may be needed for better predictive accuracy. The statistical measures of model adequacy further confirm its weak predictability with an R^2 value of 0.4393, indicating that only 43.93% of the variability in P_t is explained by the model. The adjusted R^2 of 0.1442 suggests that the model does not effectively account for predictor variables, and the negative predicted R^2 (-1.6758) implies that the overall mean response would be a better predictor than the model itself. Despite the adequate precision value of 4.915, which meets the acceptable signal-to-noise ratio threshold, the poor R^2 values and high lack of fit suggest that the model is unreliable for making accurate predictions.

Equation 2.19 suggests that pH and ACN content have the most influence on P_t, with pH having the largest coefficient. Temperature has a minor negative effect, indicating that higher temperatures may slightly reduce P_t, while interaction effects are minimal.

$$AZI\ P_t = -158.99133 + 2.58540(A) + 23.67504(B) + 0.271625(C) - 0.41150(D) - 0.358085(AB) + 0.000722(AC) + 0.000415(AD) - 0.016633(BC) + 0.017099(BD) + 0.008542(CD)$$ ***Equation 2.19***.

Where:

A = Acetonitrile content as a %,

B = pH

C = buffer molarity (mM), and

D = column temperature as °C

The contour plot of ACN content versus pH, presented in Figure 2.25, shows the impact of these two factors on P_t. The x-axis represents acetonitrile percentage, while the y-axis represents pH, with the colour gradient indicating the extent of P_t. Darker blue regions correspond to higher P_t, whereas the lighter blue and green represents lower P_t values. From the plot, it is evident that pH has a more pronounced effect on P_t compared to ACN content, as showed from the gradient change along the pH axis. Increasing pH results in lower P_t, especially a higher pH range. This aligns with the ANOVA table, where pH had a relatively higher F-value compared to other variables. The effect of ACN is less significant but still contributes to variations in P_t. Lower ACN percentages shows a slight reduction in P_t. The contour lines further indicate that the interaction between pH and ACN is not significant, as

the gradient follows a single direction rather than curving sharply. This suggests that pH optimisation is more important for reducing P_t.

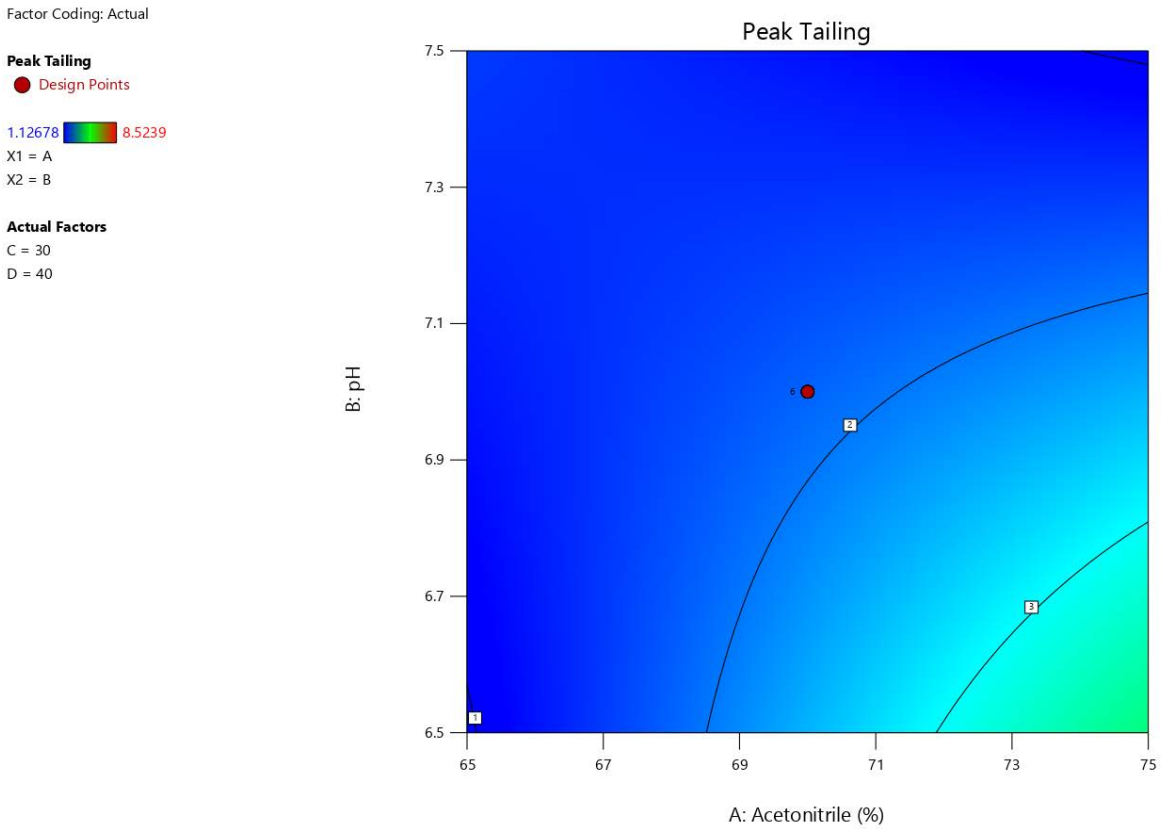

Figure 2.25. Contour plot depicting the impact of ACN content and pH on Pt of AZI.

2.4.4. Optimised chromatographic conditions

The overall solution in Table 2.8 for optimised chromatographic conditions were generated using Design Expert® statistical software (Stat-Ease Inc., Minneapolis, MN, USA).

Table 2.8. Optimised chromatographic conditions for HPLC-UV analysis of AZI.

Process Variable	Optimised conditions
***A* (%ACN content)**	75% (v/v)
***B* (pH)**	7.5
***C* (Buffer molarity)**	20.23mM
***D* (Column temperature)**	37.6°C

A typical chromatogram of the separation of AZI and CLA (IS) was generated using these conditions is shown in Figure 2.26. It is evident that both peaks sharp and well-resolved. AZI

obtained R_t of 6.488 and CLA R_t of 5.282 minutes. The retention times were suitable for the analysis of AZI as the total run time for sample analysis was less than 10 minutes. The % RSD for the R_t of AZI in relation to the predicted R_t was 2.42%. This was within the acceptable limits of less than 5% RSD set in our laboratory.

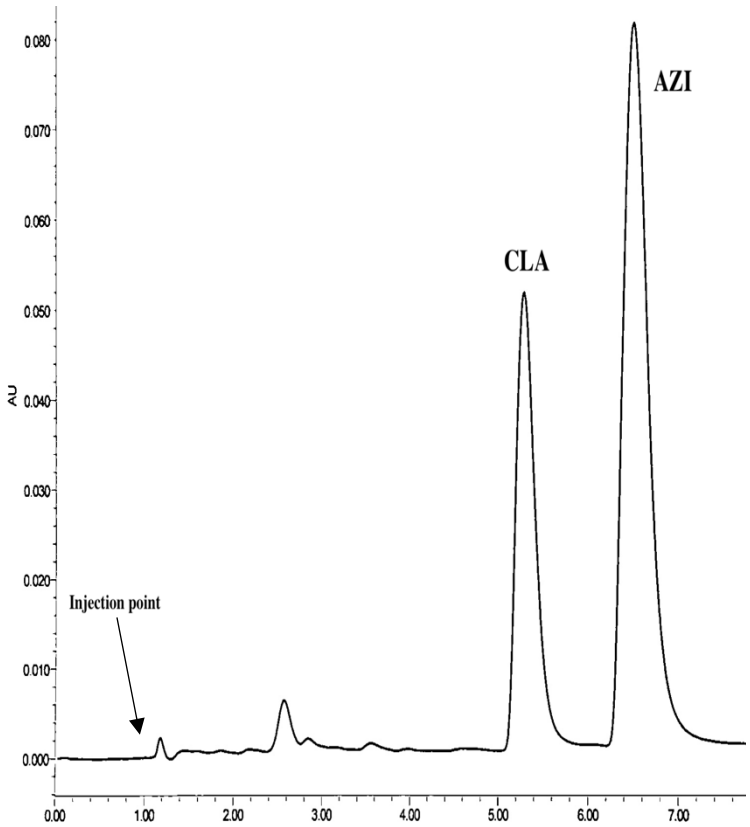

Figure 2.26. Typical chromatogram showing the separation of AZI (150 ug/mL) and CLA (75 ug/mL).

2.5. METHOD VALIDATION

2.5.1. Introduction

Method validation plays a vital role in the development of the HPLC method, which ensures the accuracy, precision, and consistency of analytical results [67,68,88]. Regulatory authorities, including the International Council for Harmonisation (ICH) and the U.S. Food and Drug Administration (FDA), have established guidelines that outline the essential validation parameters. These parameters include column suitability (§ 2.3.3.6), linearity, accuracy, precision, limit of detection (LOD), limit of quantification (LOQ), specificity, and stability studies [67,68,88]. The ICH Q2(R1) guideline provides a structure for validating analytical

procedures, ensuring they meet regulatory expectations for pharmaceutical quality control [92]. The HPLC method developed for the analysis of AZI was validated in accordance with the ICH guidelines.

2.5.2. Calibration, linearity and range

Calibration and linearity are essential for ensuring accurate and proportional responses to varying an analyte concentration [67,68,88]. These parameters are critical in pharmaceutical analysis for accuracy, precision, and reproducibility. The ICH Q2(R1) guidelines suggest evaluating linearity by testing at least five concentration levels within the expected working range [92]. Least-squares regression analysis is used to assess the relationship, with an R^2 value of 0.990 or higher being sufficient [92].

The linearity of the HPLC method was evaluated by analysing n = 6 replicates of ten calibration standards using the optimised chromatographic conditions (§ 2.4.4). The standards of AZI (0.5, 1, 2, 5, 10, 20, 30, 40, 50, and 150 µg/mL) were mixed with CLA (IS) as per § 2.3.3.3. The AZI/CLA peak height ratio was plotted against concentration (Figure 2.27), and a least-squares regression analysis was conducted to assess the calibration model. The regression equation, $y = 0.0121x + 0.0032$ with a $R^2 = 0.9999$, demonstrates an almost perfect linearity across the calibration range. The ICH Q2(R1) guidelines state that the y-intercept should be close to zero to minimize systematic bias [92]. The intercept of 0.0032 satisfies this criterion.

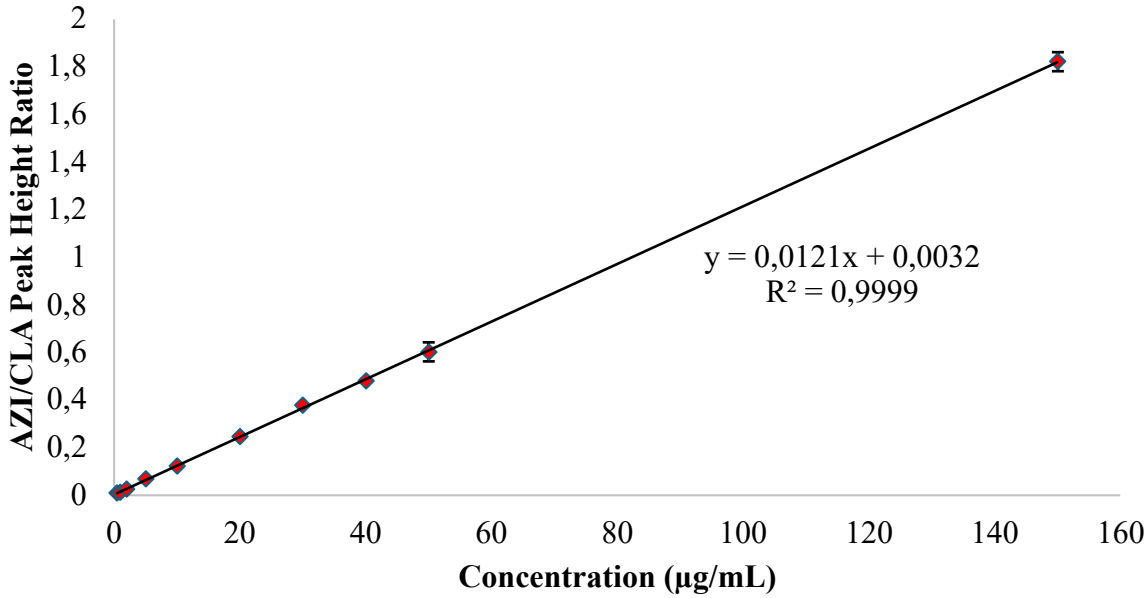

Figure 2.27. Typical calibration curve for AZI over a concentration range 0.5-150µg/mL

2.5.3. Precision

Precision refers to how consistent and reproducible the results is, when the same sample is analysed multiple times under the same conditions [92]. Precision is evaluated at three levels: repeatability (intra-day precision), intermediate precision (inter-day precision), and reproducibility [92]. It is determined by analysing multiple replicates of a sample and calculating the RSD value, which must be within 2% [92]. However, in these studies the RSD tolerance was set at ≤ 5% to account for low concentration calibration range, PDA detector and equipment sensitivity.

2.5.3.1. Repeatability or intra-day precision

Repeatability assesses the consistency of an analytical method when the same sample is analysed multiple times under the same conditions within a single day [67,68,88]. It helps determine the sensitivity of the HPLC system. The ICH Q2(R1) guideline recommends assessing repeatability using a minimum of nine determinations over the calibration range, such as three replicates at three concentrations, or at least six determinations at 100% of the target concentration [92].

The precision of the method was evaluated by analysing AZI at three different concentration levels (low, medium, and high within the calibration range) in six replicates each. The results

obtained in Table 2.9 demonstrate that %RSD is less than ≤ 5% acceptance criteria and also adhere to the ICH Q2(R1) requirement of ≤2%. These results confirm that the method demonstrates excellent repeatability, ensuring precise and reliable quantification of AZI across the tested concentration range.

Table 2.9. Repeatability data for AZI analysis (n=6)

Theoretical concentration (µg/mL)	Calculated Concentration Mean ± SD	% RSD
40	40.50 ± 0.28	0.70
90	89.42 ± 1.52	1.11
150	151.69 ± 1.98	1.30

2.5.3.2. Intermediate or inter-day precision

Inter-day precision evaluates the reproducibility of an analytical method over multiple days under the same experimental conditions [67,68,88]. This assesses the method's reliability in routine analysis [67,68,88]. The inter-day precision of the method was determined by analysing AZI at three concentration levels (n=6) over three consecutive days. The calculated concentrations and % RSD values for each day are presented in Table 2.10. The % RSD values ranged from 0.45% to 1.68%, all within the ≤ 2% acceptance limit as outline within the ICH Q2(R1) requirement. The consistency of % RSD values across different days indicates minimal variability, confirming that the method maintains high precision over time.

Table 2.10. Inter-day precision data for the analysis of AZI

Quality Control	AZI Day 1			Day 2			Day 3		
Theoretical concentration (µg/mL)	40	90	150	40	90	150	40	90	150
Calculated concentration (µg/mL)	40.50	90.05	151.69	40.82	91.22	151.16	40.92	90.59	152.43
% RSD	0.70	1.68	1.31	1.22	0.82	1.40	0.45	1.07	1.21

2.5.3.3. Reproducibility

According to the ICH Q2(R1) guideline, reproducibility measures the precision of an analytical method across different laboratories in collaborative studies [92]. It ensures consistency in results irrespective of variations in equipment, analysts, and laboratories. However, reproducibility was not assessed in this study, as all analyses were conducted by a single analyst within the same laboratory throughout the MSc project.

2.5.4. Accuracy and bias

Accuracy measures how close the experimental results are to the true value, ensuring that the analytical method provides correct and unbiased measurements [67,68,88]. According to ICH Q2(R1), accuracy should be assessed across the analytical range by comparing the calculated concentration of known standards to their theoretical values [92]. It is evaluated using percent bias (% Bias), which quantifies the deviation from the true concentration as seen in equation 2.20.

$$\%Bias = \frac{(True\ Value - Measured\ Value)}{True\ Value} \times 100 \qquad \textbf{\textit{Equation 2.20}}.$$

From Table 2.11, the % Bias values ranged from -1.68% to +3.34%, all within the acceptable range of ±5% as set in the laboratory. These results indicate that the method is accurate, with minimal errors that will affect quantification.

Table 2.11. Accuracy data for the analysis of AZI

Theoretical concentration (µg/mL)	Calculated concentration Mean ± SD	% RSD	%Bias
40	41.34 ± 0.30	0.73	+3.34
90	88.49 ± 0.68	0.77	-1.68
150	150.60 ± 1.81	1.82	+1.21

2.5.5. Limits of quantitation and detection

The limit of detection (LOD) and limit of quantification (LOQ) shows an analytical method's sensitivity by determining the smallest detectable concentration and lowest quantifiable concentration respectively [67,68,88]. According to ICH Q2(R1), there are three ways for

estimating LOD and LOQ [92]. The signal (S) to noise (N) method defines LOD as the concentration where the signal is at least three times the noise level (S/N = 3) and LOQ where the signal is at least ten times the noise (S/N = 10), which is suitable for HPLC methods [92]. The second method is based on the standard deviation of the response and the slope of the calibration curve as seen in equation 2.21 and 2.22 [67,68,88].

$$LOD = \frac{3.3\sigma}{Slope} \qquad \textit{Equation 2.21}.$$

$$LOQ = \frac{10\sigma}{Slope} \qquad \textit{Equation 2.22}.$$

Where:

σ = standard deviation of the response

Slope = slope of the calibration curve

The third way of evaluating the LOQ is that the % RSD must be ≤ 5% of the response as set in the laboratory [67,68,88]. This approach was used in the validation of the HPLC method. Solutions of low concentrations of AZI (10 µg/mL) were prepared, and the lowest concentration at which a quantifiable response was obtained with acceptable accuracy and precision was determined as the LOQ. The LOD was determined as 0.3 x LOQ. The % RSD values were used to determine the LOQ, with 10 µg/mL selected as the lowest concentration meeting the required precision limit of under 5%. The LOD was then calculated as 3 µg/mL based on the standard 0.3 × LOQ equation. The results are summarized in Table 2.12 indicate that the method is sufficiently sensitive for detecting and quantifying AZI at low concentrations. This level of sensitivity is relevant for evaluating drug release profiles from the nanosuspension formulation, where accurate quantification at low concentrations is critical for assessing dissolution behaviour over time..

Table 2.12. LOQ data for HPLC analysis of AZI

Concentration (µg/mL)	Peak height ratio (AZI/CLA) Mean ± SD (n=6)	% RSD
20	0.2454 ± 0.0054	2.20
15	0.1886 ± 0.0068	3.61
10	0.1093 ± 0.0049	4.48
7.5	0.0856 ± 0.0092	10.75

2.5.6. AZI Assay

Twenty Zithromax 500mg tablets were crushed and powdered in a pestle and mortar. Approximately 0.9281g of powder equivalent to 500 mg AZI was weighed directly into a 100 mL A-grade volumetric flask and dissolved in 100 mL of ACN: 0.02 M phosphate buffer adjusted to pH 7.5 in a ratio 75:25 v/v, vortexed for 5 mins, and sonicated for 30 minutes respectively. A 2 ml aliquot was filtered using a GVS® 0.45 µm syringe filter attached to a 10 mL plastic syringe (Rickmansworth, Hertfordshire, England) into a 100 mL A-grade volumetric flask. The solution was made up to volume with ACN: 0.02 M phosphate buffer adjusted to pH 7.5 in a ratio 75:25 v/v. A 1.5 mL aliquot of the solution was transferred into a 2 mL Waters® amber glass screw top vial (Milford, Massachusetts, USA) and analysed by RP-HPLC. The same procedure was followed for Zithrolide 500 mg and Austell-Azithromycin 500 mg tablets. The respective masses of powder used were 0.9004 g and 0.9366 g, each equivalent to 500 mg AZI. The results are summarized in Table 2.13.

Table 2.13. Assay results for a commercially available AZI tablets 500mg

Product	% AZI recovered	Assay content w/w %
Commercial A 500mg Tablet	103.96 ± 1.17	56.01 ± 0.63
Commercial B 500mg Tablet	105.58 ± 1.04	56.36 ± 0.56
Commercial C 500mg Tablet	104.97 ± 1.14	56.43 ± 1.17

The recovery following analysis of all tablets was 100 ± 10% for AZI and complied with the laboratory specifications. The tablets are therefore of suitable quality and the extraction procedure was adequate for the assessment of AZI content formulations.

2.5.7. Forced degradation studies and stability of AZI

Forced degradation studies are essential in validating a HPLC method for the analysis of AZI [93]. By exposing AZI to controlled stress conditions such as acidic, basic, oxidative, thermal, and photolytic conditions these studies can simulate potential degradation scenarios that the compound might encounter during its product lifecycle [93]. This process verifies that the method can accurately distinguish between the intact compound and its degradation products, ensuring specific analytical performance. These studies will provide value on understanding the stability and degradation pathways of AZI [93]. This knowledge informs optimal storage conditions, and supports accurate shelf-life predictions, thereby ensuring the method meets regulatory requirements [93].

Stress studies were performed on AZI by subjecting it to various conditions including acidic, alkaline, neutral, hydrogen peroxide, light, and heat exposures [92,93]. All experiments were conducted in solution, however, when applying dry heat, the powdered form of AZI was utilized. A stock solution of 150 µg/mL was prepared according to § 2.3.3.3 and then exposed to the stress conditions prior to analysis with the validated optimised analytical method. For method validation purposes, it is generally accepted that degradation between 5% and 20% of the API is tolerable [93]. In this study, a 5% degradation threshold was adopted to assess whether AZI had significantly degraded following stress exposure. The chromatogram of the untreated AZI sample, used as a baseline reference, is depicted in Figure 2.28, while Figure 2.29, 2.30, 2.31, 2.32, 2.33, 2.34, 2.35 present chromatograms of AZI after it had been subjected to the stress conditions, including acidic, alkaline, neutral, hydrogen peroxide, light and heat conditions.

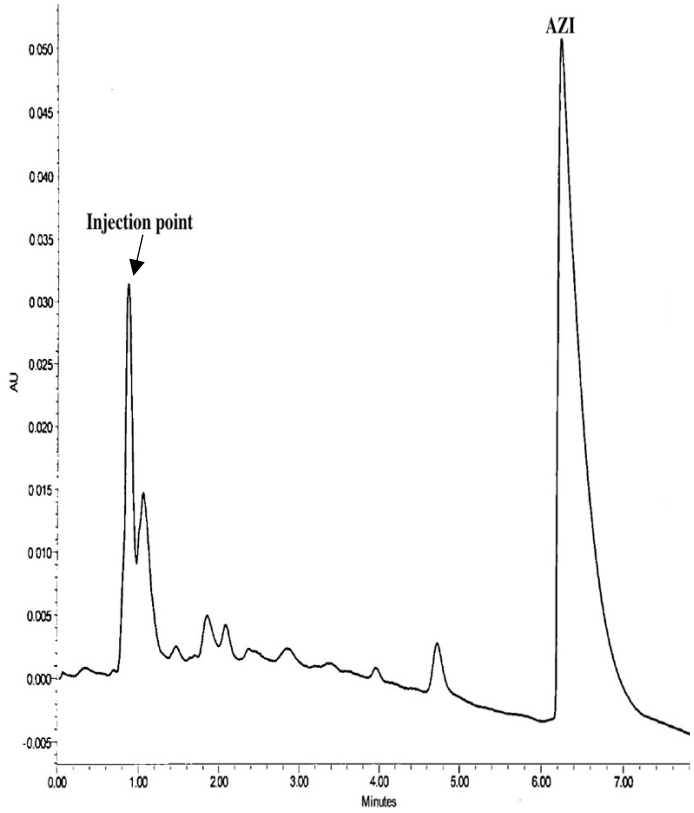

Figure 2.28. HPLC chromatogram of untreated AZI sample used as a baseline reference in forced degradation studies.

2.5.7.1. Photostability studies

According to the ICH Q1B guidelines, APIs should be exposed to light as part of stress studies to assess their photostability and determine protective packaging if needed. In this method, photolytic degradation of AZI was assessed by subjecting a 150 µg/mL solution to a light exposure to 750W h/m² for 8 hours in a photostability chamber (Suntest® CPS+, Atlas, Linsengericht, Germany). The testing conditions are sufficient at a minimum 200 W h/m² or 1.2 million lux hours for UV analysis. Post-exposure as shown in Figure 2.29, the analysis revealed that 94.85 ± 0.0051% of AZI was recovered with no change in retention time or peak purity compared to the control sample (Figure 2.28). Minor eluting peaks were observed, possibly representing trace photodegradation products, but the main peak remained sharp and symmetrical. These results (Figure 2.29) indicate that AZI demonstrates acceptable photostability, with minimal degradation under ICH recommended conditions.

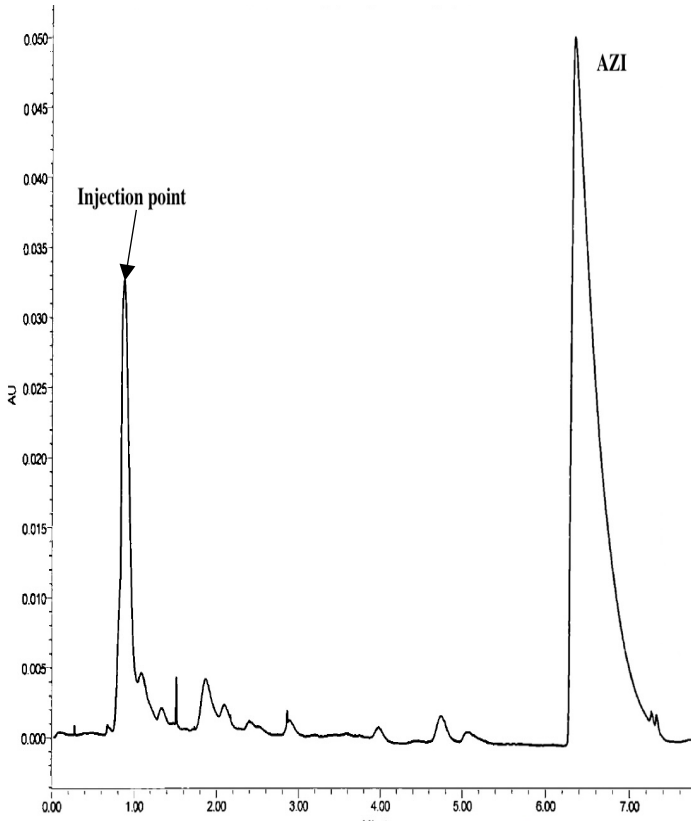

Figure 2.29. HPLC chromatogram of AZI after exposure to photolytic conditions.

2.5.7.2. Temperature stress studies

Temperature stress testing is crucial for understanding the thermal stability of a drug substance. The ICH Q1A(R2) guidelines suggest conducting thermal degradation studies at temperatures at least 10°C higher than those used for accelerated stability testing (above 50°C) [93]. This

helps identify degradation pathways and ensures that the drug maintains stability under storage conditions. For this study, a 150 µg/mL solution of AZI was exposed to increasing temperatures (50, 60, 70, and 80°C) for 8 hours in a water bath. The samples were then cooled to room temperature (22°C) before HPLC analysis. The chromatogram in Figure 2.30 for the sample heated to 80°C showed that 100.67 ± 0.0022% of AZI was recovered, with no significant shift in retention time or peak shape compared to the unstressed control (Figure 2.28). No additional peaks suggestive of degradation products were observed. This confirms that AZI maintains thermal stability in solution even under elevated temperature conditions.

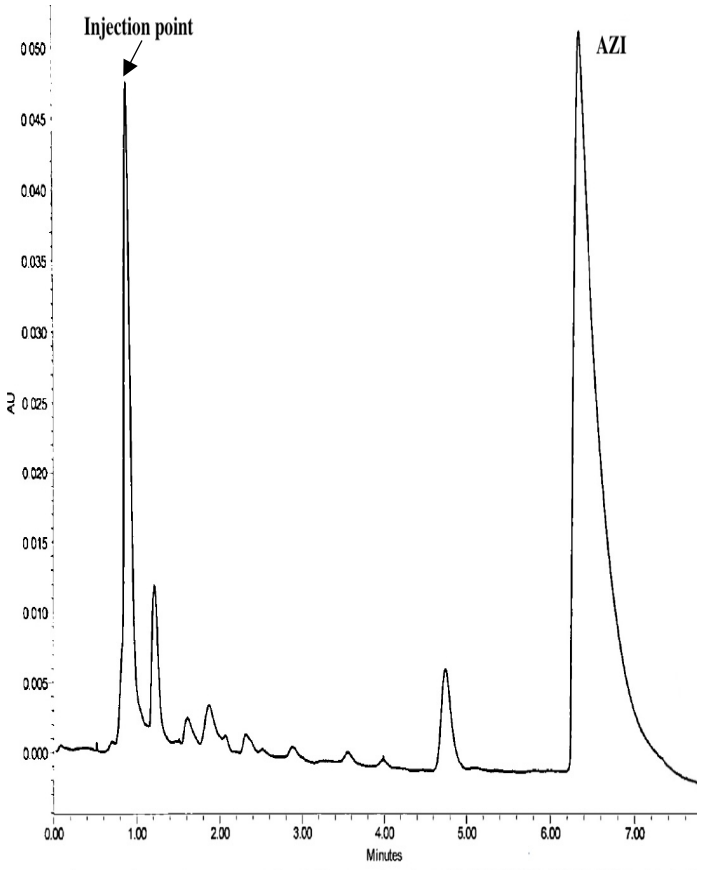

Figure 2.30. HPLC chromatogram of AZI after exposure to elevated temperatures.

2.5.7.3. Acid degradation studies

Acid hydrolysis is a common degradation pathway for APIs, and it often leads to the cleavage of bonds sensitive to acidic conditions [93]. The ICH recommends refluxing drug substances in acidic conditions to assess their susceptibility to hydrolysis and identify any major degradation products. To evaluate acid stability, a 150 µg/mL solution of AZI was mixed in a 1:1 ratio with 0.1 M HCl and refluxed at 70°C for 8 hours. Chromatographic evaluation (Figure 2.31) revealed complete degradation of AZI, as evidenced by the absence of the main peak at

its expected retention time. There were many early eluting peaks observed, indicating the presence of acid induced degradation products as described in § 1.4. These findings confirm that AZI is highly unstable under acidic conditions, undergoing complete hydrolysis with no measurable recovery of the parent compound. For formulation development, this highlights the need to avoid excipients that lower the pH or create acidic environments. To ensure chemical stability in the nanosuspension, the formulation should be buffered within a slightly acidic to neutral pH range, around pH 6.5–7.0.

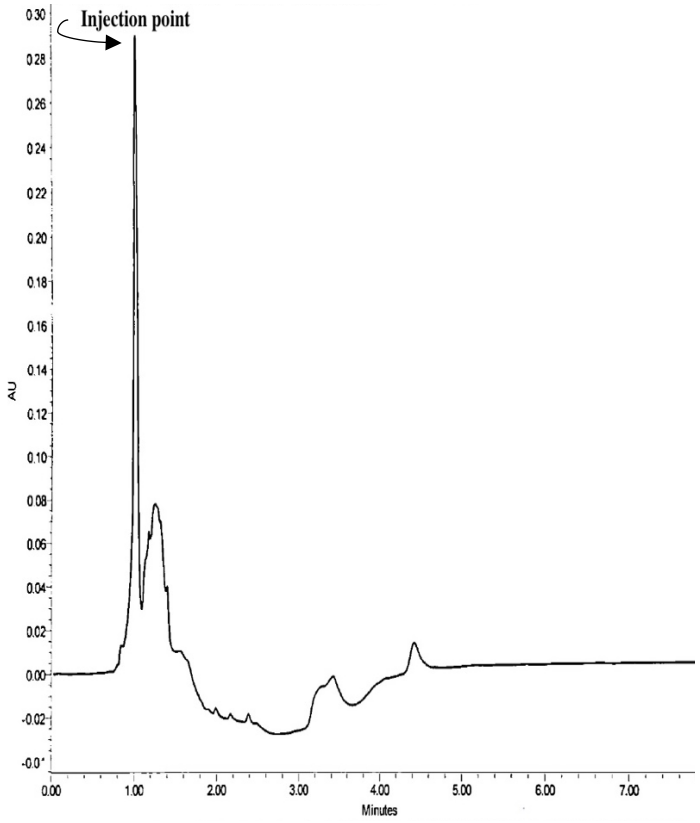

Figure 2.31. HPLC chromatogram of AZI after exposure to acidic conditions.

2.5.7.4. Alkali degradation studies

Alkaline hydrolysis can significantly impact drug stability, particularly for compounds with ester and, amine functional groups, which are highly susceptible to base-catalysed hydrolysis [93]. Evaluating degradation in basic conditions helps predict the behaviour of AZI in formulations with alkaline excipients [93]. In this study, a 150 µg/mL solution of AZI was mixed with 0.1 M NaOH (1:1) and refluxed at 70°C for 8 hours. After cooling, HPLC results showed complete degradation of AZI, as evidenced by the absence of the AZI peak at its known retention time (Figure 2.32). A very large, early eluting peak was observed near the solvent

front, corresponding to degradants resulting from the breakdown of the macrolide lactone ring and amino functionalities. These results confirm that AZI is extremely unstable under basic conditions, with 0% actual recovery, indicating its susceptible to alkaline hydrolysis.

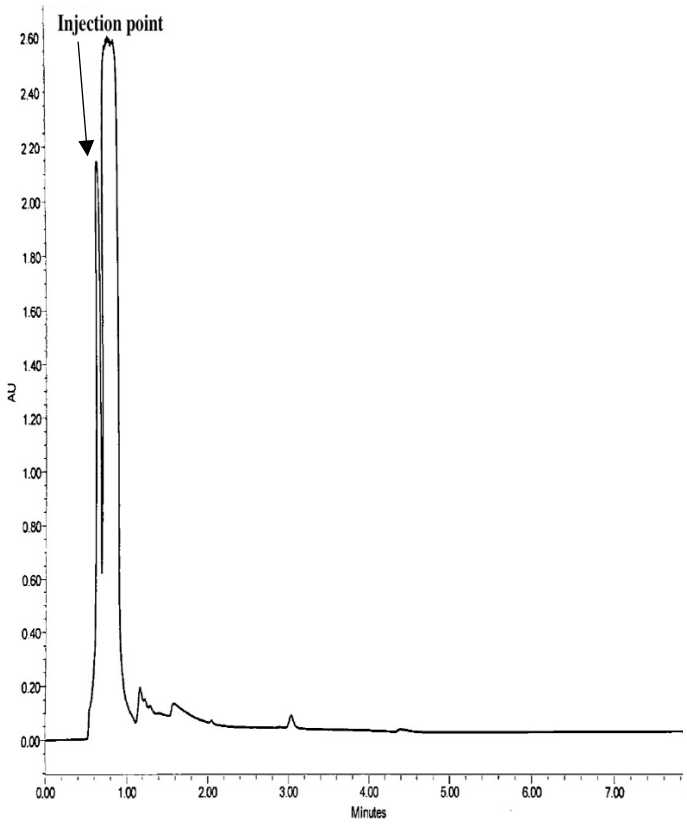

Figure 2.32. HPLC chromatogram of AZI after exposure to alkaline conditions.

2.5.7.5. Neutral hydrolysis

Neutral hydrolysis studies are performed to understand the degradation of a compound in pure aqueous environments, mimicking long-term storage in aqueous formulations [93]. This helps determine if the drug substance remains intact under mild hydrolytic conditions. To assess this, a 150 µg/mL solution of AZI was mixed with HPLC-grade water and refluxed at 70°C for 8 hours. After cooling, analysis showed a recovery of 38.68 ± 0.078% (Figure 2.33), indicating that AZI undergoes substantial degradation in neutral aqueous media. The main AZI peak at its expected retention time was significantly reduced, while new early eluting peaks were observed, likely corresponding to hydrolysis products. These findings confirm that the formulations must be tightly buffered and protected from prolonged water exposure to maintain drug integrity.

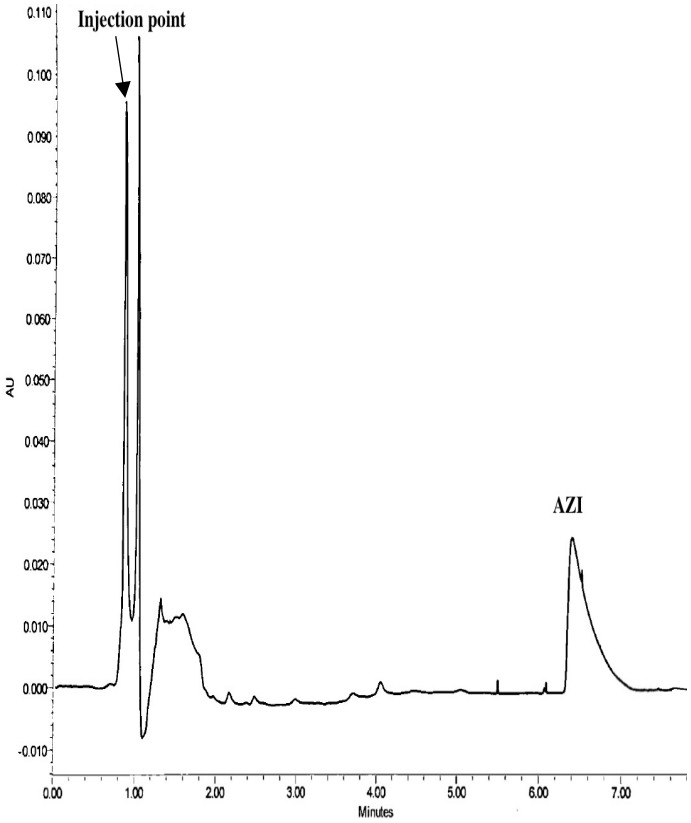

Figure 2.33. HPLC chromatogram of AZI after exposure to HPLC grade water.

2.5.7.6. Oxidative studies

Oxidation is a major degradation pathway that can occur due to environmental exposure, such as contact with air or excipients containing peroxides [93]. The use of hydrogen peroxide is a standard approach for assessing oxidative susceptibility. For this study, a 150 µg/mL solution of AZI was mixed with an equal part of 3% v/v hydrogen peroxide and refluxed at 70°C for 8 hours. After cooling, the chromatogram (Figure 2.34) revealed complete degradation of AZI, with no detectable parent peak at its expected retention time. There were multiple early eluting peaks were observed, corresponding to oxidative degradation products.

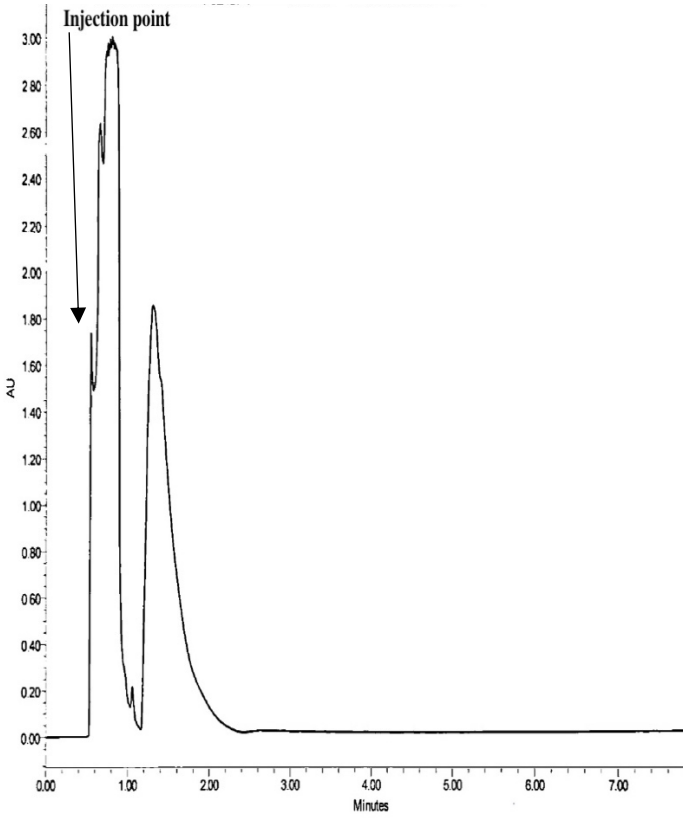

Figure 2.34. HPLC chromatogram of AZI after exposure to 3% v/v H_2O_2.

2.5.7.7. Dry heat

Dry heat degradation evaluates the stability of solid-state drugs under high-temperature conditions [93]. This is important for understanding the thermal stability of a drug substance in tablet or powder form. AZI in its powdered form was exposed to 100 °C for 8 hours in a drying cabinet. A stock solution was then prepared from the heat-exposed powder and analysed by HPLC. The results showed a recovery of 105.48%, indicating that AZI remained chemically stable in its solid form under dry heat conditions. The chromatographic profile (Figure 2.35) of the dry treated sample was nearly identical to the control, with no significant formation of degradation products or peak shifts. The slight increase in recovery may be attributed to loss of bound water from the dihydrate form during heating, leading to a more concentrated drug substance when reconstituted. However, no degradation products were observed, and the parent peak remained sharp and consistent with the control. These results suggest that azithromycin dihydrate is thermally stable in its solid state, and that dehydration under dry heat does not compromise its chemical integrity.

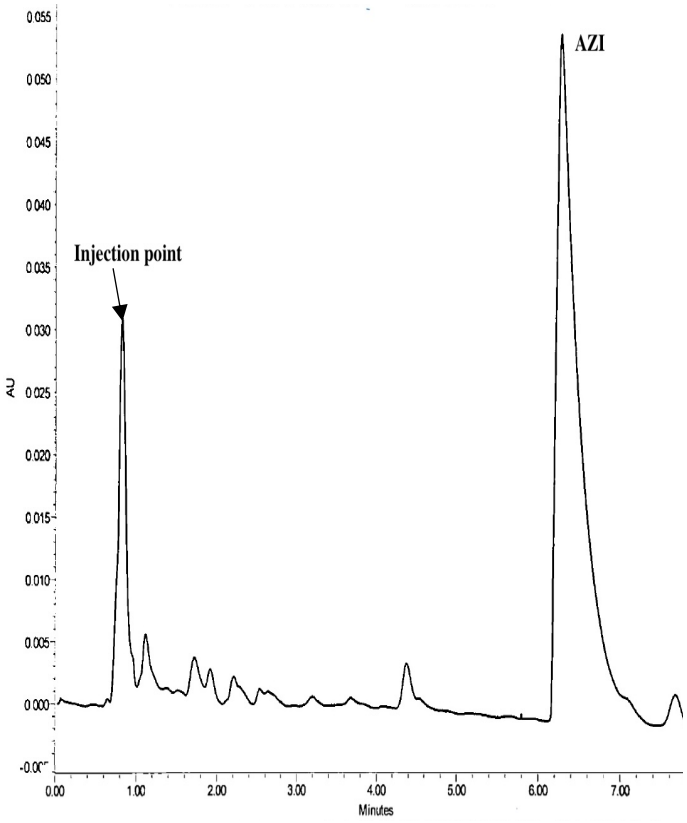

Figure 2.35. HPLC chromatogram of AZI after exposure to dry heat at 100°C.

2.6. CONCLUSION

A robust, specific, and stability indicating RP-HPLC method was successfully developed and validated for the quantitative analysis of AZI using CLA as an internal standard. Method optimisation using CCD allowed fine tuning of chromatographic parameters including buffer pH, ACN concentration, buffer molarity, and column temperature, resulting in improved peak resolution, symmetry, and retention time. The final method demonstrated excellent linearity ($R^2 = 0.9999$), precision (RSD ≤ 1.68%), and accuracy (bias within ±5%), with validated limits of detection and quantification at 3 µg/mL and 10 µg/mL, respectively.

Forced degradation studies confirmed the method's ability to distinguish AZI from its degradation products under various stress conditions. AZI exhibited high stability under thermal (solution and solid-state) and photolytic conditions, with minimal degradation observed. However, the drug was highly susceptible to acidic, alkaline, neutral hydrolysis, and oxidative environments. These results highlight the importance of controlling pH and oxidative exposure during formulation and storage.

For nanosuspension formulation development, these findings underpin the need for careful excipient selection, pH control (between 6.5–7.0), and the use of amber packaging to minimize degradation risks. Overall, the developed HPLC method is well suited for routine quality control, stability testing, and formulation development of AZI pharmaceutical products.

CHAPTER 3

NANOCRYSTALS SUSPENSION OVERVIEW

3.1. INTRODUCTION

Nanosuspensions are submicron colloidal dispersions of drug particles stabilized by surfactants. These dispersions offer a promising approach to enhance the bioavailability and therapeutic efficacy of poorly water-soluble drugs [94,95]. In this technology, drug particles are reduced to the nanocrystalline state, less than 600 nm, which leads to an increased dissolution rate and, therefore improved bioavailability [94]. AZI has limited clinical application due to its poor solubility and resulting low bioavailability [96]. To overcome these challenges, formulating AZI into a nanocrystal-based nanosuspension has emerged as a potential solution [95,96]. This approach increases saturation solubility and dissolution due to nanosizing which helps to improve drug loading, reduce required dosages, and minimize gastrointestinal response [96,97].

Nanosuspensions not only address the challenges of poor solubility and bioavailability but can also alter the pharmacokinetics of the drug, potentially improving its safety profile [95]. Various methods, such as high-pressure homogenisation and nanoprecipitation, can be employed to produce AZI nanosuspensions with desirable characteristics [96,98]. Stabilisers like poloxamer 407 (Pluronic F127) and polyvinylpyrrolidone K30 (PVP) are often added to prevent aggregation of the drug crystals and ensure the stability of the nanosuspension [97,98].

3.1.1. Colloidal drug delivery systems

A colloidal system, also known as a colloid, is a heterogeneous mixture in which one substance (the dispersed phase) is microscopically distributed throughout another substance (the continuous phase or dispersion medium) [99,100]. The dispersed particles in a colloid are larger than those in a true solution (salt dissolved in water) but smaller than those in a suspension (sand mixed in water), which ranges in size from 1 to 1000 nm [99,100]. The colloidal systems can be classified based on their state of phases (solid, liquid or gas) and structure (molecular, micelles, ions) [99,100].

Colloidal drug delivery systems have undergone significant evolution since their introduction. These systems used nanoscale carriers to enhance the solubility, stability, and bioavailability of therapeutic agents. This evolution can be categorized into distinct generations.

The first generation in the 1950s to the 1980s focused on basic controlled release systems [101,102]. In the early 1950s, the development of controlled release formulations, the Spansule® technology, introduced by Smith, Kline & French Laboratories in 1952, was one of the first to provide sustained drug release through a dissolution-controlled process [101,102]. This technology used micro-pellets coated with varying thicknesses of water-soluble wax to achieve a gradual release of medication over time [101,102]. In the late 1970s and early 1980s, significant advancements included the introduction of liposomes as drug carriers. Liposomes are lipid-based vesicles that encapsulate drugs, enhancing their solubility and stability while allowing for targeted delivery [103,104].

The second generation system focused on biodegradable polymers and microparticles in the 1980s to 1990s [101,102]. These systems allowed for controlled release through degradation over time [101,102]. These include microspheres and nanoparticles which provided enhanced targeting characteristics and reduced side effects [101,102]. In 1990, the first polyethylene glycol conjugated protein (PEGylated) was introduced which improved the pharmacokinetics and reduced immunogenicity [101,104]. This innovation allowed the way for products like Doxil®, a PEGylated liposomal formulation of doxorubicin that demonstrated enhanced efficacy in cancer treatment [101,104].

The third generation was introduced in the early 2000s and made a shift towards targeted nanocarriers. Products such as Mylotarg®, an antibody-drug conjugate, and Rapamune®, a sirolimus nanocrystal formulation have recently been developed [101]. The focus included enhancing the circulation time for PEGylation, using ligands conjugated to carriers for specific cell targeting and using the enhanced permeability and retention effect to accumulate drugs in tumour tissues [103,104].

For an AZI nanosuspension to be formulated, the dispersed phase can exist in various nanostructured forms as abovementioned. The most favourable option is nanocrystals, which are defined as pure drug particles reduced to 100 to 500 nm, and stabilized with surfactants or polymers [105]. This approach is advantageous for poorly soluble drugs like AZI, as it significantly enhances the dissolution rate, bioavailability, and stability while requiring minimal excipients compared to lipid-based systems [105]. Solid lipid nanoparticles (SLNs) encapsulate the drug within a lipid matrix, such as glyceryl monostearate or stearic acid [106].

While SLNs enhance stability and provide controlled release, they have a lower drug loading capacity compared to nanocrystals, making them less suitable for AZI use [106]. Nanostructured lipid carriers (NLCs) use a blend of solid and liquid lipids. NLCs offer higher drug loading capacities than SLNs and improved physical stability [107]. However, they are not desirable for AZI formulations since sustained release is not needed [107].

3.1.2. Nanocrystals nanosuspensions

Nanocrystals have emerged as a transformative approach in drug delivery systems for poorly water-soluble drugs [108]. With approximately 40% of marketed drugs facing solubility challenges and around 70% of new chemical entities exhibiting poor aqueous solubility, the development of nanocrystal formulations has become increasingly relevant in pharmaceutical drug delivery [109].

Nanocrystals are defined as crystalline nanoparticles of size 200 nm to 600 nm. Their small dimensions increase the surface area to volume ratio, which enhances their dissolution rates and bioavailability compared to larger particles [108]. The morphology of nanocrystals can be influenced by the method of preparation, the physicochemical properties of the drug, and the choice of stabilisers used during formulation. The crystallinity of nanocrystals influences their dissolution behaviour. Nanocrystals can exist as amorphous, crystalline, or semi-crystalline forms. Amorphous nanocrystals generally dissolve faster due to their lack of a defined lattice structure which is desirable [108]. Figure 3.1 illustrates the spring and parachute model, explaining how amorphous structures act like a spring that releases energy quickly upon contact with a solvent, leading to rapid dissolution [108].

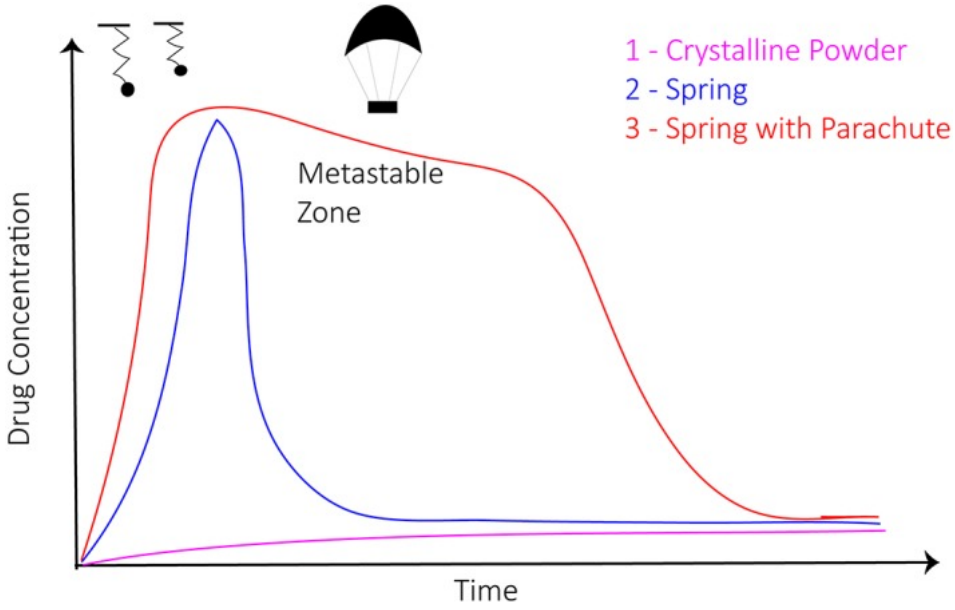

Figure 3.1. Schematic representing the spring and parachute model for nanocrystal dissolution as a function of time vs drug concentration. (Adapted from [108]).

The pink line represents crystalline powders, which dissolve slowly due to their rigid lattice structure, leading to low drug concentrations over time and poor bioavailability. The blue line represents an amorphous form of the drug, which dissolves rapidly like a compressed spring releasing energy, resulting in a sharp increase in drug concentration. However, without stabilization, the drug may precipitate out of solution, causing a decline in bioavailability. The red line depicts the ideal scenario, an amorphous nanocrystal formulation stabilized with surfactants or polymers, preventing recrystallisation and ensuring a sustained high drug concentration over time. This spring with parachute effect balances rapid dissolution with long-term stability, making it the most effective approach for enhancing drug absorption [108].

The surface characteristics of nanocrystals play a pivotal role in their interaction with biological systems. Factors like surface charge (zeta potential), hydrophilicity/hydrophobicity, and morphology (shape) can affect cellular uptake and biodistribution [108]. Nanocrystals with a positive zeta potential exhibit higher cellular uptake due to electrostatic attraction to negatively charged cell membranes [108]. To enhance stability and prevent particle aggregation the addition of stabilisers and surfactants helps [108]. The uniformity of particle size distribution (polydispersity) is crucial for ensuring consistent drug release profiles [110]. A low polydispersity index (PDI) indicates homogeneous nanoparticles, which are desirable for reproducible pharmacokinetic behaviour [110]. Nanocrystals can be prone to agglomeration

due to high surface energy [108]. This phenomenon can lead to Ostwald ripening, where smaller particles dissolve and redeposit onto larger ones, resulting in an increase in average particle size over time [108]. To reduce these issues, stabilisers such as surfactants or polymers are often incorporated into the formulation to maintain physical stability during storage and administration [108].

By reducing particle size, nanocrystals improve the dissolution rate of poorly soluble drugs like AZI. This is important for AZI, which has low solubility in gastrointestinal fluids. In particular, fine particles with high surface area exhibit a high soluble rate, and that can be practically demonstrated by Noyes-Whitney equation (Equation 3.6). The increased dissolution rates lead to improved absorption across biological membranes, enhancing bioavailability [111]. Nanocrystal formulations can reduce the required dosage for effective treatment due to improved bioavailability [109]. This is particularly beneficial for patients who may struggle with high pill burdens or those requiring chronic dosing regimens [109]. Nanocrystal nanosuspensions can be easily incorporated into various dosage forms such as tablets, capsules, or liquid preparations without changes to existing manufacturing processes [109]. This flexibility allows for broader application across different patient populations and treatment conditions [109].

3.2. PRODUCTION APPROACHES FOR THE MANUFACTURE OF NANOCRYSTAL NANOSUSPENSION

Nanocrystal nanosuspensions have emerged as a promising formulation strategy for poorly water-soluble drugs, offering enhanced dissolution rates, bioavailability, and stability [34,112–115]. These nanosuspensions are produced using top-down, bottom-up, or combined technologies as shown in Figure 3.2. The choice of production method depends on the physicochemical properties of the drug, desired particle size, scalability, and application [116].

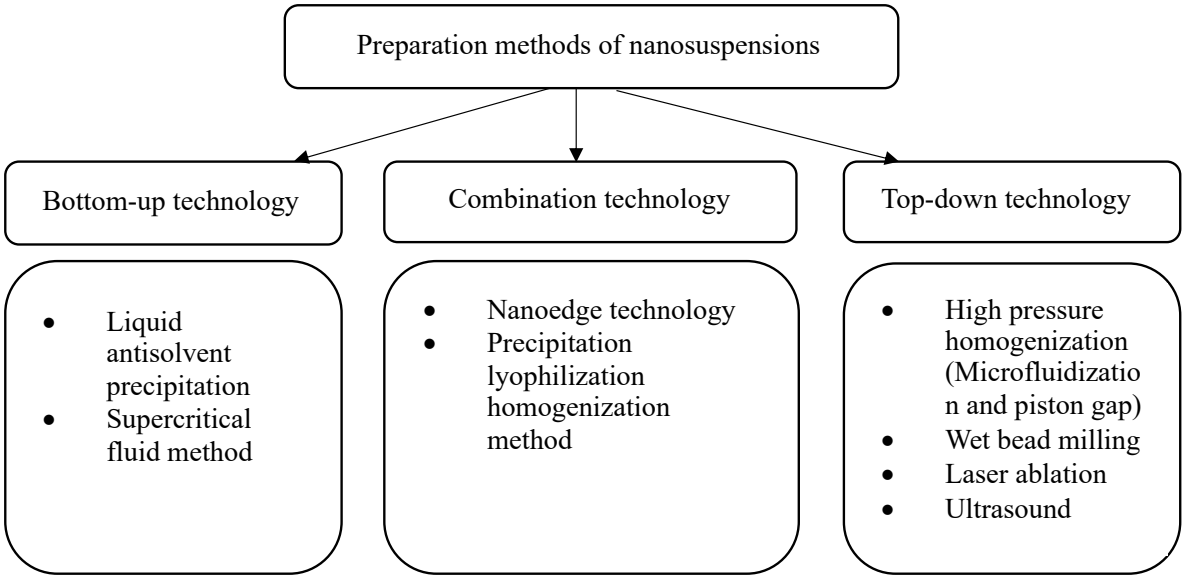

Figure 3.2. Nanosuspension preparation methods

3.2.1. Top-Down Technology

Top-down approaches involve breaking down larger drug particles into nanometre-sized crystals through mechanical processes as seen in Figure 3.3 [34,112–115]. These methods are widely used due to their manufacturing scalability and ability to handle high drug loads [34,112–115]. It is suitable for drugs which are insoluble in both aqueous and organic phases.

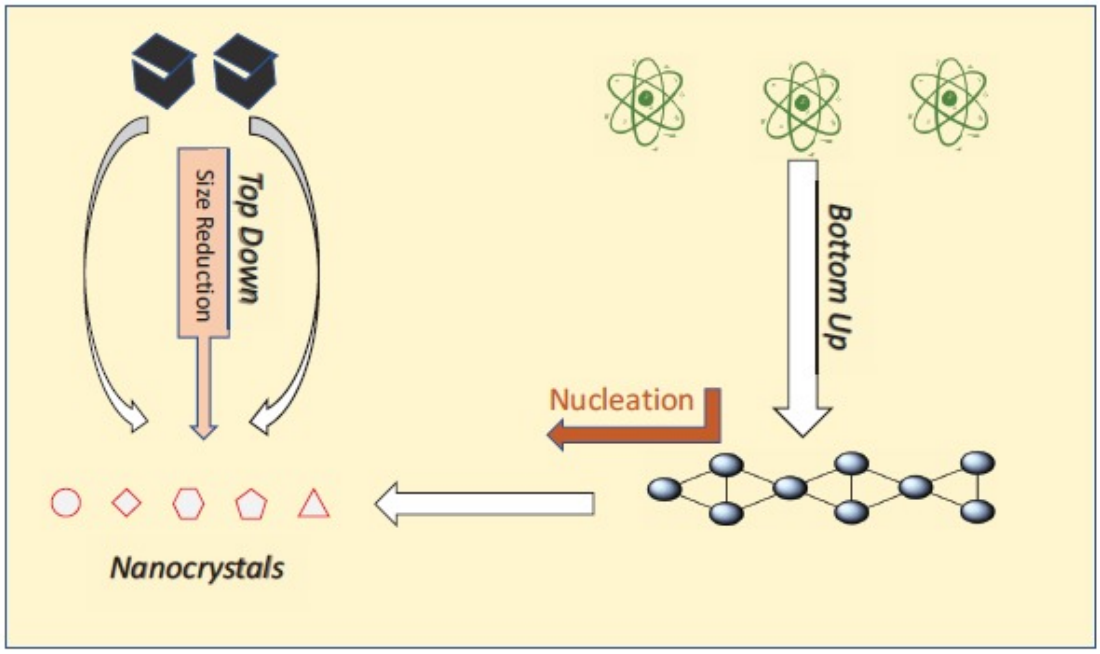

Figure 3.3. Schematic representing the top-down and bottom-down approaches (Adapted from [117])

3.2.1.1. High-Pressure Homogenisation (HPH)

HPH in Figure 3.4 reduces particle size by forcing a coarse drug suspension through a narrow gap under high pressure, generating shear forces that break down particles [34,112–115]. This technique produces uniform nanosuspensions with narrow particle size distributions and is scalable for industrial production [116]. The issue with this is multiple processing cycles may be required to achieve the desired size, and heat generation during processing may affect thermolabile drugs [34,112–116]. HPH has been successfully used in the formulation of drugs like fenofibrate and paliperidone. There are two types of HPH, micro-fluidization and piston gap homogenisation [34,112–116].

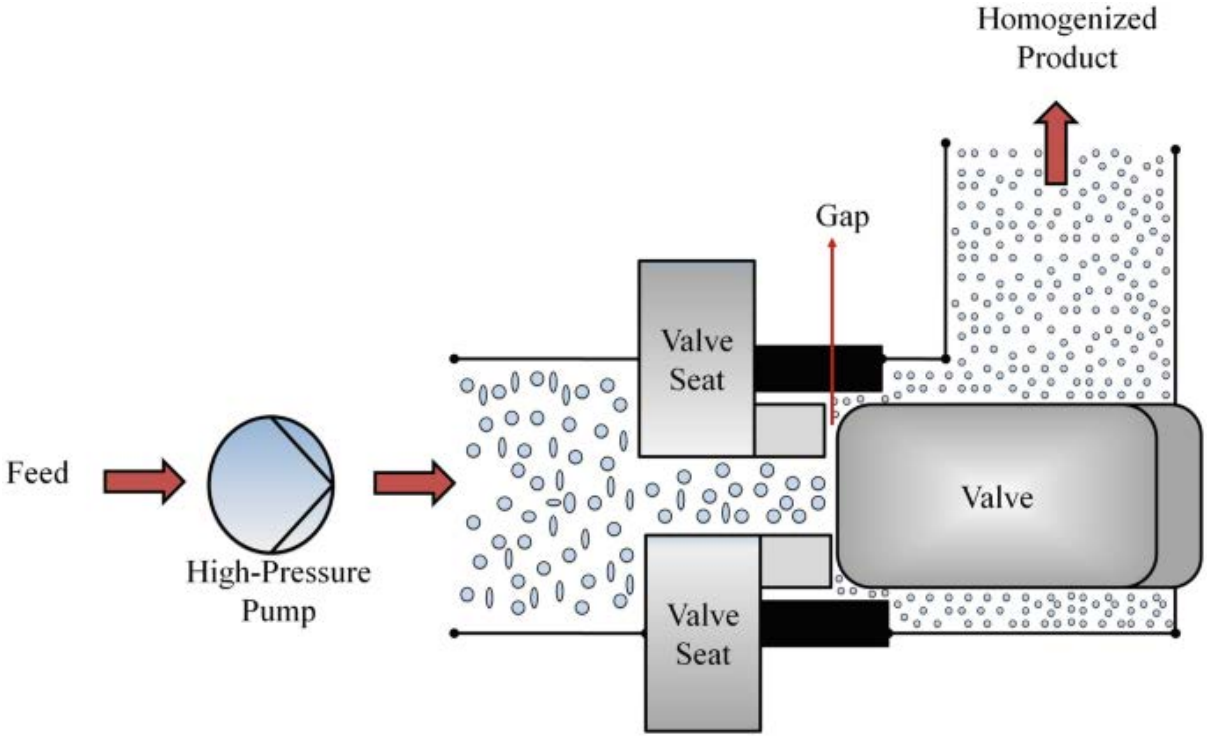

Figure 3.4. Schematic representing the HPH method in the nanosizing process (Adapted from [118]).

3.2.1.1.1. Microfluidization

Microfluidization is a specialized form of HPH that uses a microfluidizer, where a drug suspension passes through interaction chambers containing microchannels [34,112–116]. The suspension splits into two streams, which then collide at high velocities within the chamber [34,112–116]. This collision, along with the resulting shear forces, leads to a reduction in

particle size [34,112–116]. The nanosuspension is collected at the outlet, often requiring multiple passes through the system to reach the desired particle size distribution [34,112–116]. It is advantageous for heat-sensitive materials, processing time is short, and the rapid dissipation of heat during high-velocity collisions minimizes thermal degradation [34,112–116]. However, the process can be energy-intensive, and clogging of the microchannels may occur if drug concentrations are too high or if pre-processing is insufficient [34,112–116]. Microfluidization is widely used for thermolabile compounds [116].

3.2.1.1.2. Piston gap homogenisation

Piston gap homogenisation is another approach that employs a HPH, where a drug suspension is forced through a narrow gap between a piston and a valve seat [34,112–116]. As the suspension is forced through the narrow gap, it experiences intense shear stress and cavitation, leading to a reduction in particle size [34,112–116]. The resulting nanosuspension is collected, and additional homogenisation cycles may be performed to achieve further size reduction. Piston-gap homogenisation is well suited for large-scale production and can handle high drug concentrations [34,112–116]. The process is also highly versatile, allowing for adjustments in pressure and the number of homogenisation cycles to optimise particle size [34,112–116]. However, the high pressures used in this technique can lead to an increase in temperature, which may affect the stability of thermolabile drugs [34,112–116]. The risk of clogging remains a concern, for suspensions with poor dispersion properties [34,112–116].

3.2.1.2. Wet Bead Milling

Drug particles are ground in a liquid medium using high-energy collisions with milling beads [34,112,115,116]. Figure 3.5 illustrates the wet milling process used to produce nanoparticles using NanoCrystal™ technology. The drug and stabilisers is circulated from a storage chamber into the milling chamber by a pump. Inside the milling chamber, high-energy collisions between the drug particles and milling beads are driven by a rotating shaft powered by a motor which reduce the particle size to the nanometer range. A coolant system is integrated to prevent heat buildup, which is critical for maintaining the stability of heat-sensitive drugs. As the drug particles are broken down, a media separator ensures that the milling beads are retained within the chamber while the processed nanosuspension is returned to the circulating chamber for further milling or collection. This method is effective for reducing particle size to below 200 nm and is suitable for drugs with high melting points such as Paclitaxel, and Phenytoin

[34,112,115,116]. However, it carries a risk of contamination from the milling media and requires careful optimisation of bead material and size [34,112,115,116].

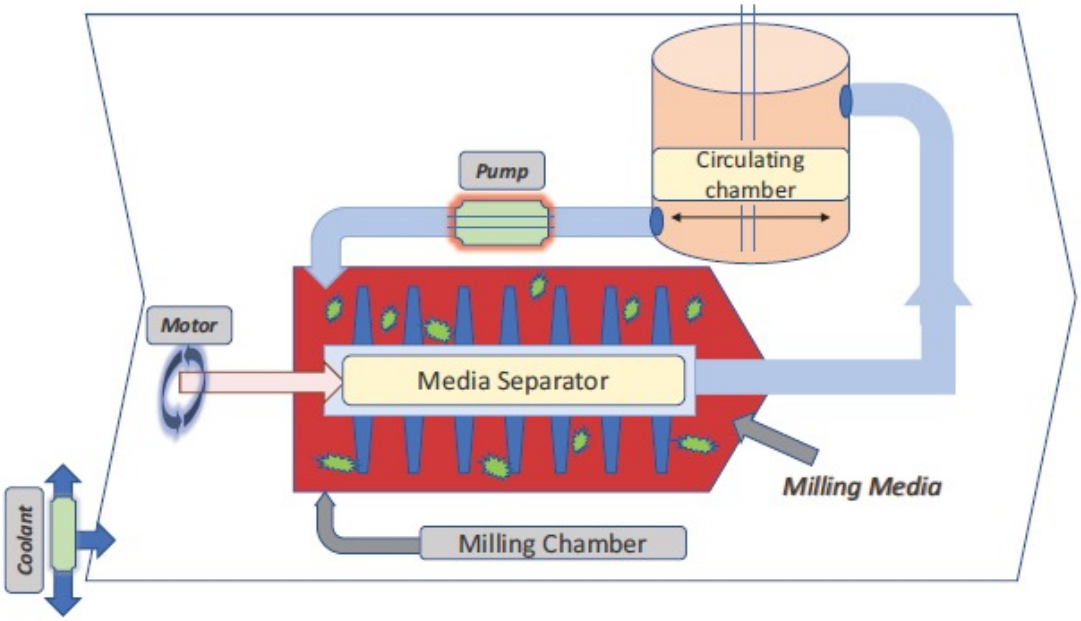

Figure 3.5. The media milling setup (Adapted from [117])

3.2.1.3. Laser Ablation

Laser ablation utilizes high-energy laser beams to vaporize drug particles into nanoscale dimensions [116,119]. This method produces highly pure nanocrystals without solvent residues, making it ideal for applications requiring high-purity nanosuspensions [116,119]. However, scalability is limited due to the high cost of equipment, restricting its use primarily to academic research settings [116,119].

3.2.1.4. Ultrasound

Ultrasound based methods use cavitation bubbles generated by ultrasonic waves, which collapse violently and create localized high energy that reduces particle size [116,120]. This approach is simple, cost-effective, and can be performed under ambient conditions [116,120]. However, it has limited control over particle size distribution and is not ideal for large-scale production. It is often employed for small-scale laboratory experiments [116,120].

3.2.2. Bottom-Up Technology

Bottom-up methods involve assembling nanoparticles from molecular solutions via two basic principles, precipitation and evapouration as seen in Figure 3.3 [116]. These techniques are

useful for producing highly pure nanocrystals with precise control over size and morphology [116].

3.2.2.1. Liquid Antisolvent Precipitation (LASP)

Liquid antisolvent (LAS) precipitation, also known as nanoprecipitation or solvent displacement, is a widely employed bottom-up technique for the production of drug nanocrystals [121]. This method involves dissolving a drug in a suitable, miscible solvent and then rapidly mixing it with an antisolvent (water), in which the drug is poorly soluble, to induce supersaturation and precipitation of the drug in the form of nanocrystals as shown in Figure 3.6 [112,122,123]. The resulting nanocrystals are then stabilized using surfactants or polymers to prevent agglomeration and maintain their nanoscale dimensions [122]. The solvent-antisolvent precipitation method is advantageous as it is a simple and cost-effective technique that requires only basic equipment and common solvents [116]. It is suitable for thermolabile drugs like AZI, as it avoids high temperatures and mechanical stress, ensuring drug stability [116]. This method also produces highly pure nanocrystals with minimal contamination and can be scaled up for industrial production [116]. However, residual solvents may need additional purification steps, and improper stabilization can lead to particle agglomeration, requiring careful selection of stabilisers and mixing conditions [122]. The process is also highly sensitive to variations in parameters, making reproducibility a challenge [122].

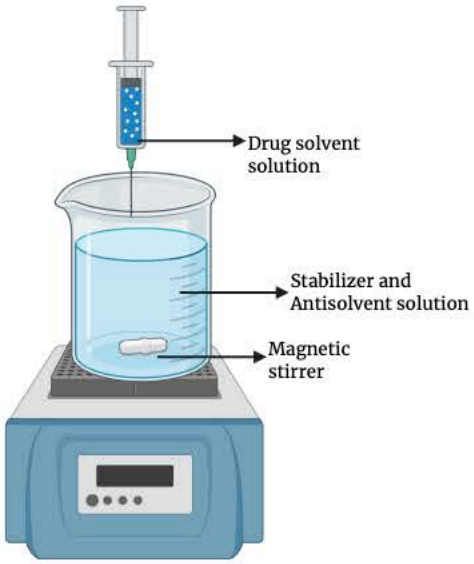

Figure 3.6. Schematic representation of LAS precipitation method.

The fundamental principle of LAS precipitation is based on the rapid creation of supersaturation conditions, which drive the nucleation and growth of nanocrystals [115]. This process is driven by supersaturation and can be described by classical nucleation theory and the Ostwald-Miers super solubility diagram [124,125].

Supersaturation (S) is the key parameter that dictates nucleation and crystal growth. S is defined as the ratio of the actual drug concentration (C) in solution to its equilibrium solubility (C*) in the same solvent system is shown in Equation 3.1 [124,125].

$$S = \frac{C}{C^*} \qquad \textbf{\textit{Equation 3.1}}.$$

Where:

S = the supersaturation ratio

C = the actual concentration of the drug in solution

C* = the equilibrium solubility of the drug in the solvent

A higher supersaturation ratio (S) implies a greater thermodynamic driving force for nucleation, meaning higher rate of nucleus formation. However, if supersaturation is not well controlled, it can result in rapid nucleation followed by uncontrolled crystal growth, leading to polydisperse particle sizes and particle aggregation [124,125].

To fully understand how nucleation occurs and how it influences crystal formation, classical nucleation theory (CNT) must be understood. CNT explains how stable nuclei form within a supersaturated solution [124,125]. The theory states that for a nucleus to form and grow, it must overcome an energy barrier, known as the critical free energy of nucleation (ΔG^*) [124,125]. CNT states that nucleation occurs in two stages, molecular clustering (Drug molecules randomly aggregate due to intermolecular forces) and formation of a stable nucleus which is if a cluster reaches a critical size, it becomes thermodynamically stable and grows into a crystal [124,125]. The formation of nuclei is opposed by two competing thermodynamic factors, volume free energy (ΔGv), and thermodynamic driving force that promotes nucleation by reducing overall system energy [124,125]. This is proportional to the degree of supersaturation and surface free energy (ΔGs), a resistance force that opposes nucleation . This arises because forming a new surface requires energy due to surface tension [124,125]. The

total free energy change (ΔG) associated with nucleus formation is given in equation 3.2 [124,125].

$$\Delta G = \frac{4}{3}\pi r^3 \Delta G_v + 4\pi r^2 \gamma \qquad \textbf{\textit{Equation 3.2}}.$$

Where:

R = the nucleus radius

ΔG_v = the volume free energy change per unit volume

γ = the interfacial surface tension

At a critical radius r^*, the nucleus reaches a point where further growth is spontaneous [124,125]. The critical nucleation free energy barrier (ΔG^*) is given in Equation 3.3 [124,125].

$$\Delta G^* = \frac{16\pi\gamma^3}{3(\Delta G_v)^2} \qquad \textbf{\textit{Equation 3.3}}.$$

Higher supersaturation (ΔGv) reduces the nucleation energy barrier (ΔG^*), increasing nucleation rate. Higher surface tension (γ) increases the nucleation barrier, making nucleation less favourable. There are two types of nucleation, homogenous and heterogenous nucleation. Homogeneous nucleation occurs spontaneously in a uniformly supersaturated solution, without any external surfaces or impurities [124,125]. It follows Equation 3.4 [124,125].

$$J = A \exp\left(\frac{-16\pi\gamma^3 v^2}{3k^3T^3(\ln S)^2}\right) \qquad \textbf{\textit{Equation 3.4}}.$$

Where:

J = the nucleation rate (number of nuclei per unit volume per unit time)

A = a pre-exponential factor

γ = the surface tension of the forming nucleus

v = the molecular volume of the solute

k = Boltzmann's constant

T = the absolute temperature

S = the supersaturation ratio

Figure 3.7 demonstrates the interaction between surface free energy and volume free energy.

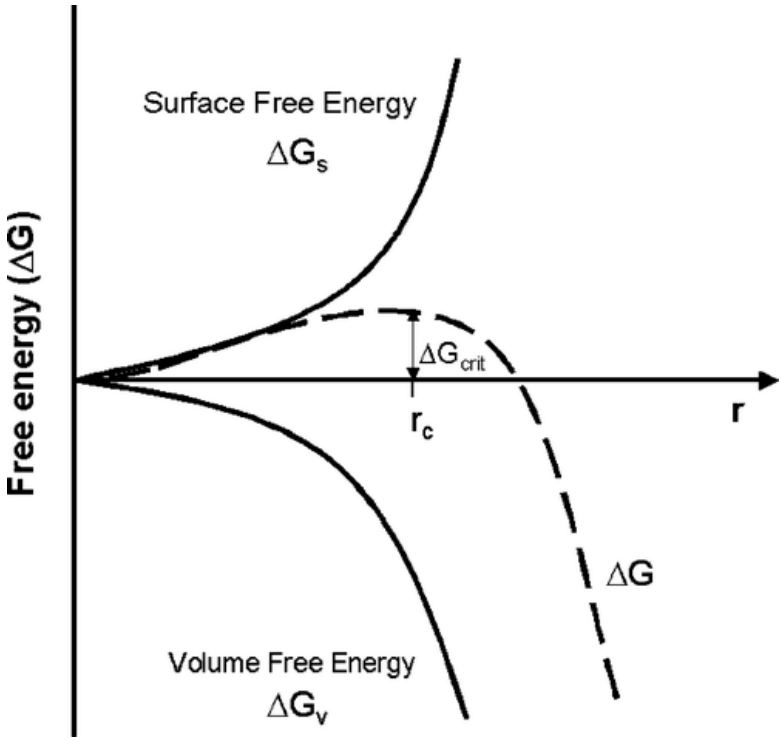

Figure 3.7. Free energy diagram for nucleation (Adapted from [126]).

The total free energy change (ΔG) for nucleus formation is the sum of positive surface energy and negative volume free energy. Initially, when the nucleus is very small, the surface free energy dominates, increasing the total free energy and acting as a barrier to nucleation. However, beyond a critical nucleus radius (r_c), the volume free energy becomes more favourable, leading to spontaneous crystal growth. The energy barrier that must be overcome for stable nucleation is the critical nucleation free energy. If the nucleus size is below r_c, it is unstable and dissolves back into solution and if the nucleus surpasses r_c, it continues to grow spontaneously [126].

A higher supersaturation ratio (S) exponentially increases the nucleation rate (J), leading to a larger number of small nuclei instead of a few large ones. However, homogeneous nucleation requires very high supersaturation levels, which may result in polydisperse and unstable particles [124,125].

Heterogeneous nucleation occurs on foreign surfaces such as pre-existing particles, container walls, or stabilisers [124,125]. It requires less energy than homogeneous nucleation because the external surface lowers the energy barrier needed for stable nuclei formation [124,125]. The nucleation energy barrier for heterogeneous nucleation is lower, making this process more thermodynamically favourable [124,125]. As a result, heterogeneous nucleation occurs at lower supersaturation levels than homogeneous nucleation [124,125].

Once nucleation occurs, drug molecules from the supersaturated solution deposit onto the stable nuclei, leading to crystal growth [124,125]. The rate of crystal growth depends on supersaturation level (a higher supersaturation leads to faster growth rates), diffusion rate of drug molecules (the rate at which drug molecules reach the growing crystal surface), and stabilisers in the system (can control growth by steric hindrance or electrostatic repulsion). The crystal growth rate (G) is approximated by equation 3.5 [124,125].

$$G = k_g(C - C^*) \qquad \textbf{\textit{Equation 3.5}}.$$

Where:

G = the crystal growth rate

k_g = the growth rate constant, dependent on temperature and system properties

C = the actual concentration of the drug in solution

C^* = the equilibrium saturation concentration

If supersaturation is too high, rapid nucleation occurs, but uncontrolled crystal growth can follow, leading to large, polydisperse particles [124,125]. Conversely, if supersaturation is too low, nucleation is slow, leading to fewer but larger particles. To achieve uniform nanocrystals, the process must be precisely controlled by adjusting solvent-antisolvent composition, mixing rate, temperature, stabiliser, drug concentration, and stabiliser concentration [124,125].

The Ostwald-Miers diagram is a graphical representation that shows the relationship between supersaturation levels and the processes of nucleation and crystal growth as shown in Figure 3.8. It defines three zones based on solubility conditions [127]. The metastable zone or metastable zone width (MSZW) is where the solution remains supersaturated, but nucleation does not occur spontaneously. Pre-existing nuclei or seed crystals gradually grow through controlled crystal growth mechanisms, making this zone ideal for achieving uniform

nanocrystal formation without excessive nucleation. The labile (nucleation) zone exists at high supersaturation levels, where spontaneous nucleation occurs rapidly, leading to the formation of numerous small nuclei. While this helps generate fine nanocrystals, uncontrolled nucleation in this zone can result in particle aggregation and polydispersity, compromising the stability of the nanosuspension. The undersaturated zone, where the concentration of the solute (C) is below its equilibrium solubility (C^*), prevents both nucleation and crystal growth. In this region, any existing crystals will dissolve back into the solution. For successful nanocrystal production, the strategy is to briefly enter the labile zone to trigger nucleation and then quickly return to the metastable zone to enable controlled crystal growth while minimising unwanted aggregation [127].

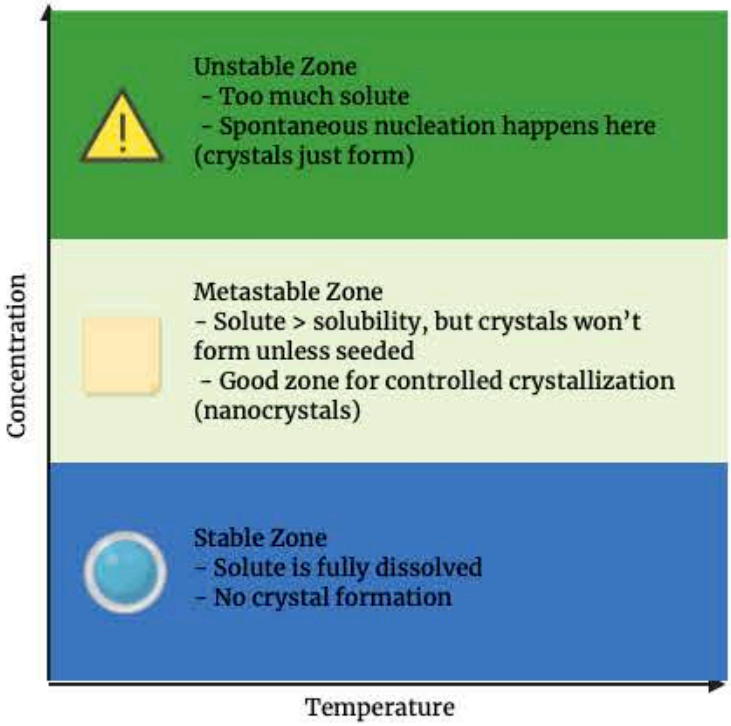

Figure 3.8. Ostwald-Miers diagram

Several poorly water-soluble drugs have been successfully formulated using the LASP method, demonstrating its efficiency in enhancing solubility and bioavailability. Atorvastatin calcium was formulated into nanoparticles via LASP, resulting in improved dissolution rates and enhanced oral bioavailability [128,129]. Similarly, cilostazol, a BCS Class II drug, showed significantly increased dissolution when formulated through LASP combined with ultrasonication [130]. In another study, albendazole, an antiparasitic agent, was transformed into stable nanosized particles using LASP, achieving a substantial increase in dissolution rate

and potential bioavailability [131]. Since AZI is poorly soluble in water but dissolves readily in organic solvents, this method enables rapid nanocrystal formation by inducing supersaturation. By briefly entering the labile zone to trigger nucleation and then shifting to the metastable zone, controlled crystal growth can be achieved, preventing excessive aggregation and polydispersity. This technique eliminates the need for heat exposure, preserving the stability of AZI, making it an ideal approach for the small-scale laboratory production of its nanocrystals.

3.2.2.2. Supercritical Fluid Method

The supercritical fluid method utilizes supercritical carbon dioxide to dissolve the drug under high pressure, followed by rapid expansion to induce nanoparticle precipitation [112,116,132]. This method is solvent-free and environmentally friendly, producing uniform particles with controlled morphology [112,116,132]. Numerous poorly water-soluble drugs have been successfully processed into nanosuspensions using supercritical fluid technology, as reviewed by Misra and Pathak [133]. Techniques such as Rapid Expansion of Supercritical Solutions (RESS) and Supercritical Antisolvent (SAS) methods have enabled particle size reduction into the nanometer range, resulting in enhanced solubility and bioavailability [133]. For example, RESS has been used to generate nanoparticles of cefuroxime axetil, diclofenac, and digitoxin, with particle sizes as low as 68 nm and marked improvements in dissolution profiles [133]. Similarly, SAS has been applied to drugs like telmisartan and atorvastatin calcium, yielding amorphous nanoparticles with superior solubility [133]. However, high operational costs and the requirement for specialized equipment limit its widespread application. It is primarily used for thermally sensitive compounds [112,116,132].

3.2.3. Combination Technology

Combination technologies integrate top-down and bottom-up approaches to optimise particle size reduction while maintaining product quality and stability [116].

3.2.3.1. Precipitation Lyophilization Homogenisation Method

This method combines precipitation, freeze-drying (lyophilization), and homogenisation to produce stable nanosuspensions [116,134]. Precipitation ensures high purity, lyophilization improves stability, and homogenisation ensures narrow particle size distribution [116,134]. The precipitation lyophilization homogenisation method has been successfully applied to

formulate nanosuspensions of poorly water-soluble drugs, enhancing their bioavailability. For instance, ursodeoxycholic acid, a bile acid used to dissolve gallstones and treat liver disorders was formulated into nanocrystals using the precipitation lyophilization homogenisation approach, resulting in significantly improved dissolution rates [135]. Isradipine, a calcium channel blocker used to treat high blood pressure, was also formulated using precipitation lyophilization homogenisation, achieving a marked increase in dissolution and oral bioavailability [136].

3.2.3.2. Nanoedge Technology

Nanoedge technology integrates microprecipitation with high-pressure homogenisation to achieve rapid size reduction while maintaining stability [113,117]. This technique is particularly effective for poorly soluble drugs requiring enhanced bioavailability [113,117]. Glabridin, a natural isoflavone known for its anti-inflammatory and skin whitening properties, was developed into a nanosuspension using a combination of anti-solvent precipitation and high-pressure homogenisation, characteristic of the Nanoedge process [137]. This formulation method improved glabridin's skin penetration capabilities, as demonstrated in both *in vitro* and *in vivo* studies, where it showed enhanced flux through rat skin without a lag phase. This finding highlights the effectiveness of Nanoedge technology in enhancing the topical delivery and stability of poorly water-soluble compounds.

3.3. CHARACTERISATION OF NANOCRYSTALS

Characterisation of nanocrystals is a crucial aspect of nanotechnology to ensure that quality of the product is produced. Nanocrystals are made to have specific characteristics such as size, shape, surface area, and crystallinity. These properties significantly influence their dissolution velocity, saturation solubility, which are essential for improving drug efficacy and delivery systems [109,138]. The characterisation process involves a range of techniques including, transmission electron microscopy (TEM), differential scanning calorimetry (DSC), and X-ray diffraction (XRD), and in *vitro* dissolution studies [109,139]. Understanding these properties is vital for optimizing nanocrystal formulations and ensuring stability and effectiveness [138].

3.3.1. Particle size and polydispersity index

Particle size (PS) is a key parameter in the performance of nanocrystals. This affects the dissolution rate as smaller particles have a larger surface area therefore increasing dissolution in accordance with the Noyes–Whitney equation (Equation 3.6) [140,141]. In this equation, the dissolution rate of a solid material is proportional to its surface area [140,141]. By having a larger surface area, it aids dissolution of poorly soluble drugs like AZI.

$$\frac{dm}{dt} = \frac{DA}{h}(s - c) \qquad \textit{Equation 3.6}.$$

Where:

$\frac{dm}{dt}$ = the dissolution rate

D = the diffusion coefficient of the solute

A = the effective surface area of the particles

h = the diffusion boundary layer thickness

s = the saturation solubility

c = the concentration of the solute in the bulk medium

The nature of a drugs PS is also based on the Ostwald–Freundlich equation, which stated that smaller particles exhibit increased apparent solubility due to its increased surface energy [141]. Enhanced dissolution leads to improved gastrointestinal absorption, therefore increasing the bioavailability, which is essential for BCS Class II drugs like AZI [140]. Nanocrystals may aggregate if their particle size distribution is not well-controlled, hence it is vital that we control the PS.

The polydispersity index (PDI) is a measure that describes the distribution of PS within a sample, ranging from 0 to 1 [142]. It is a critical parameter in evaluating the uniformity and stability of nanoparticles [142]. A PDI less than 0.1 indicates that the particles are monodisperse and is highly uniform. A PDI between 0.1 and 0.3 suggests a narrow PS distribution, which is generally acceptable for pharmaceutical applications [142]. Maintaining a PDI within this range ensures batch-to-batch consistency and minimizes the risk of particle aggregation, which can affect drug dissolution and efficacy [142]. A PDI greater than 0.3 indicates a broad PS distribution, which may suggest aggregation or instability [142]. High PDI

values can lead to inconsistent performance and reduced therapeutic effectiveness of the formulation [142].

Dynamic light scattering (DLS) is a technique used for measuring the size and size distribution of nanoparticles in dispersion [143]. The principle of DLS is based on the Brownian motion of particles in a fluid [143]. When a laser beam illuminates a sample, the particles scatter light in all directions [143]. The scattered light intensity fluctuates due to the random motion of the particles, which is caused by collisions with solvent molecules [143]. These fluctuations are analysed over time to determine the diffusion coefficient of the particles, from which their hydrodynamic diameter can be calculated using the Stokes-Einstein equation as seen in Equation 3.7 [143].

$$D_u = \frac{k_B T}{3\pi\eta d} \qquad \textit{Equation 3.7.}$$

Where:

D_u = the hydrodynamic diameter of the particle

k_B = the Boltzmann constant

T = the absolute temperature (K)

η = the viscosity of the medium

d = the diffusion coefficient

3.3.2. Particle charge, zeta potential, and electrophoretic mobility

Zeta potential (ζ) is the electrostatic potential at the surface layer of a nanoparticle, which influences the colloidal stability, bioavailability, and dissolution [144–146]. High ζ values indicate strong electrostatic repulsion, reducing particle aggregation [144,145]. The charge interactions with biological membranes affect drug absorption. enhancing or hindering drug uptake [144,145]. A stable ζ prevents particle settling and flocculation, ensuring uniform dispersion in the formulation [144,145]. Electrophoretic light scattering (ELS) is a technique used to measure ζ by observing the movement of charged particles in an applied electric field [144,145]. During ELS, particles move toward the electrode of opposite charge, scattering light as they move [144,145]. The Doppler shift of the scattered light is proportional to the particle velocity, which is used to calculate electrophoretic mobility and ζ [144,145]. High

electrophoretic mobility indicates a high ζ, suggesting strong electrostatic repulsion between particles and thus a stable dispersion [144,145]. A low mobility corresponds to a low ζ, indicating a higher likelihood of particle aggregation [144,145]. The relationship between electrophoretic mobility and ζ can be described by Henry's Equation 3.8 [146].

$$\zeta = \frac{4\pi\eta\mu_e}{\epsilon f(\kappa a)} \qquad \textit{Equation 3.8}.$$

Where:

η = the viscosity of the medium

ϵ = the dielectric constant

f(κa) = Henry's function

μ_e = Electrophoretic mobility of the particle

Particles with zeta potentials greater than ± 30 mV are considered highly stable [147]. This high magnitude of ζ indicates strong electrostatic repulsion between particles, preventing them from aggregating [147]. Nanoparticles with a ζ larger than ± 60 mV have excellent stability [147]. Particles with ζ between ± 15 and ± 30 mV are moderately stable [147]. While they exhibit some degree of repulsion, they may still be prone to aggregation under certain conditions, such as changes in pH or ionic strength [147]. Particles with zeta potentials less than ± 15 mV are considered unstable. They lack sufficient electrostatic repulsion, making them prone to aggregation [147].

3.3.3. Crystallisation, polymorphism and compatibility

Fourier transform infrared spectroscopy (FTIR) is a crucial analytical tool for characterizing AZI nanocrystals as it shows their molecular structure and interactions [148,149]. The FTIR analysis works by exposing the sample to infrared radiation, which excites molecular bonds into higher vibrational states, producing an absorption spectrum that serves as a molecular fingerprint [148,149]. This fingerprint helps identify the presence of specific functional groups and assess any changes in the molecular environment of AZI upon nanoparticle formation [148,149]. By analysing these spectra, scientists can confirm that its chemical structure remains intact, which is essential for maintaining its antimicrobial efficacy [148,149]. This is governed by Beer-lambert's law which is essential when trying to understand FTIR [150,151]. This law states that the absorbance (A) of light passing through a sample is directly proportional to both

the concentration (c) of the absorbing species and the path length (L) of the light through the material is shown in equation 3.9 [150,151].

$$A = \epsilon Lc \qquad \textbf{\textit{Equation 3.9}}.$$

Where:

ϵ = the molar absorptivity

c = the concentration the drug

L = the length of the path of light

When AZI is loaded into chitosan nanoparticles, FTIR spectra can reveal distinct peaks that indicate the presence of both the drug and the polymer. Peaks such as those at 3273, 2982, 1406, 1589, 1401, and 1037 cm^{-1} are observed, which can be attributed to various functional groups like C-H stretches, N-H stretches, and carbonyl stretches, confirming the interaction between AZI and chitosan [152]. Similarly, in formulations involving Eudragit RL 100, FTIR spectra of AZI-loaded nanoparticles show characteristic peaks of both the drug and the polymer, indicating their compatibility and successful encapsulation [153].

Differential scanning calorimetry (DSC) provides insights into their thermal behaviour and crystallinity [139,154]. DSC measures the heat flow associated with phase transitions in a material as a function of temperature [139,154]. It helps determine melting point, glass transition temperature, crystallinity, polymorphic transitions, and drug-excipient compatibility [139,154]. A DSC instrument has two identical pans, a sample pan (drug/excipient) and a reference pan (contains an inert material) [139,154]. Both pans are heated at a controlled rate, and the difference in heat flow between the sample and reference is recorded. If the sample undergoes a thermal event (melting, crystallisation, decomposition), it absorbs or releases heat, leading to an endothermic or exothermic peak [139,154]. The glass transition occurs in amorphous materials, showing a gradual baseline shift [139,154]. The melting point shows a sharp endothermic peak for crystalline substances [139,154]. For crystallisation, an exothermic peak, where amorphous material transforms into a crystalline form [139,154]. DSC follows the heat flow and enthalpy change in equation 3.10 and 3.11 [154]. The enthalpy change quantifies the energy required for phase transitions, therefore distinguishing the difference between crystalline and amorphous forms [154].

$$q = mC_p\Delta T$$ ***Equation 3.10***.

Where:

q = heat flow (J/s)

m = mass of the sample (g)

Cp = specific heat capacity (J/g·K)

ΔT = change in temperature (K)

$$\Delta H = \int q\ dt$$ ***Equation 3.11***.

Where:

ΔH = enthalpy change (J/g)

q = heat flow rate (J/s)

When AZI is encapsulated into nanoparticles, DSC is used to analyse the thermal transitions of the drug within the polymeric matrix. In the studies involving AZI-loaded nanoparticles, DSC thermograms have shown that the drug often transitions into an amorphous state upon encapsulation, which is crucial for enhancing its solubility and bioavailability [155].

X-ray diffraction (XRD) is a technique used to characterise the crystalline structure of nanocrystals [139]. XRD is based on the diffraction of X-rays by crystal lattice planes [139]. Crystalline materials scatter X-rays at specific angles, producing a diffraction pattern that reveals atomic structure [139]. When AZI is encapsulated in Eudragit RL 100 nanoparticles, XRD analysis can reveal whether the drug remains in its crystalline form or transitions into an amorphous state upon encapsulation [153]. Pure AZI exhibits sharp peaks in its XRD pattern, indicating its crystalline nature, with peaks at specific diffraction angles such as 7.75°, 9.22°, 9.63°, 9.74°, 11.87°, 11.94°, 16.26°, and 18.63° [153]. When AZI is successfully encapsulated in nanoparticles, these characteristic peaks often disappear or become less intense, suggesting that the drug is dispersed in an amorphous form within the polymer matrix [153]. This amorphous state can enhance the solubility and bioavailability of AZI [153].

3.3.4. Imaging Analysis

Image analysis provides a details about their size, shape, surface morphology, and internal structure [156]. Transmission electron microscopy (TEM), and scanning electron microscopy (SEM) are used to obtain high-resolution images of nanoparticles [156]. These images are then subjected to various image analysis methods to extract quantitative data and qualitative insights [156]. TEM is a preferred method for directly measuring the particle size, grain size, size distribution, and morphology of nanoparticles [156]. It can visualize particles from 5 nm to 1 micron [156]. SEM is useful for examining the surface morphology and dispersion of nanoparticles in matrices [156].

3.3.5. In *vitro* release studies

In *vitro* release studies are conducted to evaluate the dissolution and drug release kinetics of AZI nanocrystals, which predict the in vivo bioavailability [157]. These studies are performed using USP dissolution apparatus II (paddle) or IV (flow-through cell) [107,158]. The dissolution medium includes simulated gastric fluid (SGF, pH 1.2), simulated intestinal fluid (SIF, pH 6.8), or phosphate buffer (pH 7.4) to mimic different physiological environments [107,158]. To enhance the solubility of poorly water-soluble drugs like AZI, surfactants such as sodium lauryl sulphate (SLS, 0.5–1%) or Tween 80 are sometimes added [107,158]. During the test, aliquots of the dissolution medium will be withdrawn at predetermined intervals, filtered, and analysed using the HPLC method in § 2.4.4. The release profiles will be plotted and fitted to mathematical models to determine the release mechanism. The Noyes-Whitney equation governs the dissolution rate (equation 3.6).

3.4. CONCLUSIONS

Nanotechnology-based formulations have emerged in the last few decades as a strategic approach to improve the bioavailability of poorly soluble drugs such as AZI. This method was specifically chosen for AZI due to its low aqueous solubility, high molecular weight, and pH-dependent dissolution profile, which limit its absorption and therapeutic efficiency when administered orally. Nanocrystal technology directly addresses these issues by increasing the surface area available for dissolution and enabling more rapid drug release at physiological pH levels, thus improving bioavailability. By reducing AZI particles to 100–600 nm, nanocrystals enhance surface area-to-volume ratio, facilitating better gastrointestinal absorption and higher

therapeutic efficacy. Nanocrystals offer advantages over lipid-based carriers like solid lipid nanoparticles (SLNs) and nanostructured lipid carriers (NLCs) due to their high drug loading capacity and minimal excipient requirements. Various top-down (high-pressure homogenisation, wet bead milling) and bottom-up (antisolvent precipitation, supercritical fluid) methods are employed for nanocrystal production, with stabilisers (Poloxamer 407, PVP K30, Tween 80) ensuring colloidal stability. The effectiveness of nanocrystal-based delivery is closely linked to the physicochemical properties of the drug. However, challenges remain in selecting appropriate analytical and characterisation methods to ensure the scientific reliability and quality control of AZI nanocrystals. The samples need to be characterised using multiple parameters are the same times such as DLS (particle size and PDI), zeta potential (stability), FTIR (chemical integrity), DSC & XRD (crystallinity and polymorphism) confirm the physicochemical properties of AZI nanocrystals. In *vitro* release studies using USP dissolution apparatus (Type II & IV) demonstrate enhanced drug release. AZI nanocrystal nanosuspensions provide an effective strategy to enhance drug solubility and therapeutic performance.

CHAPTER 4

PREFORMULATION AND PRELIMINARY STUDIES

4.1. INTRODUCTION

Pre-formulation and preliminary studies form the foundation of a successful pharmaceutical product. These studies are critical in ensuring that the formulation is stable, effective, and exhibits the desired physicochemical properties [159,160]. The focus is on the development of an AZI nanosuspension. Nanosuspensions maintain a high drug load and do not require extensive excipients [108]. The advantage of nanocrystals is their ability to enhance solubility and dissolution rate through an increased surface area, leading to improved bioavailability and faster onset of action [108]. Low bioavailability is one of the many challenges seen with poorly soluble drugs. Thus, there is a growing necessity for presenting a unique strategy to tackle the formulation challenges related to the delivery of hydrophobic drugs & improve their clinical efficacy.

Selecting the right solvent antisolvent pair is crucial as it influences particle size, growth rate, and overall stability of the nanocrystals within the suspension [161]. The solvent must efficiently dissolve the drug, while the antisolvent must induce rapid precipitation under controlled conditions. If the precipitation process is too fast or uncontrolled, non-uniform particle formation, excessive aggregation, or uncontrolled crystal growth may occur, leading to larger, less soluble particles [161]. If the precipitation process is too slow, incomplete nucleation may result in poor drug loading efficiency and inconsistent particle size distribution, which can affect dissolution and bioavailability [161,162]. Drug and stabiliser compatibility is essential for ensuring a stable nanocrystal formulation. Stabilisers prevent particle aggregation by adsorbing onto the nanocrystal surface and creating a protective barrier that prevents uncontrolled growth and agglomeration [161]. The nanosuspension needs to be stabilized by a minimum amount of suitable ionic or steric stabiliser. If an incompatible stabiliser is used, it fails to adhere properly to the nanocrystal surface, leading to instability, poor dispersion, and increased particle size over time [161,163]. This can compromise the nanosuspension's long-term stability and result in rapid sedimentation. Another factor in formulation stability is polymorphic transformation, which can occur if excipients or processing conditions alter the drug's crystal structure. Different polymorphic forms exhibit varying solubility, dissolution rates, which can impact the pharmacokinetics of AZI [161,162]. If an unstable or less soluble polymorph is formed during precipitation, it

may reduce the formulation's effectiveness, lead to unwanted recrystallisation, or cause a decline in therapeutic efficiency over time [161,162]. By conducting thorough preformulation studies these potential incompatibilities can be identified and addressed early in the development process, ensuring optimal solubility, and stability of the final nanocrystal nanosuspension formulation.

In this study, Fourier transform infrared spectroscopy (FTIR), Differential scanning calorimetry (DSC), and Powder X-Ray diffraction (PXRD) are conducted to characterise the drug-excipient interactions and assess their compatibility [159,160]. FTIR is used to identify functional groups and detect any drug-excipient interactions [159,160]. DSC assesses the thermal stability and polymorphic transitions of the drug [159,160]. PXRD identifies the crystalline or amorphous nature of the drug [159,160]. Ideally all drug and excipient must be compatible to ensure optimal particle size (100–500 nm), prevent aggregation or degradation, and ensure dispersibility.

4.2. MATERIALS AND METHODS

4.2.1. Materials

4.2.1.1. Ethanol

Ethanol is a colourless, hygroscopic liquid with a boiling point of 78° to 79°C [3]. It is an organic solvent and is miscible with water and evaporates quickly, hence minimising solvent residues in formulations [3]. In nanocrystal formulation, ethanol helps completely dissolve AZI and facilitates rapid precipitation when introduced into an antisolvent like water. It should be stored below 30°C and protected from light [3].

4.2.1.2. Acetone

Acetone (propanone) is a volatile, clear, colourless liquid with a strong solvent action [3]. It is miscible with water and ethanol (96%), making it useful for dissolving a wide range of compounds [3]. Due to its high volatility, it evaporates quickly, reducing the risk of residual solvent in formulations. Acetone is commonly used in solvent antisolvent precipitation methods to aid in the rapid crystallisation of drugs.

4.2.1.3. Tween®80

Tween®80 (Figure 4.1), also known as polysorbate 80 or polyoxyethylene (20) sorbitan monooleate is a non-ionic surfactant widely used in pharmaceutical industry [164]. It is composed of a polyoxyethylene sorbitan headgroup esterified with oleic acid, making both hydrophilic and lipophilic properties [164].

Figure 4.1. Structure of polysorbate 80 (Tween®80).

This amphiphilic nature allows it to be a versatile emulsifier, solubilizer, and stabiliser [165]. Tween®80 reduces surface and interfacial tension in aqueous systems and has a high Hydrophilic-Lipophilic Balance value, making it suitable for solubilising poorly water-soluble compounds [165]. Tween®80 adsorbs at the interface of immiscible phases, lowers the interfacial tension and facilitates the formation of a stable dispersion [165]. Tween®80's large hydrophilic headgroup provides steric repulsion between particles, preventing aggregation in suspensions [165]. Tween®80 is a clear to slightly cloudy, oily liquid that is hygroscopic and ranges from colourless to brownish yellow [3]. It is soluble in water, ethanol, ethyl acetate, and methanol, but practically insoluble in fatty oils and liquid paraffin [3].

4.2.1.4. Polyvinylpyrrolidone K30

Polyvinylpyrrolidone K30 (PVP K30) shown in Figure 4.2 is a white or yellowish-white, hygroscopic powder or flakes that is freely soluble in water, ethanol (96%), and methanol, but very slightly soluble in acetone [3]. The K-value refers to the polymers viscosity to molecular weight suggesting that K30 has a medium weight and viscosity [166]. It plays a role in both the nanocrystal formation and nanosuspension formulation of AZI by enhancing solubility and stability. As a stabiliser, PVP K30 forms a hydrophilic layer around drug

particles, preventing aggregation and ensuring uniform nanocrystal size [166]. This controls particle size and prevents uncontrolled crystal growth, leading to smaller, more stable nanocrystals [166].

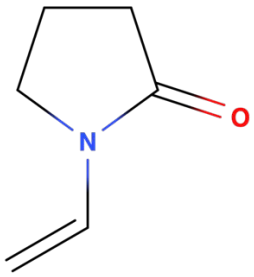

Figure 4.2. Chemical structure of Polyvinylpyrrolidone (PVP).

4.2.1.5. Potassium hydrogen orthophosphate

Potassium dihydrogen orthophosphate is an anhydrous inorganic salt that occurs as a white and water-soluble powder [3]. The compound is used as a buffering agent in this study as used in § 2.3.3.1.

4.2.2. Methods

4.2.2.1. Screening solvents

The solubility screening of AZI (Figure 4.3) was conducted using ethanol, deionized water, acetone, and phosphate buffer (pH 7.5) as solvents. A supersaturated solution was prepared by measuring 5 mL of each solvent using a graduated measuring cylinder, followed by the addition of an excess amount of AZI. The mixture was stirred using a magnetic stirrer on a VWR hotplate/stirrer (Radnor, Pennsylvania, USA) to enhance solubilization. To maintain physiological conditions, the samples were maintained at 37 °C throughout the process. The samples were centrifuged using a MiniStar® Plus centrifuge (Hangzhou Allsheng instruments, China) at 10000 rpm for 10 minutes to separate any undissolved drug particles. The supernatant was extracted and filtered through a 0.45 µm GVS Ablu filter (Sanford, ME, USA) to remove particulate matter. The filtered solution was then transferred into HPLC vials for analysis. The solubility of AZI in each solvent was determined by extrapolating the peak height ratio from the validated calibration curve using the RP-HPLC method.

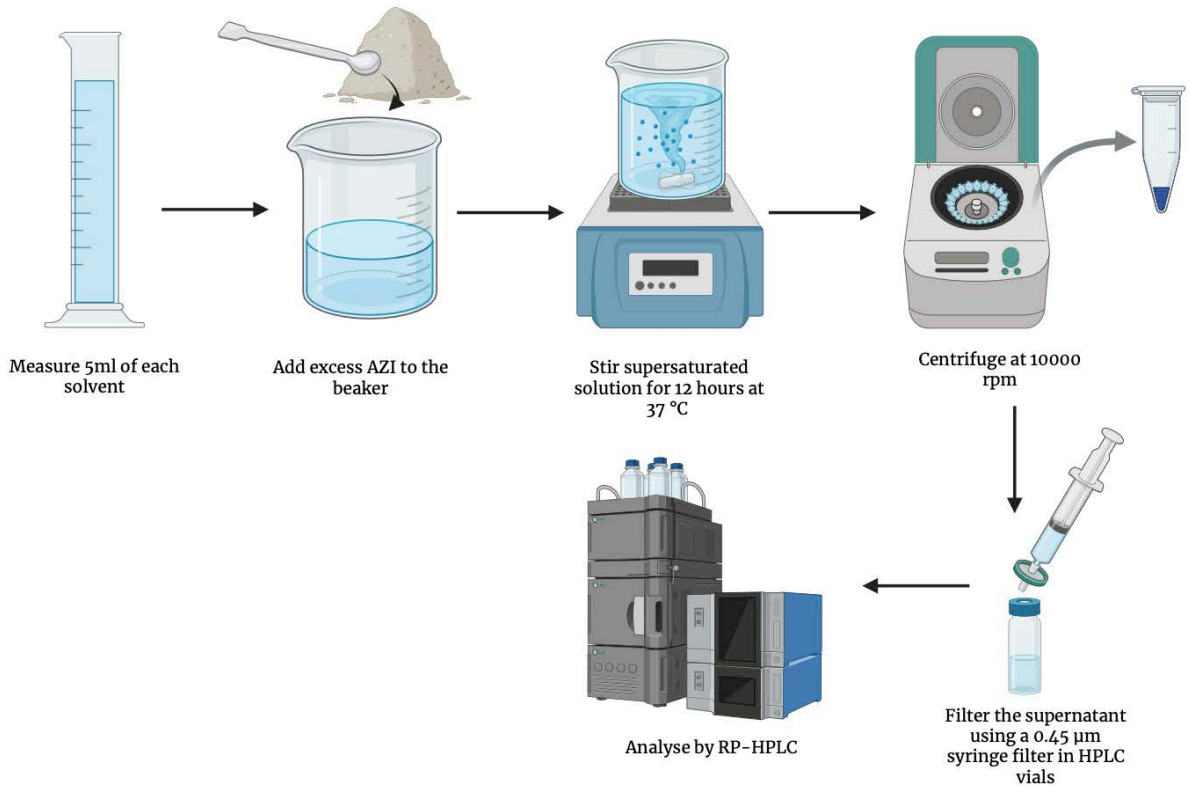

Figure 4.3. Schematic representation of solvent screening method for AZI.

4.2.2.2. FT-IR characterisation

The drug excipient interaction study was carried out by using physical observation. A spectrum two FTIR ATR spectrophotometer (Perkin Elmer® Ltd, Beaconsfield, England) was used to analyse AZI and investigate potential interactions between AZI and excipients. The mixture of AZI and each excipient (1:1) ratio was placed in the FTIR sample holder. The AZI sample was placed and scanned over the range of 4000–400 cm^{-1}. The obtained spectrum was recorded.

4.2.2.3. DSC characterisation

For thermal analysis of AZI, 1:1 w/w ratio binary mixtures of AZI and excipients, a model Q100 DSC (TA instruments, New Castle, DE, USA) coupled with a RCS (90) Refrigerated Cooling System (TA Instruments, New Castle, DE, USA) was used. Approximately 1 mg of each sample were weighed out onto an aluminium pan and the pans were covered with an aluminium lid (§ 1.2.7). The thermograms were analysed using a TA Universal Analysis software (TA Instruments, New Castle, DE, USA).

4.2.2.4. XRD characterisation

XRD patterns of AZI were recorded using a Model D8 Discover X-ray diffractometer (Bruker, Billerica, MA, USA) that was equipped with a PSD LynxEye detector coupled to a copper anode (Cu-Kα radiation, λ = 1.5405 Å, 30 kV). Samples were placed on a zero-background silicon wafer embedded in a generic sample holder. The data were recorded at room temperature (22 °C) using a 2θ range between 10˚ and 100˚, a scanning rate of 1˚ min^{-1}, a filter time constant of 2.0 s per step, and a slit width of 6.0 mm. The data were fitted using evaluation (Eva) curve-fitting software (Bruker, Billerica, MA, USA). All samples used for XRD analysis were identical to those used for DSC studies to ensure ease of data comparison and characterisation.

4.3. RESULTS AND DISCUSSION

4.3.1. Screening solvents

The comparative solubility analysis of AZI in various solvents was determined with the aim of selecting a solvent with the best solubilising potential for AZI. This was conducted in four different solvents: ethanol, deionized water, acetone and a phosphate buffer pH 7.5. Phosphate buffer at pH 7.5 was included in the solubility screening study to represent a biorelevant aqueous environment and to understand how AZI behaves in physiological pH conditions. Although not an organic solvent, assessing solubility in pH 7.5 buffer helps determine whether AZI can be effectively dissolved in aqueous conditions. This allows confirmation that an aqueous solvent alone cannot sufficiently dissolve the drug, thus justifying the use of a more effective organic solvent like ethanol or acetone in the solvent–antisolvent process. The resultant data are shown and expressed in logarithmic scale in Figure 4.4.

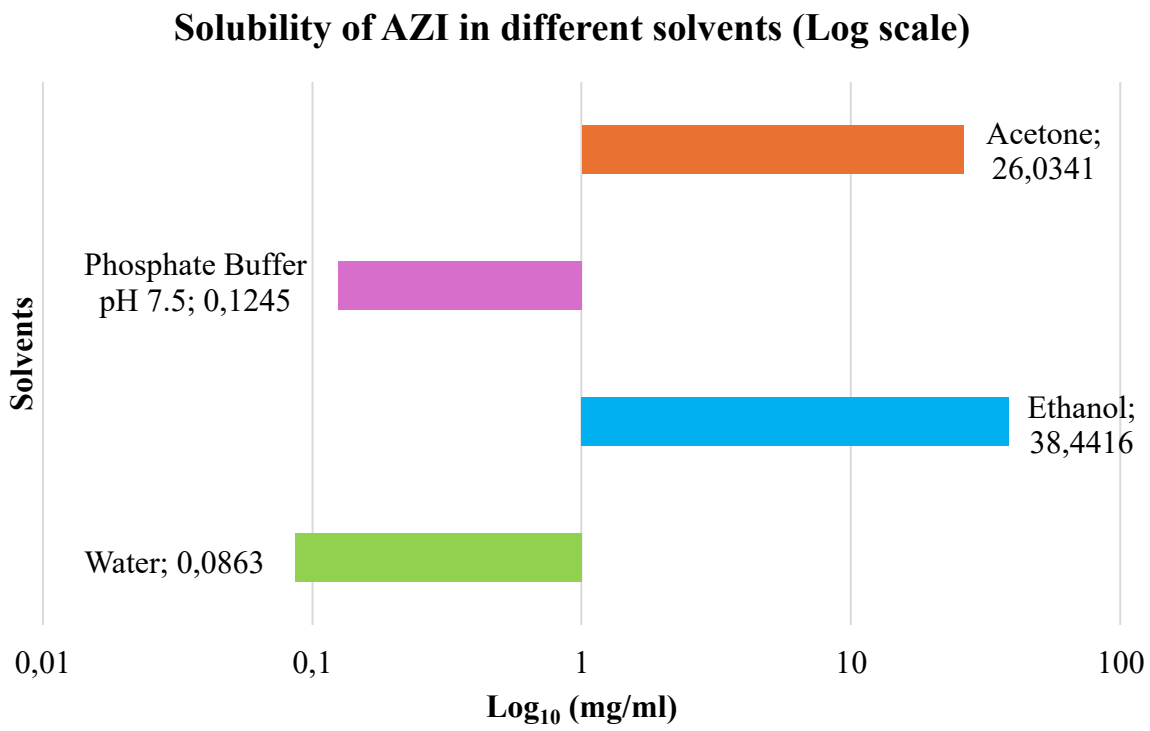

Figure 4.4. Solubility of AZI (log_{10} scale) in four different solvents at 37 °C, showing highest solubility in ethanol (38.4416 mg/mL), followed by acetone (26.0341 mg/mL), phosphate buffer pH 7.5 (0.1245 mg/mL), and water (0.0863 mg/mL).

The results demonstrate that AZI exhibits low solubility in highly polar media (water and phosphate buffer), while its solubility is significantly enhanced in organic solvents (acetone and ethanol). On a log scale, the solubility in acetone and ethanol is from $10^{1.4}$–$10^{1.6}$ mg/mL, whereas in water and phosphate buffer it is below 10^{-1} mg/mL. AZI's limited solubility (under 0.2 mg/mL) indicates its lipophilic nature with highly polar environments. The slight increase from water to phosphate buffer (pH 7.5) suggests that pH adjustment in the tested range does not improve solubility significantly. AZI's solubility increases by over two orders in acetone and ethanol compared to water. This demonstrates AZI's affinity for less polar organic solvents which is common with API's containing lipophilic functional groups. Given AZI's highest solubility in ethanol (38.4416 mg/mL), ethanol was chosen as the primary solvent for the nanosuspension formation using the solvent antisolvent precipitation method.

4.3.2. FT-IR characterisation

The FTIR spectroscopy analysis was conducted to identify the key functional groups present in AZI and confirm its structural integrity and compatibility with other excipients. The

spectrum of AZI revealed characteristic absorption peaks corresponding to the molecular vibrations of specific functional groups as mentioned in § 1.2.5. A broad absorption around 3561 cm^{-1} and 3422 cm^{-1} confirmed the presence of hydroxyl (-OH) and amine (-NH) groups, indicating hydrogen bonding interactions. Peaks in the 2968–2830 cm^{-1} range correspond to C-H stretching vibrations of aliphatic hydrocarbons, while the sharp peak at 1726 cm^{-1} is attributed to the carbonyl (C=O) stretching of the lactone group. Absorptions in the 1652–1509 cm^{-1} region are characteristic of C=C bonds, likely from the AZI macrolide ring system.

The FTIR spectra of PVP K30, Tween®80 and 1:1 w/w ratio binary mixtures of AZI and excipients are shown in Figure 4.5, 4.6, 4.7, 4.8.

Figure 4.5. illustrates the FTIR spectrum of PVP K30. The O-H stretching vibration, associated with water absorption in PVP, appears at 3395 cm^{-1} and 3385 cm^{-1}, confirming the presence of hydroxyl groups. The C-H stretching vibrations of alkyl groups are observed at 2950 cm^{-1} and 2923 cm. The amide carbonyl (C=O) stretch, a defining feature of the pyrrolidone ring, is present at 1645 cm^{-1}. The strong correlation between these spectral peaks and known functional groups in PVP K30 confirms the identity and purity of the sample

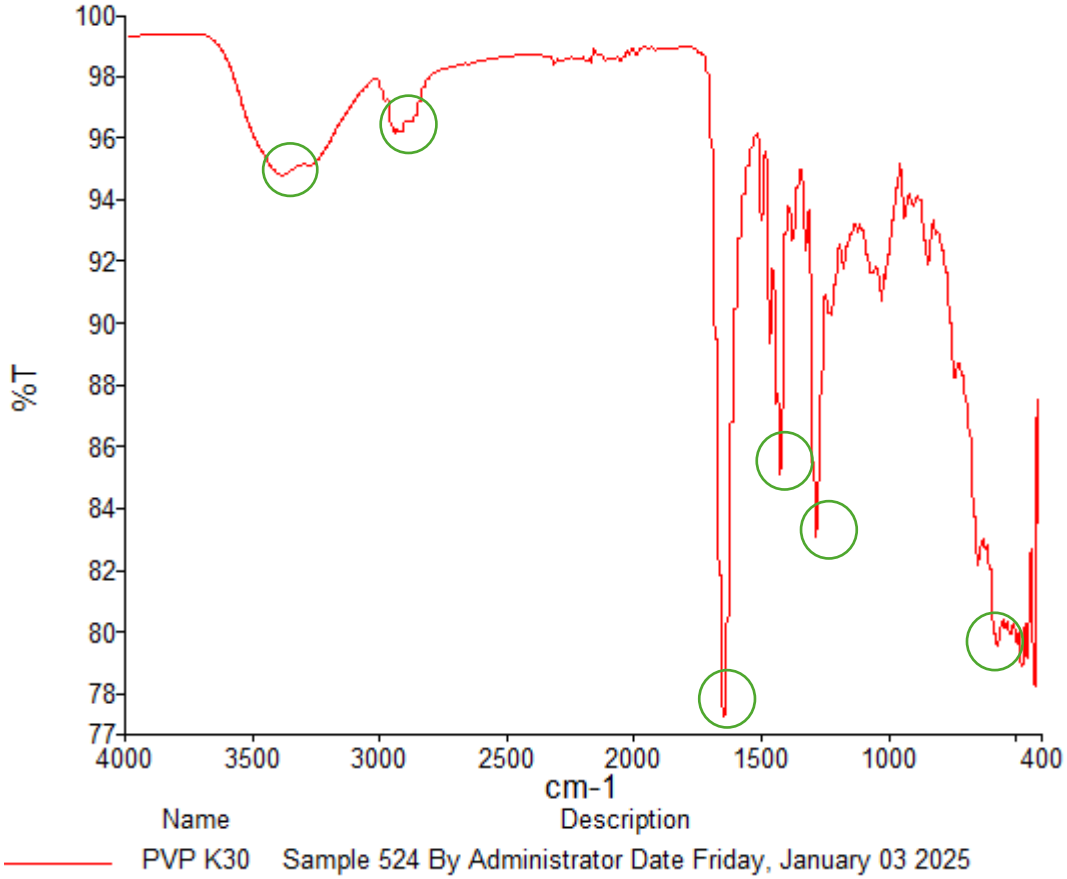

Figure 4.5. FTIR absorption spectrum for PVP K30.

Figure 4.6. demonstrates that AZI exhibits an O-H stretching peak at 3561 cm^{-1}. PVP K30 has a broad O-H absorption around 3395 cm^{-1} and 3385 cm^{-1}, the AZI-PVP K30 mixture, the O-H peak shifts to 3563 cm^{-1}, indicating minor hydrogen bonding between AZI and PVP K30. The amide carbonyl (C=O) stretch of AZI is observed at 1726 cm^{-1}, PVP K30 shows a C=O stretching peak at 1645 cm^{-1}, in the binary mixture, the C=O peak appears slightly shifted or broadened, which suggests minor interactions between AZI's amide groups and PVP's carbonyl functional groups. The C-H stretching vibrations of AZI are found at 2968 cm^{-1}, 2937 cm^{-1}, and 2898 cm^{-1}. PVP K30 shows similar C-H stretching at 2950 cm^{-1} and 2923 cm^{-1}, indicating overlapping alkyl functional groups. In the binary mixture, these peaks remain relatively unchanged (2969 cm^{-1}, 2936 cm^{-1}, 2890 cm^{-1}), indicating that the structural integrity of AZI is preserved, meaning no significant degradation occurs upon mixing. PVP K30 exhibits pyrrolidone ring vibrations around 732 cm^{-1}, showing its cyclic amide structure. This peak remains detectable in the binary mixture, confirming that PVP K30 retains its structure upon mixing with AZI. The observed minor shifts and broadening in the hydroxyl, carbonyl, and

amide peaks suggest minor hydrogen bonding interactions between AZI and PVP K30. The absence of new peaks and the preservation of AZI's characteristic functional groups indicate that no significant chemical degradation. These findings suggest that PVP K30 is compatible with AZI.

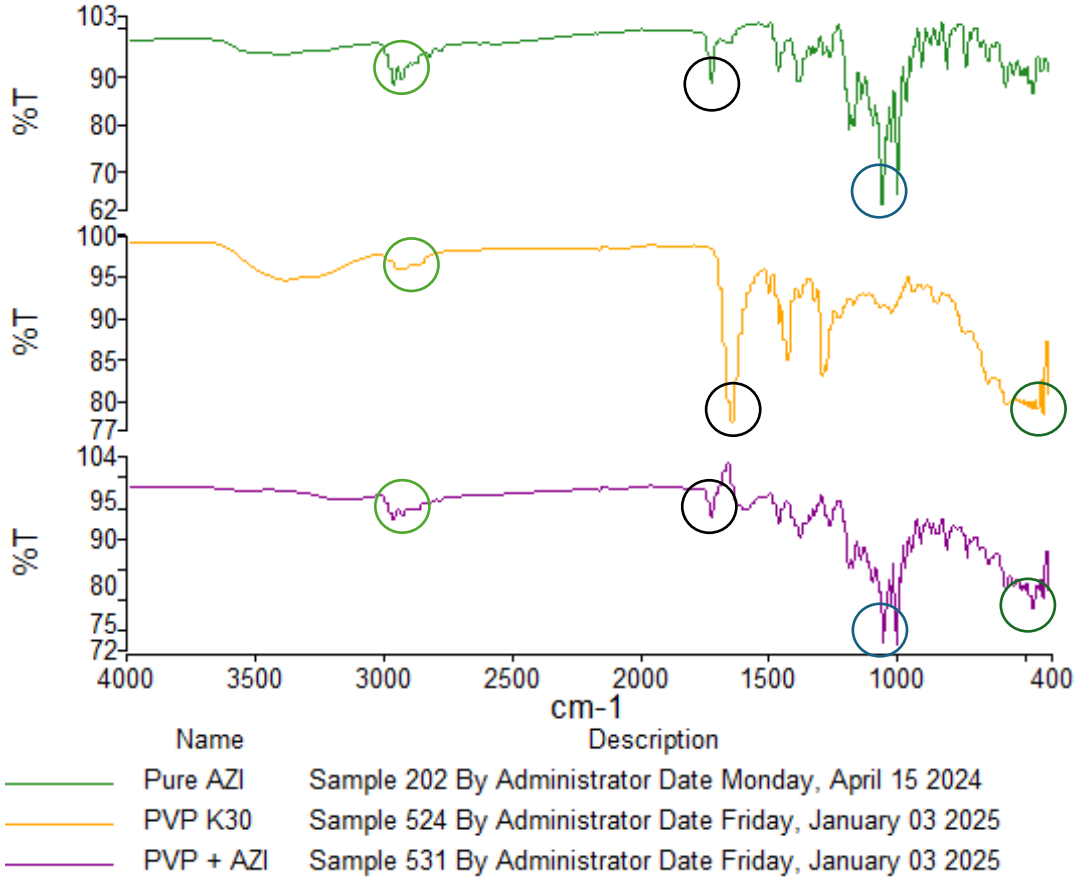

Figure 4.6. FTIR absorption spectrums for AZI, PVP K30 and 1:1 binary mixture of AZI and PVP K30

Figure 4.7. shows a broad O-H stretching vibration at 3474 cm^{-1} is indicative of hydroxyl groups, which contribute to its hydrophilic nature. The C-H stretching vibrations at 2921 cm^{-1} and 2857 cm^{-1} correspond to alkyl chains, confirming the presence of hydrocarbons. The ester C=O stretching is expected in the 1700–1750 cm^{-1} region, indicating the presence of polyoxyethylene and fatty acid ester groups. The C-O stretching vibrations between 1000–1300 cm^{-1} indicate ether groups in Tween®80's structure. These characteristics confirm the identity of Tween®80.

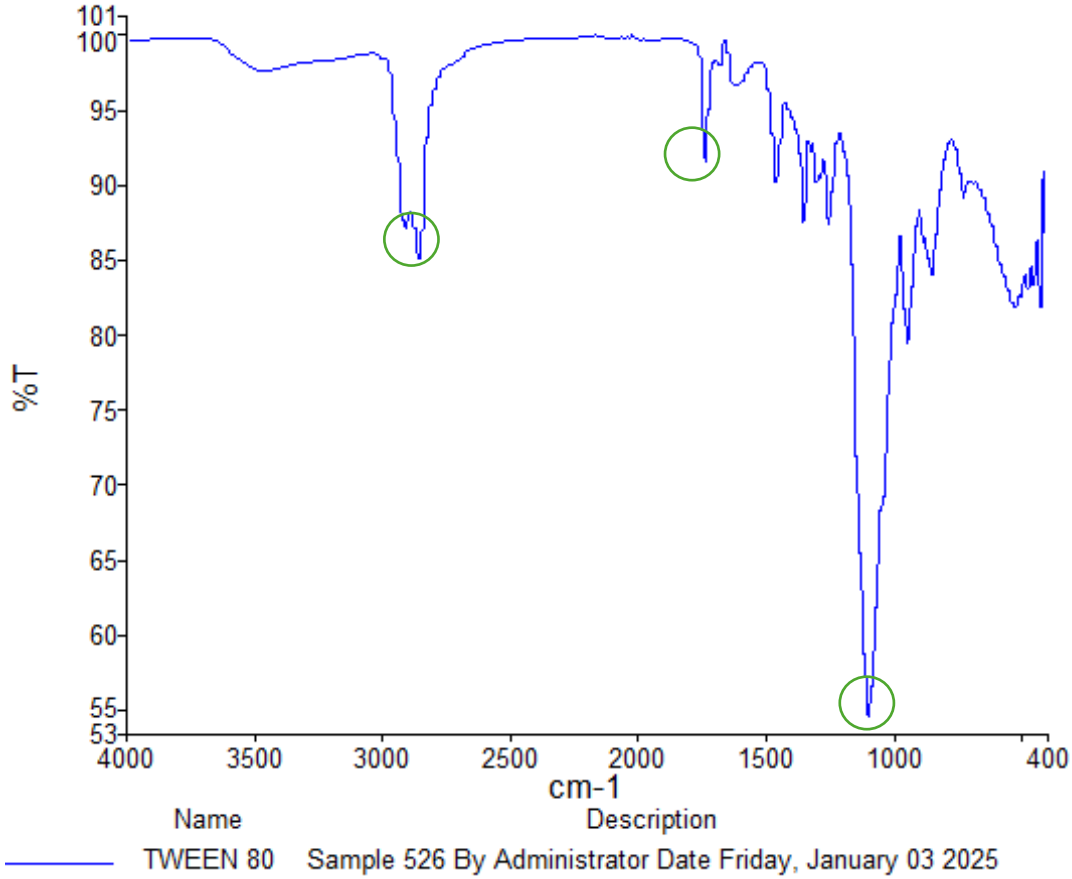

Figure 4.7. FTIR absorption spectrum for Tween®80

Figure 4.8 demonstrates AZI exhibits an O-H stretching peak at 3561 cm^{-1}. Tween®80 has a broad O-H absorption at 3474 cm^{-1}. In the AZI-Tween®80 mixture, the O-H peak shifts slightly to 3562 cm^{-1}, suggesting the possibility of hydrogen bonding between the hydroxyl groups of AZI and Tween®80. The amide carbonyl (C=O) stretch of AZI is observed at 1726 cm^{-1}, Tween®80 contains C=O stretching in the range of 1700–1750 cm^{-1}, in the binary mixture, the C=O peak shows slight broadening or shifting, which may suggest interactions between AZI's amide groups and Tween®80's ester groups. The C-H stretching vibrations of AZI are found at 2968 cm^{-1}, 2937 cm^{-1}, and 2898 cm^{-1}. Tween®80 has C-H stretching at 2921 cm^{-1} and 2857 cm^{-1}, in the binary mixture, these peaks appear at 2922 cm^{-1} and 2859 cm^{-1}, remaining largely unchanged, which indicates that AZI retains its structural integrity upon mixing with Tween®80. The minor shifts and broadening in hydroxyl, carbonyl, and amide-related peaks suggest weak hydrogen bonding interactions between AZI and Tween®80. The absence of new peaks or major shifts indicates that no strong chemical interactions or incompatibility issues are present.

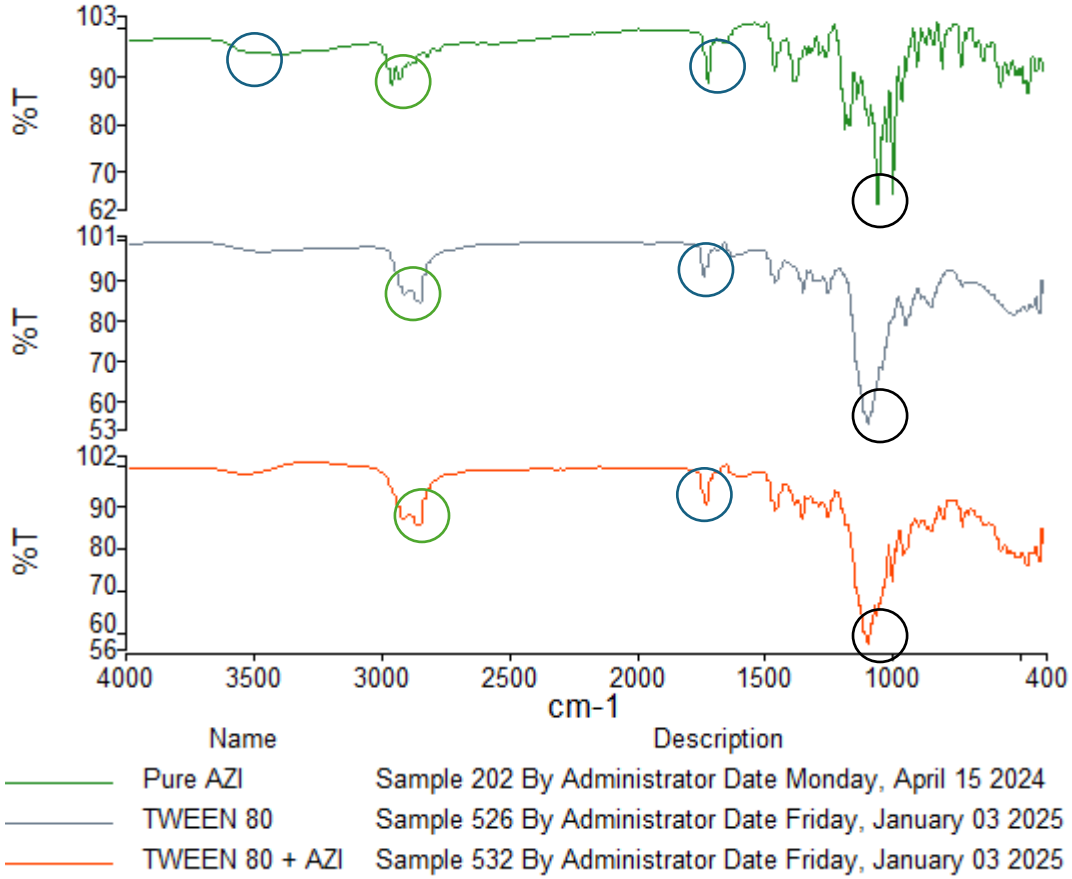

Figure 4.8. FTIR absorption spectrums for AZI, Tween®80 and 1:1 binary mixture of AZI and Tween®80

4.3.3. DSC characterisation

The DSC thermograms for pure AZI, pure PVP K30, pure Tween®80, and their binary mixtures (AZI-PVP K30 and AZI-Tween®80) provide information about the thermal behaviour, crystallinity, and potential molecular interactions of these compounds. The DSC thermogram of pure AZI (Figure 4.9) shows a sharp, well defined endothermic peak with an onset at 120.33°C and a peak melting temperature of 125.71°C, with an enthalpy of 22.109 J/g. The presence of a single, distinct melting peak demonstrates that the compound is of a highly crystalline material with a well-ordered lattice structure. The enthalpy confirms the purity of the crystalline form, suggesting that the drug is present in a single polymorphic state. The narrow width of the melting peak confirms the uniformity of the crystalline state, which means that AZI consists of a single, stable polymorphic form. The steep slope of the peak further suggests that AZI undergoes a rapid phase transition from solid to liquid, which is typical for

highly crystalline compounds with strong intermolecular forces (hydrogen bonding and van der Waals interactions) which is needed to maintain their rigid lattice structure.

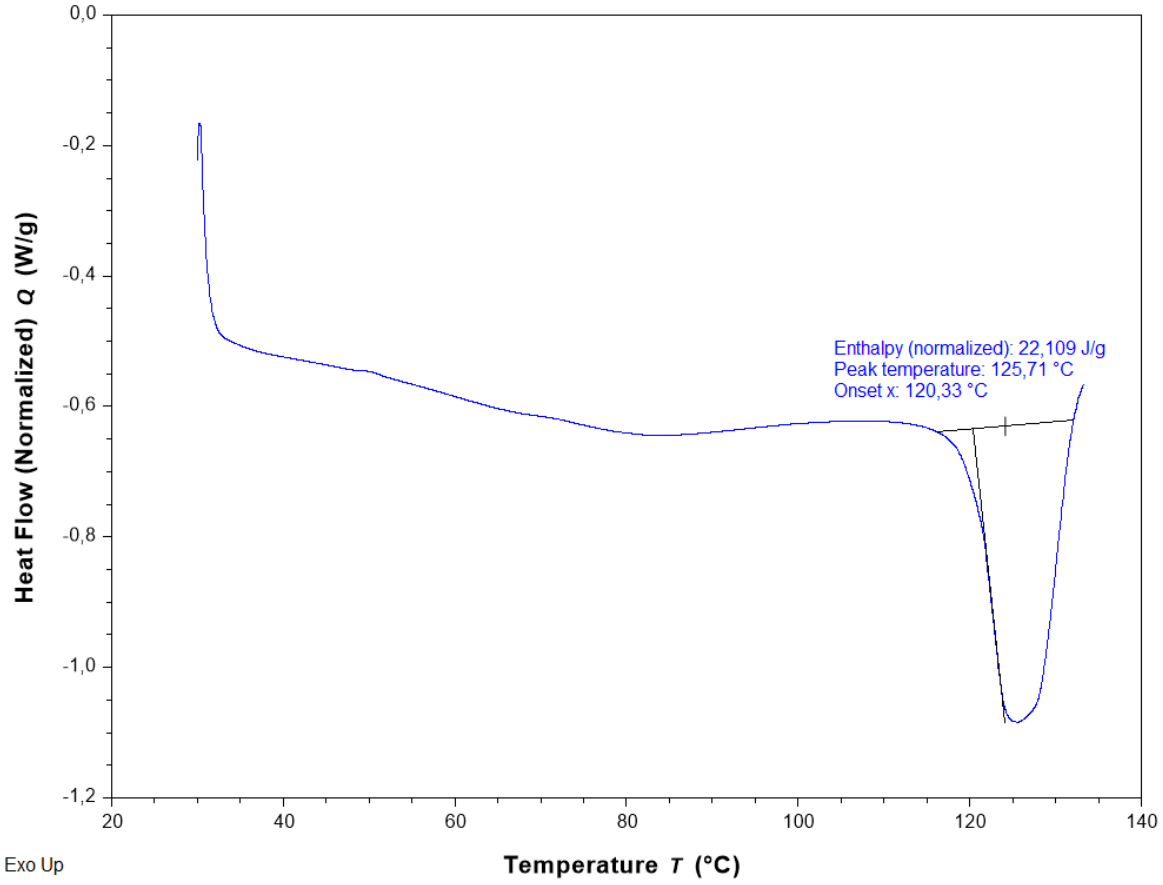

Figure 4.9. DSC thermogram of AZI.

The DSC thermogram of PVP K30 (Figure 4.10) does not exhibit a sharp melting peak like AZI. It displays a glass transition temperature (Tg) at 76.51°C, with an onset at 39.06°C and an enthalpy of 142.30 J/g. This is a characteristic of an amorphous polymer. The high enthalpy of transition shows that PVP K30's ability to absorb thermal energy as it transitions from a glassy to a rubbery state. Since amorphous materials lack a well-defined crystalline structure, there is board and exhibit gradual segmental motion.

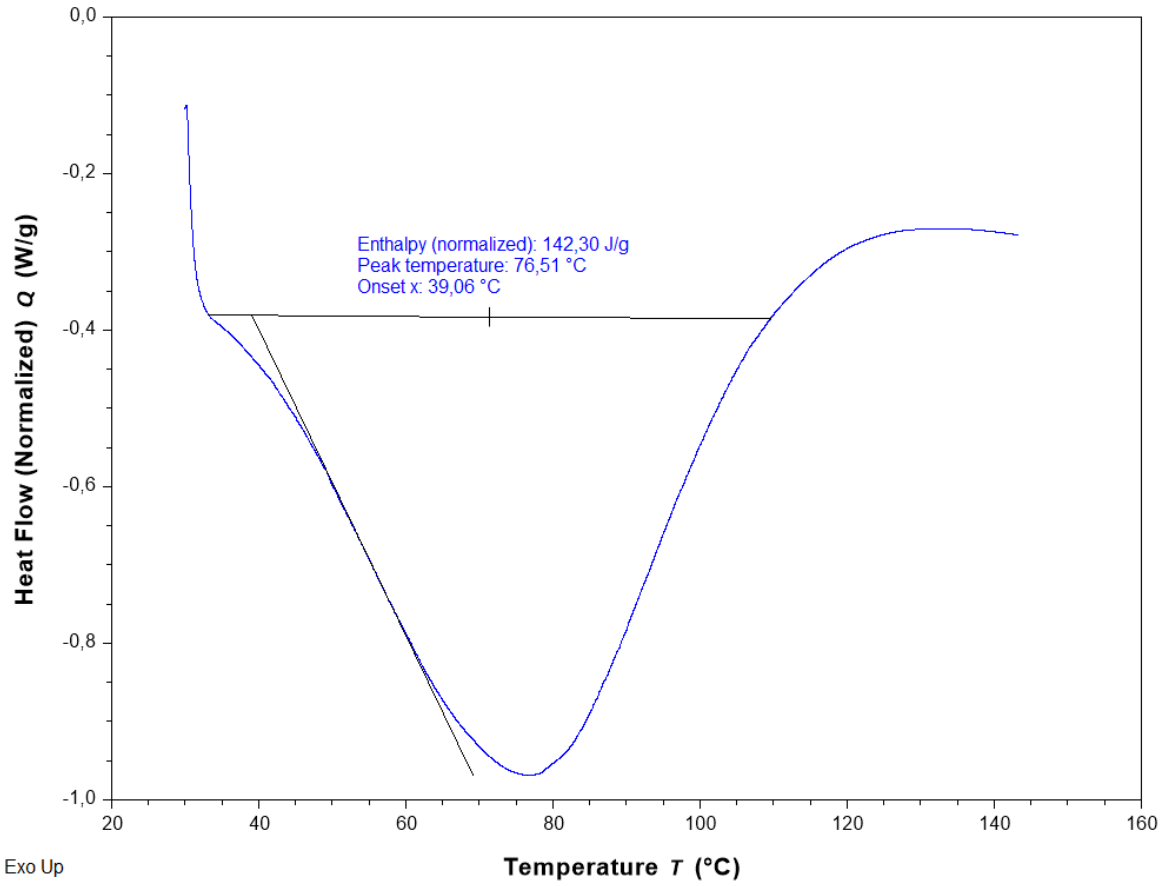

Figure 4.10. DSC thermogram of PVP K30.

The DSC thermogram of Tween®80 (Figure 4.11) shows a very low glass transition temperature at -11.26°C, with an onset at -25.27°C, and an enthalpy of 116.63 J/g. This is expected, as Tween®80 is a non-crystalline, liquid surfactant that lacks a defined lattice structure. The low Tg confirms its high molecular mobility and fluidity. The broad nature of the thermal transition is characteristic of a highly flexible, non-crystalline material with molecular mobility.

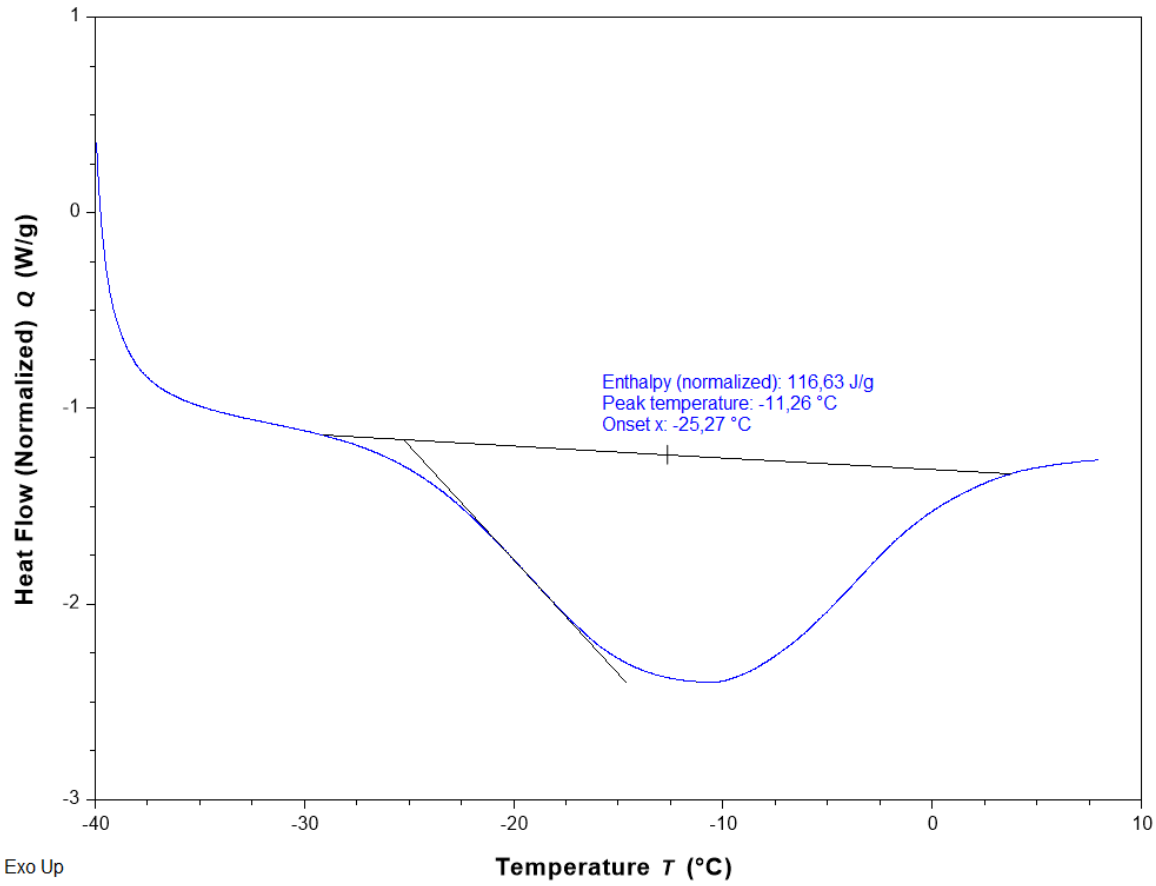

Figure 4.11. DSC thermogram of Tween®80.

The DSC thermogram of the 1:1 binary mixture of AZI and PVP K30 (Figure 4.12) mixture exhibits two thermal events. The first is a glass transition at 81.39°C, which represents an increase in the Tg of PVP K30 from its original value of 70.51°C. This shift in Tg suggests that AZI is miscible within the amorphous polymer, leading to an alteration of the polymer's molecular mobility. The second is an endothermic peak at 122.93°C, which represents the melting of AZI. This peak is broader and shifted downward from its original melting point of 125.71°C, indicating a reduction in crystallinity. The observed broadening of the melting peak is indicative of partial amorphization of AZI, therefore meaning that some of the drug molecules have been incorporated into the PVP K30 polymer. This is likely due to hydrogen bonding interactions between the hydroxyl (-OH) groups in PVP K30 and polar functional groups in AZI, which disrupt the ordered crystalline packing of AZI and promote a more disordered, partially amorphous phase. Since no new exothermic peaks are observed, no evidence of degradation is present. The interaction between AZI and PVP K30 appears to be physical. This indicates that PVP K30 can function as a stabiliser, reducing AZI's crystallinity and enhancing its solubility.

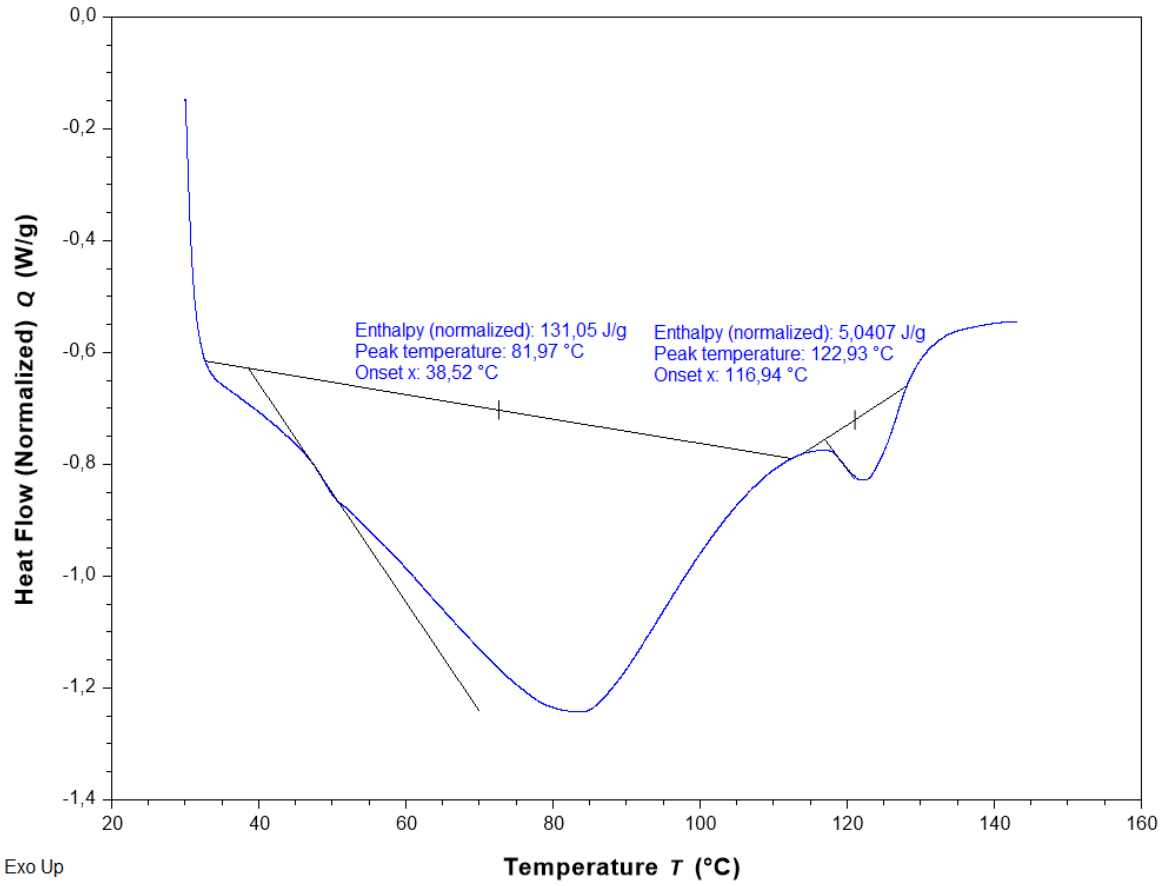

Figure 4.12. DSC thermogram of a 1:1 mixture of AZI and PVP K30

The DSC thermogram of the 1:1 binary mixture of AZI and Tween®80 (Figure 4.13) presents two thermal events. The first is a glass transition at -13.60°C, which is slightly lower than the Tg of pure Tween 80 (-11.26°C). This downward shift suggests that Tween 80 slightly alters the molecular mobility of AZI, but has a weaker interaction compared to PVP K30. The second event is a melting peak for AZI at 119.34°C, which is lower than its original melting point of 125.71°C as also observed by Bharat *et* al. [167].

The decrease in AZI's melting temperature in the presence of Tween®80 suggests that Tween® 80 has disrupted the crystallinity of AZI, could be due to the surface adsorption. The fact that the melting peak remains relatively sharp and distinct indicates that AZI has not fully transitioned into an amorphous form, and remains crystalline. The presence of an additional minor endothermic transition suggests possible phase separation, which means that AZI and Tween®80 are not fully miscible in the solid state. This is why the solvent antisolvent precipitation method was used. The absence of new exothermic peaks confirms that AZI and Tween®80 are physically stable when combined, meaning that no degradation has occurred.

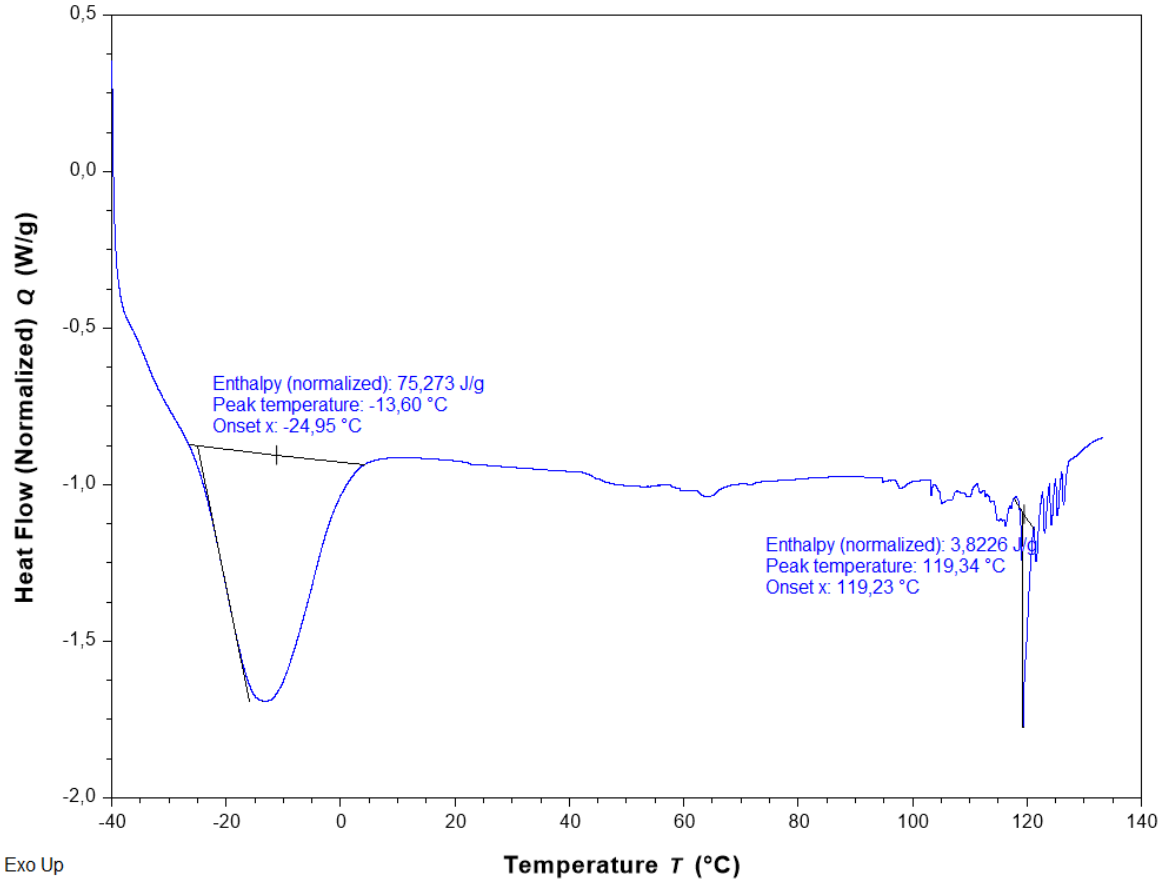

Figure 4.13. DSC thermogram of a 1:1 mixture of AZI and Tween®80.

4.3.4. XRD characterisation

XRD was employed to investigate the crystalline nature of AZI and to assess potential physicochemical interactions with PVP K30 upon mixing (Figure 4.14). The XRD pattern of pure AZI exhibited multiple sharp, high intensity diffraction peaks between 7° and 30° 2θ, indicating a highly crystalline material. These peaks correspond to well-ordered lattice planes within the AZI crystal structure. The presence of multiple sharp reflections at consistent angular positions confirms the existence of a long-range molecular order in the drug. In contrast, the XRD pattern of PVP K30 revealed a broad halo centered around 20° 2θ, with the complete absence of sharp diffraction peaks. This is characteristic of an amorphous polymer and confirms that PVP K30 lacks long-range periodicity.

The XRD pattern of the AZI–PVP K30 physical mixture displayed no significant deviation from the individual patterns of AZI and PVP K30. The sharp diffraction peaks of AZI were retained in the mixture without evidence of peak broadening, shifting, suppression, or

disappearance, and the amorphous halo of PVP K30 remained unchanged. The characteristic AZI peaks at 2θ values (~8.7°, ~13.4°, and ~20.2°) were preserved, both in position and relative intensity, suggesting that the crystal lattice of AZI remained unaltered upon mixing. This observation strongly implies that no solid-state interaction occurred between AZI and PVP K30, and that the mixture represents a physical blend.

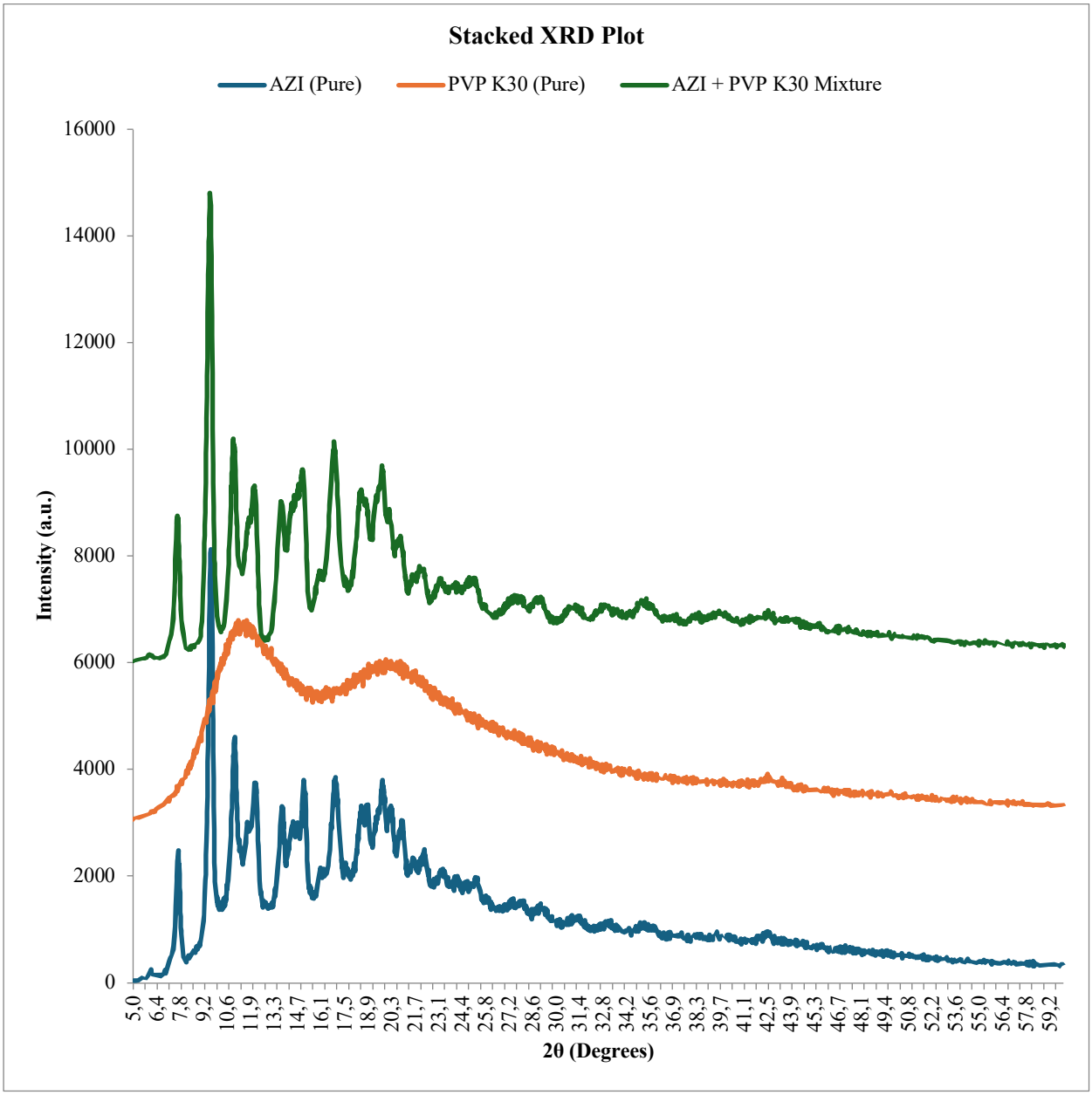

Figure 4.14. Stacked XRD patterns of AZI, PVP K30, and a 1:1 binary mixture of AZI and PVP K30

4.4. CONCLUSIONS

This chapter focused on the pre-formulation and preliminary characterisation studies essential for the development of a stable AZI nanosuspension. These studies evaluated the solubility profile of AZI, as well as the physicochemical compatibility between AZI and two excipients, PVP K30 and Tween®80 using analytical techniques including FTIR, DSC, and XRD. Solubility screening revealed that AZI exhibits poor aqueous solubility but demonstrates significantly higher solubility in ethanol and acetone, with ethanol being selected as the preferred solvent due to its highest solubilising capacity. These findings confirmed AZI's lipophilic nature and supported the rationale for using a solvent–antisolvent precipitation method to produce nanocrystals.

FTIR analysis demonstrated that AZI retains its characteristic functional groups in both PVP K30 and Tween®80 binary mixtures. Minor shifts and broadening in hydroxyl and carbonyl peaks indicated weak hydrogen bonding in both systems, suggesting physical interactions but no evidence of chemical degradation or incompatibility. DSC results supported the FTIR findings by revealing distinct thermal behaviours for each system. The AZI–PVP K30 binary mixture showed a shift in the glass transition temperature (Tg) of PVP K30 and a broadened AZI melting peak. In contrast, the AZI–Tween®80 system exhibited minimal Tg depression and a retained sharp melting peak, suggesting weaker interaction. Most importantly, no new exothermic peaks were observed in any system, confirming thermal stability and the absence of degradation upon mixing. XRD analysis further reinforced these observations. AZI retained its crystalline peaks in the presence of both excipients. In the AZI–PVP K30 mixture, the crystalline reflections of AZI remained sharp and unshifted, and the amorphous halo of PVP K30 was preserved, indicating that no solid-state transformation or polymorphic change occurred. These results suggest that the AZI–PVP K30 system remains a physical mixture without the formation of a new crystalline phase, confirming compatibility and stability.

The preformulation studies confirmed that PVP K30 and Tween®80 are suitable excipients for nanosuspension development. Thus, this study supports that it is a particularly feasible approach to prepare AZI nanosuspension suitable for designing effective drug preparations for oral delivery of a poorly soluble drug. Continued research and innovation in this field will likely lead to more effective, safe, and accessible treatments.

CHAPTER 5

FORMULATION DEVELOPMENT AND CHARACTERISATION OF AZITHROMYCIN NANOSUSPENSION

5.1. INTRODUCTION

Suspensions have been a great tool of pharmaceutical formulations for delivering poorly water-soluble drugs. A suspension is a dispersion of solid drug particles in a liquid medium where the drug is not readily soluble. The traditional suspension's drug particle sizes range from 1 to 50 μm which also assisted easier administration [168]. Suspensions are challenged by physical instability such as sedimentation and particle aggregation, which can compromise their uniformity and efficacy [169]. For BCS Class II and IV drugs, these systems suffer from poor dissolution due to intrinsic low solubility, limiting bioavailability [169].

The late 1990s and early 2000s marked the shift to nanosuspensions with advancements in nanotechnology. Müller and Keck introduced drug nanocrystals by particle size reduction to the nanometer scale [113]. Nanosuspensions are colloidal dispersions of drug particles reduced to nanoscale dimensions [113]. Nanosizing significantly enhances the solubility of poorly water-soluble drugs, facilitates better absorption and bioavailability, and can be used across multiple routes of administration, including oral, ocular, topical, nasal, and transdermal [117,170]. The dissolution rate of a drug in a nanosuspension is governed by the Noyes-Whitney equation as previously mentioned. This states that by reducing the particle size to the nanometer scale, the surface area increases, leading to faster dissolution rates and improved absorption [140,141].

The formation of stable nanosized drug particles in nanosuspensions is governed by nucleation and crystal growth dynamics, as described by LaMer's theory of nucleation [171]. This theory explains the process in three stages, supersaturation, nucleation, controlled crystal growth [171]. Stabilisers (Tween®80 and PVP K30) reduce the interparticle attraction hence preventing agglomeration and Ostwald ripening [172]. In this study, solvent antisolvent precipitation is chosen over HPH for nanosuspension formulation with low energy input, making it more cost-effective, and uses simple laboratory equipment [95]. Solvent antisolvent precipitation offers good control over particle size through nucleation, ensuring more uniform nanoparticles. It can reduce crystallinity, enhancing dissolution rates and bioavailability without inducing unwanted polymorphic changes. In contrast, HPH requires high energy,

involves complex and expensive equipment, and need multiple cycles to achieve uniform particle sizes, with the potential to induce polymorphic changes [95].

Traditional commercial suspensions exhibit limitations that nanosuspensions aim to overcome. Micronized suspensions contain drug particles in the micrometre range, whereas nanosuspensions achieve particle sizes in the range of 100–500 nm, significantly enhancing drug dissolution and absorption [173–175]. The dissolution rate of conventional suspensions is relatively slow, leading to a delayed onset of action, whereas nanosuspensions dissolve rapidly due to their increased surface area [173–175]. Another drawback is poor taste masking, which can lead to poor patient adherence to treatment regimen in paediatric and geriatric populations [173–175]. Nanosuspensions improve taste masking by increasing surface interactions with stabilisers, making them more palatable [173–175]. Conventional suspensions require frequent dosing due to incomplete absorption, whereas nanosuspensions offer longer lasting effects due to enhanced bioavailability and reduced dose variability [173–175]. Sedimentation issues are common in commercial suspensions, leading to uneven drug distribution, while nanosuspensions exhibit better physical stability and lower sedimentation rates due to the steric stabilization provided by surfactants and polymers [173–175].

This chapter focuses on the development, optimisation, and characterisation of an AZI nanosuspension to improve solubility, stability, and drug delivery efficiency. A Box-Behnken Design approach will be employed to optimise critical formulation parameters, including the concentrations of Tween®80 and PVP K30, as well as the solvent to antisolvent ratio. The nanosuspension formulations will be characterised based on particle size, PDI, zeta potential, DSC, and FTIR to ensure stability and compatibility of the formulation. The drug release profile of the nanosuspension will be compared with that of conventional AZI suspensions to evaluate dissolution rate enhancement and bioavailability improvement. The stability of the optimised nanosuspension will be assessed under various storage conditions to confirm its shelf-life.

5.2. MATERIALS AND METHODS

5.2.1. Materials

All reagents were of analytical reagent grade. AZI was procured from Skyrun® Inc. (Nanjing, Jiangsu, China). Tween®80 was procured from Merck® laboratories (Sigma Aldrich®,

Wadeville, Gauteng). Kollidon® 30 (PVP K30) powder was procured from BASF® (Ludwigshafen, Rhineland-Palatinate, Germany). Ethanol 96% was procured Spellbound Laboratory Solutions (Port Elizabeth, South Africa). HPLC-grade water was prepared by reverse osmosis using a Direct Pure UP 10 UV with TOC water purification system by Microsep® (Port Elizabeth, Eastern Cape, South Africa). The water was pre-filtered through 3 stage stack filter kit (RephiLe® Inc., Boston, Massachusetts, USA). This purified water was used to prepare all buffer solutions. Potassium dihydrogen orthophosphate, and sodium hydroxide pellets were purchased from Associated Chemical Enterprises (Pty) Ltd Laboratories (Johannesburg, Gauteng, South Africa).

5.2.2. Methods

5.2.2.1. Formulation development

5.2.2.1.1. Box-Behnken Design (BBD)

A rotatable BBD was used to investigate the impact of three variables, formulation variables on the AZI nanosuspension. The input variables were Tween®80 content (X_1), PVP K30 content (X_2), solvent to antisolvent ratio (X_3), and sonication time (X_4). Twenty-nine (29) experimental runs were generated using Design Expert® 13.0.5 statistical software (Stat-Ease Inc., Minneapolis, USA). The number of experiments performed for the formulation process using BBD was established using Equation 2.7 in § 2.3.2. The actual and coded factors and their respective ranges are listed in Table 5.1. The selected ranges for each input variable were informed by prior nanosuspension studies involving AZI and other poorly soluble drugs.

Table 5.1. Levels of input variables monitored for BBD.

Input Factor	Low Level: Actual [Coded]	Medium Level: Actual [Coded]	High Level: Actual [Coded]
X_1 = Tween®80 (mg/ml)	0.2 [-1]	0.5 [0]	0.8 [+1]
X_2 = PVP K30 (mg/ml)	0.5 [-1]	1.0 [0]	1.5 [+1]
X_3 = Solvent: Antisolvent Ratio	0.063 [-1]	0.115 [0]	0.167 [+1]
X_4 = Sonication time	3 [-1]	6 [0]	9 [+1]

The responses that were monitored included particle size (Y_1), polydispersity index (Y_2), zeta potential (Y_3), drug release (Y_4) after 10 minutes.

5.2.2.2. Production of AZI nanosuspension

A solvent antisolvent precipitation technique (Figure 5.1) was used to produce the AZI nanosuspension. The formulation parameters used in the manufacture of the nanosuspension are summarized in Table 5.2.

A batch size based predetermined ratios (35mL, 50mL, and 85mL) was used for the manufacture of the AZI nanosuspension using the solvent antisolvent precipitation method. The antisolvent phase consisted of an aqueous solution of Tween®80 (0.5–1.5% w/v) and PVP K30 (0.5–2% w/v) in deionized water, maintained at room temperature. The solvent phase, containing AZI dissolved in ethanol (5 mL), was introduced into the antisolvent dropwise using a separator funnel with a PTFE stopper. The solvent was added at a rate of one drop every 3 seconds, while maintaining constant magnetic stirrer at 1600 rpm. After the addition of the solvent phase, stirring was continued for 10 minutes. Thereafter the formulation sonicated using a Sonoplus Bandelin UW 200 probe sonicator (GmbH & Co. KG, Berlin, Germany) and cooled in an ice bath. After stabilization, the nanosuspension was characterised for particle size, PDI, zeta potential, and in *vitro* dissolution. All formulations were prepared and characterised on the same day to maintain consistency and prevent stability variations.

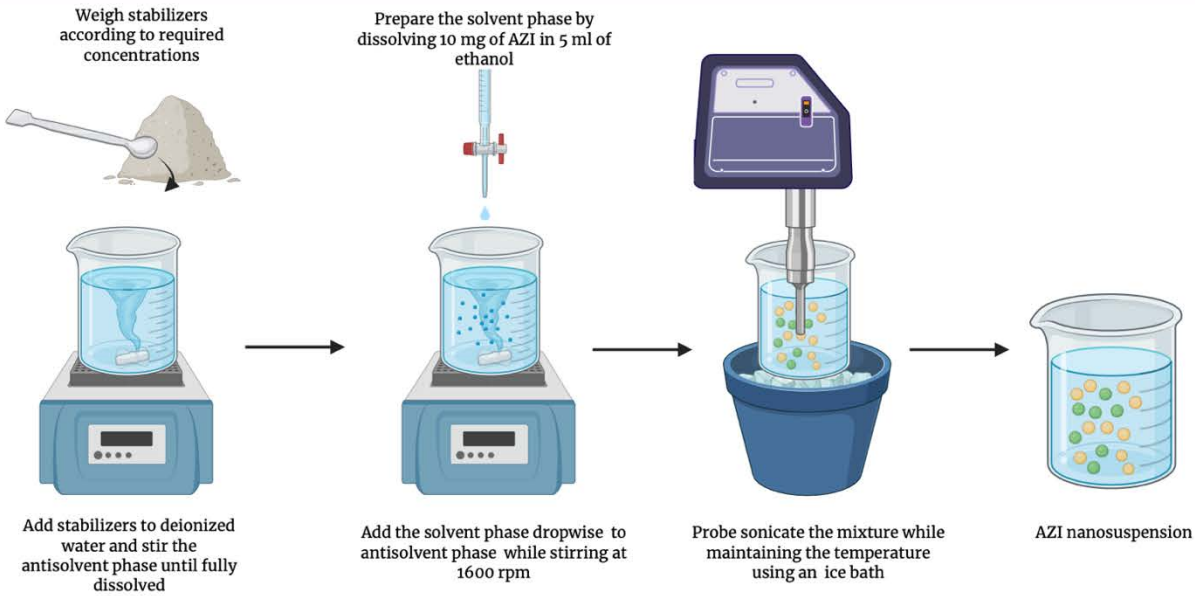

Figure 5.1. Schematic representation of AZI nanosuspension preparation via solvent-antisolvent precipitation method.

Table 5.2. Experimental design for the AZI obtained using BBD studies.

Std	Run	Tween®80 (mg/mL)	PVP K30 (mg/mL)	Solvent: Antisolvent Ratio	Sonication time (min)
21	1	1	0.5	0.115	3
1	2	0.5	0.5	0.115	6
23	3	1	0.5	0.115	9
26	4	1	1.25	0.115	6
8	5	1	1.25	0.167	9
17	6	0.5	1.25	0.063	6
16	7	1	2	0.167	6
27	8	1	1.25	0.115	6
18	9	1.5	1.25	0.063	6
19	10	0.5	1.25	0.167	6
5	11	1	1.25	0.063	3
10	12	1.5	1.25	0.115	3
12	13	1.5	1.25	0.115	9
28	14	1	1.25	0.115	6
29	15	1	1.25	0.115	6
25	16	1	1.25	0.115	6
7	17	1	1.25	0.063	9
6	18	1	1.25	0.167	3
9	19	0.5	1.25	0.115	3
15	20	1	0.5	0.167	6
24	21	1	2	0.115	9
11	22	0.5	1.25	0.115	9
4	23	1.5	2	0.115	6
22	24	1	2	0.115	3
3	25	0.5	2	0.115	6
20	26	1.5	1.25	0.167	6
14	27	1	2	0.063	6
13	28	1	0.5	0.063	6
2	29	1.5	0.5	0.115	6

5.2.2.3. Characterisation of AZI nanosuspension

5.2.2.3.1. Particle size analysis

The mean PS and PDI of the AZI nanosuspension were measured using a Model Nano-ZS Zetasizer (Malvern Instruments Ltd, Worcestershire, UK) set to photon correlation spectroscopy mode. Before measurement, 30 µL of the nanosuspension was diluted with 10 mL of deionized water prior to analysis to ensure optimal scattering intensity and to prevent multiple scattering effects that may occur at higher particle concentrations. The dilute sample was then placed in a cuvette. All measurements were conducted in triplicate (n = 3) at a scattering angle of 90° and a temperature of 25°C. The real and imaginary refractive indices of the AZI nanosuspension were set to 1.456 and 0.01, respectively for accurate particle size distribution analysis.

5.2.2.3.2. Zeta Potential (ZP)

The ZP of the AZI nanosuspension was measured using a Nano-ZS Zetasizer (Malvern Instruments Ltd, Worcestershire, UK), operating in laser doppler anemometry mode. The sample was prepared as described in § 5.2.2.3.1, with proper dilution and dispersion. The diluted sample was loaded into a capillary cell. All measurements were performed in triplicate (n = 3) at an applied electric field strength of 20 V/cm. Equation 3.8 in § 3.3.2 was applied to calculate the ZP values.

5.2.2.3.3. Imaging analysis

Transmission electron microscopy (TEM) was utilized to examine the shape and surface morphology of the nanoparticles. A small drop of the nanosuspension was deposited onto a carbon-coated copper grid to ensure even particle distribution. Any excess liquid was gently absorbed using hydrophilic filter paper. The sample was then left to dry at room temperature (22°C) for 24 hours to allow for proper adhesion and structural stability before imaging. Visualization was conducted to capture high resolution images of the nanoparticles.

5.2.2.3.4. DSC

As described in § 4.2.2.3 the degree of crystallinity and polymorphisms of the nanosuspension was be determined using a model Q100 DSC (TA instruments, New Castle, DE, USA) coupled with a RCS (90) Refrigerated Cooling System (TA Instruments, New Castle, DE, USA). Approximately 1 mg of each sample were weighed out onto an aluminium pan and the pans

were covered with an aluminium lid (§ 1.2.7). The thermograms were analysed using a TA Universal Analysis software (TA Instruments, New Castle, DE, USA).

5.2.2.3.5. FTIR

A spectrum two FTIR ATR spectrophotometer (Perkin Elmer® Ltd, Beaconsfield, England) was used to analyse AZI nanosuspension. The sample was placed onto a diamond ATR crystal using an applied force of 85 N and scanned in a range of 4000 to 6520 cm^{-1} at a resolution of 4 cm^{-1}.

5.2.2.3.6. Loading capacity (LC)

The drug loading of the AZI nanosuspension was determined using the validated RP-HPLC method used in Chapter 2. One millilitre (1 mL) of the sample was transferred to a 1.5 mL centrifuge vial and was subjected to centrifugation using a MiniStar® Plus centrifuge (Hangzhou Allsheng instruments, China) at 10000 rpm for 15 minutes to separate any undissolved drug particles. The supernatant was extracted transferred into HPLC vials for analysis. The drug loading capacity was determined using Equation 5.1 [176].

$$Drug\ Loading\ \% = \frac{Drug\ content\ (mg)}{Drug + stabilizers\ (mg)} \times 100 \qquad \textbf{\textit{Equation 5.1}}.$$

5.2.2.3.7. In *Vitro* release

The in *vitro* drug release profile of the AZI nanosuspension was evaluated using the USP dissolution Apparatus II (paddle method). The study was conducted using 900 mL of phosphate buffer (pH 6.8) as the dissolution medium, maintained at a temperature of 37 ± 0.5°C to mimic physiological conditions. The paddle speed was set at 50 rpm to ensure uniform dispersion of the nanosuspension throughout the medium. A 5 mL aliquot of the AZI nanosuspension, equivalent to a known dose, was introduced directly into the dissolution vessel near the paddle. The release of AZI was monitored over 60 minutes, with 5 mL samples withdrawn at predetermined time intervals (0, 5, 10, 15 minutes) using a syringe equipped with a 0.45 µm GVS Ablu filter (Sanford, ME, USA) to remove undissolved particles. To maintain sink conditions, an equal volume (5 mL) of fresh phosphate buffer was immediately replaced after each sampling. The in *vitro* release studies were performed in triplicate and the amount of AZI released was quantified using validated RP-HPLC used in Chapter 3.

5.2.2.4. Kinetics and mechanism of AZI release

Mathematical modelling plays a central role in drug delivery research quantifying how APIs are released from drug systems. These models are based on physicochemical and mechanisms such as diffusion, dissolution, and erosion or swelling [177]. Selecting an appropriate kinetic model not only helps identify the release pathway but also allows for better prediction and control of the in *vivo* behaviour of the formulation. Zero order kinetics suggests a constant release rate over time, first order kinetics implies concentration dependent release, and the Higuchi model is diffusion based for water insoluble drugs [177]. Prior studies involving AZI loaded nanoparticles, solid lipid systems, and transethosomal carriers have reported that Higuchi and first order models frequently provide the best fit, reflecting a balance between diffusion through a stabiliser rich interface and release governed by concentration gradients [178]. The kinetics and mechanism of release of AZI from the nanosuspension were evaluated using zero order, first order and Higuchi models.

5.2.2.4.1. Zero order release model

The zero order release model, presented in Equation 5.2, describes drug release that occurs at a constant rate, independent of drug concentration:

$$Q_t = Q_0 + K_0 t \qquad \textbf{\textit{Equation 5.2}}.$$

Where:

Q_t = amount of API dissolved in time, *t*.

Q_0 = initial amount of API in the solution.

K_0 = zero order release constant.

Zero order kinetics are desirable in controlled drug delivery systems because they allow for the maintenance of constant plasma drug levels, reducing the frequency of dosing and minimising peak trough fluctuations in drug concentration [178]. This type of release is commonly observed in coated formulations, osmotic systems, and matrix tablets where the surface area available for release does not significantly change with time [178].

5.2.2.4.2. First-order release model

The first order release model is described by Equation 5.3, and it assumes that the rate of drug release is concentration dependent, meaning that the release rate decreases over time as the amount of remaining drug diminishes:

$$\log Q_t = \log Q_0 + \frac{K_1 t}{2.303}$$ ***Equation 5.3***.

Where:

Q_t = amount of API dissolved in time, *t*.

Q_0 = initial amount of API in the solution.

K_1 = first order release constant.

First order kinetics are typically observed in systems where drug diffusion occurs through a hydrated matrix or is influenced by dissolution into surrounding fluids [178]. It is commonly associated with formulations like hydrophilic matrix tablets, suspensions, and microparticles, where the release rate slows down over time as the concentration gradient between the dosage form and the release medium decreases [178].

5.2.2.4.3. Higuchi release model

The Higuchi model, represented in Equation 5.4, describes drug release from a homogeneous matrix system where the mechanism is governed by Fickian diffusion:

$$\frac{M_t}{M_\infty} = kt^{\frac{1}{2}}$$ ***Equation 5.4***.

Where:

M_t = amount of API dissolved in time, *t.*

M_∞ = total amount of drug that can be released (i.e., 100% release).

$\frac{M_t}{M_\infty}$ = fraction released at time, *t.*

k = Higuchi release rate constant.

This model assumes that the drug is dispersed uniformly within a porous matrix, and the release occurs due to a concentration gradient between the saturated drug particles and the surrounding medium [178]. The Higuchi equation is applied in the analysis of semi-solid and solid drug delivery systems, including topical formulations, transdermal patches, and nanosuspensions [178]. In nanosuspension systems containing water soluble drugs like AZI, Higuchi kinetics often dominate due to the high surface area to volume ratio and gradual drug diffusion from the particle surface into the dissolution medium [178].

5.2.2.5. Determination of best fit model

To identify the most suitable mathematical model describing the release kinetics of AZI from the nanosuspension, various linear regression models were evaluated using the cumulative drug release data. The following models were applied to: zero order model, cumulative % AZI released vs time; first order model, natural logarithm of cumulative % remaining vs time, and Higuchi model, cumulative % AZI released vs the square root of time. R^2 was used as a statistical measure to determine the best fit kinetic model. A higher R^2 value indicates a stronger correlation between the experimental data and the respective kinetic model [177].

5.2.2.6. Stability studies

The stability of the optimised AZI nanosuspension were conducted at 40°C/75% RH and 25°C/60% RH. The RH was prepared using a saturated solution of sodium chloride and sodium nitrite placed at the base of an airtight desiccator. The humidity was measured using a General SAM800HI sports heat index monitor (General®, New York, USA) which was placed inside the desiccator and allowed to equilibrate before sample introduction. The desiccator was then transferred into a calibrated oven set at 40 °C to mimic the temperature required for accelerated stability testing (40°C/75% RH) and another desiccator was left at room temperature (25°C/60% RH), as recommended in ICH Q1A(R2) guidelines. The optimised AZI nanosuspension was filled into 100 mL bottles, sealed tightly, and stored inside the desiccator. Samples were withdrawn at 0, 1, 2, 4, and 8 weeks for analysis. At each point, parameters including particle size, PDI, zeta potential and loading capacity. This procedure simulated accelerated stability studies over a 2-month period for the optimised AZI nanosuspension.

5.2.2.7. Data Analysis

The data collected from the monitored responses were analysed using Design Expert® statistical software Version 13.0.5 (Stat-Ease Inc., Minneapolis, MN, USA). Analysis of Variance (ANOVA) with Fisher's test was used to assess whether the tested factors had significant effects on the responses. The optimised model was then used to explore the design space, helping to determine the best conditions for formulation development.

5.3. RESULTS AND DISCUSSION

5.3.1. Formulation Development

The formulation of the AZI nanosuspension was systematically optimised using a Box–Behnken Design (BBD), generating 29 experimental runs that examined the influence of formulation and process variables on four critical quality attributes (CQA): particle size (PS, Y_1), polydispersity index (PDI, Y_2), zeta potential (ZP, Y_3), and release rate at 10 mins (RR, Y_4). Table 5.3 outlines the observed outcomes across all experimental runs. Mathematical models were used to assess AZI's release rate. To evaluate the stability of the optimised formulation under varying environmental conditions, accelerated stability studies were conducted. These studies confirmed that the formulation maintained its quality and performance over a storage period of 8 weeks under stress conditions such as elevated temperature and humidity.

Table 5.3. Responses from BBD experiments of AZI nanosuspension formulation

Runs	Response variables			
	Y_1 (PS) nm	Y_2 (PDI)	Y_3 (ZP) mV	Y_4 (RR) %
1	385	0.53	-20.7	86.45
2	21.2	0.4	-22.6	84.87
3	1315	0.98	-23.4	84.59
4	133	0.4	-21.5	83.99
5	304	0.55	-18.2	71.98
6	455	0.62	-23.3	80.41
7	321	0.39	-23.4	80.52
8	236	0.29	-26.1	93.48
9	199	0.46	-23.9	89.94
10	198	0.39	-22.6	96.01
11	702	0.7	-20.9	96.86
12	1799	1	-19.9	98.36
13	1341	0.94	-25	82.06
14	247	0.38	-22.3	82.44
15	342	0.41	-27.8	98.32
16	372	0.43	-24	98.38
17	401	0.45	-29.8	90.37
18	456	0.74	-23.8	80.42
19	2137	1	-26.4	102.76
20	316	0.45	-23.1	86.41
21	101	0.39	-24	95.41
22	2049	1	-20.4	81.65
23	471	0.52	-28.3	93.03
24	735	1	-21	92.69
25	336	1	-23.6	89.51
26	99.4	0.31	-26.6	98.86
27	321	0.47	-24.8	100.93
28	652	0.7	-24.9	99.04
29	401	0.87	-23.7	88.27

5.3.1.1. Model fitting and statistical analysis

To analyse the data presented in Table 5.3, statistical methods including ANOVA and the regression coefficient (R^2) were employed. Diagnostic plots, such as normal probability plots of residuals, residuals, Box-Cox transformations, contour maps, and 3D surface plots were utilized to visually interpret the behaviour of the dataset. Experimental data were fitted to linear, two-factor interaction, and quadratic models.

5.3.1.2. Model fit equations and their regression coefficients

The data in Table 5.3 indicate PS ranged from 21.2 nm to 2100 nm. The PDI values varied between 0.29 and 1.00, reflecting both monodisperse and highly polydisperse systems within the formulation space. ZP values ranged from -18.2 mV to -29.8 mV. RR was between 71.98% and 102.76%. To assess experimental variability and ensure the reliability of the dataset, five centre points were incorporated into the design. These runs provided a measure of reproducibility. Model selection was guided by the sum of squares approach, which identified the most suitable polynomial model by evaluating the significance of terms. The final models were derived and expressed in terms of coded variables (Equations 5.5 – 5.8).

$$\sqrt{PS} = 16.08 - 0.4157(X_1) - 0.8971(X_2) - 2.24(X_3) - 1.46(X_4) - 3.02(X_1X_2) + 0.7729(X_1X_3) - 1.21(X_1X_4) + 1.94(X_2X_3) - 8.42(X_2X_4) + 0.6356(X_3X_4) + 5.78(\mathrm{X}_1^2) - 1.44(\mathrm{X}_2^2) - 3.06(\mathrm{X}_3^2) + 12.56(\mathrm{X}_4^2)$$ ***Equation 5.5***.

$$\mathrm{PDI} = 0.3802 - 0.0262(X_1) - 0.0144(X_2) - 0.0479(X_3) - 0.0560(X_4) - 0.2365(X_1X_2) + 0.0210(X_1X_3) - 0.0150(X_1X_4) + 0.0420(X_2X_3) - 0.2652(X_2X_4) + 0.0143(X_3X_4) + 0.2131(\mathrm{X}_1^2) + 0.1103(\mathrm{X}_2^2) - 0.0735(\mathrm{X}_3^2) + 0.3087(\mathrm{X}_4^2)$$ ***Equation 5.6***.

$$\mathrm{ZP} = -23.65 - 0.7125(X_1) - 0.5633(X_2) + 0.8250(X_3) - 0.6758(X_4) - 0.8875(X_1X_2) - 0.8500(X_1X_3) - 2.77(X_1X_4) - 0.1000(X_2X_3) - 0.0725(X_2X_4) + 3.63(X_3X_4)$$ ***Equation 5.7***.

$$Release\ rate\ (\%) = 89.93 + 1.28(X_1) + 1.87(X_2) - 3.61(X_3) - 4.29(X_4)$$ ***Equation 5.8***.

The polynomial equations include different types of terms. The intercept, main effects (influence of individual factors), interaction effects (combined influence of two factors), and quadratic terms. The sign and size of each coefficient show how much that factor affects the response, where positive values suggest a synergistic effect, while negative values indicate an opposing effect. Interaction terms like (X_1X_2), (X_1X_3), and (X_1X_4) reveal how the response changes when two variables are adjusted at the same time. The squared terms (X_1^2, X_2^2, X_3^2, X_4^2) are used to detect any non-linear behaviour in the system. This modelling approach is common in optimisation studies using Design of Experiments (DoE) as explained by Montgomery [179].

To assess the reliability and predictive strength of the models, both the correlation coefficient (R^2) and the standard deviation were examined. An R^2 value approaching 1.0 suggests a strong correlation between the predicted and actual responses. A summary of the R^2 values and corresponding standard deviations for each response variable is presented in Table 5.4.

Table 5.4. Correlation coefficients of the response models.

Response	Response Surface Model					
	SD	**R^2**	**Adj R^2**	**Pred R^2**	**Adeq Prec**	**C.V %**
Y_1 (PS)	9.13	0.6167	0.2335	-1.1560	4.3211	41.54
Y_2 (PDI)	0.1252	0.8764	0.7528	0.3182	8.4881	20.48
Y_3 (ZP)	2.08	0.5923	0.3658	-0.0047	6.9509	8.79
Y_4 (RR)	7.25	0.2580	0.1344	-0.0913	5.2481	8.06

The statistical evaluation of the models was performed using the coefficient of determination (R^2), adjusted R^2, predicted R^2, standard deviation (SD), adequate precision, and coefficient of variation (C.V.%) as seen in Table 5.4. The R^2 values for particle size (Y_1), polydispersity index (Y_2), zeta potential (Y_3), and release rate at 10 minutes (Y_4) were 0.6167, 0.8764, 0.5923, and 0.2580, respectively. These values indicate that approximately 61.67%, 87.64%, 59.23%, and 25.80% of the total variation in the responses can be explained by the experimental variables. These R^2 values suggest a strong model fit for Y_2, a moderately acceptable fit for Y_1 and Y_3, and a weak fit for Y_4. But the model fitness is not evaluated in isolation. The adjusted R^2 and predicted R^2 values offer insights into model robustness. While the adjusted R^2 for Y_2 remained

high at 0.7528, the predicted R^2 dropped to 0.3182, indicating poor generalisation but still acceptable predictive capacity. In contrast, the negative predicted R^2 values for Y_1 (–1.1560), Y_3 (–0.0047), and Y_4 (–0.0913) suggest limited or no predictive reliability. This can also be attributed to insufficient factor influence therefore limiting the model's ability to reliably predict data.

All models exhibited good signal to noise ratios, with adequate precision values greater than the value of 4 [179]. Y_1, Y_2, Y_3, and Y_4 yielded precision values of 4.3211, 8.4881, 6.9509, and 5.2481, respectively, indicating statistical reliability in exploring the experimental space. The coefficient of variation (C.V.%) values were found to be Y_3 (8.79%) and Y_4 (8.06%), suggesting consistent responses. However, the high C.V. observed for Y_1 (41.54%) and Y_2 (20.48%) indicate that these models may need a refinement of the design space. While the PDI model (Y_2) demonstrated the most reliable outcome for prediction, the remaining models serve as useful tools for interpreting formulation trends but may require further optimisation before being applied for predictive. These results can be further justified by ANOVA.

5.3.1.3. Analysis of Variance (ANOVA)

ANOVA was used to determine the statistical significance of the models and individual model terms. The statistical significance of the response surface models was assessed using the model F-value and corresponding p-value, with significance established at a 95% confidence level ($p < 0.05$) as described in Chapter 2.

5.3.1.3.1. Response surface quadratic model for square root transformed particle size (Y_1)

The analysis of the Box-Cox plot revealed that the optimal transformation parameter was $\lambda = 0.5$, corresponding to a square root transformation. The current lambda value of 1, which represents the untransformed data (Figure 5.2), is shown by the blue vertical line and clearly lies outside the 95% confidence interval (bounded by red vertical bars). This indicates that the original untransformed model does not reside within the statistically acceptable region and is therefore not optimal in terms of variances or residuals. A square root transformation was applied to the PS data, improving the model and assumptions for valid ANOVA. This transformation also reduced heteroscedasticity.

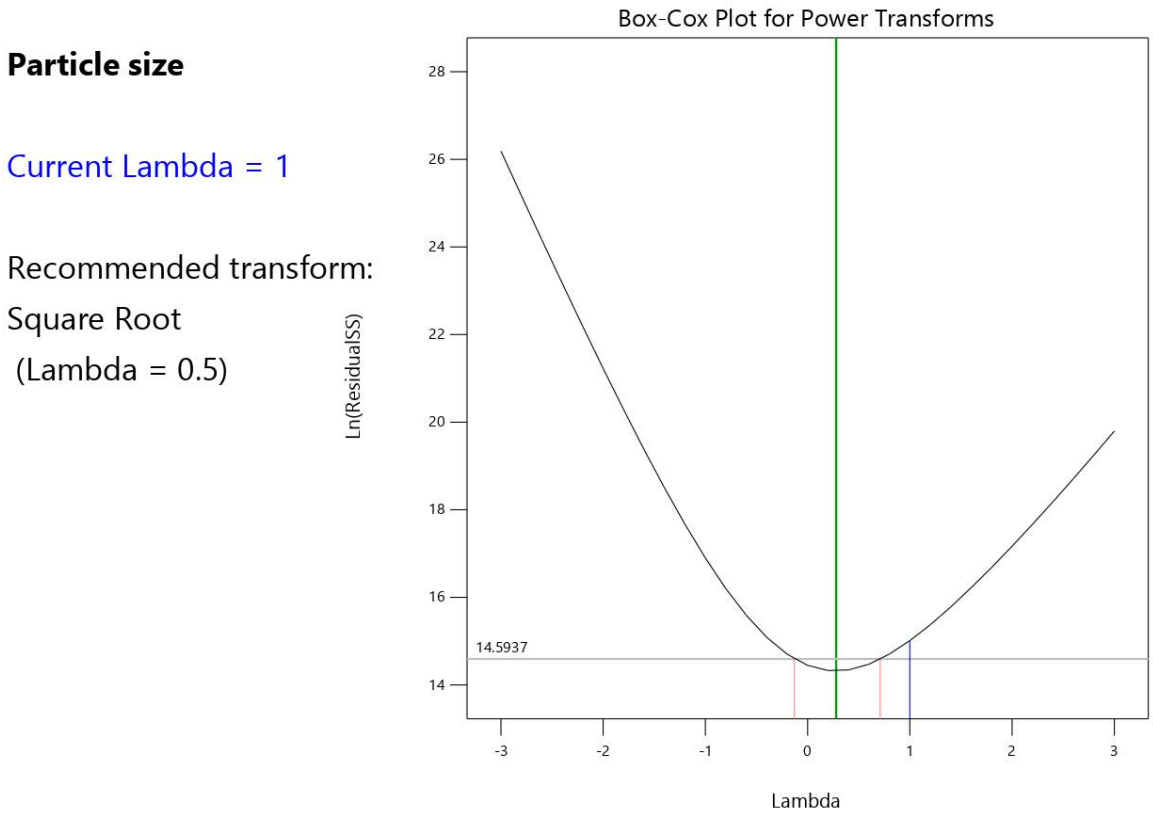

Figure 5.2. Box-Cox plot for the power transformation for particle size (before square root transformation)

A summary of the ANOVA analysis for the quadratic model for square root transformed particle size is shown in Table 5.5. The quadratic response surface model constructed for square root transformed PS did not reach statistical significance, as indicated by the p-value of 0.1921, which is greater than 0.05. This suggests that the combined effects of the variables were not sufficient to explain a statistically significant variation observed. *A, B, C* and *D* had p-values greater than 0.05, indicating that none of these variables independently had a statistically significant impact on PS. This lack of significance may be attributed to a narrow experimental range. The quadratic term D^2 (sonication time squared), which was highly significant ($p = 0.0035$) had an F-value of 12.27. This result strongly suggests that sonication time influences PS, too little or too much sonication may increase particle size due to inadequate energy input or thermal degradation. The interaction term *BD* showed a low p-value of 0.0864. This may suggest a potential synergistic interaction between polymer concentration and energy input during sonication.

Table 5.5. ANOVA analysis for the quadratic model for square root transformed particle size

Source	Sum of Squares	df	Mean Square	F-value	p-value	
Model	1879.40	14	134.24	1.61	0.1921	not significant
A-Tween®80 concentration	2.07	1	2.07	0.0249	0.8770	
B-PVP K30 concentration	9.66	1	9.66	0.1158	0.7387	
C-Solvent: antisolvent ratio	60.26	1	60.26	0.7224	0.4097	
D-Sonication Time	25.71	1	25.71	0.3082	0.5875	
AB	36.39	1	36.39	0.4362	0.5197	
AC	2.39	1	2.39	0.0286	0.8680	
AD	5.84	1	5.84	0.0700	0.7952	
BC	15.02	1	15.02	0.1801	0.6778	
BD	283.75	1	283.75	3.40	0.0864	
CD	1.62	1	1.62	0.0194	0.8913	
A^2	216.99	1	216.99	2.60	0.1291	
B^2	13.46	1	13.46	0.1614	0.6939	
C^2	60.64	1	60.64	0.7270	0.4082	
D^2	1023.95	1	1023.95	12.27	0.0035	
Residual	1167.88	14	83.42			

Figure 5.3 presents the normal probability plot of externally studentized residuals for the square root transformed particle size. The data points closely align along the reference line, indicating that the residuals are approximately normally distributed. Therefore, the square root transformation successfully improved the normality of the residuals and contributed to model adequacy

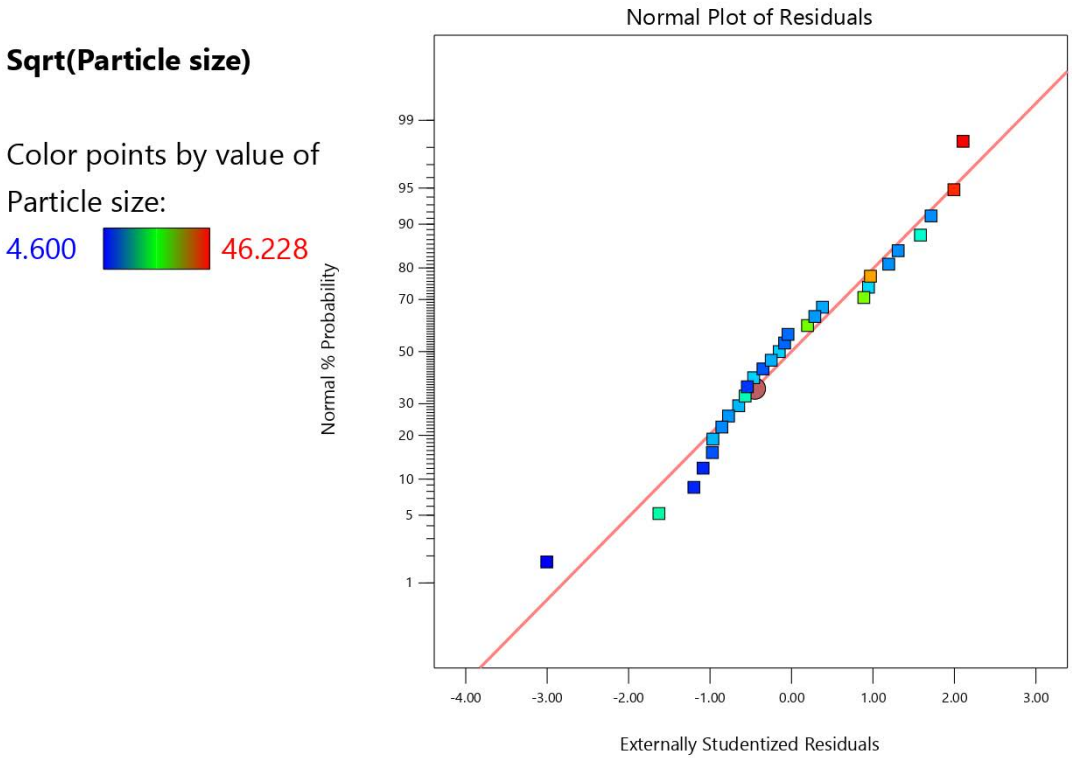

Figure 5.3. Normal probability plot of residuals for particle size square root transformation

Figure 5.4 shows the plot of studentized residuals versus predicted values for the transformed PS model. In this plot, residuals are randomly scattered around the zero line without forming any pattern, supporting homoscedasticity. All residuals fall within the control limits (±3), confirming that no significant outliers or influential data points are present. Figure 5.5 displays the Box-Cox plot for the power transformation, which was used to statistically determine the most appropriate transformation for PS data. The minimum of the curve occurs at a lambda (λ) value of 0.5, suggesting that a square root transformation is optimal.

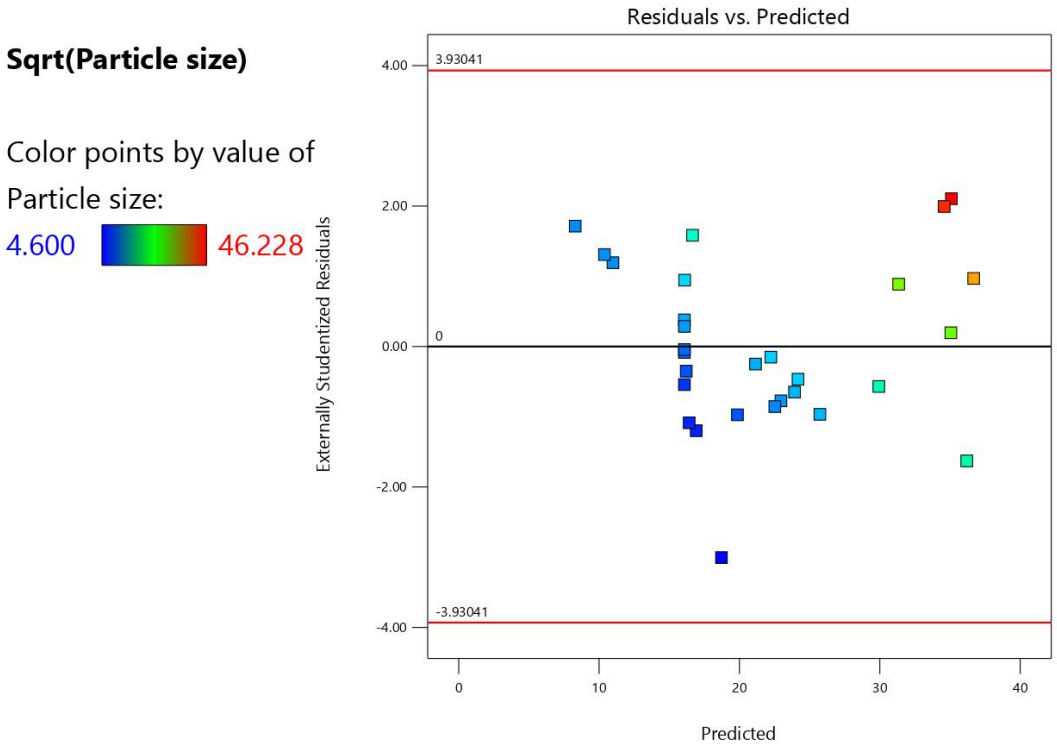

Figure 5.4. Plot of studentized residuals versus predicted responses for particle size after square root transformation

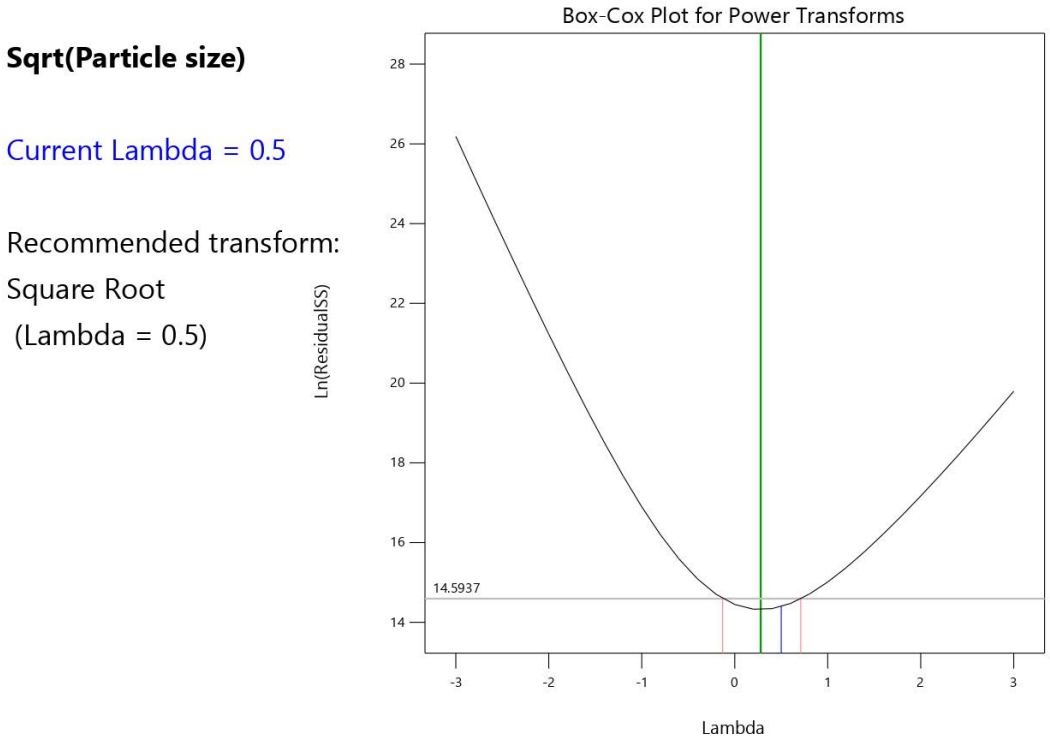

Figure 5.5. Box-Cox plot for the power transformation for particle size after square root transformation)

5.3.1.3.2. Response surface 2FI model for polydispersity index (Y_2)

The ANOVA results in Table 5.6 show that the 2FI model for PDI is statistically significant ($p = 0.0004$) with an F-value of 7.09. While none of the individual main effects were significant on their own ($p > 0.05$), other interaction and quadratic terms were highly significant. The interaction between Tween®80 and PVP K30 concentrations (AB) and between PVP K30 and sonication time (BD) were both strongly significant, showing that the combined influence of these variables plays a role in determining PDI. Significant quadratic terms, Tween®80 (A^2), PVP K30 (B^2), and sonication time (D^2), suggest non-linear effects.

Table 5.6. ANOVA analysis for PDI

Source	Sum of Squares	df	Mean Square	F-value	p-value	
Model	1.56	14	0.1112	7.09	**0.0004**	**significant**
A-Tween®80 concentration	0.0082	1	0.0082	0.5239	0.4811	
B-PVP K30 concentration	0.0025	1	0.0025	0.1590	0.6961	
C-Solvent:antisolvent ratio	0.0276	1	0.0276	1.76	0.2062	
D-Sonication Time	0.0376	1	0.0376	2.40	0.1437	
AB	0.2237	1	0.2237	14.27	0.0020	
AC	0.0018	1	0.0018	0.1125	0.7423	
AD	0.0009	1	0.0009	0.0574	0.8141	
BC	0.0071	1	0.0071	0.4499	0.5133	
BD	0.2814	1	0.2814	17.95	0.0008	
CD	0.0008	1	0.0008	0.0518	0.8233	
A^2	0.2947	1	0.2947	18.79	0.0007	
B^2	0.0789	1	0.0789	5.03	0.0416	
C^2	0.0350	1	0.0350	2.23	0.1573	
D^2	0.6179	1	0.6179	39.40	< 0.0001	
Residual	0.2195	14	0.0157			

Figure 5.6 shows the normal probability plot of externally studentized residuals for the PDI model. The points align closely with the red diagonal reference line, indicating that the

residuals follow a normal distribution. Figure 5.7 presents the plot of studentized residuals versus predicted PDI values, used to assess homoscedasticity. The residuals are randomly scattered around zero with no trend pattern. This confirms that the variance is independent of predicted PDI values and that the model is stable across the range of predictions. Figure 5.8 displays the Box-Cox power transformation plot for PDI. The curve reaches its minimum at a lambda value (λ) of 1, with the blue vertical line falling at this point and well within the 95% confidence interval. This indicates that the model based on untransformed PDI values is appropriate, and no transformation is needed.

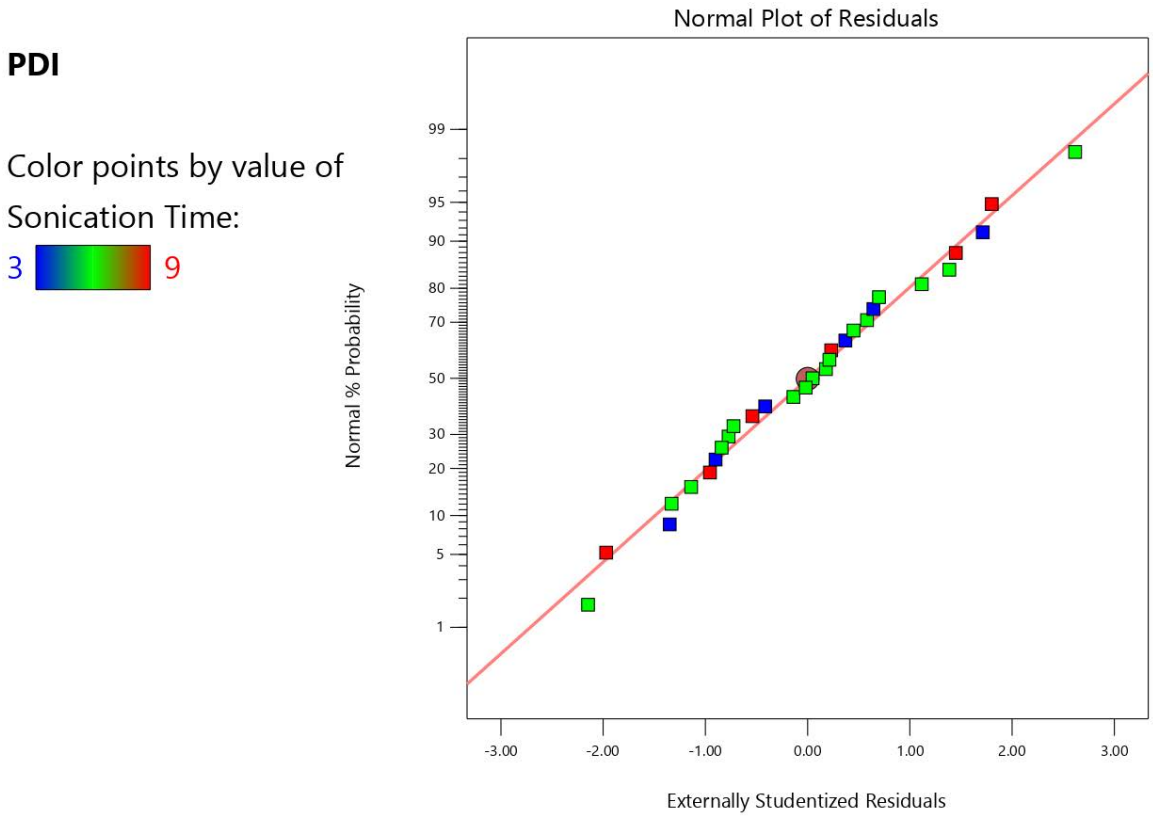

Figure 5.6. Normal probability plot of residuals for PDI

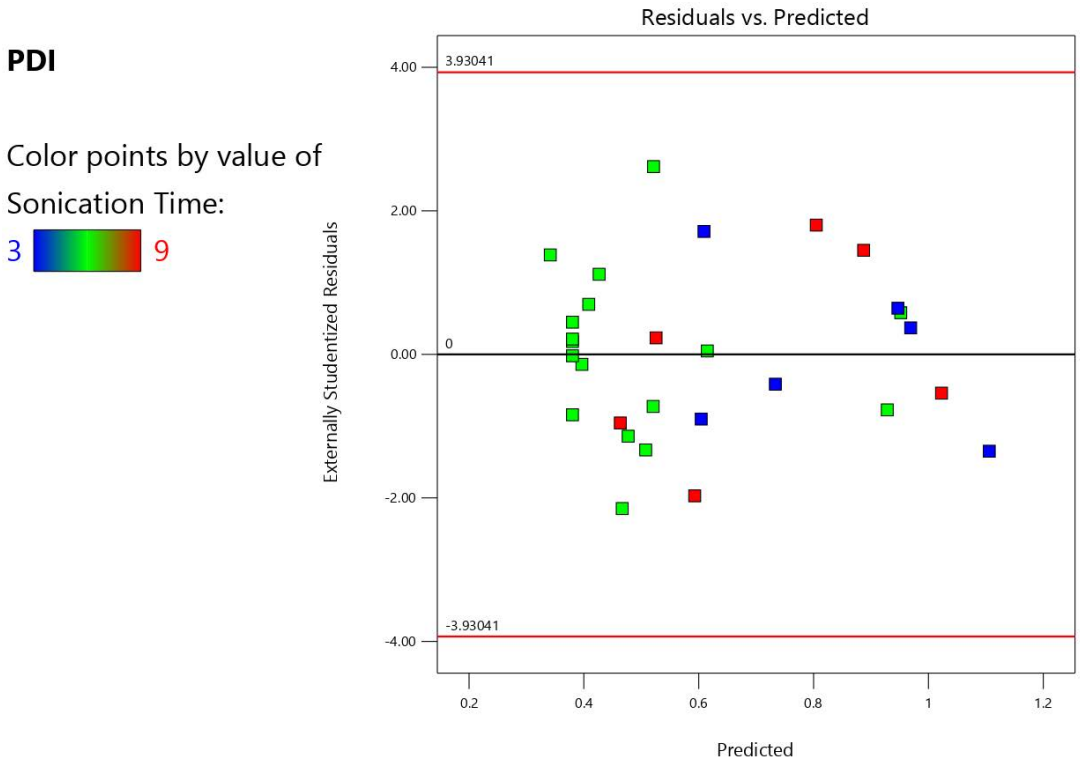

Figure 5.7. Plot of studentized residuals versus predicted responses for PDI.

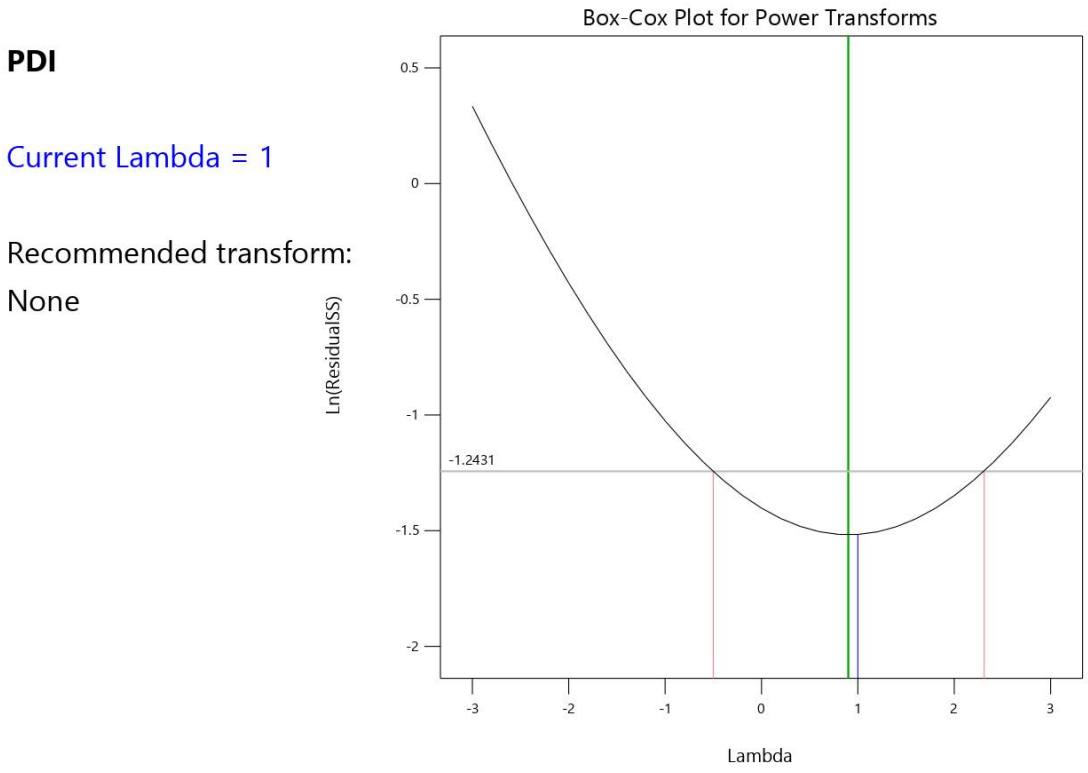

Figure 5.8. Box-Cox plot for the power transformation for PDI

5.3.1.3.3. Response surface linear model for zeta potential (Y_3)

The ANOVA data for zeta potential is summarized in Table 5.7. The linear model for zeta potential was statistically significant, with an F-value of 2.61 and a p-value of 0.0365. While most individual main effects and interactions were not statistically significant ($p > 0.05$), two interaction terms demonstrated strong influence. The interaction between Tween®80 and sonication time (AD) was significant with an F-value of 7.13 ($p = 0.0156$), and the interaction between solvent: antisolvent ratio and sonication time (CD) was highly significant with an F-value of 12.16 ($p = 0.0026$). These results suggest that zeta potential is more strongly affected by combinations of process conditions than by individual variables alone.

Table 5.7. ANOVA analysis for ZP

Source	Sum of Squares	df	Mean Square	F-value	p-value	
Model	113.02	10	11.30	2.61	0.0365	significant
A-Tween®80 concentration	6.09	1	6.09	1.41	0.2506	
B-PVP K30 concentration	3.81	1	3.81	0.8811	0.3603	
C-Solvent: antisolvent ratio	8.17	1	8.17	1.89	0.1861	
D-Sonication Time	5.48	1	5.48	1.27	0.2749	
AB	3.15	1	3.15	0.7289	0.4044	
AC	2.89	1	2.89	0.6686	0.4242	
AD	30.80	1	30.80	7.13	0.0156	
BC	0.0400	1	0.0400	0.0093	0.9244	
BD	0.0210	1	0.0210	0.0049	0.9452	
CD	52.56	1	52.56	12.16	0.0026	
Residual	77.80	18	4.32			

Figure 5.9 shows the normal probability plot of externally studentized residuals for the zeta potential model. The residuals closely follow the red reference line, indicating that the error terms are normally distributed. Figure 5.10 presents the Box-Cox transformation plot, which evaluates the need for a power transformation of the zeta potential response. The current lambda value is 1, and it falls within the 95% confidence interval (bounded by red lines), with the curve reaching its minimum near this point. This confirms that no transformation is needed, and the zeta potential model based on untransformed data is statistically appropriate. Figure

5.11 displays the plot of studentized residuals versus predicted values, which tests for homoscedasticity. The residuals are randomly scattered around the zero line without a pattern shape, indicating that the variance is stable across the range of predicted values. All residuals fall within the control limits (±3.714).

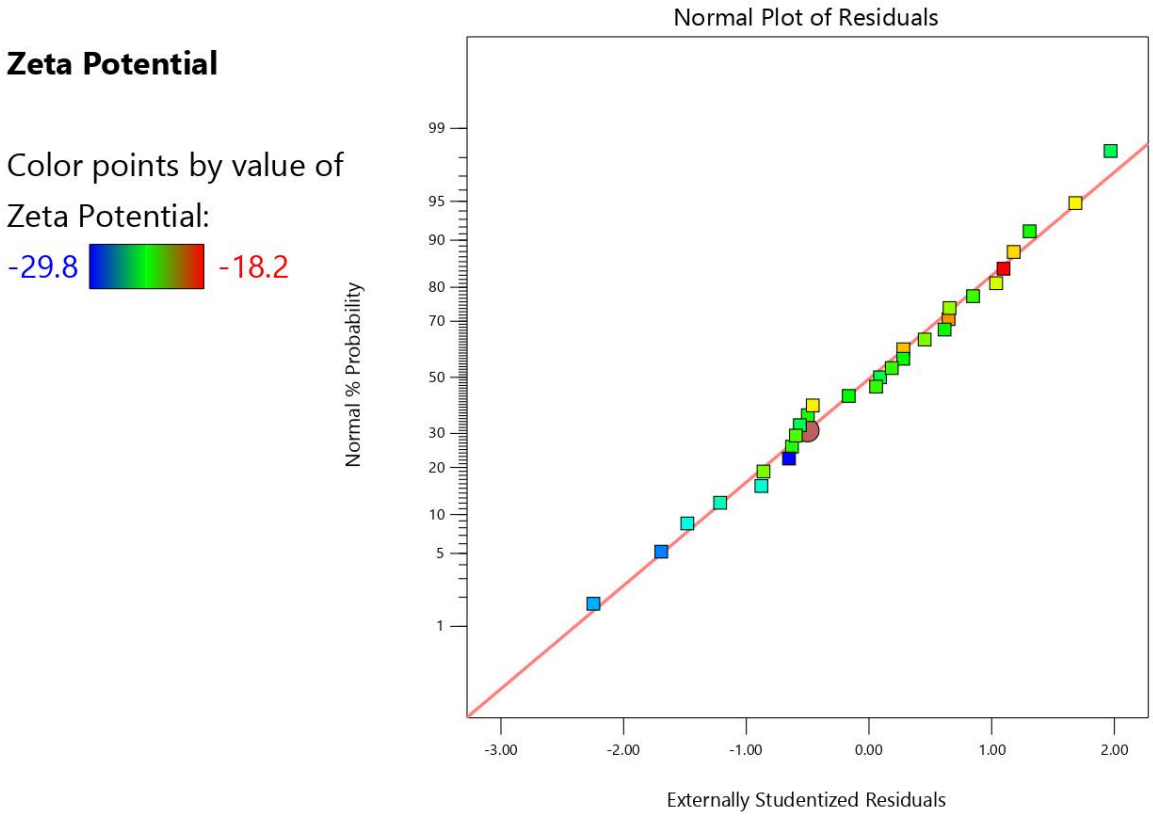

Figure 5.9. Normal probability plot of residuals for zeta potential.

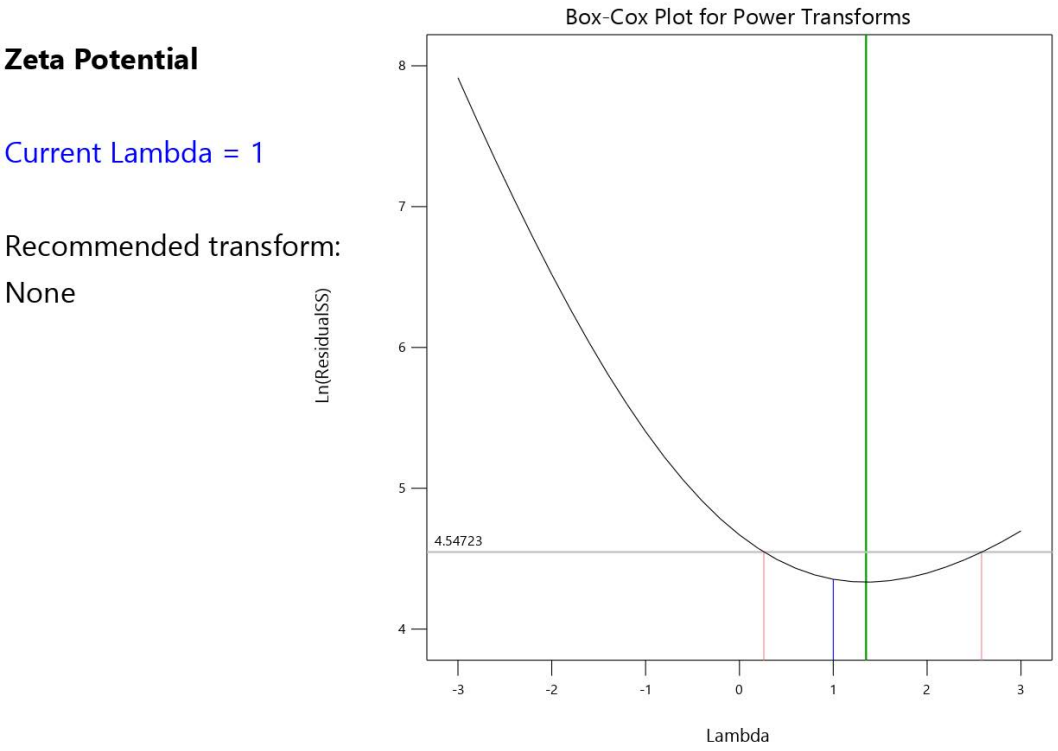

Figure 5.10. Box-Cox plot for the power transformation for zeta potential

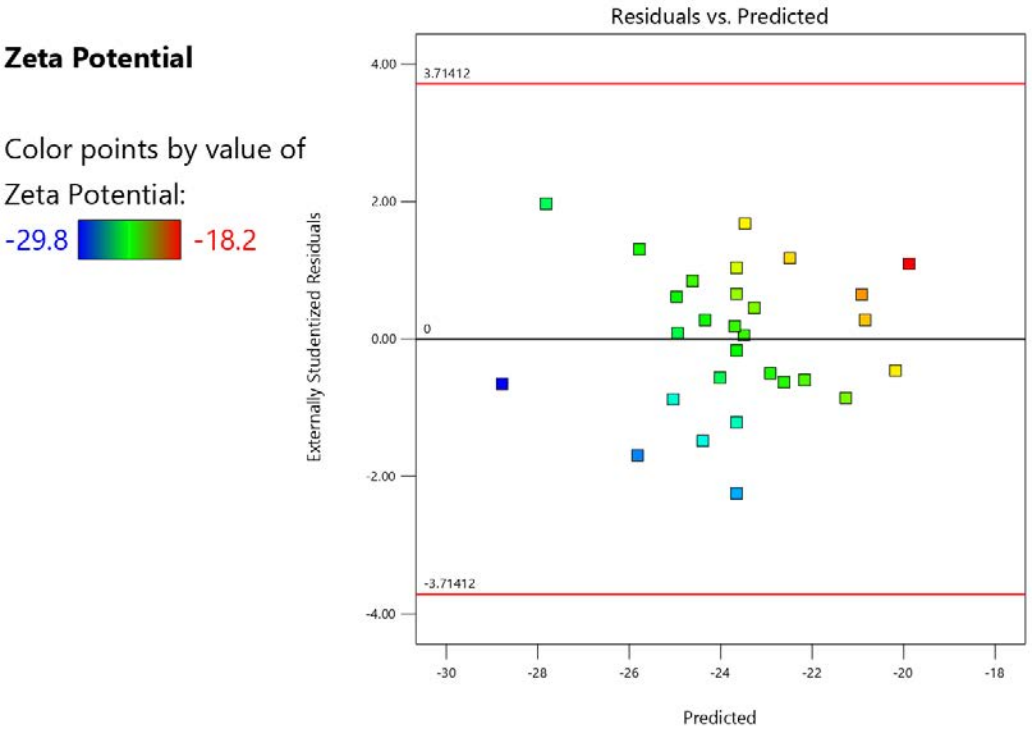

Figure 5.11. Plot of studentized residuals versus predicted responses for zeta potential

5.3.1.3.4. Response surface linear model for drug release (Y_4)

The ANOVA data is summarized in Table 5.8. The linear response surface model for drug release was not statistically significant, with an overall F-value of 2.09 and a p-value of 0.1140. Sonication time (D) approached significance (F = 4.20, p = 0.0515), suggesting a potential influence on drug release. Similarly, the solvent:antisolvent ratio (C) showed a moderately low p-value (p = 0.0973). Tween®80 and PVP K30 concentrations (A and B) had high p-values and low F-values, indicating minimal individual effect on drug release.

Table 5.8. ANOVA analysis for release rate.

Source	Sum of Squares	df	Mean Square	F-value	p-value	
Model	439.02	4	109.76	2.09	0.1140	**not significant**
A-Tween®80 concentration	19.53	1	19.53	0.3713	0.5480	
B-PVP K30 concentration	42.04	1	42.04	0.7991	0.3802	
C-Solvent: antisolvent ratio	156.60	1	156.60	2.98	0.0973	
D-Sonication Time	220.85	1	220.85	4.20	0.0515	
Residual	1262.48	24	52.60			

Figure 5.12 presents the normal probability plot of externally studentized residuals for the drug release rate model. The residuals lie closely along the red reference line, indicating that the data is normally distributed. Figure 5.13 shows the Box-Cox transformation plot. The current lambda ($\lambda = 1$), representing the untransformed model, lies near the minimum of the curve and within the 95% confidence interval. This confirms that no transformation was required, and that the original model of the drug release data was appropriate. Figure 5.14 displays the plot of studentized residuals versus predicted values, which checks for homoscedasticity. The residuals are randomly scattered around the zero line without any distinct pattern, indicating that the variance is consistent across predicted values. All residuals fall within the control limits (±3.556).

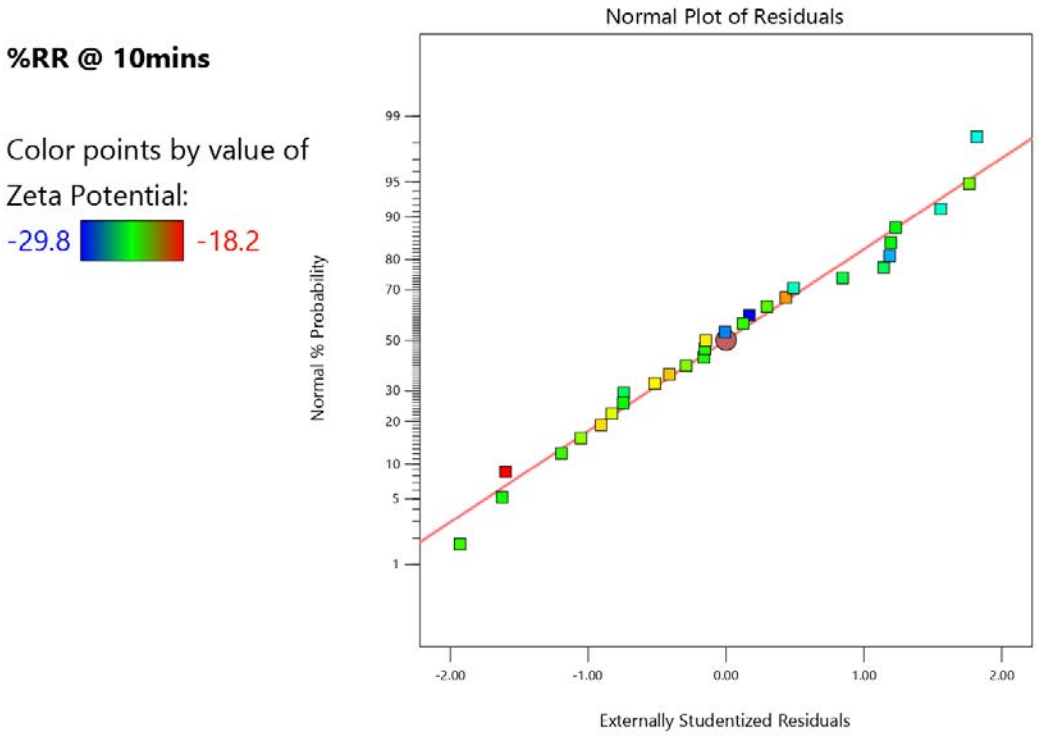

Figure 5.12. Normal probability plot of residuals for drug release rate at 10 mins.

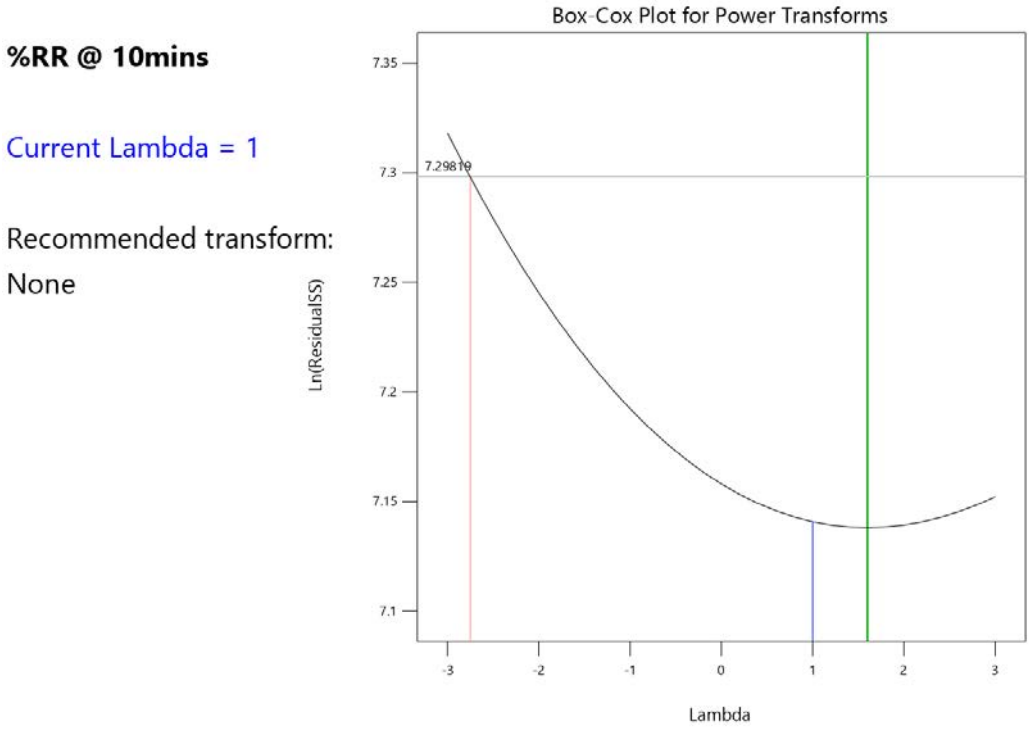

Figure 5.13. Box-Cox plot for the power transformation for drug release rate at 10 mins.

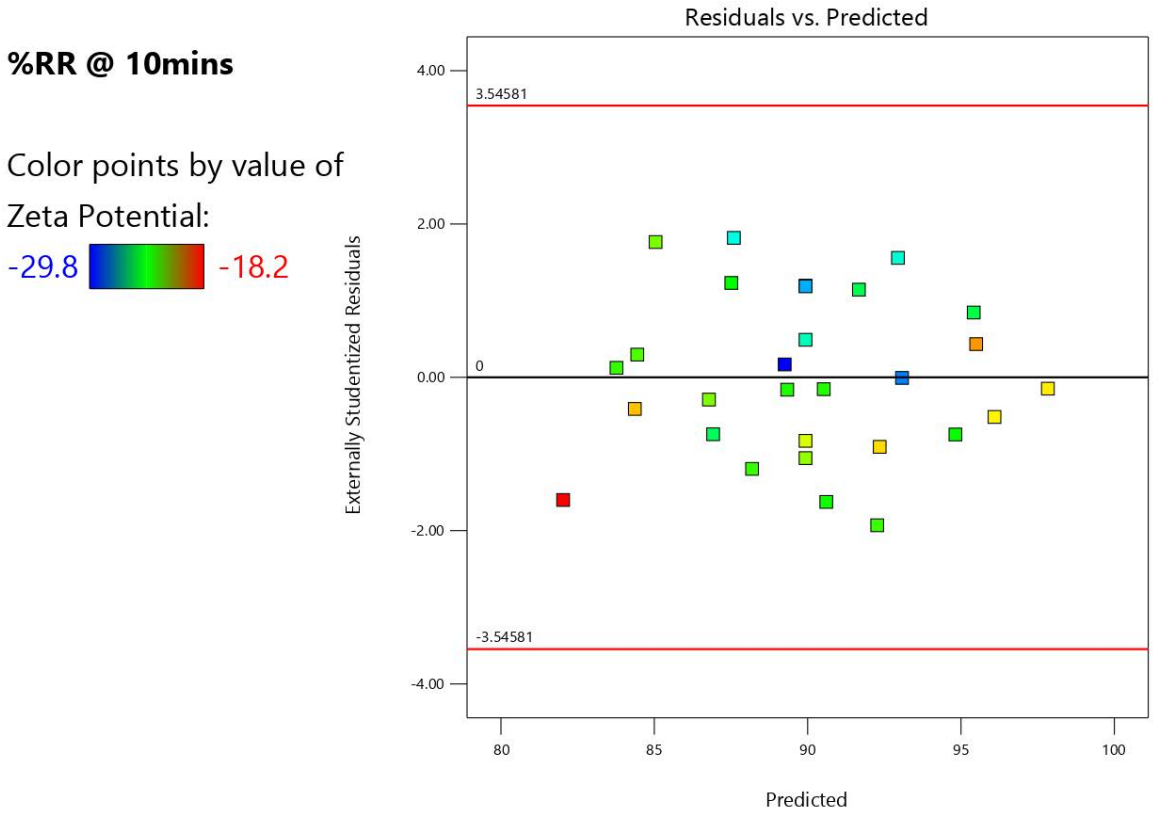

Figure 5.14. Plot of studentized residuals versus predicted responses for drug release rate at 10mins

5.3.1.4. Process and formulation variable effects on particle size, PDI, zeta potential and drug release rate.

Using RSM, 2D contour plots and 3D surface plots were generated to graphically visualize the effects and interactions of Tween®80 concentration, PVP K30 concentration, solvent:antisolvent ratio, and sonication time on particle size, polydispersity index (PDI), zeta potential, and drug release rate. The selected plots highlight the most relevant factor combinations based on ANOVA statistical significance and model diagnostics discussed above.

5.3.1.4.1. Particle size

Figure 5.15 illustrates the contour plot depicting the interactive effect of PVP K30 concentration (Y-axis) and sonication time (X-axis) on the square root transformed PS, with Tween®80 and solvent: antisolvent ratio held constant. The contour gradient moves from green (larger PS) on the left toward blue (smaller PS) on the right, indicating that longer sonication

times consistently result in reduced particle size. In contrast, PVP K30 concentration have minimal influence on PS across the range. The vertical contour lines and uniform colour indicate that increasing polymer concentration does not substantially alter PS. The region corresponding to high sonication time and moderate PVP concentration (upper-right quadrant of the plot) displays the lowest PS values. However, as sonication time increases beyond this point, thermal effects can be introduced, which could impact drug stability or induce re-aggregation.

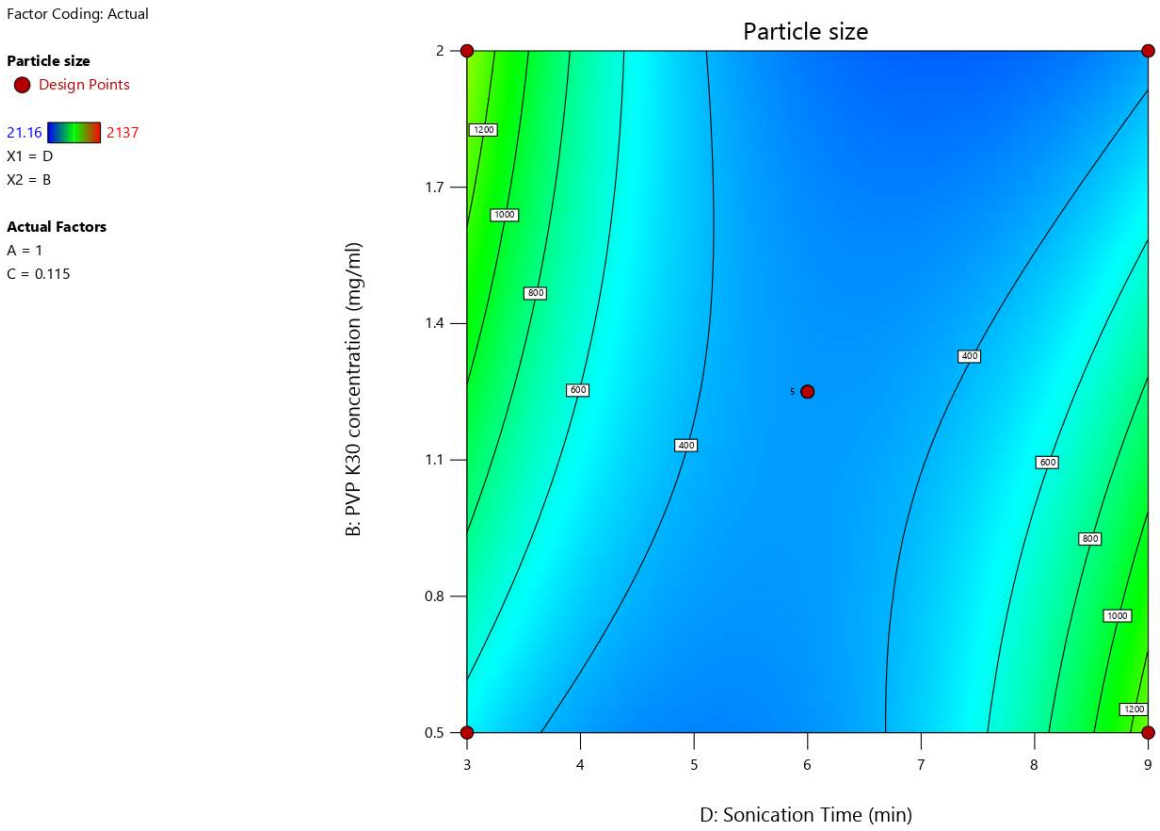

Figure 5.15. Contour plot showing the effect of PVP K30 concentration and sonication time on particle size.

Figure 5.16 illustrates the 3D surface plot representing the combined influence of PVP K30 concentration and sonication time on the PS. This plot complements the 2D contour plot (Figure 5.15), allowing a clearer observation of response surface curvature and interaction between the selected variables. The surface reveals a distinct concave shape, due to the quadratic influence of sonication time (D^2). As sonication time increases along the X-axis (from 3 to 9 minutes), PS decreases to a minimum region around 7 minutes, after which the slope begins to rise, suggesting a non-linear effect. PVP K30 concentration (Y-axis) exerts a much

flatter and less influential effect on the surface. The gentle gradient across this axis confirms that changes in polymer concentration within the tested range do not result in major fluctuations in PS. This aligns with the ANOVA results, where PVP K30 were not statistically significant. The central depression in the surface graph, corresponding to mid to high sonication time and moderate PVP K30 levels, an optimal zone for achieving smaller PS.

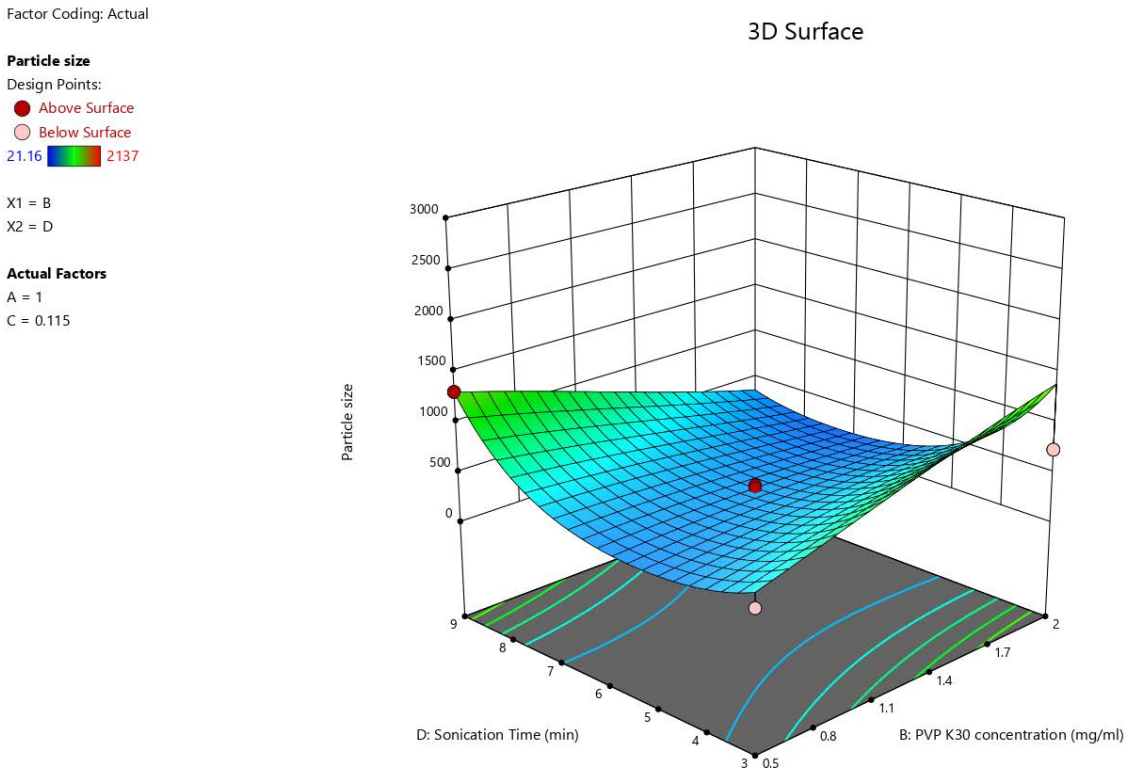

Figure 5.16. 3D surface plot showing the effect of PVP K30 and sonication time on particle size.

5.3.1.4.2. Polydispersity index (PDI)

Figure 5.17 presents a 2D contour plot demonstrating the interaction between PVP K30 concentration (Y-axis) and sonication time (X-axis) on the PDI. In this plot, Tween®80 concentration and solvent: antisolvent ratio were held constant. The colour gradient from green to blue represents a decrease in PDI, with lower PDI values observed toward the centre of the plot, moderate PVP K30 concentrations and sonication times around 6 minutes. The nearly vertical contour lines suggest that PVP K30 concentration has minimal impact on PDI.

However, sonication time exerts a more visible influence, as shown by the gradual horizontal gradient.

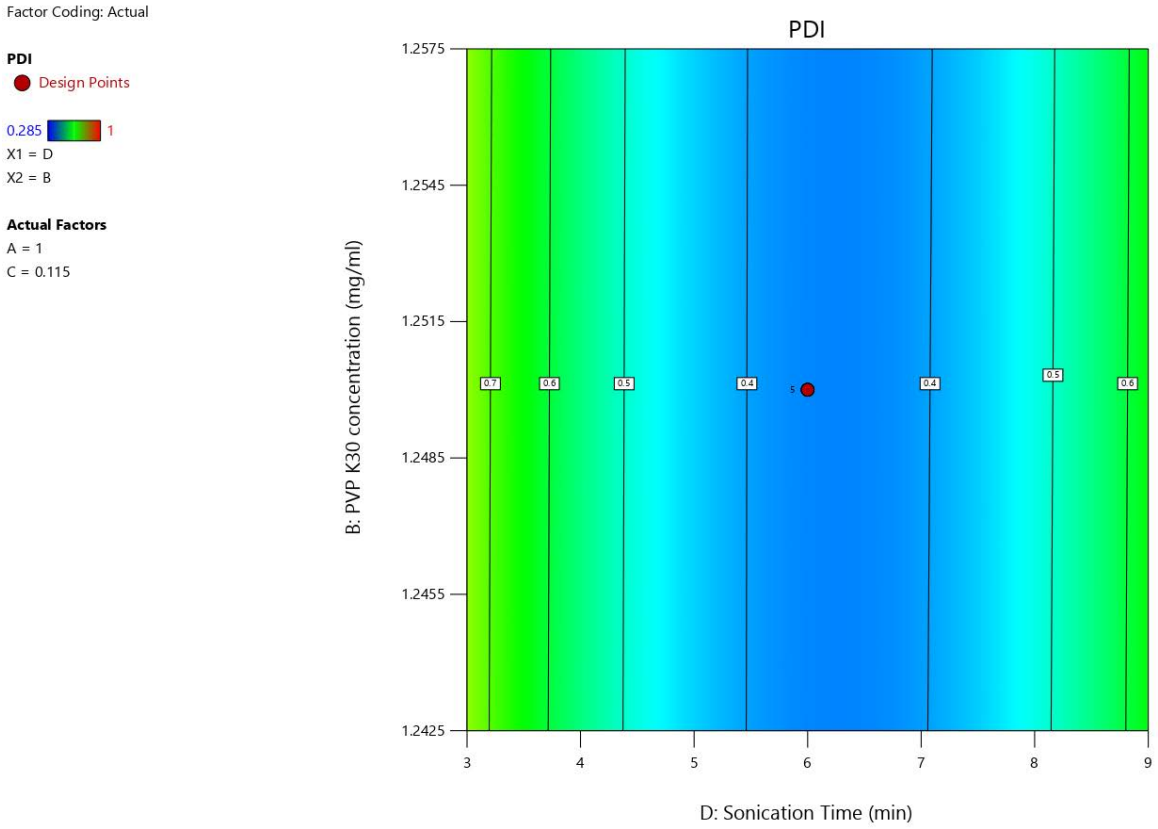

Figure 5.17. Contour plot showing the effect of PVP K30 concentration and sonication time on PDI.

Figure 5.18 displays a 3D surface plot illustrating the combined effects of Tween®80 concentration and sonication time on the PDI. The surface exhibits a concave curvature along the sonication time axis, indicating that PDI decreases with increasing sonication time. The Tween®80 concentration axis remains relatively flat, suggesting minimal independent influence on PDI. The surface indicates that sonication time is the dominant factor in reducing PDI, while Tween®80 plays a limited role when evaluated independently. The lowest PDI values are achieved in the mid to high sonication range, reinforcing the importance of optimised mechanical energy input for producing a uniform nanosuspension.

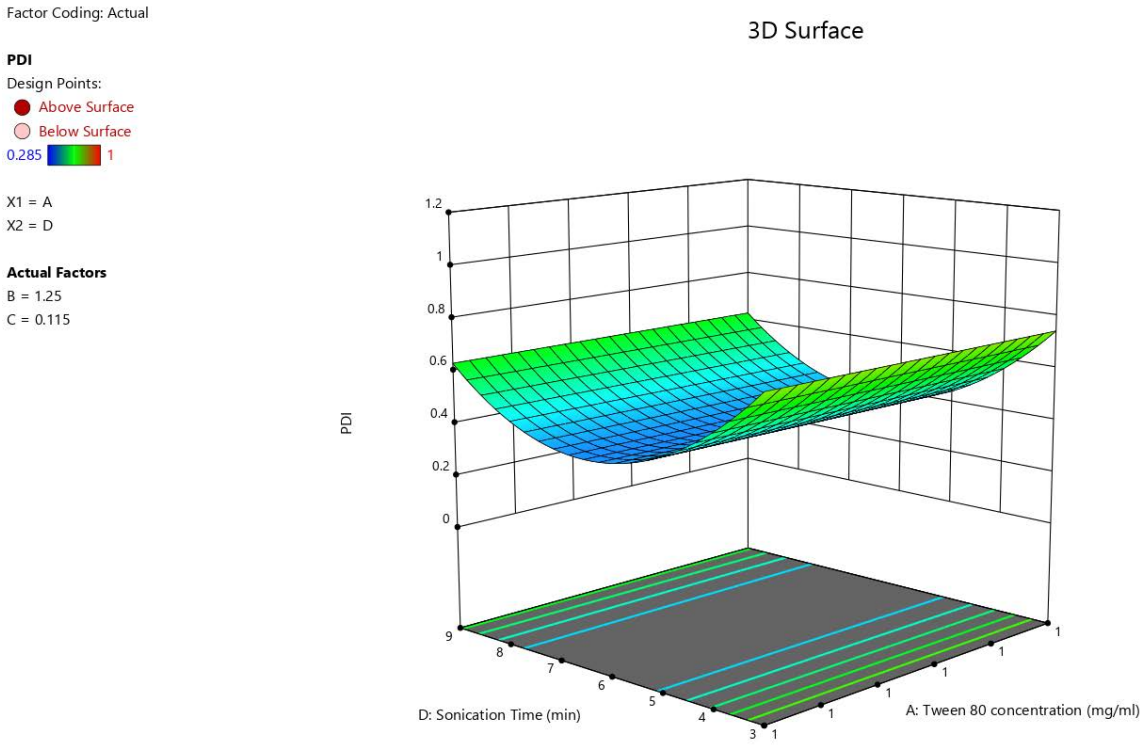

Figure 5.18. 3D surface plot showing the effect of Tween®80 and sonication time on PDI.

Figure 5.19 presents a one factor plot illustrating the isolated effect of sonication time on the PDI, with all other variables held constant. The plot shows a distinct U-shaped curve, where PDI initially decreases with increasing sonication time, reaching a minimum around 6 minutes, before beginning to rise again at higher durations. This trend highlights a non-linear (quadratic) relationship, confirming the statistically significant D^2 term ($p < 0.0001$) from the ANOVA model. The 95% confidence bands (dashed lines) closely follow the fitted curve, indicating a reliable model fit.

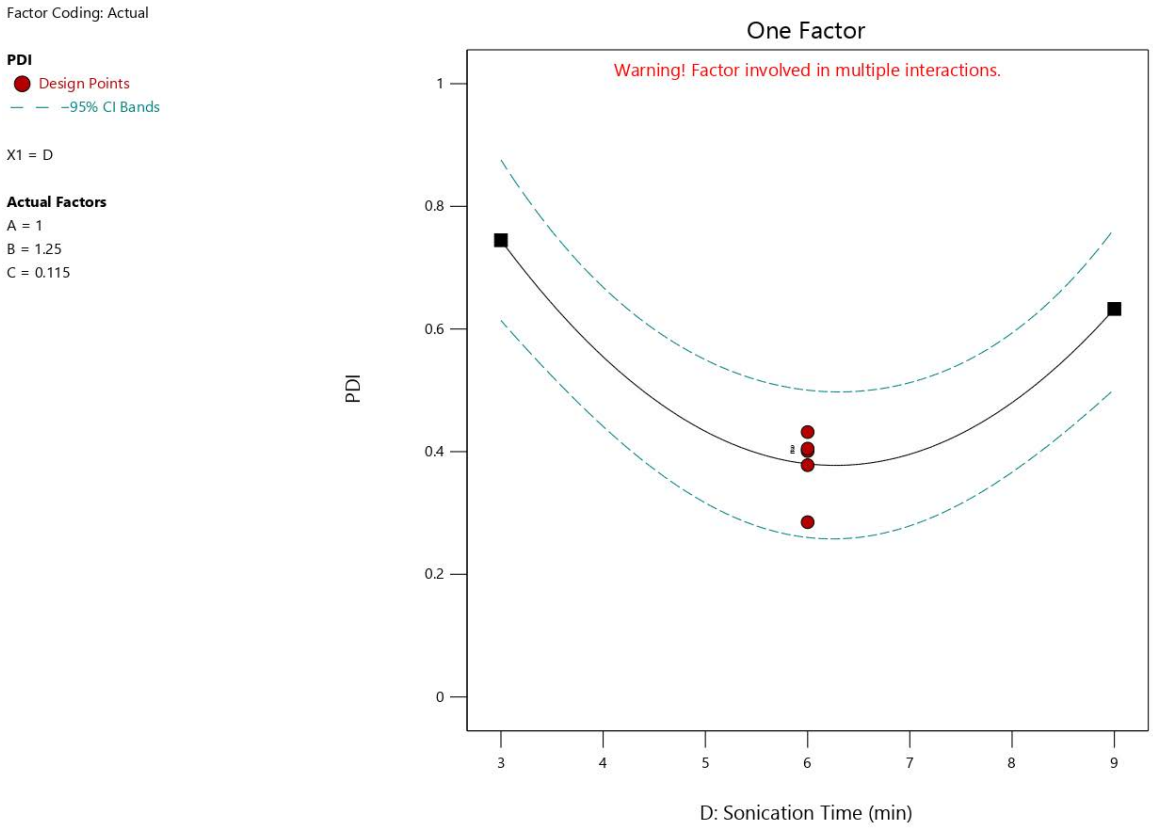

Figure 5.19. Effect of sonication time on PDI

5.3.1.4.3. Zeta potential

Figure 5.20 displays a 2D contour plot representing the interactive effect of Tween®80 concentration and sonication time on the zeta potential. The colour gradient, ranging from red (less negative) to blue (more negative), indicates how formulation and process variables affect the surface charge of the particles. The plot reveals that zeta potential becomes increasingly negative as sonication time increases, especially at lower Tween®80 concentrations. This trend is in line with the significant interaction term AD (Tween®80 and sonication time) observed in the ANOVA ($p = 0.0156$), which suggests that the effect of Tween®80 on zeta potential is influenced by the duration of sonication. At low sonication times (3–5 min) and higher Tween®80 concentrations (≥ 1.2 mg/mL), the zeta potential is less negative (–18 to –20 mV), indicating weaker electrostatic stabilization. The most negative zeta potentials (up to –29.8 mV) occured at longer sonication times and lower surfactant levels, where energy input likely enhances nanoparticle dispersion and surface exposure, increasing surface charge.

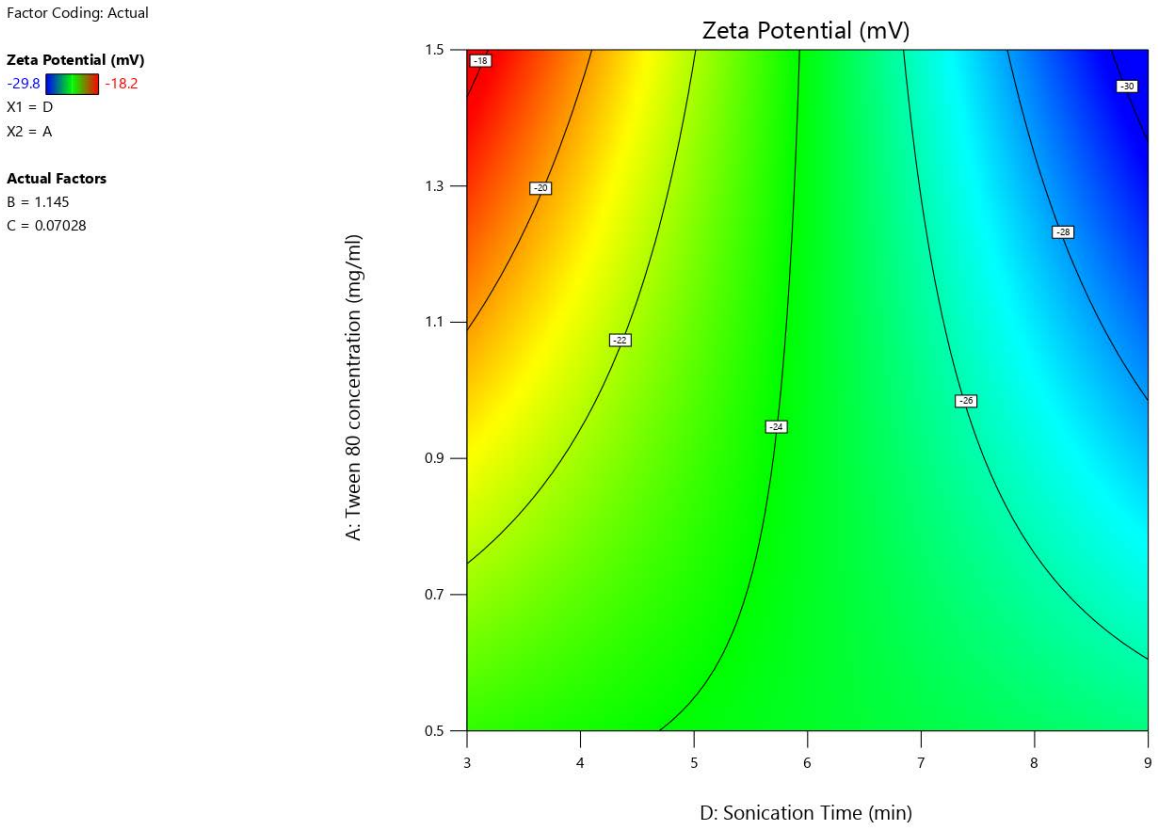

Figure 5.20. Contour plot showing the effect of Tween®80 concentration and sonication time on zeta potential.

Figure 5.21 presents a 3D surface plot illustrating the interactive effect of solvent: antisolvent ratio and sonication time on the zeta potential. The surface shows a pronounced downward slope along both axes, indicating that increasing sonication time and reducing the solvent: antisolvent ratio led to more negative zeta potential values. This trend is consistent with the statistically significant interaction term CD (solvent: antisolvent ratio and sonication time) from the ANOVA ($p = 0.0026$), suggesting that the combined influence of these two process parameters strongly affects surface charge. The sharp gradient toward the back right of the plot shows that the most stable (most negative) zeta potentials are achieved when the solvent: antisolvent ratio is low and sonication time is high. Longer sonication likely enhances particle dispersion and surface energy, increasing the exposure of ionizable groups that contribute to surface charge and a lower solvent: antisolvent ratio facilitates more rapid precipitation and smaller particle formation, further enhancing charge stabilization due to a higher surface area to volume ratio.

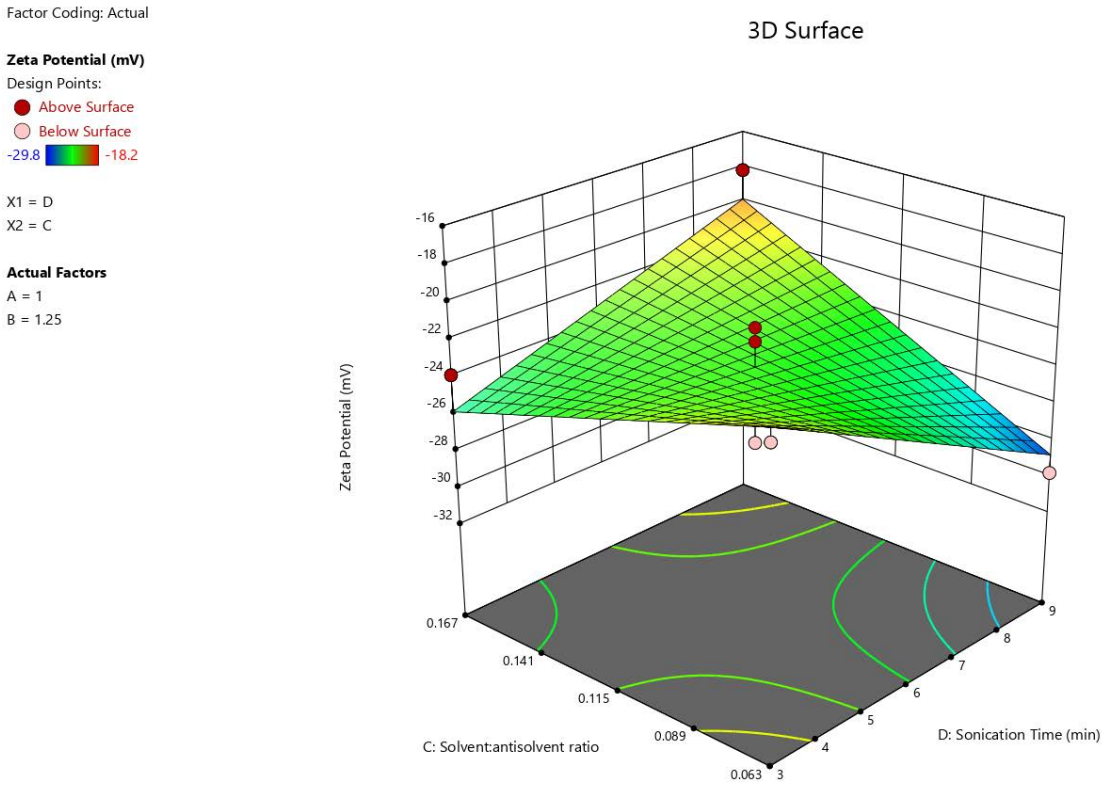

Figure 5.21. 3D surface plot showing the effect of solvent: antisolvent ratio and sonication time on zeta potential.

5.3.1.4.4. Drug release rate

Figure 5.22 presents a contour plot depicting the effect of PVP K30 concentration and sonication time on the percentage of drug released at 10 minutes (%RR). The colour gradient from yellow to green indicates increasing drug release across the design space. The plot shows that sonication time has a greater influence on drug release compared to PVP K30 concentration. As sonication time increases from 3 to 9 minutes, %RR increases steadily, suggesting enhanced drug diffusion with higher energy input. This trend corresponds with the borderline significance of sonication time in the ANOVA ($p = 0.0515$). PVP K30 concentration has minimal effect, as evidenced by the nearly vertical contour lines. This aligns with the model results, where PVP K30 was not a statistically significant factor ($p = 0.3802$).

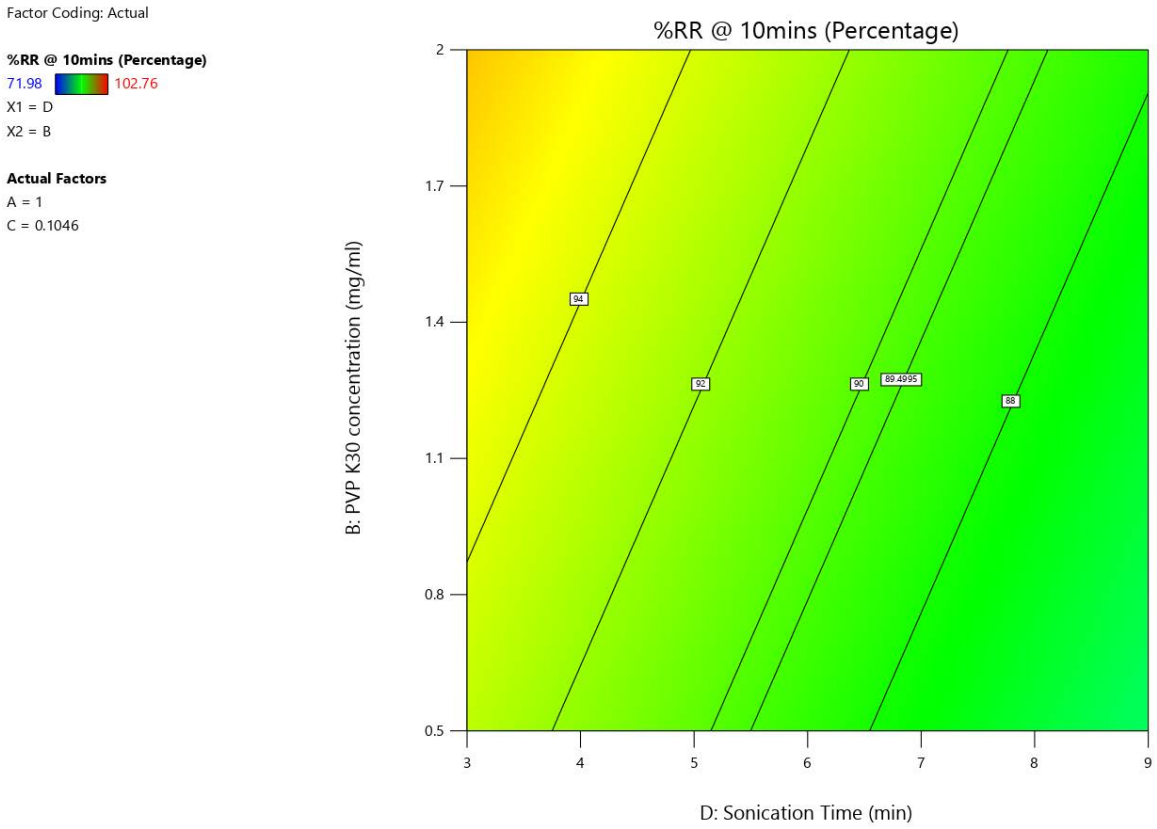

Figure 5.22. Contour plot showing the effect of PVP K30 concentration and sonication time on drug release rate at 10 mins.

Figure 5.23 presents a 3D surface plot illustrating the combined effect of solvent: antisolvent ratio and sonication time on the percentage of AZI released at 10 minutes (%RR). The surface displays a gentle upward slope along the sonication time axis, indicating that drug release improves with longer sonication durations. In contrast, the solvent: antisolvent ratio shows minimal effect, as evidenced by the nearly flat surface along that axis. The overall surface is relatively flat, indicating no strong curvature or synergistic interaction between the two variables.

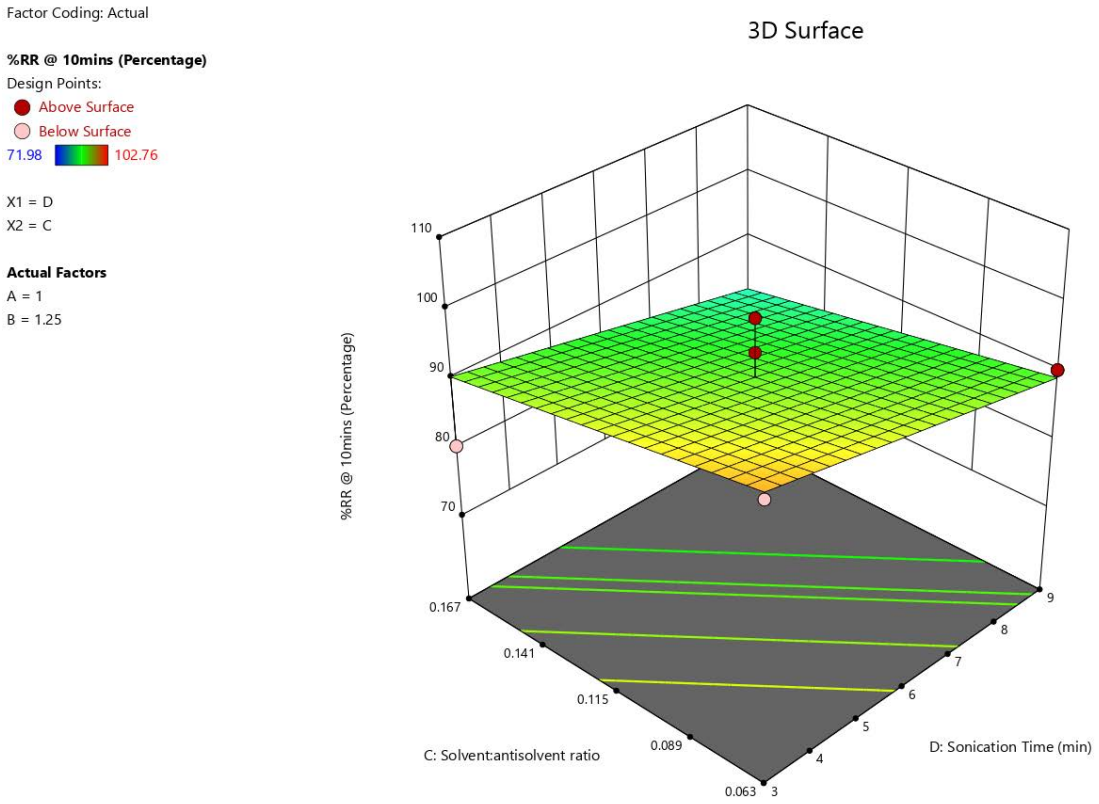

Figure 5.23. 3D surface plot showing the effect of solvent: antisolvent ratio and sonication time on drug release rate at 10 mins.

5.3.2. Formulation Optimisation

Formulation optimisation was conducted using the numerical optimisation function in Design-Expert® 13.0.5 statistical software (Stat-Ease Inc., Minneapolis, USA), with the goal of identifying the combination of process variables that would yield the most desirable formulation characteristics of a nanosuspension. The objective was to minimize particle size (Y_1) and polydispersity index (Y_2), while maximizing zeta potential magnitude (Y_3, more negative) and drug release (Y_4). The optimised formulation was predicted at the following process conditions as shown in Table 5.9. The overall desirability score of 0.891 indicates a high level of optimisation efficiency and confidence in the predicted formulation performance.

Table 5.9. Predicted values for process variables and respective formulation responses.

Process variables				Formulation responses				Desirability
X_1	X_2	X_3	X_4	Y_1	Y_2	Y_3	Y_4	
1.464	2.000	0.063	7.79	175.55	0.230	-29.80	94.03	0.891

Based on the numerical optimisation results, the final process parameters for the manufacture of the AZI nanosuspension are summarized in Table 5.10.

Table 5.10. Optimised conditions for the manufacture of AZI nanosuspension

Process variable	Optimised condition
X_1 (Tween®80 concentration)	1.5 mg/mL
X_2 (PVP K30 concentration)	2.0 mg/mL
X_3 (Solvent: Antisolvent Ratio)	1:15
X_4 (Sonication time)	8 mins

The optimised formulation was experimentally prepared under the predicted conditions to validate the accuracy of the numerical optimisation model. The experimental values were compared with the predicted responses for PS(Y_1), PDI (Y_2), ZP (Y_3), and %RR at 10 minutes (Y_4), and the percentage prediction errors were calculated (Table 5.11). The model showed good predictive capability for ZP and %RR, with low prediction errors of –5.03% for both, indicating strong agreement between experimental and predicted outcomes. The prediction error for PS was –23.50%, which suggests a larger deviation, possibly due to batch-to-batch variability to processing conditions. For PDI, the prediction error was +29.57%, showing a moderate deviation from the predicted value. This could be probably attributed to minor changes in particle aggregation.

Table 5.11. Experimental and predicted response with prediction errors for the optimised formulation

Response	Experimental value	Predicted value	% Prediction error
Y_1	134.30	175.55	-23.50
Y_2	0.298	0.230	29.57
Y_3	-28.30	-29.80	-5.03
Y_4	89.3%	94.03%	-5.03

5.3.3. Kinetics and mechanism of AZI release

The in *vitro* release profiles of the AZI nanosuspension formulations were evaluated by fitting the data to three commonly used kinetic models: zero order, first order, and Higuchi. The aim was to determine the dominant release mechanism and identify the best fit model for each formulation based on the highest correlation coefficient (R^2). The results are summarized in

Table 5.12. Across the 29 BBD formulations, the Higuchi model emerged as the predominant release mechanism, best fitting 21 out of 29 formulations. This suggests that the drug release from the nanosuspension system is primarily diffusion controlled, consistent with Fickian kinetics. This is expected for nanosuspension systems where drug diffusion occurs from a particle surface into the surrounding medium. A smaller group of formulations (8 out of 29) were better described by first order kinetics, which may be influenced by formulation specific attributes such as particle aggregation, or stabiliser concentration. The optimised formulation also followed Higuchi kinetics with an R^2 of 0.7974, confirming that the optimised system exhibits a controlled release behaviour governed primarily by diffusion.

Table 5.12. Summary of AZI release kinetics for BBD and OPT formulations.

Formulation	R^2			Mechanism
	Zero order	First order	Higuchi	
AZI-NS 001	0.5147	0.6887	0.7930	Higuchi
AZI-NS 002	0.4889	0.725	0.7642	Higuchi
AZI-NS 003	0.5036	0.7336	0.7765	Higuchi
AZI-NS 004	0.5399	0.7389	0.8117	Higuchi
AZI-NS 005	0.5495	0.7295	0.8148	Higuchi
AZI-NS 006	0.6262	0.8224	0.8759	Higuchi
AZI-NS 007	0.6543	0.9195	0.8956	First order
AZI-NS 008	0.4836	0.8662	0.7623	First order
AZI-NS 009	0.4819	0.6071	0.7662	Higuchi
AZI-NS 010	0.5588	0.8023	0.8241	Higuchi
AZI-NS 011	0.5203	0.8326	0.7802	First order
AZI-NS 012	0.3976	0.3102	0.6912	Higuchi
AZI-NS 013	0.6636	0.8980	0.8983	Higuchi
AZI-NS 014	0.5323	0.7548	0.8952	Higuchi
AZI-NS 015	0.4614	0.6247	0.7456	Higuchi
AZI-NS 016	0.5115	0.5319	0.7897	Higuchi
AZI-NS 017	0.5881	0.9263	0.8489	First order
AZI-NS 018	0.7049	0.9691	0.9245	First order
AZI-NS 019	0.4172	0.2196	0.7061	Higuchi
AZI-NS 020	0.6343	0.9295	0.8822	First order
AZI-NS 021	0.4568	0.6925	0.7413	Higuchi
AZI-NS 022	0.6696	0.9256	0.9036	First order
AZI-NS 023	0.5069	0.8283	0.7869	First order
AZI-NS 024	0.5556	0.6534	0.8226	Higuchi
AZI-NS 025	0.5443	0.7362	0.8095	Higuchi
AZI-NS 026	0.4155	0.3266	0.7052	Higuchi
AZI-NS 027	0.4241	0.3981	0.7121	Higuchi
AZI-NS 028	0.4862	0.5652	0.7674	Higuchi
AZI-NS 029	0.5145	0.6492	0.7896	Higuchi
AZI-NS OPT	0.5211	0.7846	0.7974	Higuchi

5.3.4. Characterisation of optimised AZI nanosuspension

5.3.4.1. Visual assessment

The optimised azithromycin nanosuspension (Figure 5.24) was visually assessed following preparation. The formulation exhibited a homogenous, clear, transparent dispersion with a slightly opalescent appearance. No visible sedimentation, or aggregation was observed upon standing at room temperature. The formulation remained uniformly suspended with no settling, and gentle movement was sufficient to ensure complete redispersion. The clarity and ease of redispersion are consistent with a stable nanosuspension.

Figure 5.24. Visual appearance of the optimised azithromycin nanosuspension.

5.3.4.2. Particle size and PDI

PS and PDI are considered critical quality attributes (CQAs) in nanosuspension formulation. For the optimised AZI nanosuspension (AZI-NS-OPT), the mean PS was 134.3 ± 26.6 nm, and the PDI was 0.298 ± 0.092, both measured immediately post manufacture using DLS. These values confirm that the formulation are within the nanoscale range and exhibits a monodisperse particle population. The relatively low PDI value (<0.3) indicates a narrow size distribution and minimal aggregation, which is crucial for the long term colloidal stability of the nanosuspension. The steric stabiliser (Tween®80) and the polymer (PVP K30) was critical in achieving uniform size reduction during precipitation and sonication. These excipients prevent

Ostwald ripening and particle agglomeration by forming a hydrophilic coating around the nanocrystals, enhancing repulsion.

The use of solvent antisolvent precipitation method, followed by controlled sonication, allowed for rapid nucleation and prevention of uncontrolled crystal growth. The solvent to antisolvent ratio, stabiliser concentration, and sonication time were optimised and shown to significantly affect both PS and PDI, as previously discussed in § 5.3.1.3.1. The final particle size lies within the optimal range for nanosuspensions (<500 nm).

5.3.4.3. Zeta potential

The AZI-NS-OPT exhibited a zeta potential (ZP) of –28.3 ± 5.6 mV, measured on the day of manufacture using a 10 mM sodium chloride in HPLC grade water as the dispersion medium. The moderately high negative surface charge suggests that the system is stabilized to resist aggregation and sedimentation over time. The negative value can be attributed to the adsorptive behaviour of Tween®80, a non-ionic surfactant onto the surface of the AZI nanocrystals. Tween®80 does not ionize in solution, its polar structure may still influence the formation of an electrical double layer at the particle to water interface, thereby contributing to the net surface charge [180,181].

In nanoparticle formulations, a ZP value exceeding ±30 mV is cited as the minimum threshold for colloidal stability. The use of PVP K30 and Tween®80 provides an additional steric barrier, reducing the likelihood of particle collision and aggregation, even though the ZP does not cross the ±30 mV. The ZP value observed for AZI-NS-OPT is thus considered adequate for long-term colloidal stability, when interpreted with the PDI = 0.298 ± 0.012 observed in the same formulation. These parameters suggest that the AZI-NS-OPT system is both electrokinetically and sterically stabilized, with repulsive forces to maintain nanocrystal dispersion over time [180].

5.3.4.4. Drug loading capacity (LC)

The AZI-NS OPT exhibited a drug loading capacity of 3.23 ± 1.21%, indicating that a relatively small proportion of the formulation mass consisted of active drug. This drug loading was considered acceptable for early-stage formulation, as it helped reduce material use. Despite the

modest value, the loading achieved was sufficient to meet the intended objectives of enhancing dispersibility and solubility at the intended particle size.

5.3.4.5. Polymorphism

5.3.4.5.1. FT-IR characterisation

FTIR was used to assess the crystallinity nature of the optimised AZI nanosuspension. The spectra of the individual excipients (PVP K30 and Tween®80) and AZI were compared to that of the final nanosuspension formulation (Figure 5.25). Reference spectra of PVP K30, Tween®80, and AZI are shown in Figures 4.4, 4.6, and 4.5 respectively. The optimised formulation retained the characteristic bands of all three components. The sharp peaks vibrations of AZI (–OH stretch at 3561 cm^{-1} and the lactone C=O at 1726 cm^{-1}) were present but slightly broadened and of reduced intensity, suggesting dispersion of AZI within the nanosuspension. The broad absorption bands of PVP K30 (amide C=O at 1645 cm^{-1} and O–H at 3395 cm^{-1}) remained unchanged, indicating that the polymer retained its structure and did not undergo crystallisation during processing. The spectrum of Tween®80 also displayed the ester C=O and C–O ether stretches, which remained visible in the final formulation. The band intensity of the optimised nanosuspension spectrum was lower and less defined compared to pure crystalline AZI. This reduction in intensity supports the partial amorphization of AZI, likely due to surface adsorption onto PVP K30 and Tween®80 during precipitation. The absence of new functional group bands or major shifts indicates that the formulation is chemically stable, with no evidence of degradation or new interactions.

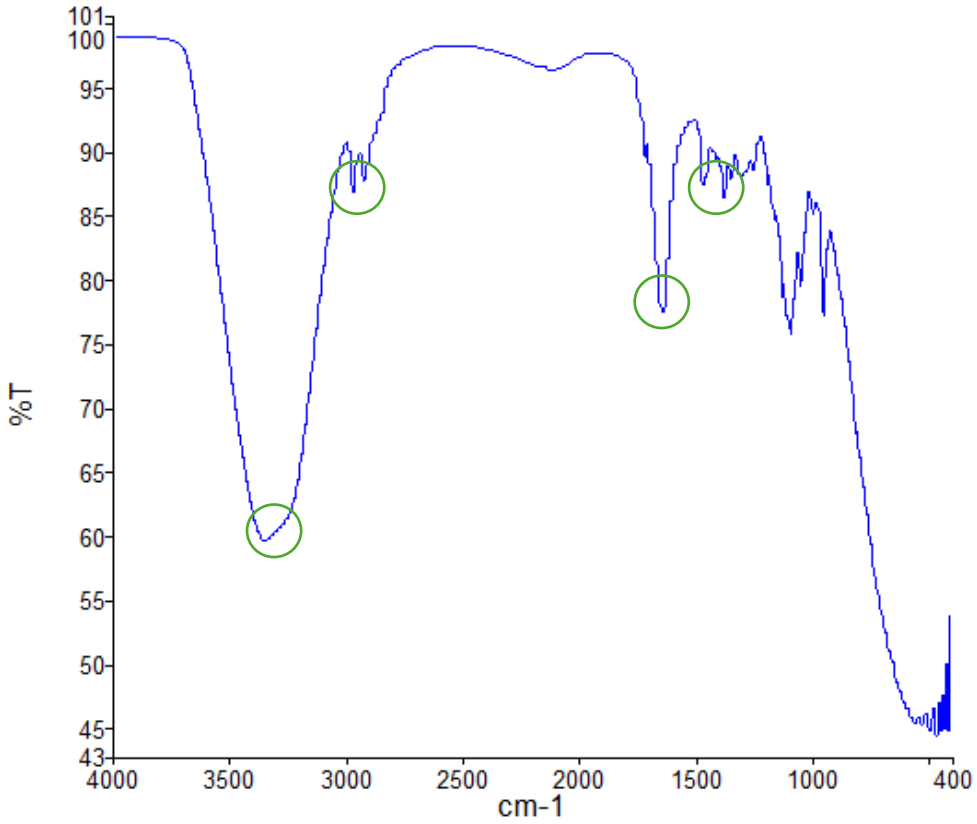

Figure 5.25. FTIR profiles of optimised AZI nanosuspension.

5.3.4.6. Shape and surface morphology

5.3.4.7. Transmission electron microscopy

TEM was used to examine the morphology, and size distribution of the optimised AZI nanosuspension. The TEM micrographs presented in Figures 5.26 and Figure 5.27 illustrate both high resolution and low-resolution views, providing insights into particle structure at different scales. Figure 5.26 presents a high-resolution TEM image of the AZI-NS-OPT nanoparticles. The particle is distinctly observed in the centre of the image, with dark contrast indicative of a dense, drug-rich core. The visible lattice fringes within the nanoparticle suggest crystal formulation. The interplanar spacing observed from these fringes supports the conclusion that AZI exists in a crystalline form following solvent-antisolvent precipitation. The surrounding matrix appears amorphous, which are attributed to the presence of the stabilisers,

Tween®80 and PVP K30 adsorbed at the particle interface. This image confirms that the optimised formulation successfully produced discrete, nanosized crystalline drug entities.

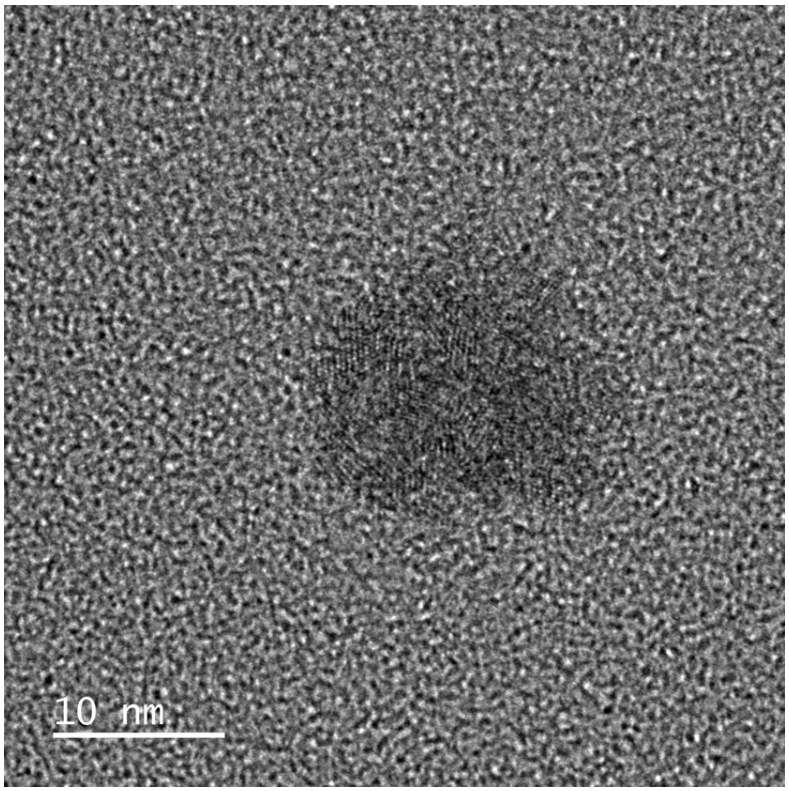

Figure 5.26. High resolution TEM micrograph of the optimised AZI nanosuspension (Scale: 10 nm).

Figure 5.27 depicts a lower magnification TEM image showing multiple nanoparticles. The particles are spherical to near spherical in morphology, with sizes under 200 nm. The presence of individual, well separated nanoparticles indicates good dispersion stability under TEM sampling conditions, consistent with the low polydispersity index. The morphology remains consistent with expected nanosuspension characteristics, suggesting that the formulation method yielded uniform, non-rod-like particles without irregular agglomerates.

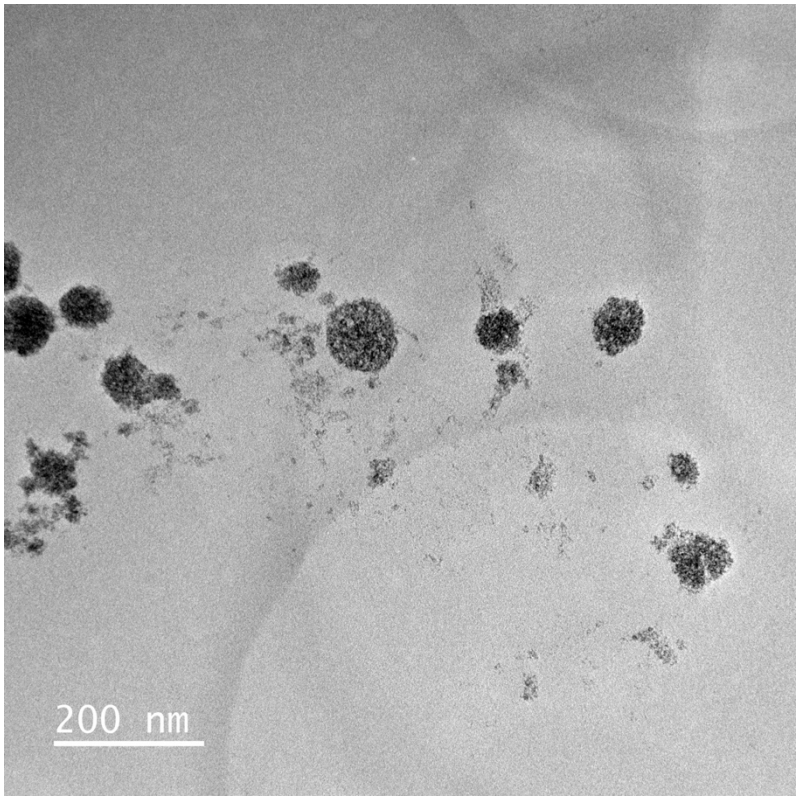

Figure 5.27. Low resolution TEM micrograph of the optimised AZI nanosuspension (Scale: 200 nm).

5.3.4.8. *In vitro* release

5.3.4.8.1. Comparison of AZI release

Figure 5.28 presents the *in vitro* release profile of AZI from the optimised nanosuspension compared to a commercial AZI suspension over a 60-minute period (n = 3). The AZI-NS-OPT demonstrated an enhanced dissolution rate across all time points, as seen by an initial burst release followed by a plateau phase indicating rapid saturation. At 5 minutes, the nanosuspension released 76.5% of its drug content, compared to only 28.19% from the commercial suspension. This initial burst release from the nanosuspension is a due to nanosized drug particles and has a high surface area to volume ratio, which promotes faster wetting and dissolution. This difference in release behaviour is due to the particle size reduction in AZI-NS-OPT (134.3 ± 4.6 nm), which enhances dissolution by increasing surface area in accordance with the Noyes–Whitney equation. The presence of surface-active agents, Tween®80 and PVP K30 contributes to improved wettability and dispersion of AZI nanocrystals in the dissolution medium.

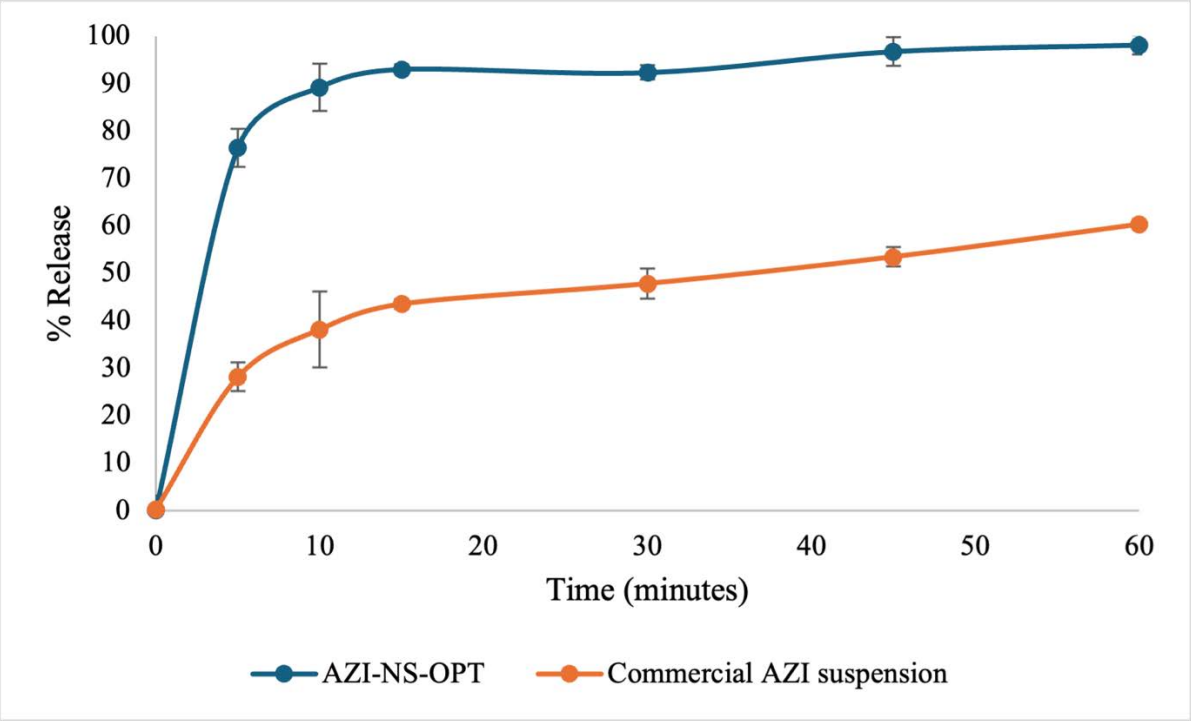

Figure 5.28. *In vitro* release profile of AZI from the optimised AZI nanosuspension versus commercial AZI suspension (n=3).

5.3.5. Stability testing

Following the successful formulation and characterisation of the AZI-NS-OPT, it was essential to evaluate its stability under controlled environmental conditions. Stability testing plays a pivotal role in determining the shelf life, storage requirements, and overall reliability of pharmaceutical products [92]. For nanosuspensions, particle size, PDI, and zeta potential are sensitive and must remain within acceptable limits to ensure consistent performance and patient safety [182]. Stability studies were performed under both intermediate (25 ± 2 °C/60 ± 5% RH) and accelerated (40 ± 2 °C/75 ± 5% RH) conditions over an 8-week period to simulate real world and stress storage environments [92]. These conditions predict the formulation's behaviour over time and support the appropriate shelf-life specifications.

5.3.5.1. Particle size and size distribution

The PS and PDI of the AZI-NS-OPT following storage at 25°C/60% RH and 40°C/75% RH is shown in Figures 5.29 and 5.30 respectively.

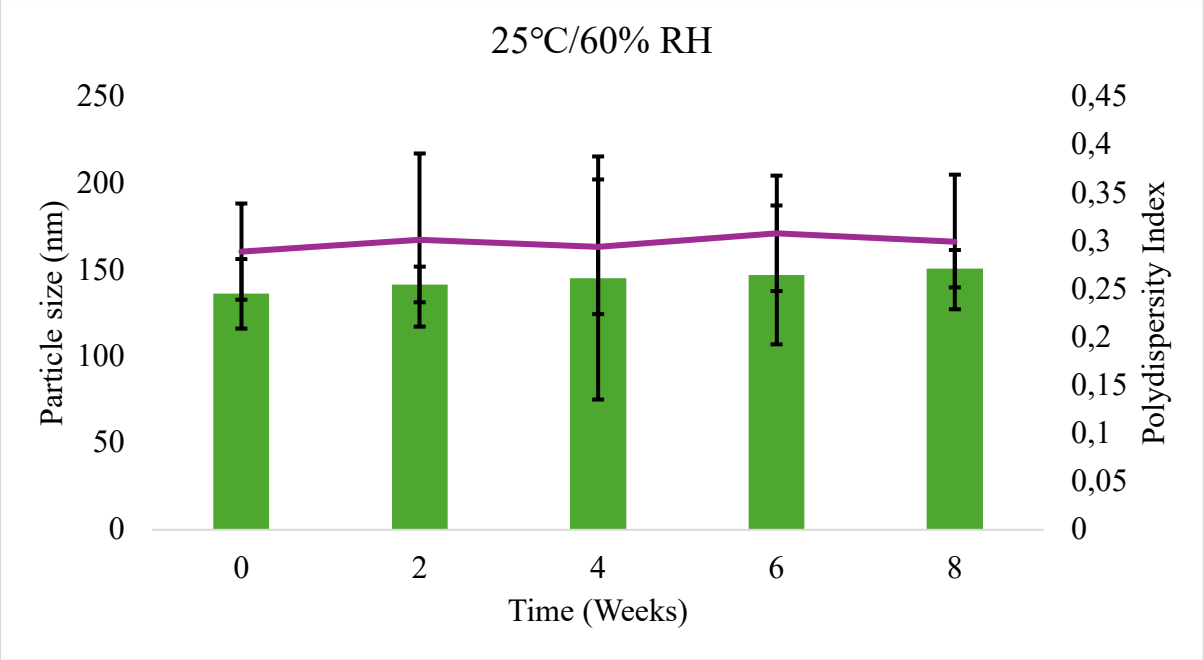

Figure 5.29. Particle size and size distribution of AZI-NS-OPT at storage of 25°C/60%RH

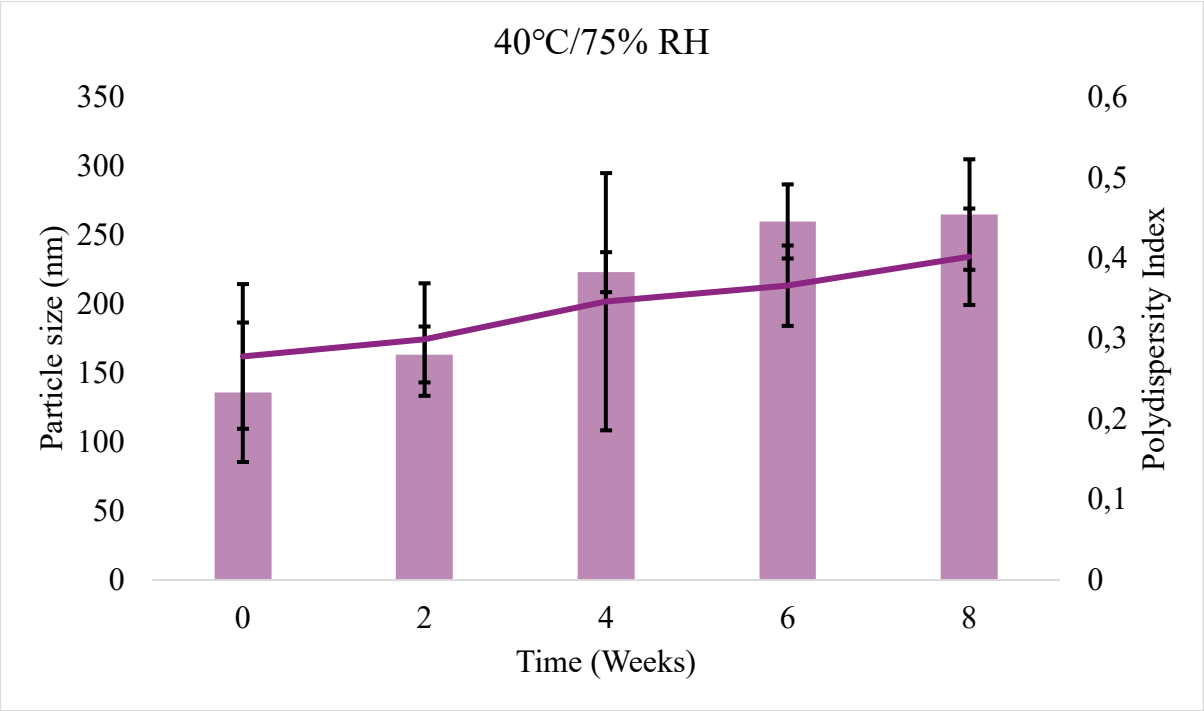

Figure 5.30. Particle size and size distribution of AZI-NS-OPT at storage of 40°C/75%RH

At 25°C/60% RH, AZI-NS-OPT exhibited minimal fluctuation in PS, with values increasing only slightly from 136.2 nm at week 0 to 150.7 nm at week 8. Throughout the storage period,

the PDI remained relatively stable between 0.289 and 0.299, suggesting a uniform size distribution and absence of significant aggregation or Ostwald ripening. These results confirm that the formulation maintained colloidal stability under intermediate conditions, reflecting a favourable shelf-life profile for products stored at controlled room temperature.

Accelerated storage conditions (40°C/75% RH) triggered a gradual increase in both PS and PDI. The mean particle size increased from 136.2 nm at week 0 to 265.1 nm at week 8, while PDI rose from 0.278 to 0.402, indicating a broader size distribution. This destabilization can be attributed to thermal stress (excess kinetic energy), which compromises the microscopic viscosity of the surfactant layer surrounding the particles [183,184]. At elevated temperatures, the local viscosity around the nanoparticles decreases, reducing the resistance to particle movement [185,186]. This enhances Brownian motion by and increases the frequency of particle-to-particle collisions per unit time, leading to coalescence, increased crystal growth, and perikinetic aggregation [185,186].

5.3.5.2. Zeta potential

The ZP of the AZI-NS-OPT following storage at 25°C/60% RH and 40°C/75% RH is shown in Figures 5.31 and 5.32 respectively.

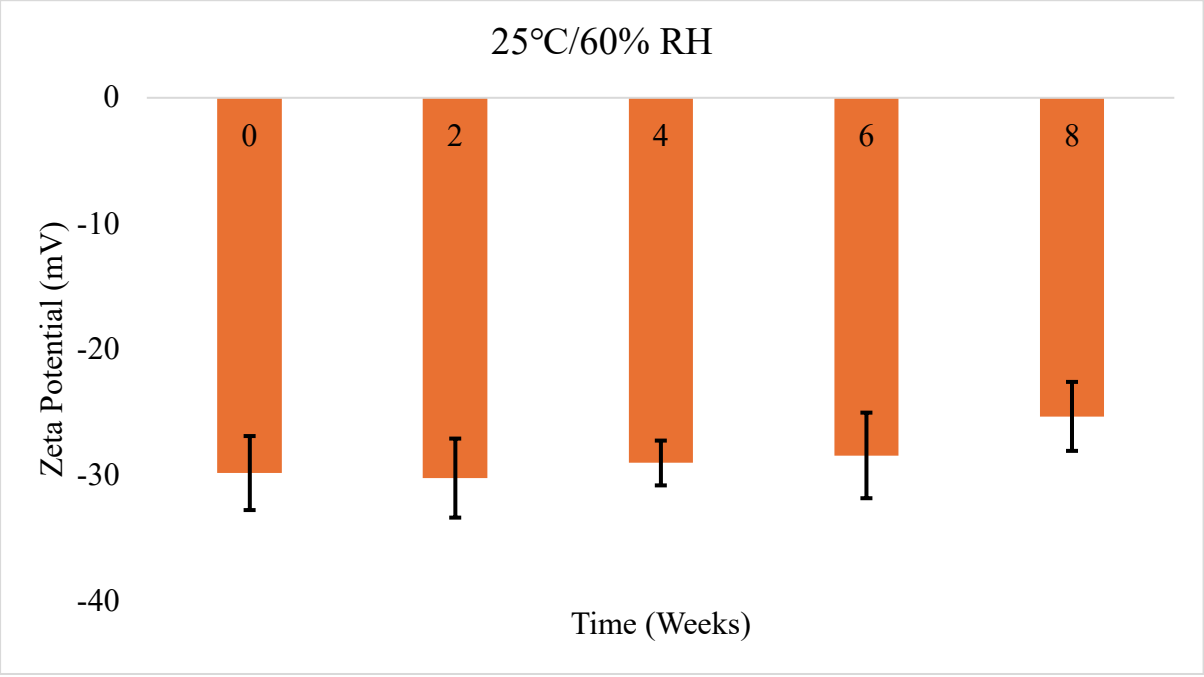

Figure 5.31. Zeta potential of AZI-NS-OPT at storage of 25°C/60%RH

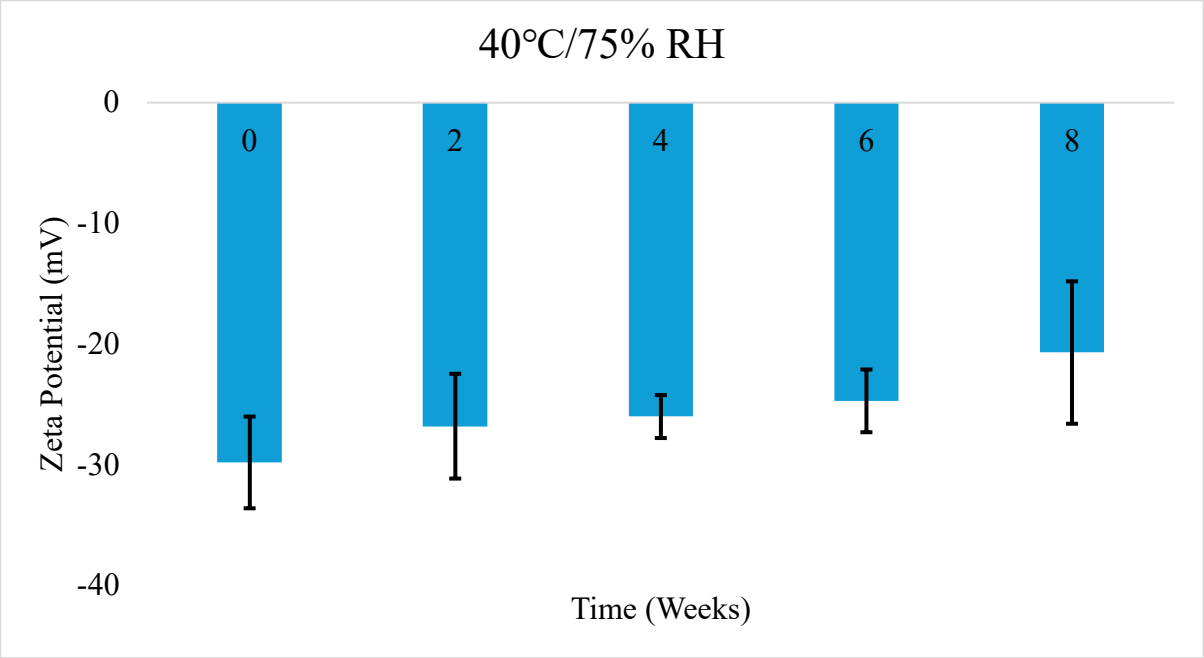

Figure 5.32. Zeta potential of AZI-NS-OPT at storage of 40°C/75%RH

AZI-NS-OPT formulation exhibited a consistently negative ZP, fluctuating between −29.8 mV and −25.3 mV throughout the 8-week period. This stability indicates robust electrostatic repulsion between particles, effectively preventing aggregation. The maintenance of ZP values aligns with the observed stability in PS and PDI under these conditions, confirming the formulation's physical stability.

At accelerated storage conditions, this led to a gradual decrease in the magnitude of the ZP, from −29.8 mV at week 0 to −20.7 mV at week 8. The observed ZP decline suggests a reduction in electrostatic repulsion, which compromises colloidal stability over time rendering the system more prone to particle aggregation and instability. The thermal stress can lead to partial desorption of the surfactant layer. Elevated temperatures can also promote increased molecular motion and disrupt hydrogen bonding interactions that contribute to surface stabilization [185,186]. The increased humidity at 75% RH may lead to changes in the ionic strength of the dispersion medium, which compresses the electrical double layer surrounding each particle [1].

This observed reduction in ZP under stress conditions aligns with the previously reported increase in PS and PDI in § 5.3.5.1, suggesting that the loss of electrostatic repulsion contributes to progressive particle aggregation. These results suggest that strict control of storage conditions is essential to preserve formulation stability.

5.3.5.3. Loading capacity

The drug loading capacity of the AZI-NS-OPT following storage at 25°C/60% RH and 40°C/75% RH is shown in Figures 5.33 and 5.34 respectively.

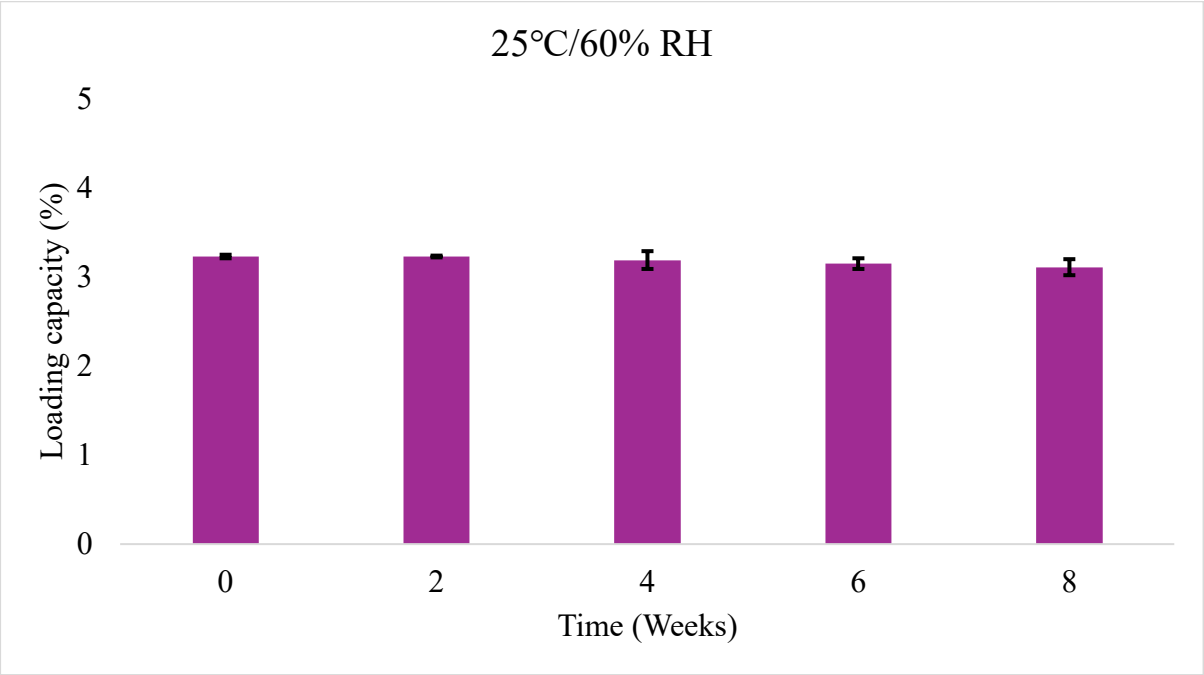

Figure 5.33. Loading capacity of AZI-NS-OPT at storage of 25°C/60%RH

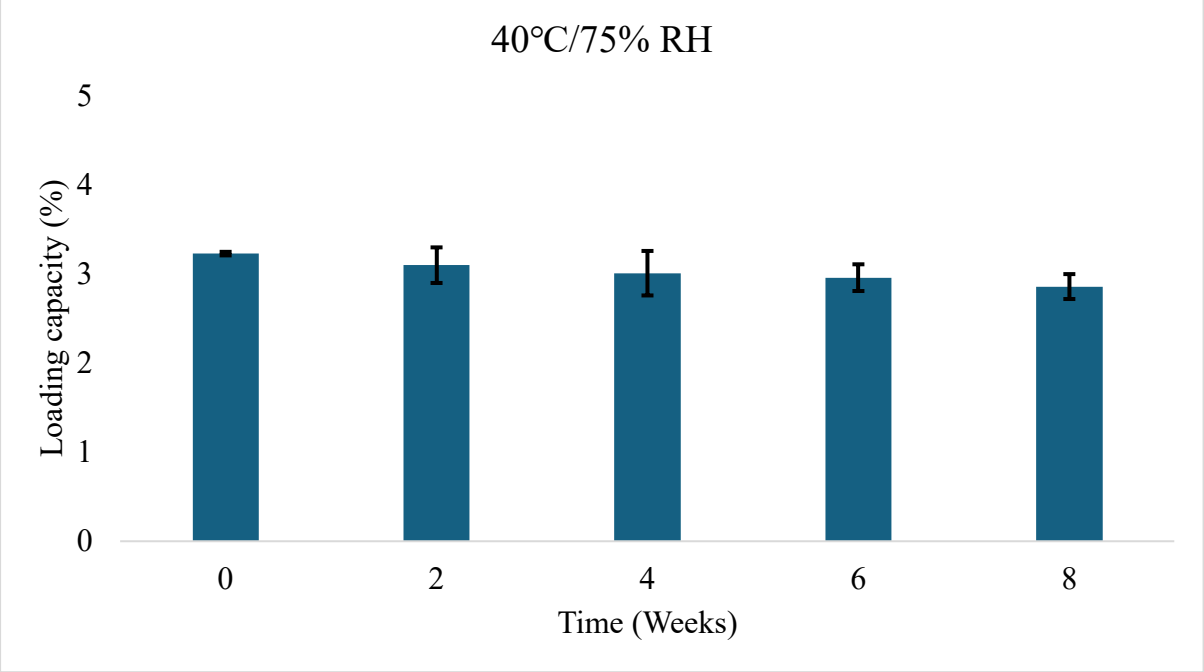

Figure 5.34. Loading capacity of AZI-NS-OPT at storage of 40°C/75%RH

Under intermediate conditions (25 °C/60% RH), the AZI-NS-OPT formulation exhibited minimal fluctuation in loading capacity, remaining relatively stable around 3.23% ± 1.21%. There were no statistically significant reductions observed, suggesting that the nanosuspension maintained drug loading efficiency and was not prone to crystallisation, or degradation under room temperature storage. This stability implies that the combination of Tween®80 and PVP K30 was effective in sustaining the colloidal matrix and maintaining sufficient interaction with the AZI molecules.

A trend was noted under accelerated storage conditions (40 °C/75% RH). As shown in Figure 5.34, the loading capacity gradually decreased over time, from an initial value of 3.23% at week 0 to around 2.86% by week 8. This indicates thermal and humidity destabilization, which can promote drug desorption, diffusion out of the polymer-surfactant matrix. Elevated temperatures increase molecular mobility within colloidal systems, disrupting hydrophobic interactions that retain the drug within the nanosuspension [185,186]. The high RH can facilitate water ingress into the system, altering microscopic viscosity and further destabilizing the drug–surfactant interface [185,186]. This trend is consistent with the concurrent increase in PS and PDI under the same conditions, as well as the observed decrease in ZP.

5.4. CONCLUSIONS

The development, optimisation, and characterisation of an AZI nanosuspension using a solvent antisolvent precipitation technique supported by DoE via a Box Behnken design was successfully described in this chapter. The formulation strategy aimed to overcome the limitations associated with conventional AZI suspensions, poor aqueous solubility, slow dissolution, and limited bioavailability. By reducing the PS of AZI into the nanometer range and stabilizing it with Tween®80 and PVP K30, the formulation enhanced drug wettability, surface area, and dispersion stability.

The optimisation process done by RSM identified formulation and process parameters that influenced quality attributes, PS, PDI, ZP, and initial drug release rate. The AZI-NS-OPT exhibited a mean PS of 134.3 ± 4.6 nm and a PDI of 0.298 ± 0.012, indicating a monodisperse and physically stable formulation. ZP values around –28.3 mV confirmed the presence of electrostatic repulsion, further strengthened by steric stabilization from the Tween®80 and PVP

K30. The drug loading capacity of 3.23 ± 1.21% was considered adequate for early-stage development and demonstrated drug loading efficiency without excessive drug loss.

In *vitro* release studies confirmed an enhancement in dissolution rate compared to a commercial AZI suspension, with over 76% drug release observed within the first 5 minutes. Kinetic modelling revealed that the release followed Higuchi diffusion-controlled mechanism, indicating that drug release was governed by gradual diffusion from the nanocrystal surface. The use of mathematical modelling provided an insight into the diffusion pathway, validating the performance of the nanosuspension.

Stability studies conducted under both intermediate (25 °C/60% RH) and accelerated (40 °C/75% RH) conditions over 8 weeks demonstrated that the optimised formulation maintained structural integrity and performance under controlled room temperature storage. Minimal changes were observed in PS, PDI, ZP, and loading capacity at 25 °C, indicating strong physicochemical stability. At elevated temperature and humidity, accelerated the deterioration of these parameters, which was attributed to thermal stress, reduced microscopic viscosity in the stabiliser matrix, and partial desorption of the surfactant layer. These changes were consistent with Ostwald ripening, and weakening of the electrical double layer, leading to aggregation, as supported by literature.

The findings from this chapter confirm that the solvent antisolvent approach, in combination with rational design and statistical optimisation, can yield a stable nanosuspension of AZI. The formulation showed promising improvements in dissolution behaviour, colloidal stability, and drug release kinetics. These results justify further evaluation of the nanosuspension in biological models and support its potential for scale up and commercial application.

CHAPTER 6

TASTE MASKING AND EVALUATION OF AZITHROMYCIN NANOSUSPENSION USING AN ELECTRONIC TONGUE

6.1. INTRODUCTION

AZI is a macrolide antibiotic used to treat bacterial infections. Despite its clinical effectiveness, one of the major issues with its extremely bitter taste, which reduce patient adherence to therapy [187–189]. Taste perception is a complex process that involves the interaction of dissolved drug molecules with taste receptors on the tongue, leading to the activation of sensory pathways [187–190]. This challenge becomes more of a problem in nanosuspensions, where the increased surface area of the particles enhances dissolution in saliva and increase receptor exposure, worsening the bitterness [187].

To address this, various taste masking strategies have been developed. like microencapsulation and lipid nanoparticles, pH buffering, complexation, or ion-exchange [187–189]. To test new formulations, in *vivo* human taste panels have been used. While effective, they are limited by subjectivity, ethical concerns, and variability [187–190]. In *vitro* techniques like the electronic tongue offer a modern solution for providing reproducible, rapid, and non-invasive evaluation of taste profiles [187–190]. This chapter explores the principles of taste perception, the taste masking strategies, and the use of the electronic tongue system to evaluate the in *vitro* taste profile of an AZI nanosuspension, buffered at different pH's.

6.2. PRINCIPLES OF TASTE PERCEPTION

Taste, or gustation, is a highly complex sensory system that allows organisms to evaluate the chemical composition of substances entering the oral cavity [191]. Taste is the brain's interpretation of molecular interactions occurring in the oral environment. Taste begins when soluble molecules interact with epithelial sensory cells called gustatory receptor cells, which is located on the tongue's papillae [192,193]. These molecules must be water soluble to move into the salivary medium and activate the receptors. Once activated, these cells transduce chemical energy into electrical impulses that travel via cranial nerves (CN) VII, IX, and X (facial, glossopharyngeal, and vagus) to the gustatory cortex of the brain [193,194].

Taste sensations are classified into five categories, sweet, salty, sour, bitter, and umami as shown in Figure 6.1 [194,195]. Sweet represents richness like sugar and salty signals the electrolyte presence [194,195]. Sour is associated with acidity and rancid foods while bitterness is a signal that protects the body from toxic compounds like API's (AZI) [194,195]. Umami represents amino acid or protein presence [191,194,195]. Taste perception is quantitatively and qualitatively influenced by concentration of the stimulus, salivary pH and composition, surface area, rate of dissolution, temperature, expectation, prior experience, and cultural background [7,8]. Taste is not the equivalent to flavour. Flavour is a multisensory experience that combines taste, smell (olfaction), texture [196].

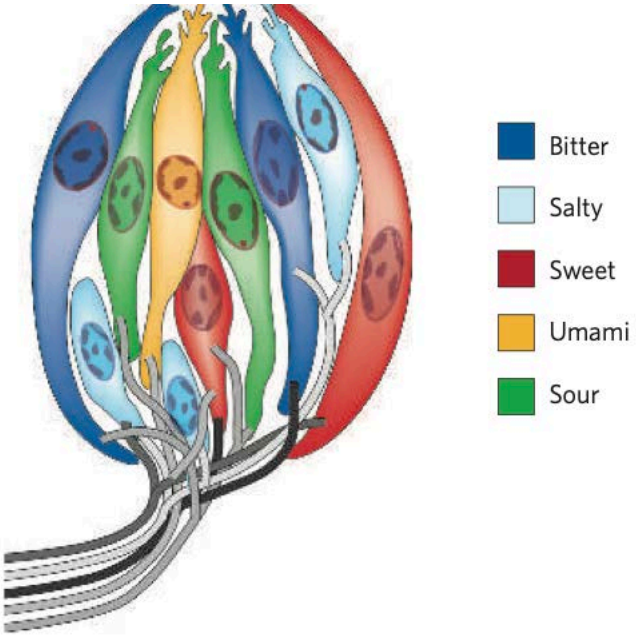

Figure 6.1. Cellular organisation of the taste receptor cells on the taste bud (Adapted from [191]).

6.2.1. Anatomy and physiology of the taste buds

The taste bud is a neuroepithelial organ that represents the structural unit of gustation. Each taste bud functions as a biochemical sensor designed to breakdown molecular signals from food, drugs, and environmental stimuli into neural impulses interpreted by the gustatory cortex [191]. Taste buds are localized within four types of lingual papillae, fungiform, foliate, circumvallate, and filiform (Figure 6.2). Fungiform papillae are located on the anterior two thirds of the tongue that contain 1–5 taste buds each and are among thermal receptors [191]. Foliate papillae are found on the posterolateral of the tongue that contain taste buds within epithelial clefts, most common in children [180,191,192]. Circumvallate papillae are arranged

in a V-shaped row at the posterior tongue [180,191,192]. Filiform papillae lack taste buds and serve as mechanical functions [180,191,192].

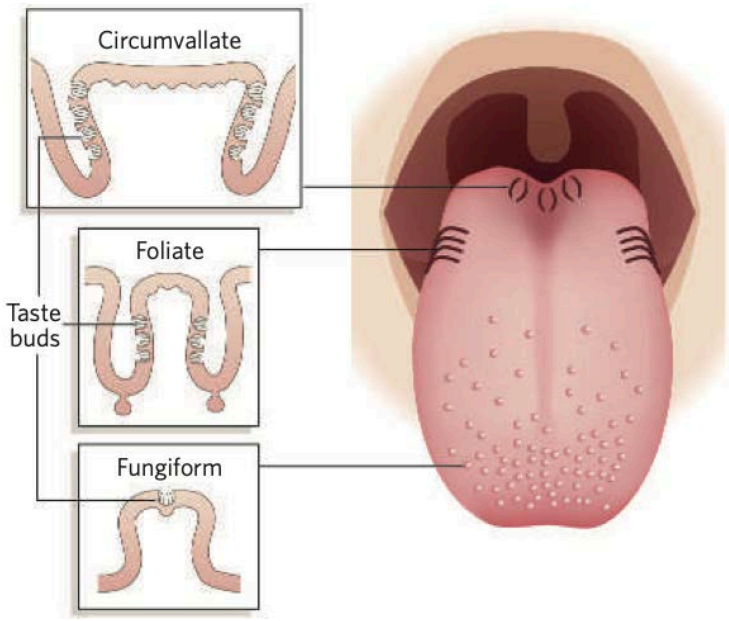

Figure 6.2. Anatomical distribution and structure of the taste bud papillae on the tongue. (Adapted from [191]).

Each taste bud is a cluster of 50–100 specialized cells. Type I are Glial like cells which are responsible for scavenging extracellular potassium and neurotransmitters and structurally supporting the bud [197]. Type II are receptor cells, which detect sweet, umami, and bitter stimulants using G-protein coupled receptors (GPCRs) [197]. These cells lack synapses but release adenosine triphosphate (ATP) via pannexin and calcium homeostasis modulator 1 (CALHM1) channels to activate neighbouring cells [197]. Type III is presynaptic cells which respond to sour and salty stimuli [197]. These cells form synapses and release neurotransmitters such as serotonin and gamma aminobutyric acid (GABA) [197]. Type IV are basal cells regenerates all taste cell types on a turnover cycle of approximately 10 days [197]. The apical microvilli of Type II and III cells protrude into the taste pore, where they are exposed to stimulus molecules dissolved in saliva. This is the first point of biochemical interaction between the molecule and the nervous system. Taste bud activation leads to afferent signalling via CN VII, IX, and X. The CN VII from the chorda tympani branch innervates fungiform papillae [197]. CN IX innervates circumvallate and foliate papillae [197]. CN X carries the taste signals from the epiglottis and pharynx [193]. These nerves connect to nucleus of the thalamus, and to the gustatory cortex [192].

6.2.2. Taste receptors and signal transduction

Type II cells are responsible for detecting sweet, bitter, and umami stimuli. These cells express a family of GPCR, including TAS1Rs, for sweet and umami and TAS2Rs for bitter. TAS2Rs initiate intracellular signalling cascades through the G-protein gustducin. When a tastant molecule binds to GPCR on the apical membrane of a Type II cell (Figure 6.3), it activates a G-protein complex gustducin [191,197]. Upon activation, gustducin dissociates into an alpha subunit and a beta-gamma subunit [191,197]. The beta-gamma subunit is responsible for activating phospholipase C β2 (PLCβ2), while the alpha subunit contributes to signal amplification or modulation [191,197]. PLCβ_2 hydrolyses phosphatidylinositol 4,5-bisphosphate (PIP_2) into two second messengers, inositol 1,4,5-triphosphate (IP_3) and diacylglycerol (DAG). The IP_3 binds to its receptors on the endoplasmic reticulum, causing a release of calcium ions (Ca^{2+}) into the cytoplasm [191,197]. This rise in intracellular calcium concentration activates the transient receptor potential cation channel subfamily M member 5 (TRPM5), a calcium-activated non-selective cation channel [191,197]. TRPM5 permits the influx of sodium and other monovalent cations into the taste receptor cell [191,197]. This movement of positively charged ions, driven by the unequal distribution of ions across the membrane, leads to change in membrane electrical potential [191,197]. This leads to the opening of CALHM1 channels which allow ATP to be released directly into the extracellular space [197,198]. This ATP acts as a fast neurotransmitter, binding to purinergic receptors on afferent sensory nerve fibers, converting the intracellular chemical signal into a neural impulse [197,198].

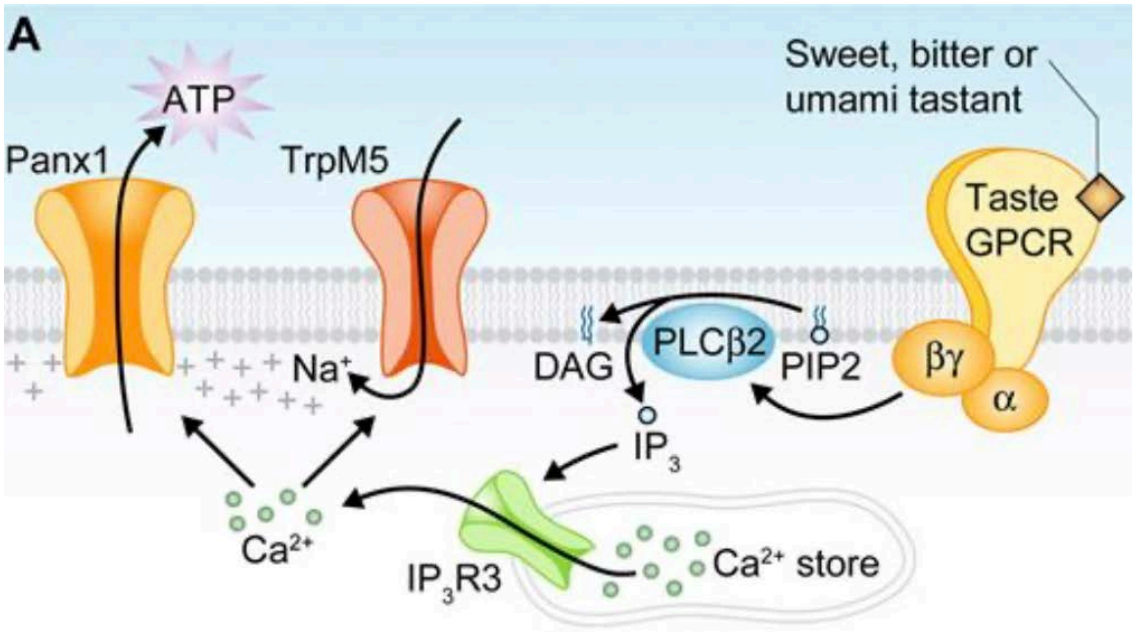

Figure 6.3. Signal transduction pathway in Type II taste receptor cells for sweet, bitter, and umami taste stimulus. (Adapted from [197]).

Sour taste is transduced via Type III cells which form synapses. H^+ ions enter the taste receptor cell through OTOP1 (otopetrin 1) ion channels as shown in Figure 6.4 [191,197]. Proton influx causes change in membrane electrical potential, which activates voltage gated calcium channels located on the membrane. The resulting influx of Ca^{2+} triggers the vesicular release of serotonin (5HT) and GABA, which synaptically stimulate the afferent gustatory neurons [193].

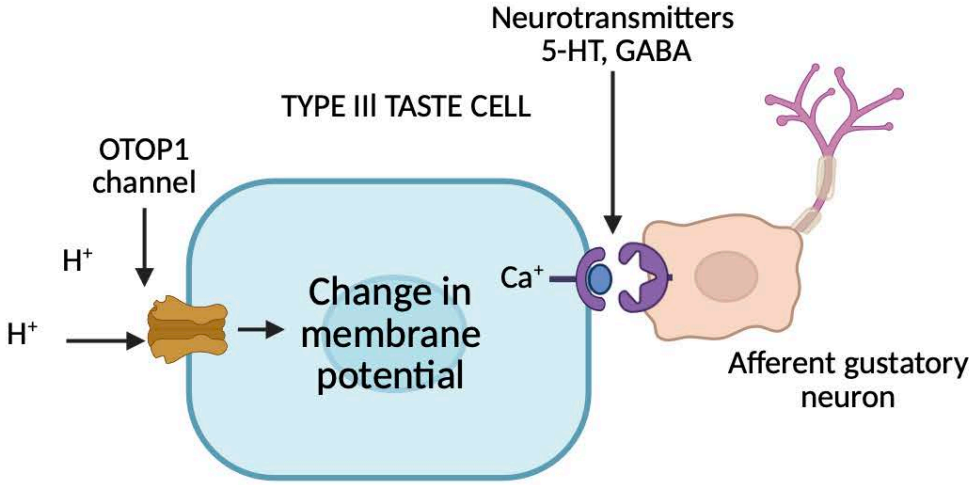

Figure 6.4. Signal transduction mechanism for sour taste from proton channels in Type III taste receptor cells.

The salty taste is mediated through epithelial sodium channels (ENaCs), which are sensitive to sodium ions in low concentrations and are shown in Figure 6.5 [197]. These ionotropic receptors reside on glial like Type I cells. When sodium enters the cell through ENaC channels, it causes direct depolarization of the cell membrane and is involved in non-vesicular communication and can recruit paracrine pathways within the taste bud [197]. Sodium is an essential mineral because it is the major cation of the extracellular fluid and helps maintain the body fluid volume, homeostasis and various cellular functions [197].

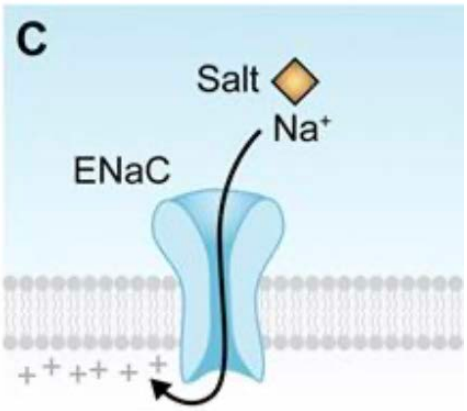

Figure 6.5. Signal transduction pathway of salty taste via ENaCs. (Adapted from [197]).

6.3. TASTE MASKING STRATEGIES

AZI is widely used due to its broad-spectrum antimicrobial activity. However, AZI bitterness makes it a challenging medicine for oral administration, especially in paediatric and geriatric formulations. Effective taste masking is essential not only for patient adherence to therapy but also to ensure consistent dosing. The current taste masking that has been employed on AZI includes, reverse micelles [187], cyclodextrin inclusion complexation, and complexing AZI with polystyrene sulfonate resin, which have all reduced the bitterness of AZI [199]. In this section, taste masking of AZI was approached using a pH-buffered nanosuspension system. By optimizing the formulation to maintain a pH and employing stabilisers like PVP K30 and Tween®80, the immediate drug release into saliva is minimized.

6.3.1. Physical

6.3.1.1. Microencapsulation, SLNs, NLCs, liposomes

Microencapsulation is where drug particles are enclosed within a protective coating, designed to prevent direct interaction with taste buds, reducing unpleasant taste. It is effective for bitter APIs, that are readily soluble in saliva and activate TAS2R bitter taste receptors upon contact [200]. The encapsulating materials used are lipids, polymers, or polysaccharides, due to their ability to either delay drug release or prevent release in the oral cavity [201]. These materials include ethyl cellulose, Eudragit® polymers, alginate, gelatine, and starch derivatives. Microencapsulation can be achieved via spray drying, fluidized bed coating, coacervation, and solvent evaporation [201].

Solid lipid nanoparticles are colloidal carriers composed of solid lipids stabilized by surfactants [202]. They form a solid lipid matrix that entraps the drug, minimising its interaction with taste receptors in the oral cavity [202]. The drug remains embedded within the solid lipid core, its release is delayed until after swallowing [202]. Nanostructured lipid carriers are the second generation of SLNs, developed to overcome their low drug loading capacity [203]. They contain a blend of solid and liquid lipids, resulting in a lipid matrix that accommodates more drug molecules and reduces drug expulsion [203]. Liposomes are phospholipid bilayer vesicles that can encapsulate both hydrophilic drugs and lipophilic drugs [204]. Liposomes shield the drug from saliva, preventing it from interacting with oral taste receptors [204].

6.3.1.2. Polymer coating

Polymer coating involves surrounding the drug particle with a insoluble or pH polymer layer [189]. This physical barrier prevents immediate drug release in the saliva, thus reducing contact between the drug and taste receptors [188]. These polymers include hydroxypropyl methylcellulose, methacrylic acid copolymers (Eudragit®), which are normally based on their solubility [188,189]. Eudragit® E100 is pH sensitive and dissolves only in gastric pH [188,189]. The coating process is done using fluidized bed coating or pan coating, where the drug is sprayed with a polymer solution and dried to form a thin film [205].

6.3.1.3. Solid dispersions

Solid dispersions are one or more APIs are dispersed or finely distributed in a polymer matrix [206]. The taste masking occurs because the drug is trapped in the polymeric matrix, preventing immediate release into saliva and thus reducing interaction with taste receptors [207]. The reduced drug solubility in saliva leads to slower diffusion to taste buds, making bitterness less perceptible during oral administration. Depending on method of preparation, solvent evaporation, hot melt extrusion, or spray drying, the drug may exist in an amorphous state, which contributes to both taste masking and improved bioavailability [200].

6.3.1.4. Viscosity modifiers

Viscosity modifiers, also known as thickeners, are used in oral suspensions to suppress the release of APIs into saliva, thereby reducing interaction with taste receptors [1]. By increasing the viscosity, the diffusion rate of the drug molecules is reduced, limiting their contact with taste buds [188]. Generally Recognised as Safe (GRAS) excipients included are hydroxypropyl methylcellulose, carboxymethylcellulose, xanthan gum, guar gum, acacia, carbomers, poloxamer [208].

6.3.2. Chemical

6.3.2.1. Prodrugs

Prodrugs are pharmacologically inactive derivatives of APIs designed to undergo enzymatic conversion in the body to release the active drug [209]. This strategy is used not only to enhance bioavailability or solubility, but also to mask unpleasant taste. The bitterness of APIs occurs due to free functional groups, such as amines or carboxylic acids [210]. By chemically modifying these groups, the prodrug becomes less soluble in saliva, thereby eliminating the bitter taste. Chloramphenicol palmitate is a prodrug where esterification of the hydroxyl group reduces bitterness without compromising therapeutic action post hydrolysis in the gastrointestinal tract [211].

6.3.2.2. Complexation

Complexation is when an API binds to a complexing agent, reducing its interaction with taste receptors. The most used complexing agents are cyclodextrins, β-cyclodextrin, due to their ability to encapsulate hydrophobic regions of bitter APIs within their hydrophobic cavity while

remaining water soluble [212]. When the API forms a inclusion complex, its free concentration in saliva is reduced, thereby minimising interaction with bitter taste receptors [188]. The complex remains stable in the oral cavity, but dissociates in the gastrointestinal tract, where the drug is released for absorption due to lower pH and enzymatic activity, ensuring therapeutic effect is maintained [213].

6.3.2.3. Ion exchange resins

Ion exchange resins are insoluble polymers containing ionizable functional groups capable of reversibly binding ionic drug molecules through electrostatic interactions [214]. Bitter cationic APIs can be complexed with cation exchange resins, reducing the free concentration in saliva and preventing interaction with taste receptors [214]. The binding efficiency of ion exchange resins depends on pKa, resin type, particle size, swelling capacity, and drug to resin ratio [188].

6.3.2.4. pH buffering

pH adjustment using buffers plays a role in modulating the taste perception of APIs. Bitterness is influenced by the ionization state of the drug molecule. Bitter drugs are weak bases that exhibit stronger receptor interactions when in their unionized form [1]. Ionized molecules, due to their lower membrane permeability, interact less with bitter taste receptors [215]. By buffering the pH of the oral formulation to a range where the drug remains ionized can reduce bitterness. pH buffering becomes essential due to the enhanced surface area of drug particles. Buffering helps mitigate this issue by stabilizing the ionization equilibrium, thus minimising the concentration of free base available to interact with receptors [216]. An advantage of using buffers over traditional flavourings or sweeteners is that they do not alter caloric content, or viscosity of the suspension [217]. pH buffering was the preferred technique that was used in this chapter.

6.4. EVALUATION OF TASTE

6.4.1. *In vivo*

In *vivo* evaluation of taste involves the direct assessment of a pharmaceutical product's taste by human subjects, under controlled experimental conditions [218]. Taste perception is a complex topic as it depends on chemical, physiological, and psychological factors. In *vivo* methods provide palatability, mouthfeel, aftertaste, and flavour masking attributes that in *vitro*

methods may fail to capture fully [188]. The most common and validated approach is the human taste panel method, in which trained or untrained volunteers are asked to evaluate taste on a standardized scale, a hedonic scale ranging from “extremely unpleasant” to “extremely pleasant” [188,218]. The product is placed on the tongue for a specific exposure time, followed by rinsing with water [218]. Subjects are then asked to record their perceived intensity of bitterness. To minimize inter-subject variability, crossover designs are often used, where the same subjects evaluate both the test and reference formulations in randomized order [218].

6.4.2. *In vitro*

In *vitro* evaluation of taste using the electronic tongue (e-tongue) offers an ethical alternative to human sensory panels for assessing the bitterness and palatability of pharmaceutical formulations [190,218]. The e-tongue mimics human gustatory systems through biosensor arrays that respond to chemical stimuli in a manner similar to taste receptors, allowing quantitative and qualitative assessment of taste profiles without relying on subjective human interpretation [190,218]. The e-tongue is a multisensor system that translates chemical information into digital signals, using potentiometric, voltametric sensors [190,218]. Each sensor is coated with a lipid/polymer membrane that simulates the lipid matrix of biological taste receptor cells [190,218]. When a sample interacts with these membranes causes a change in membrane potential. This shift is recorded and interpreted through statistical models, principal component analysis (PCA), producing a taste fingerprint [190,218].

6.5. ELECTRONIC TONGUE ANALYSIS IN THE TASTE EVALUATION OF AZI NANOSUSPENSION

6.5.1. Sample preparation

All samples were equilibrated and stabilized to room temperature 24 hours prior to analysis. Measurements were conducted in triplicate. Each sample was placed into a 25 mL beaker, ensuring immersion depth for sensor exposure. Between samples, the sensors were rinsed with HPLC grade water. All reagents were of analytical grade. Glassware used in all procedures was Grade A, and dilutions were performed using HPLC grade water as outlined in Chapter 2 (§ 2.3.3.1).

6.5.1.1. Optimised AZI nanosuspension

Six batches of AZI nanosuspensions were formulated with a constant drug load (100 µg/mL) and excipient composition, varying only in pH (5.0, 5.5, 6.0, 6.5, 7.0, and 7.5) to study the effect of buffering on reducing bitterness. pH adjustments were performed using potassium dihydrogen orthophosphate buffers, prepared and standardized in accordance with Chapter 2 (§ 2.3.3.4). These pH variant nanosuspensions were labelled as AZINSPH5, AZINSPH55, AZINSPH6, AZINSPH65, AZINSPH7, AZINSPH75. Each sample was diluted with HPLC grade water to achieve a final AZI concentration of 100 µg/mL.

6.5.1.2. Placebo nanosuspension

A control formulation composed of all excipients used in the nanosuspension, but excluding AZI, was prepared and diluted. This sample was used to determine the baseline taste response contributed by the excipient system alone and served as the non-API control.

6.5.1.3. Pure AZI solution

A solution of unformulated AZI was prepared in ethanol and HPLC grade water at 100 µg/mL to serve as the bitterness reference standard. This sample allowed direct assessment of the APIs intrinsic aversiveness and was used to benchmark all other formulations.

6.5.1.4. Buffer only samples

Phosphate buffer solutions at pH 5.0, 5.5, 6.0, 6.5, 7.0, and 7.5 were prepared using potassium dihydrogen orthophosphate and sodium hydroxide. Each buffer sample was diluted and analysed independently to ensure that buffering agents themselves did not contribute to sensor interference. These were used to validate observed taste masking was due to formulation effects and not buffer interference.

6.5.1.5. Commercial AZI suspension

A commercially available AZI suspension was reconstituted, then diluted with HPLC grade water to match a final drug concentration of 100 µg/mL. This reference sample served as the market standard control, allowing comparison of the optimised nanosuspensions with a clinically accepted formulation.

6.5.2. Instrument

The e-Tongue system used in this study was the ALPHA-ASTREE® model (Alpha MOS, Toulouse, France), equipped with a 48 position autosampler. The sensor array is comprised seven ChemFET (chemical field effect transistor) liquid sensors, designated by the manufacturer as AHS, PKS, CTS, NMS, CPS, ANS, and SCS, with a silver/silver chloride (Ag/AgCl) reference electrode. Each sensor exhibited selective sensitivity. SCS is bitterness, ANS is sweetness, AHS is sourness, CTS is saltiness, NMS is umami, while PKS and CPS served as general sensors. The measurement procedure is 2 minutes per sample, followed by a 1-minute wash cycle using HPLC grade water to prevent cross contamination. To ensure sensor stabilization and reproducibility, eight repeated measurements were conducted for each sample, with data from the middle three replicates used for analysis.

6.6. RESULTS AND DISCUSSION

6.6.1. Analysis

To investigate how pH affects the taste masking performance of AZI nanosuspensions, a comparative evaluation was conducted using principle component analysis (PCA), sensor response bar graphs, and radar plots for samples formulated at pH 5.0 to 7.5.

Figure 6.6 presents the PCA plot for AZINSP samples at different pH values. The analysis demonstrates a clear progression in sensor response clustering as pH increases from 5.0 to 7.5. The increasing separation between clusters, along PC1, suggests growing dissimilarity in the taste profile. AZINSPH5 samples group furthest from the commercial formulation and placebo, indicating a unique and strongly masked sensory profile. This suggests that minimal acidification achieved using phosphate buffers, may reduce bitterness perception [218]. Previous studies have shown that ionized drug species are less likely to interact with TAS2R bitter receptors [218].

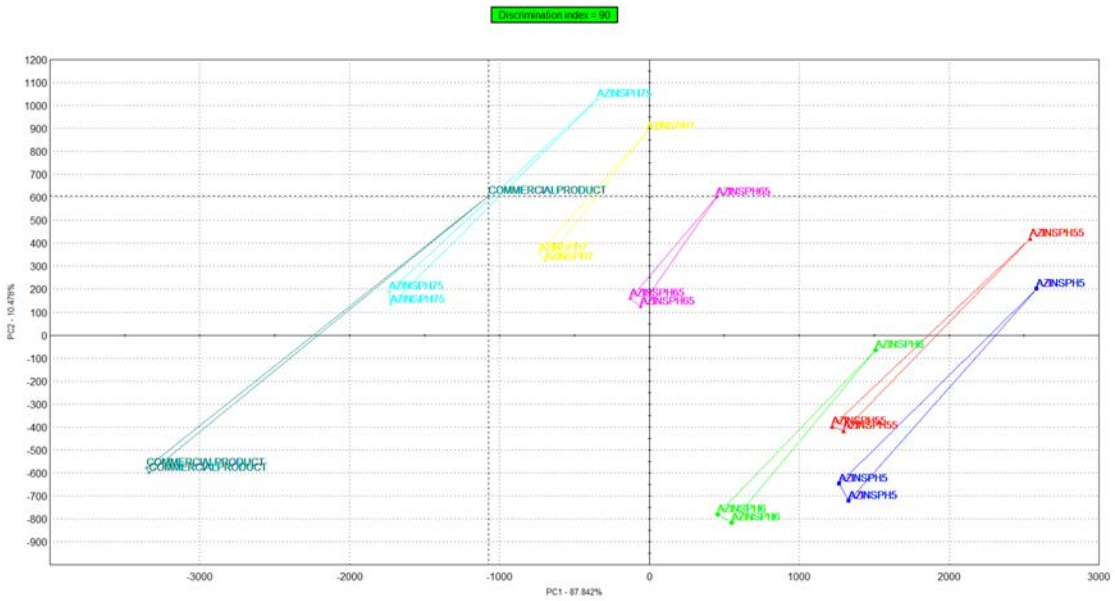

Figure 6.6. PCA plot of AZI nanosuspensions at varying pH's (5.0 - 7.5) versus placebo, pure drug and a commercially available product.

Table 6.1 shows the distance values and pattern discrimination index (%) for each pH formulation versus the commercial product. The distance between AZINSPH5 and the commercial product is the highest (81.7), accompanied by a discrimination index of 81.7%, confirming a high degree of taste profile differentiation. This supports the PCA findings and highlights pH 5.0 as potentially the most effective for taste masking AZI.

Figure 6.7 depicts the mean sensor responses across all taste profiles. From the sensors AHS (sourness), ANS (sweetness), and SCS (bitterness), AZINSPH5 showed the lowest response on the SCS channel, indicating the most effective bitterness taste masking including better than the commercial product. A modest elevation in ANS suggests a relatively improved sweetness profile, while reduced AHS values point toward minimal sourness.

Table 6.1. Distance table and pattern discrimination indices (%) between AZI nanosuspensions (pH 5.0 - 7.5) and the commercial product.

Product Name	Reference Sample	Distance	P Value	Pattern Discrimination Index (%)
AZINSPH5	AZINSPH55	4.19	0	4.19
AZINSPH5	AZINSPH6	32.5	0	32.5
AZINSPH5	AZINSPH65	70.36	0	70.36
AZINSPH5	AZINSPH7	79.54	0	79.54
AZINSPH5	AZINSPH75	80.39	0	80.39
AZINSPH5	COMMERCIAL	81.7	0	81.7
AZINSPH55	AZINSPH65	67.93	0	67.93
AZINSPH55	AZINSPH7	78.27	0	78.27
AZINSPH55	COMMERCIAL	81.59	0	81.59
AZINSPH55	AZINSPH65	58.64	0	58.64
AZINSPH55	COMMERCIAL	81.54	0	81.54
AZINSPH6	AZINSPH5	58.64	0	58.64
AZINSPH6	AZINSPH75	73.26	0	73.26
AZINSPH6	COMMERCIAL	75.79	0	75.79
AZINSPH6	AZINSPH7	78.57	0	78.57
AZINSPH6	AZINSPH65	38.42	0	38.42
AZINSPH65	AZINSPH75	56.61	0	56.61
AZINSPH65	COMMERCIAL	69.48	0	69.48
AZINSPH65	AZINSPH75	28.09	0	28.09
AZINSPH7	COMMERCIAL	58.77	0	58.77
AZINSPH75	COMMERCIAL	34.43	0	34.43

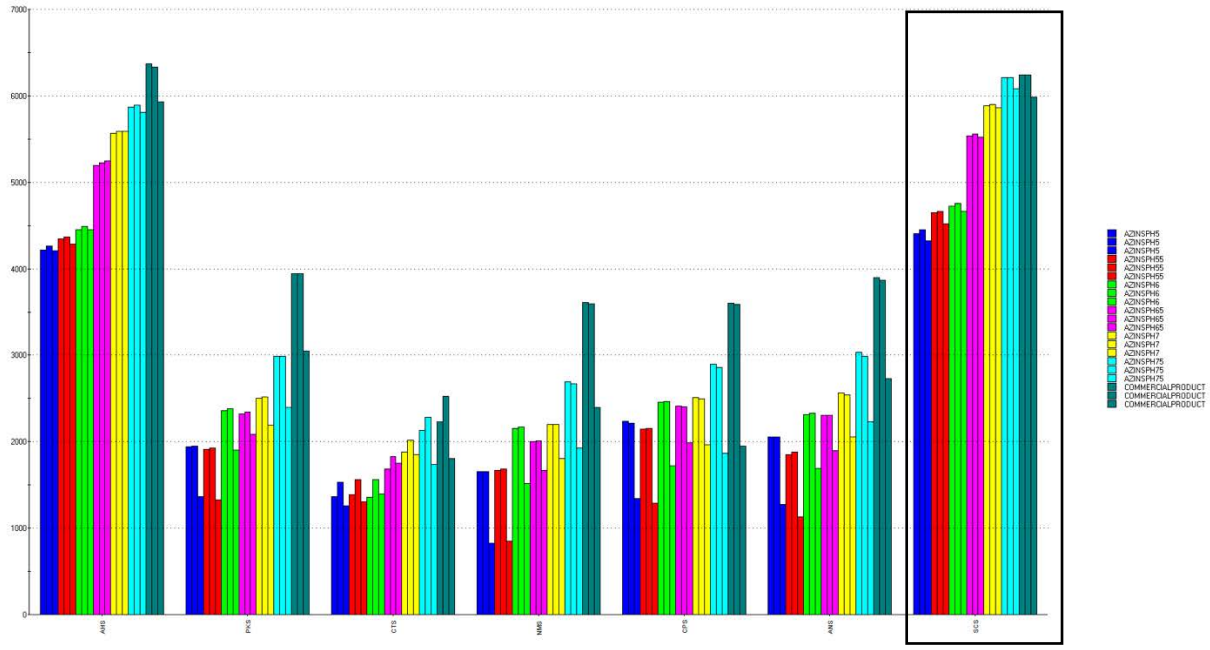

Figure 6.7. Mean sensor responses of AZI nanosuspensions (pH 5.0 – 7.5) vs. commercial formulation across all taste sensors.

Table 6.2 reports the mean, standard deviation (SD), and relative standard deviation (RSD%) for AHS, ANS, and SCS sensors. AZINSPH5 recorded the lowest RSD values among all formulations, implying consistent and reproducible taste masking performance at this pH.

Table 6.2. Mean, standard deviation (SD) and relative standard deviation (%RSD) of AHS, ANS, and SCS sensor responses of AZI nanosuspensions, buffers, placebo and pure AZI.

		AHS			ANS			SCS		
Sample	**No.**	**Mean**	**SD**	**%RSD**	**Mean**	**SD**	**%RSD**	**Mean**	**SD**	**%RSD**
AZINSPH5	3	4229.70	22.767	0.5383	1794.16	369.149	20.575	4392.81	54.100	1.232
AZINSPH55	3	4335.12	34.969	0.8066	1622.37	345.835	21.317	4609.52	63.587	1.379
AZINSPH6	3	4464.73	16.684	0.3737	2113.17	296.682	14.040	4715.49	38.003	0.8059
AZINSPH65	3	5221.83	23.702	0.4539	2169.57	193.280	8.909	5539.85	17.290	0.3121
AZINSPH7	3	5581.41	12.416	0.2225	2384.93	235.944	9.893	5886.25	15.506	0.2634
AZINSPH75	3	5855.84	34.824	0.5947	2751.35	370.280	13.458	6166.27	63.948	1.005
PH5	**3**	**3459.60**	**35.292**	**1.020**	**1254.54**	**243.335**	**19.396**	**3693.17**	**79.209**	**2.145**
PH55	3	4174.75	6.906	0.1654	1687.04	8.694	0.5153	4499.58	3.592	0.07984
PH6	3	3528.68	51.610	0.1463	1263.99	381.229	30.161	3770.14	86.904	2.035
PH65	3	5133.18	51.715	1.007	1861.79	417.0	22.398	5408.81	88.819	1.642
PH7	3	5578.46	46.422	0.8322	2061.33	413.637	20.067	5846.28	80.047	1.369
PH75	3	6514.12	33.996	0.5219	2315.54	388.351	16.772	6777.40	75.226	1.110
PLACEBO	3	4007.62	79.121	1.974	2804.40	49.816	1.776	4091.54	59.805	1.462
PURE AZI	3	4881.28	32.941	0.6748	3212.14	155.002	4.826	5166.05	18.465	0.3574

Following the pH trend analysis, AZINSPH5 was selected for a detailed comparison due to its superior taste masking performance, as evidenced by its consistently low sensor responses across SCS channel and high pattern discrimination.

Figure 6.8 presents the PCA plot of AZINSPH5 in relation to the pure AZI solution, placebo nanosuspension, and the commercial reference product. The PCA plot reveals that AZINSPH5 forms a clearly distinct cluster, well separated from the pure drug and commercial formulation. This spatial distancing confirms that the sensor response profile of AZINSPH5 is qualitatively different and dissimilar, suggesting successful taste modification of AZI through pH adjustment and nanosuspension formulation.

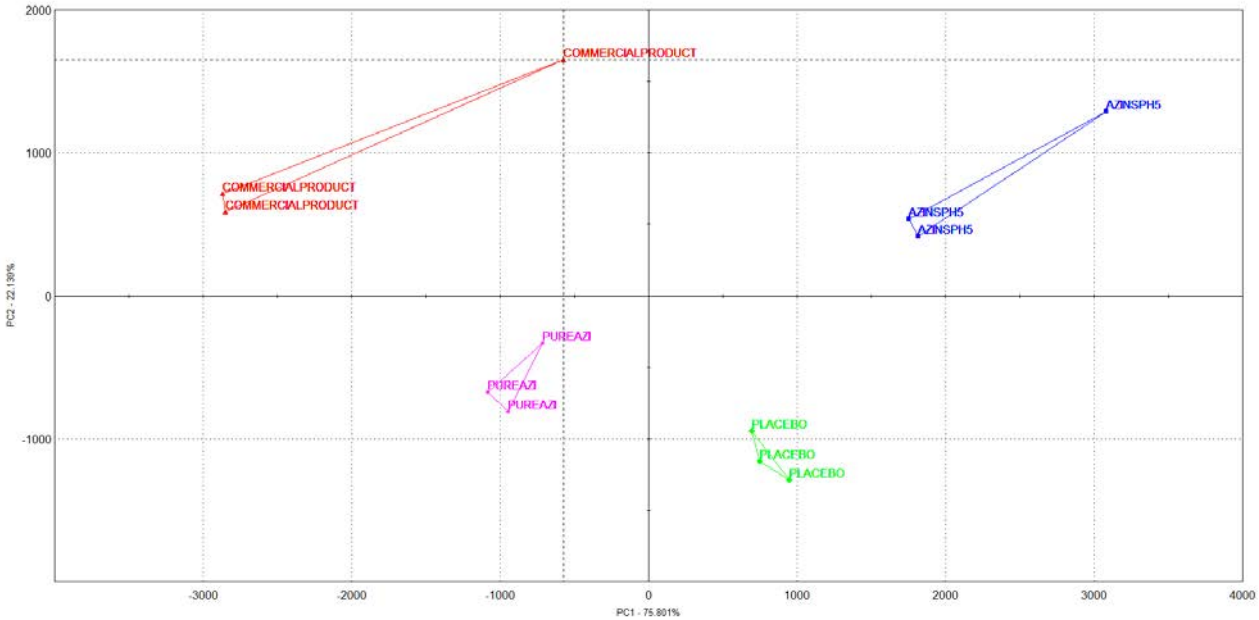

Figure 6.8. PCA plot of AZI nanosuspensions at pH 5.0 versus placebo, pure drug and a commercially available product.

Table 6.3 provides the quantitative distance values between AZINSPH5 and the reference samples. The greatest distance was observed between AZINSPH5 and the pure AZI sample, followed by the commercial formulation. This separation in taste space highlights that AZINSPH5 is the most dissimilar to the bitter control groups, reinforcing that the formulation minimizes undesirable bitterness characteristics.

Table 6.3. Distance table of AZI nanosuspensions at pH 5.0 versus placebo, pure drug and a commercially available product.

Product Name	Reference Sample	Distance	P Value	Pattern Discrimination Index (%)
AZINSPH5	COMMERCIAL	4327.19	0	81.7
AZINSPH5	PLACEBO	2377.14	0	82.33
AZINSPH5	PUREAZI	3420.7	0	90.2
COMMERCIAL	PUREAZI	3582.57	0	90.11
COMMERCIAL	PLACEBO	1999.63	0	55.2
PLACEBO	PUREAZI	1820.62	0	92.59

Figure 6.9, a bar plot of pattern discrimination distances, visually supports the data from Table 6.3 by showing the relative dissimilarity of AZINSPH5 to each control sample. The sharp contrast between AZINSPH5 and the commercial formulation, along with the distance to the placebo, emphasizes the effectiveness of taste masking at pH 5.0.

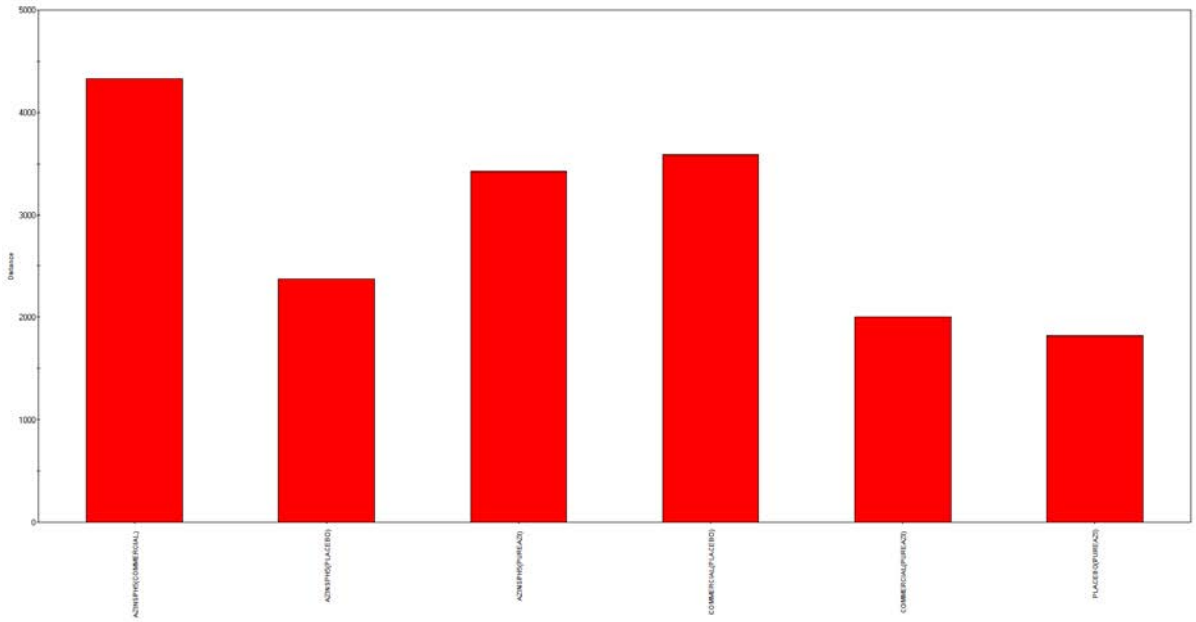

Figure 6.9. Distance plot showing dissimilarity of the AZINSPH5 relative to the reference samples.

Figure 6.10 illustrates the mean sensor responses for AZINSPH5, placebo, pure drug, and commercial formulation. SCS (bitterness) and AHS (sourness) demonstrate significantly

reduced values for AZINSPH5, while ANS (sweetness) maintains moderate response levels, implying a more palatable and less aversive profile. This aligns with research showing that weakly basic drugs like AZI exhibit reduced bitterness when ionized in acidic environments [218]. At pH 5.0, AZI is in its ionized form, which is less likely to activate TAS2R bitter taste receptors, reducing perceived bitterness despite increased surface area from nanosizing [218]. This sensor specific analysis further validates that the formulation minimizes activation of bitterness pathways.

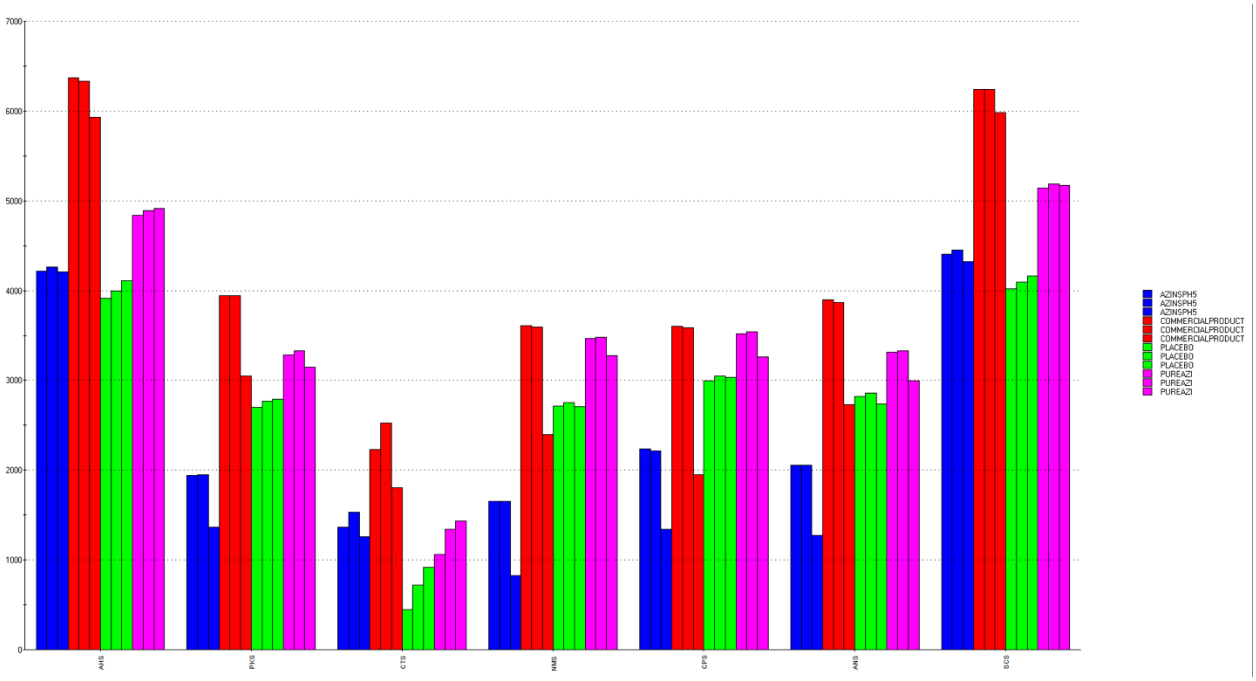

Figure 6.10. Mean sensor responses of AZI nanosuspensions at pH 5.0 versus placebo, pure drug and a commercially available product.

Figure 6.11 presents a radar plot comparing the taste profiles of AZINSPH5, pure AZI, placebo, and a commercially available formulation across the e-Tongue sensors. Each axis represents a specific sensor linked to a taste. AZINSPH5 shows a close overlap with the placebo across nearly all sensors, particularly SCS, indicating minimal bitterness perception. In contrast, pure AZI exhibits significantly higher SCS and AHS responses, confirming its intense bitter and slightly sour taste. The commercial formulation also shows elevated SCS values but to a lesser extent than pure AZI, suggesting only partial taste masking. AZINSPH5's lower sensor responses, especially on SCS, suggest that the formulation effectively masks the unpleasant taste of AZI and closely mimics the placebo's taste profile.

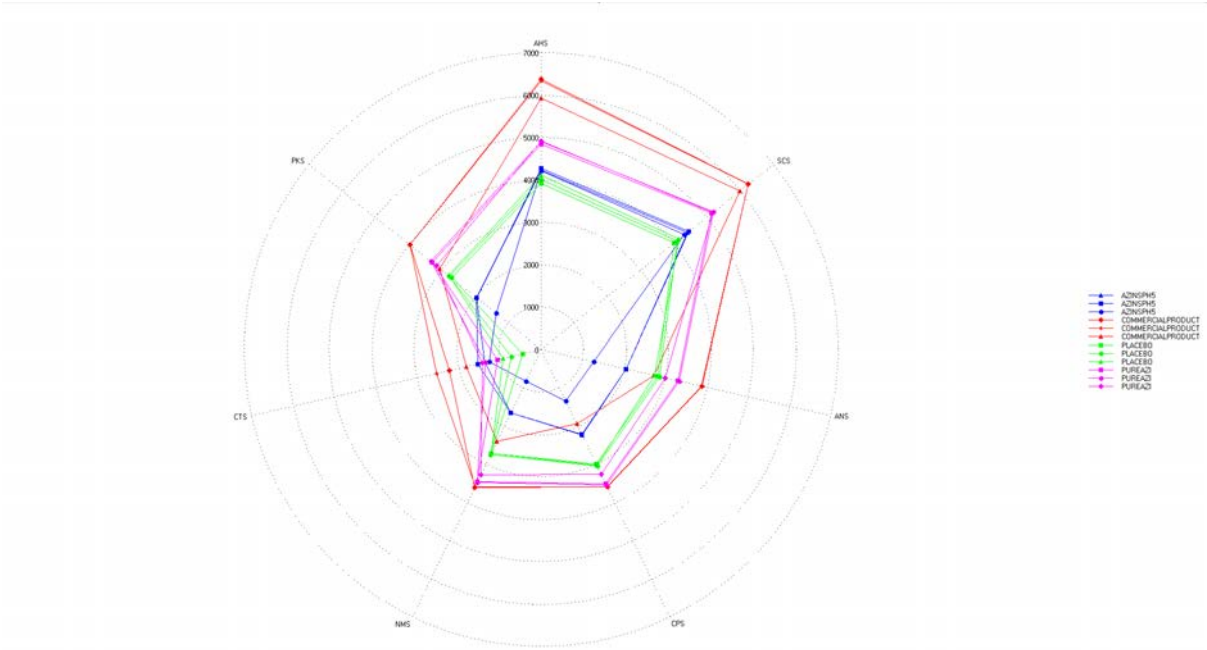

Figure 6.11. Radar plot comparing sensor responses of AZINSPH5, commercial formulation, placebo, and pure AZI.

6.7. CONCLUSION

Through a systematic evaluation via the e-Tongue involving PCA, sensor responses, pattern discrimination indices, and radar plots, the study demonstrated the influence of pH on the sensory characteristics of bitter APIs.

Initial multivariate analysis revealed that nanosuspensions formulated at lower pH values (5.0–5.5) clustered further from higher pH batches (7.0–7.5), indicating pH as a dominant modulator of taste profile. This was evident in both the PCA plots (Figure 6.6) and distance tables, where lower pH formulations showed greater dissimilarity from the commercial product and pure API. AZINSPH5 emerged as the most promising candidate, consistently showing the lowest response intensities on bitterness sensors (SCS).

AZINSPH5 (Figures 6.8–6.11) revealed its multivariate taste profile closely resembled the placebo, significantly deviating from both the commercial product and the pure drug. This was supported by its high pattern discrimination indices and reduced activation of bitterness and sourness sensors, reinforcing that AZINSPH5 effectively minimized the perception of AZI's inherent bitterness.

These findings suggest that formulation at pH 5.0 offers two advantages. It increases ionization of AZI, a weak base ~8.74 as discussed in Chapter 1, thereby reducing its ability to interact with taste receptors. By nanosizing, despite increasing surface area, did not lead to increased bitterness, due to pH driven ionization. This aligns with literature suggesting that ionized drugs are less able to interact with the lipid membranes of bitterness sensors or TAS2R receptors [218].

The e-tongue methodology proved to be a robust and reproducible tool for preclinical taste evaluation. This study provides strong evidence that AZINSPH5 (pH 5.0) achieves taste masking by a combination of pH buffering, drug ionization, and nanosuspension dispersion, making it a strong candidate for a paediatric friendly oral delivery of AZI. Future studies should correlate these findings with in vivo palatability data.

CHAPTER 7

CONCLUSION

The aim of this research was to formulate a stable, palatable nanosuspension of AZI to address the persistent challenges associated with its conventional antibiotic suspensions in paediatric applications.

Before any drug could be transformed into a stable, paediatric nanosuspension, it was imperative to develop a robust, selective, and validated analytical RP-HPLC method capable of accurately quantifying AZI from any sample. This analytical backbone ensured that all development to follow was supported by an accurate quantification tool capable of distinguishing AZI from excipients, degradants, and internal standards. A robust RP-HPLC-UV method was developed using a Phenomenex C_{18} column with ACN and 20 mM pH 7.5 phosphate buffer as the mobile phase. The method parameters included ACN content, buffer molarity, pH, and temperature. These were optimised using CCD. These inputs affected the retention time, resolution, and peak tailing of AZI. Quadratic models were fitted and evaluated using ANOVA, with high R^2 values indicating excellent predictive performance. The optimal chromatographic conditions identified through RSM produced sharp, well resolved AZI peaks with minimal tailing and satisfactory retention time. These were further confirmed by diagnostic plots. Once optimised, the method was validated according to the ICH guidelines.

The developed RP-HPLC method demonstrated excellent linearity over the concentration range of 0.5–150 µg/mL, with a R^2 consistently exceeding 0.999, indicating a strong relationship between analyte concentration and detector response. Precision was confirmed through intra-day and inter-day analysis, with relative standard deviations (%RSD) remaining below 2%, signifying high repeatability and reliability. The method also exhibited good accuracy, with recovery values falling within the acceptable range of 98–102%. The calculated limits of detection (LOD) and quantification (LOQ) were 3 µg/mL and 10 µg/mL, respectively. There was no interference observed from excipients or degradation products. Forced degradation studies validated the method's stability, making it a good tool for monitoring AZI throughout the formulation and storage processes.

The RP-HPLC method served as the backbone for both pre-formulation and formulation phases of the study. Pre-formulation studies were critical in identifying excipients with optimal

compatibility and functionality for AZI nanosuspension development. FTIR, and DSC revealed that Tween®80 and PVP K30 were compatible with AZI. Tween®80, a non-ionic surfactant was selected for its ability to reduce interfacial tension, while PVP K30 offered polymeric coverage to prevent nanoparticle agglomeration. Ethanol was chosen as the solvent phase due to its solubilising capacity for AZI (38.4 mg/mL), outperforming acetone, water and phosphate buffer. The formulation approach selected was the solvent antisolvent precipitation which was favoured over high-pressure homogenisation (HPH) owing to its simplicity, and cost effectiveness. The solvent antisolvent method enabled the formulation of nanocrystals under ambient conditions with controlled nucleation, making it more suitable for early-stage formulation trials. To systematically optimise the formulation, a Box Behnken Design (BBD) was employed. This design allowed for the optimisation of three independent variables, PVP K30 concentration, Tween®80 concentration, solvent to antisolvent ratio, and sonication time against key response parameters including particle size, polydispersity index, zeta potential, and initial drug release.

The final optimised AZI nanosuspension formulation achieved a mean particle size of 134.3 ± 26.6 nm, with a PDI of 0.298 ± 0.092, indicating a narrow and uniform particle distribution, which is good for consistent bioavailability and predictable *in vivo* behaviour. The zeta potential of –28.3 ± 5.6 mV confirmed surface charge repulsion, together with steric stabilization from Tween®80 and PVP K30, conferred physical stability against aggregation during storage. Tween®80 provided interfacial stabilization by adsorbing onto the particle surface, while PVP K30 acted as a steric barrier, preventing crystal growth and agglomeration. Together, these excipients contributed to the long-term colloidal stability of the system under both ambient and accelerated storage conditions, as verified by consistent particle size and zeta potential measurements over time. Drug release studies revealed an initial burst followed by sustained release, with the release profile best fitting the Higuchi kinetic model. The release pattern also exhibited some characteristics of first order kinetics, indicating a concentration dependent release phase. This hybrid behaviour is advantageous for maintaining therapeutic levels of AZI over extended durations, especially in paediatric applications where adherence to therapy is a concern. FTIR analysis confirmed the absence of new chemical bonds between AZI and excipients, indicating no significant drug-excipient interaction and the retention of AZI's chemical identity. Over an 8-week period, the formulation demonstrated commendable physical stability at 25 °C, with minimal fluctuations in particle size, PDI, zeta potential, and drug loading capacity. Under accelerated conditions, a slight increase in particle size and PDI

was observed, likely attributable to thermally induced desorption of surface bound surfactants and a reduction in microscopic viscosity, which in turn may have enhanced Brownian motion and aggregation. The zeta potential showed marginal decline, consistent with a shift in stabilization over time. Drug loading capacity remained relatively stable across both conditions, confirming that no significant drug degradation occurred.

This study also addressed palatability challenges in paediatric antibiotic formulations through a combination strategy that leveraged particle size reduction, stabiliser surface adsorption, and pH modulation to minimize the bitter perception of AZI. The effectiveness of this approach was validated through e-tongue analysis, where radar plots and PCA plots provided clear evidence of sensory improvement. Among all tested samples, the optimised nanosuspension at pH 5.0 (AZINSPH5) exhibited the closest sensor profile to the placebo and a marked divergence from both the commercial product and the unformulated drug. This confirmed a meaningful reduction in bitterness perception, achieved without masking agents or sweeteners. Improved taste is important in medication adherence in children, where missed doses can diminish efficacy and contribute to resistance. By offering a formulation that is both pharmaceutically and organoleptically acceptable, this study contributes to the development of child friendly medicines that align with regulatory expectations.

The nanosuspension developed in this study provides a scalable, low cost, and effective alternative to current formulations, without reliance on expensive equipment or synthetic taste masking agents. The formulation and design strategies applied can be adapted for other BCS Class II drugs facing similar solubility and taste related barriers in paediatric populations. Thus, the study not only addresses a specific need for AZI but also establishes a transferable platform for improving access to better tasting, bioavailable antibiotics for children worldwide.

There were limitations experienced in this study. The physical stability evaluation was limited to an 8-week period and did not extend to long term ICH mandated timepoints (6–12 months), which are required for commercial shelf-life claims. While in *vitro* and analytical characterisations were thorough, no in *vivo* pharmacokinetic (PK) or pharmacodynamic (PD) studies were conducted to confirm bioavailability enhancement or clinical efficacy. Batch to batch reproducibility was not experimentally verified at larger scale. While the e-tongue provided a robust predictive insight into taste masking, it cannot fully substitute for actual palatability studies involving human sensory panels or animal taste aversion models. While the

nanosuspension was successful, converting the liquid formulation into a dry powder for reconstitution could offer additional benefits for transportation, storage, and shelf-life. These limitations should be addressed in future research.

This research successfully addressed the dual formulation challenges of solubility and palatability associated with AZI for paediatric use. By integrating a validated RP-HPLC method, a formulation strategy, and taste masking techniques at nanoscale, a stable, and child acceptable nanosuspension of AZI was developed. The formulation demonstrated promising physicochemical characteristics, improved drug release, improved taste, and physical stability under real world storage conditions. This study lays a foundational framework for transforming bitter, poorly soluble antibiotics into therapeutically effective, patient friendly paediatric formulations. Changing the world, one nanodrop at a time.

APPENDIX I

BATCH PRODUCTION RECORDS

All formulations manufactured and assessed during formulation development and optimisation studies were manufacture suing good manufacturing practices (GMP).

RHODES UNIVERSITY, FACULTY OF PHARMACY
GRAHAMSTOWN, 6140, SOUTH AFRICA

BATCH PRODUCTION RECORD

Product name: AZI Nanosuspension **Page 1 of 5**

Batch ID: AZI-NS-OPT **Batch size: 50 mL**

MANUFACTURING APPROVALS

Batch record issued by_____ **Date**_____

Master record issued by_____ **Date**_____

RHODES UNIVERSITY, FACULTY OF PHARMACY
GRAHAMSTOWN, 6140, SOUTH AFRICA

BATCH PRODUCTION RECORD

Product name: AZI Nanosuspension **Page 2 of 5**

Batch ID: AZI-NS-OPT **Batch size: 85 mL**

Item	Material	Quantity	Unit	Batch Amount	Amount dispensed	Dispensed by	Checked by
1	AZI	0.0118	%w/v	0.0100 g	10.26 mg		
2	Ethanol	5.88	%v/v	5 mL	5 mL		
3	Tween®80	0.15	%w/v	0.1275 g	127.49 mg		
4	PVP K30	0.2	%w/v	0.1700 g	170.01 mg		
5	Aqua	q.s. to 85	mL	80 mL	80 mL		

RHODES UNIVERSITY, FACULTY OF PHARMACY
GRAHAMSTOWN, 6140, SOUTH AFRICA

BATCH PRODUCTION RECORD

Product name: AZI Nanosuspension **Page 3 of 5**

Batch ID: AZI-NS-OPT **Batch size: 50 mL**

EQUIPMENT VERIFICATION			
Description	**Type**	**Verified by**	**Confirmed by**
Hot Plate/Magnetic Stirrer	VWR		
Probe Sonicator			

RHODES UNIVERSITY, FACULTY OF PHARMACY
GRAHAMSTOWN, 6140, SOUTH AFRICA
BATCH PRODUCTION RECORD

Product name: AZI Nanosuspension **Page 4 of 5**
Batch ID: AZI-NS-OPT **Batch size: 50 mL**

MANUFACTURING PROCEDURE				
Step	**Procedure**	**Time**	**Done by**	**Checked by**
1	Weigh all the materials.			
2	Dissolve the AZI (Item 1) in ethanol (Item 2) until a clear solution is obtained.			
3	Add purified water (Item 5) to a beaker and begin magnetic stirring at 1500 rpm.			
4	Gradually add PVP K30 (Item 4) and Tween®80 (Item 3) separately to the water (Item 5) while stirring until completely dissolved.			
5	Add the AZI solution dropwise to the aqueous phase using a stoppered flask while maintaining stirring.			
6	Subject the mixture to probe sonication to reduce particle size.			
7	Transfer the nanosuspension into a suspension bottle and allow it to cool to room temperature.			
8	Store the formulation at room temperature (22°C) for at least 24 hours prior to characterisation.			

RHODES UNIVERSITY, FACULTY OF PHARMACY

GRAHAMSTOWN, 6140, SOUTH AFRICA

BATCH PRODUCTION RECORD

Product name: AZI Nanosuspension **Page 5 of 5**

Batch ID: AZI-NS-OPT **Batch size: 50 mL**

SIGNATURE AND INTIAL REFERENCE			
Full name (Print)	**Signature**	**Initials**	**Date**

APPENDIX II

AZI NANOSUSPENSION REPORTS

All AZI nanosuspensions manufactured and assessed during formulation development and optimisation studies were manufactured using Good Manufacturing Practice (GMP).

RHODES UNIVERSITY, FACULTY OF PHARMACY

GRAHAMSTOWN, 6140, SOUTH AFRICA

AZI NANOSUSPENSION BATCH SUMMARY REPORT

Formulator:	**Sonal Bhana**
Product:	**AZI Nanosuspension**
Batch ID:	**AZI-NS 001**
Batch size:	**85 mL**
Date of manufacture:	**04 March 2025**

Formula:

Item	Material	Quantity	Unit	Batch Amount
1	AZI	0.0118	%w/v	0.0100 g
2	Ethanol	5.88	%v/v	5 mL
3	Tween®80	0.1	%w/v	0.0850 g
4	PVP K30	0.05	%w/v	0.0425 g
5	Aqua	q.s. to 85	mL	80 mL

- **Solvent: Ethanol; Antisolvent: Aqua (solvent-antisolvent ratio is 1:16)**

Production equipment used:

Magnetic stirring: Precipitation was performed by dropwise addition of ethanolic AZI solution using a conical dropper into the antisolvent (water containing stabilisers) under magnetic stirring. Dropwise addition over 10 minutes with continuous stirring at 1500 rpm.

Probe sonication: The mixture was probe sonicated for 3 minutes post-precipitation to reduce particle size and ensure uniform dispersion.

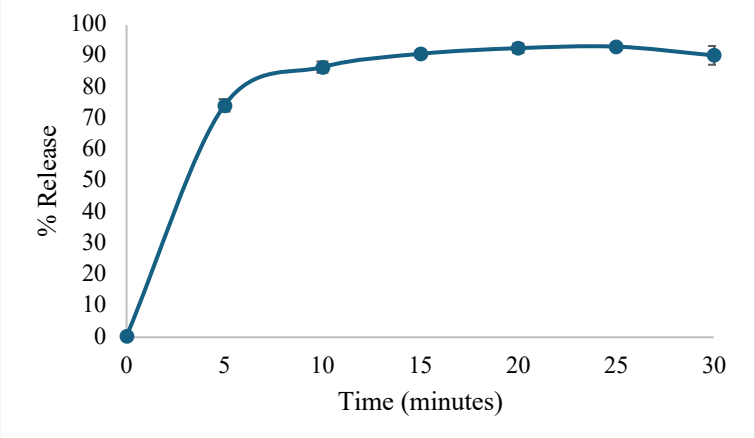

Evaluated parameters and *in vitro* dissolution profile:

ZP (Z-average): 385.2 nm

PS: -20.69 mV

PDI: 0.531

Comments: Formulation was moderately stable and a clear homogenous solution at 22°C.

RHODES UNIVERSITY, FACULTY OF PHARMACY

GRAHAMSTOWN, 6140, SOUTH AFRICA

AZI NANOSUSPENSION BATCH SUMMARY REPORT

Formulator:	**Sonal Bhana**
Product:	**AZI Nanosuspension**
Batch ID:	**AZI-NS 002**
Batch size:	**50 mL**
Date of manufacture:	**04 March 2025**

Formula:

Item	Material	Quantity	Unit	Batch Amount
1	AZI	0.02	%w/v	0.0100 g
2	Ethanol	10	%v/v	5 mL
3	Tween®80	0.05	%w/v	0.0275 g
4	PVP K30	0.05	%w/v	0.0425 g
5	Aqua	q.s. to 50	mL	45 mL

- **Solvent: Ethanol; Antisolvent: Aqua (solvent-antisolvent ratio is 1:9)**

Production equipment used:

Magnetic stirring: Precipitation was performed by dropwise addition of ethanolic AZI solution using a conical dropper into the antisolvent (water containing stabilisers) under magnetic stirring. Dropwise addition over 10 minutes with continuous stirring at 1500 rpm.

Probe sonication: The mixture was probe sonicated for 6 minutes post-precipitation to reduce particle size and ensure uniform dispersion.

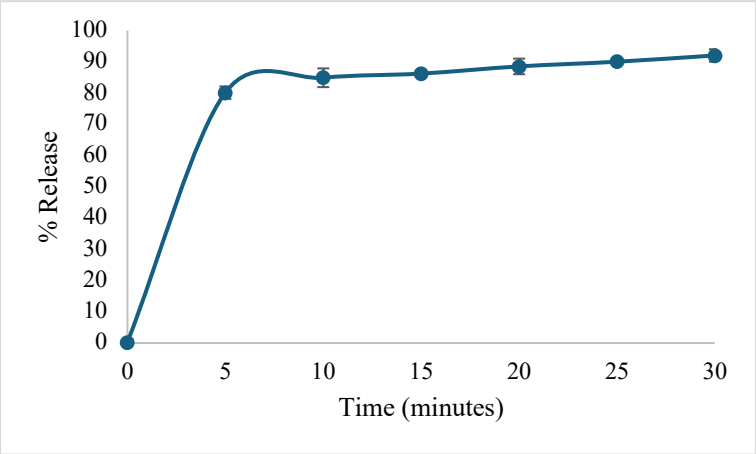

Evaluated parameters and *in vitro* dissolution profile:

ZP (Z-average): 21.16 nm

PS: -22.55 mV

PDI: 0.403

Comments: Formulation was moderately stable and a clear homogenous solution at 22℃.

RHODES UNIVERSITY, FACULTY OF PHARMACY

GRAHAMSTOWN, 6140, SOUTH AFRICA

AZI NANOSUSPENSION BATCH SUMMARY REPORT

Formulator:	**Sonal Bhana**
Product:	**AZI Nanosuspension**
Batch ID:	**AZI-NS 003**
Batch size:	**85 mL**
Date of manufacture:	**04 March 2025**

Formula:

Item	Material	Quantity	Unit	Batch Amount
1	AZI	0.0118	%w/v	0.0100 g
2	Ethanol	5.88	%v/v	5 mL
3	Tween®80	0.1	%w/v	0.0850 g
4	PVP K30	0.05	%w/v	0.0425 g
5	Aqua	q.s. to 85	mL	80 mL

- **Solvent: Ethanol; Antisolvent: Aqua (solvent-antisolvent ratio is 1:16)**

Production equipment used:

Magnetic stirring: Precipitation was performed by dropwise addition of ethanolic AZI solution using a conical dropper into the antisolvent (water containing stabilisers) under magnetic stirring. Dropwise addition over 10 minutes with continuous stirring at 1500 rpm.

Probe sonication: The mixture was probe sonicated for 9 minutes post-precipitation to reduce particle size and ensure uniform dispersion.

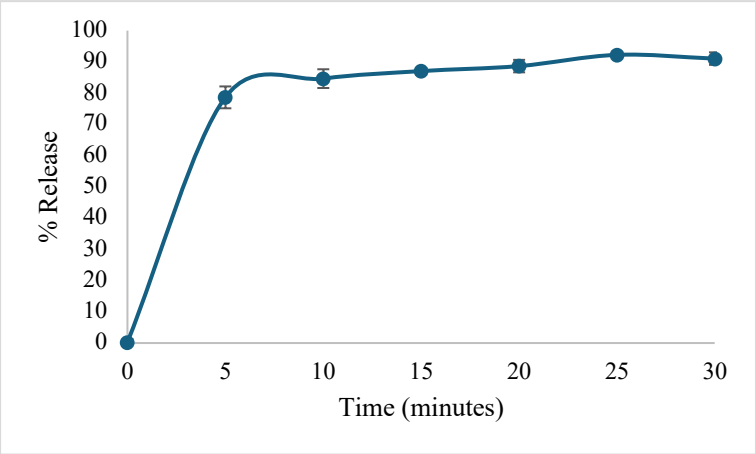

Evaluated parameters and *in vitro* dissolution profile:

ZP (Z-average): 1315 nm

PS: -23.4 mV

PDI: 0.978

Comments: Formulation was moderately stable and a clear homogenous solution at 22℃.

RHODES UNIVERSITY, FACULTY OF PHARMACY

GRAHAMSTOWN, 6140, SOUTH AFRICA

AZI NANOSUSPENSION BATCH SUMMARY REPORT

Formulator:	**Sonal Bhana**
Product:	**AZI Nanosuspension**
Batch ID:	**AZI-NS 004**
Batch size:	**85 mL**
Date of manufacture:	**04 March 2025**

Formula:

Item	Material	Quantity	Unit	Batch Amount
1	AZI	0.0118	%w/v	0.0100 g
2	Ethanol	5.88	%v/v	5 mL
3	Tween®80	0.1	%w/v	0.0850 g
4	PVP K30	0.125	%w/v	0.1062 g
5	Aqua	q.s. to 85	mL	80 mL

- **Solvent: Ethanol; Antisolvent: Aqua (solvent-antisolvent ratio is 1:16)**

Production equipment used:

Magnetic stirring: Precipitation was performed by dropwise addition of ethanolic AZI solution using a conical dropper into the antisolvent (water containing stabilisers) under magnetic stirring. Dropwise addition over 10 minutes with continuous stirring at 1500 rpm.

Probe sonication: The mixture was probe sonicated for 6 minutes post-precipitation to reduce particle size and ensure uniform dispersion.

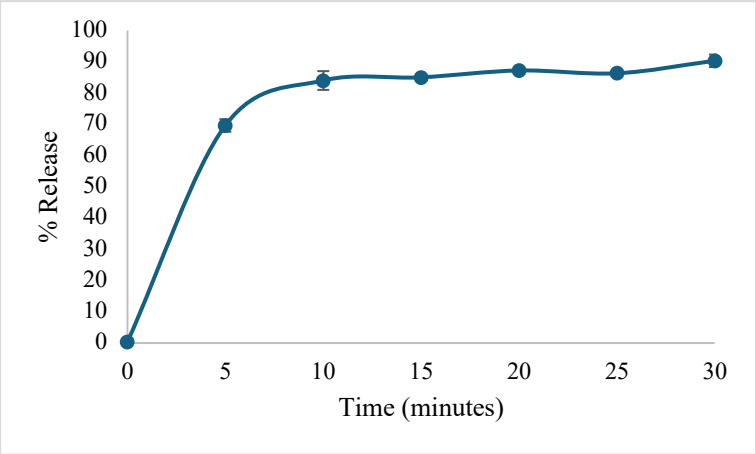

Evaluated parameters and *in vitro* dissolution profile:

ZP (Z-average): 133.2 nm

PS: -21.54 mV

PDI: 0.401

Comments: Formulation was moderately stable and a clear homogenous solution at 22℃.

RHODES UNIVERSITY, FACULTY OF PHARMACY

GRAHAMSTOWN, 6140, SOUTH AFRICA

AZI NANOSUSPENSION BATCH SUMMARY REPORT

Formulator:	**Sonal Bhana**
Product:	**AZI Nanosuspension**
Batch ID:	**AZI-NS 005**
Batch size:	**50 mL**
Date of manufacture:	**04 March 2025**

Formula:

Item	Material	Quantity	Unit	Batch Amount
1	AZI	0.02	%w/v	0.010 g
2	Ethanol	10	%v/v	5 mL
3	Tween®80	0.1	%w/v	0.050 g
4	PVP K30	0.05	%w/v	0.0625 g
5	Aqua	q.s. to 50	mL	45 mL

- **Solvent: Ethanol; Antisolvent: Aqua (solvent-antisolvent ratio is 1:9)**

Production equipment used:

Magnetic stirring: Precipitation was performed by dropwise addition of ethanolic AZI solution using a conical dropper into the antisolvent (water containing stabilisers) under magnetic stirring. Dropwise addition over 10 minutes with continuous stirring at 1500 rpm.

Probe sonication: The mixture was probe sonicated for 9 minutes post-precipitation to reduce particle size and ensure uniform dispersion.

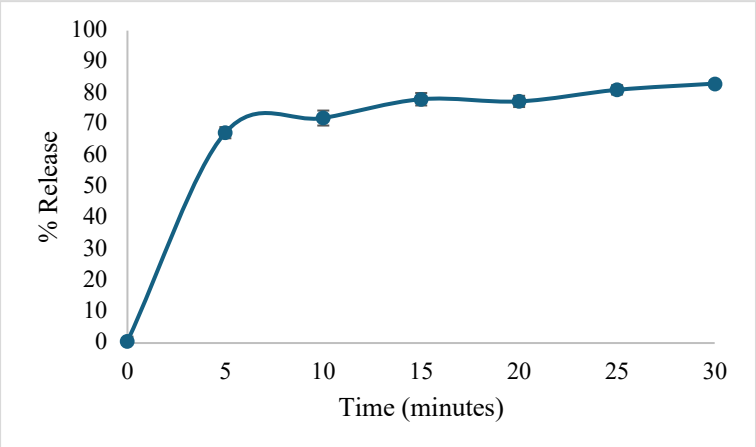

Evaluated parameters and *in vitro* dissolution profile:

ZP (Z-average): 303.8 nm

PS: -18.20 mV

PDI: 0.545

Comments: Formulation was relatively stable and a clear homogenous solution at 22℃.

RHODES UNIVERSITY, FACULTY OF PHARMACY

GRAHAMSTOWN, 6140, SOUTH AFRICA

AZI NANOSUSPENSION BATCH SUMMARY REPORT

Formulator:	**Sonal Bhana**
Product:	**AZI Nanosuspension**
Batch ID:	**AZI-NS 006**
Batch size:	**35 mL**
Date of manufacture:	**04 March 2025**

Formula:

Item	Material	Quantity	Unit	Batch Amount
1	AZI	0.0286	%w/v	0.010 g
2	Ethanol	14.29	%v/v	5 mL
3	Tween®80	0.05	%w/v	0.0175 g
4	PVP K30	0.125	%w/v	0.0437 g
5	Aqua	q.s. to 35	mL	30 mL

- **Solvent: Ethanol; Antisolvent: Aqua (solvent-antisolvent ratio is 1:6)**

Production equipment used:

Magnetic stirring: Precipitation was performed by dropwise addition of ethanolic AZI solution using a conical dropper into the antisolvent (water containing stabilisers) under magnetic stirring. Dropwise addition over 10 minutes with continuous stirring at 1500 rpm.

Probe sonication: The mixture was probe sonicated for 6 minutes post-precipitation to reduce particle size and ensure uniform dispersion.

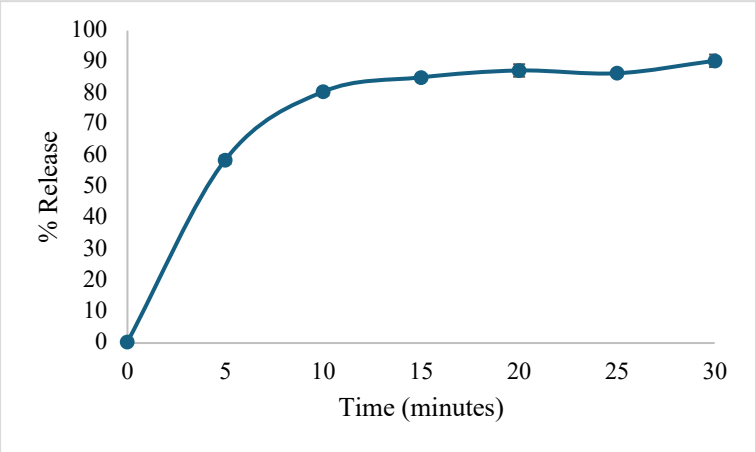

Evaluated parameters and *in vitro* dissolution profile:

ZP (Z-average): 454.5 nm

PS: -23.3 mV

PDI: 0.619

Comments: Formulation was moderately stable and a clear homogenous solution at 22℃.

RHODES UNIVERSITY, FACULTY OF PHARMACY

GRAHAMSTOWN, 6140, SOUTH AFRICA

AZI NANOSUSPENSION BATCH SUMMARY REPORT

Formulator:	**Sonal Bhana**
Product:	**AZI Nanosuspension**
Batch ID:	**AZI-NS 007**
Batch size:	**50 mL**
Date of manufacture:	**04 March 2025**

Formula:

Item	Material	Quantity	Unit	Batch Amount
1	AZI	0.02	%w/v	0.010 g
2	Ethanol	10	%v/v	5 mL
3	Tween®80	0.1	%w/v	0.0850 g
4	PVP K30	0.2	%w/v	0.1000 g
5	Aqua	q.s. to 50	mL	45 mL

- **Solvent: Ethanol; Antisolvent: Aqua (solvent-antisolvent ratio is 1:9)**

Production equipment used:

Magnetic stirring: Precipitation was performed by dropwise addition of ethanolic AZI solution using a conical dropper into the antisolvent (water containing stabilisers) under magnetic stirring. Dropwise addition over 10 minutes with continuous stirring at 1500 rpm.

Probe sonication: The mixture was probe sonicated for 6 minutes post-precipitation to reduce particle size and ensure uniform dispersion.

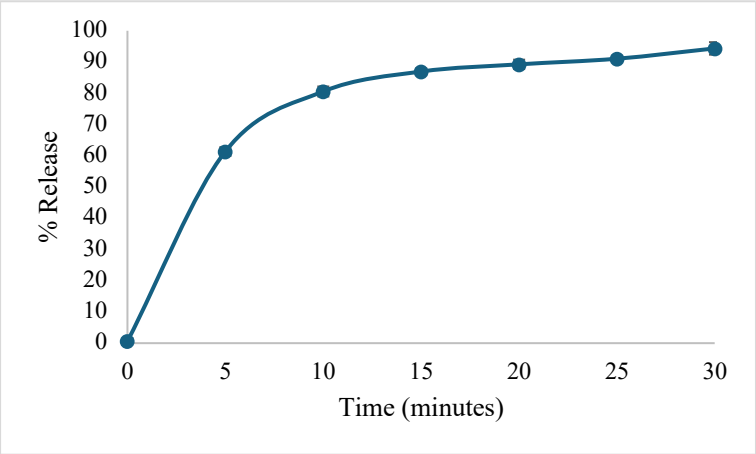

Evaluated parameters and *in vitro* dissolution profile:

ZP (Z-average): 321 nm

PS: -23.4 mV

PDI: 0.385

Comments: Formulation was moderately stable and a clear homogenous solution at 22℃.

RHODES UNIVERSITY, FACULTY OF PHARMACY

GRAHAMSTOWN, 6140, SOUTH AFRICA

AZI NANOSUSPENSION BATCH SUMMARY REPORT

Formulator:	**Sonal Bhana**
Product:	**AZI Nanosuspension**
Batch ID:	**AZI-NS 008**
Batch size:	**50 mL**
Date of manufacture:	**04 March 2025**

Formula:

Item	Material	Quantity	Unit	Batch Amount
1	AZI	0.02	%w/v	0.010 g
2	Ethanol	10	%v/v	5 mL
3	Tween®80	0.1	%w/v	0.0500 g
4	PVP K30	0.125	%w/v	0.0625 g
5	Aqua	q.s. to 50	mL	45 mL

- **Solvent: Ethanol; Antisolvent: Aqua (solvent-antisolvent ratio is 1:9)**

Production equipment used:

Magnetic stirring: Precipitation was performed by dropwise addition of ethanolic AZI solution using a conical dropper into the antisolvent (water containing stabilisers) under magnetic stirring. Dropwise addition over 10 minutes with continuous stirring at 1500 rpm.

Probe sonication: The mixture was probe sonicated for 6 minutes post-precipitation to reduce particle size and ensure uniform dispersion.

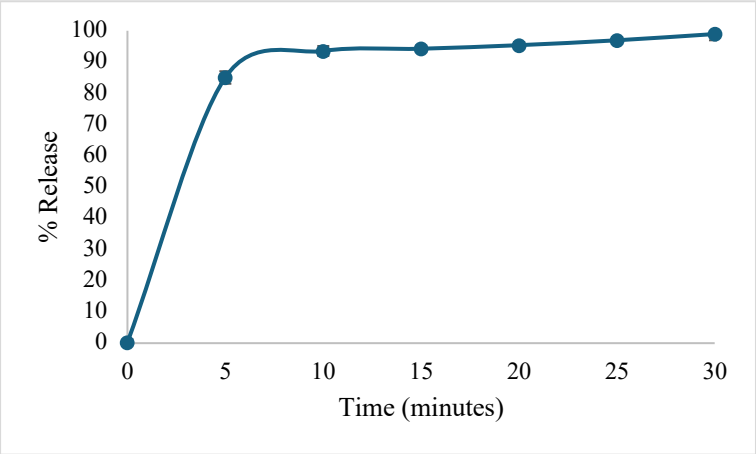

Evaluated parameters and *in vitro* dissolution profile:

ZP (Z-average): 236 nm

PS: -26.1 mV

PDI: 0.285

Comments: Formulation was moderately stable and a clear homogenous solution at 22℃.

RHODES UNIVERSITY, FACULTY OF PHARMACY

GRAHAMSTOWN, 6140, SOUTH AFRICA

AZI NANOSUSPENSION BATCH SUMMARY REPORT

Formulator: **Sonal Bhana**

Product: **AZI Nanosuspension**

Batch ID: **AZI-NS 009**

Batch size: **50 mL**

Date of manufacture: **04 March 2025**

Formula:

Item	Material	Quantity	Unit	Batch Amount
1	AZI	0.02	%w/v	0.010 g
2	Ethanol	10	%v/v	5 mL
3	Tween®80	0.15	%w/v	0.0750 g
4	PVP K30	0.125	%w/v	0.0625 g
5	Aqua	q.s. to 50	mL	45 mL

- **Solvent: Ethanol; Antisolvent: Aqua (solvent-antisolvent ratio is 1:9)**

Production equipment used:

Magnetic stirring: Precipitation was performed by dropwise addition of ethanolic AZI solution using a conical dropper into the antisolvent (water containing stabilisers) under magnetic stirring. Dropwise addition over 10 minutes with continuous stirring at 1500 rpm.

Probe sonication: The mixture was probe sonicated for 6 minutes post-precipitation to reduce particle size and ensure uniform dispersion.

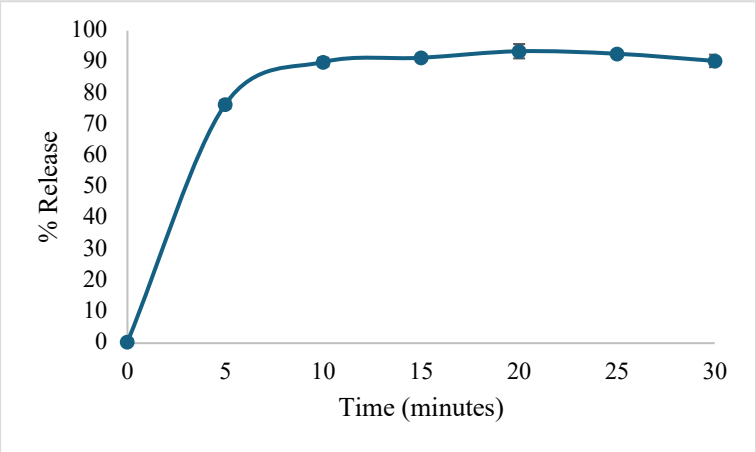

Evaluated parameters and *in vitro* dissolution profile:

ZP (Z-average): 199.4 nm

PS: -23.9 mV

PDI: 0.461

Comments: Formulation was moderately stable and a clear homogenous solution at 22℃.

RHODES UNIVERSITY, FACULTY OF PHARMACY

GRAHAMSTOWN, 6140, SOUTH AFRICA

AZI NANOSUSPENSION BATCH SUMMARY REPORT

Formulator:	**Sonal Bhana**
Product:	**AZI Nanosuspension**
Batch ID:	**AZI-NS 010**
Batch size:	**50 mL**
Date of manufacture:	**04 March 2025**

Formula:

Item	Material	Quantity	Unit	Batch Amount
1	AZI	0.02	%w/v	0.010 g
2	Ethanol	10	%v/v	5 mL
3	Tween®80	0.05	%w/v	0.0250 g
4	PVP K30	0.125	%w/v	0.0625 g
5	Aqua	q.s. to 50	mL	45 mL

- **Solvent: Ethanol; Antisolvent: Aqua (solvent-antisolvent ratio is 1:9)**

Production equipment used:

Magnetic stirring: Precipitation was performed by dropwise addition of ethanolic AZI solution using a conical dropper into the antisolvent (water containing stabilisers) under magnetic stirring. Dropwise addition over 10 minutes with continuous stirring at 1500 rpm.

Probe sonication: The mixture was probe sonicated for 6 minutes post-precipitation to reduce particle size and ensure uniform dispersion.

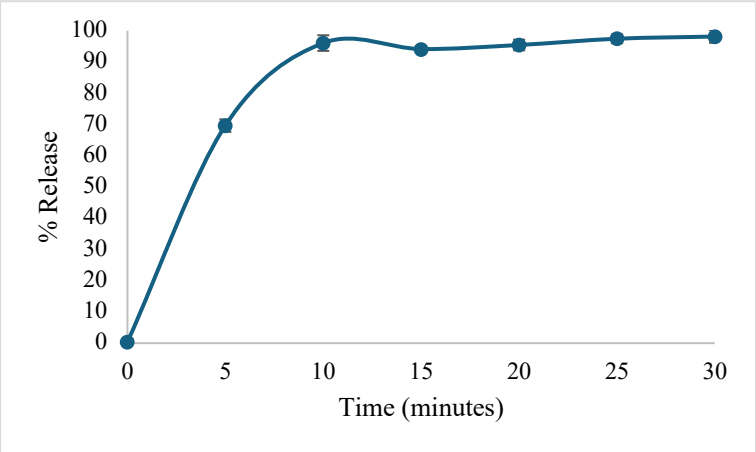

Evaluated parameters and *in vitro* dissolution profile:

ZP (Z-average): 198.1 nm

PS: -22.6 mV

PDI: 0.386

Comments: Formulation was moderately stable and a clear homogenous solution at 22℃.

RHODES UNIVERSITY, FACULTY OF PHARMACY

GRAHAMSTOWN, 6140, SOUTH AFRICA

AZI NANOSUSPENSION BATCH SUMMARY REPORT

Formulator:	**Sonal Bhana**
Product:	**AZI Nanosuspension**
Batch ID:	**AZI-NS 011**
Batch size:	**85 mL**
Date of manufacture:	**04 March 2025**

Formula:

Item	Material	Quantity	Unit	Batch Amount
1	AZI	0.0118	%w/v	0.010 g
2	Ethanol	5.88	%v/v	5 mL
3	Tween®80	0.1	%w/v	0.085 g
4	PVP K30	0.125	%w/v	0.0425 g
5	Aqua	q.s. to 85	mL	80 mL

- **Solvent: Ethanol; Antisolvent: Aqua (solvent-antisolvent ratio is 1:16)**

Production equipment used:

Magnetic stirring: Precipitation was performed by dropwise addition of ethanolic AZI solution using a conical dropper into the antisolvent (water containing stabilisers) under magnetic stirring. Dropwise addition over 10 minutes with continuous stirring at 1500 rpm.

Probe sonication: The mixture was probe sonicated for 3 minutes post-precipitation to reduce particle size and ensure uniform dispersion.

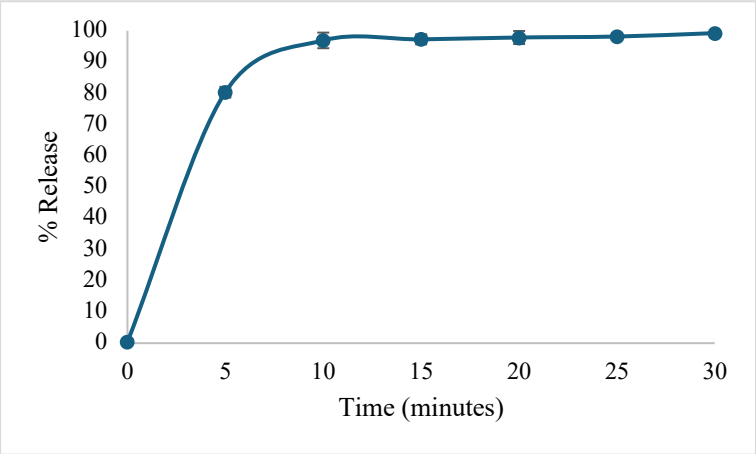

Evaluated parameters and *in vitro* dissolution profile:

ZP (Z-average): 701.8 nm

PS: -20.9 mV

PDI: 0.699

Comments: Formulation was moderately stable and a clear homogenous solution at 22℃.

RHODES UNIVERSITY, FACULTY OF PHARMACY

GRAHAMSTOWN, 6140, SOUTH AFRICA

AZI NANOSUSPENSION BATCH SUMMARY REPORT

Formulator:	**Sonal Bhana**
Product:	**AZI Nanosuspension**
Batch ID:	**AZI-NS 012**
Batch size:	**85 mL**
Date of manufacture:	**04 March 2025**

Formula:

Item	Material	Quantity	Unit	Batch Amount
1	AZI	0.0118	%w/v	0.010 g
2	Ethanol	5.88	%v/v	5 mL
3	Tween®80	0.15	%w/v	0.1275 g
4	PVP K30	0.125	%w/v	0.1062 g
5	Aqua	q.s. to 85	mL	80 mL

- **Solvent: Ethanol; Antisolvent: Aqua (solvent-antisolvent ratio is 1:16)**

Production equipment used:

Magnetic stirring: Precipitation was performed by dropwise addition of ethanolic AZI solution using a conical dropper into the antisolvent (water containing stabilisers) under magnetic stirring. Dropwise addition over 10 minutes with continuous stirring at 1500 rpm.

Probe sonication: The mixture was probe sonicated for 6 minutes post-precipitation to reduce particle size and ensure uniform dispersion.

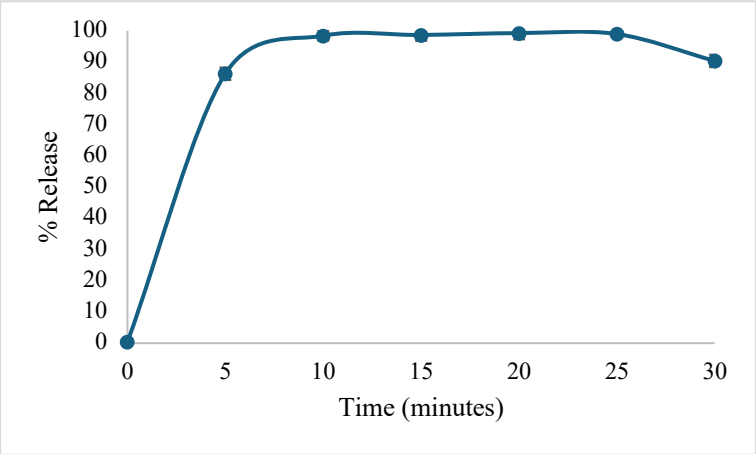

Evaluated parameters and *in vitro* dissolution profile:

ZP (Z-average): 1799 nm

PS: -19.9 mV

PDI: 1.000

Comments: Formulation was relatively stable and a clear homogenous solution at 22℃.

RHODES UNIVERSITY, FACULTY OF PHARMACY

GRAHAMSTOWN, 6140, SOUTH AFRICA

AZI NANOSUSPENSION BATCH SUMMARY REPORT

Formulator:	**Sonal Bhana**
Product:	**AZI Nanosuspension**
Batch ID:	**AZI-NS 013**
Batch size:	**50 mL**
Date of manufacture:	**04 March 2025**

Formula:

Item	Material	Quantity	Unit	Batch Amount
1	AZI	0.02	%w/v	0.010 g
2	Ethanol	10	%v/v	5 mL
3	Tween®80	0.15	%w/v	0.0750 g
4	PVP K30	0.125	%w/v	0.0625 g
5	Aqua	q.s. to 50	mL	45 mL

- **Solvent: Ethanol; Antisolvent: Aqua (solvent-antisolvent ratio is 1:9)**

Production equipment used:

Magnetic stirring: Precipitation was performed by dropwise addition of ethanolic AZI solution using a conical dropper into the antisolvent (water containing stabilisers) under magnetic stirring. Dropwise addition over 10 minutes with continuous stirring at 1500 rpm.

Probe sonication: The mixture was probe sonicated for 9 minutes post-precipitation to reduce particle size and ensure uniform dispersion.

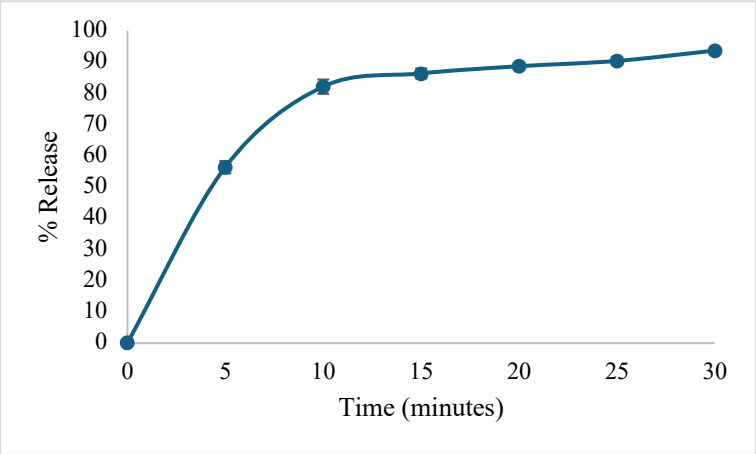

Evaluated parameters and *in vitro* dissolution profile:

ZP (Z-average): 1341 nm

PS: -25.00 mV

PDI: 0.940

Comments: Formulation was moderately stable and a clear homogenous solution at 22℃.

RHODES UNIVERSITY, FACULTY OF PHARMACY

GRAHAMSTOWN, 6140, SOUTH AFRICA

AZI NANOSUSPENSION BATCH SUMMARY REPORT

Formulator: **Sonal Bhana**

Product: **AZI Nanosuspension**

Batch ID: **AZI-NS 014**

Batch size: **50 mL**

Date of manufacture: **04 March 2025**

Formula:

Item	Material	Quantity	Unit	Batch Amount
1	AZI	0.02	%w/v	0.010 g
2	Ethanol	10	%v/v	5 mL
3	Tween®80	0.1	%w/v	0.050 g
4	PVP K30	0.125	%w/v	0.0625 g
5	Aqua	q.s. to 50	mL	45 mL

- **Solvent: Ethanol; Antisolvent: Aqua (solvent-antisolvent ratio is 1:9)**

Production equipment used:

Magnetic stirring: Precipitation was performed by dropwise addition of ethanolic AZI solution using a conical dropper into the antisolvent (water containing stabilisers) under magnetic stirring. Dropwise addition over 10 minutes with continuous stirring at 1500 rpm.

Probe sonication: The mixture was probe sonicated for 6 minutes post-precipitation to reduce particle size and ensure uniform dispersion.

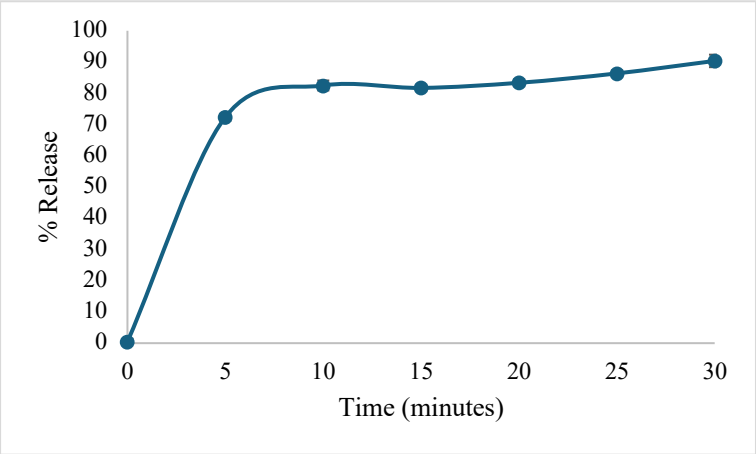

Evaluated parameters and *in vitro* dissolution profile:

ZP (Z-average): 247.1 nm

PS: -22.29 mV

PDI: 0.378

Comments: Formulation was moderately stable and a clear homogenous solution at 22℃.

RHODES UNIVERSITY, FACULTY OF PHARMACY

GRAHAMSTOWN, 6140, SOUTH AFRICA

AZI NANOSUSPENSION BATCH SUMMARY REPORT

Formulator:	**Sonal Bhana**
Product:	**AZI Nanosuspension**
Batch ID:	**AZI-NS 015**
Batch size:	**35 mL**
Date of manufacture:	**04 March 2025**

Formula:

Item	Material	Quantity	Unit	Batch Amount
1	AZI	0.0286	%w/v	0.010 g
2	Ethanol	14.29	%v/v	5 mL
3	Tween®80	0.1	%w/v	0.0350 g
4	PVP K30	0.125	%w/v	0.0437 g
5	Aqua	q.s. to 35	mL	30 mL

- **Solvent: Ethanol; Antisolvent: Aqua (solvent-antisolvent ratio is 1:6)**

Production equipment used:

Magnetic stirring: Precipitation was performed by dropwise addition of ethanolic AZI solution using a conical dropper into the antisolvent (water containing stabilisers) under magnetic stirring. Dropwise addition over 10 minutes with continuous stirring at 1500 rpm.

Probe sonication: The mixture was probe sonicated for 6 minutes post-precipitation to reduce particle size and ensure uniform dispersion.

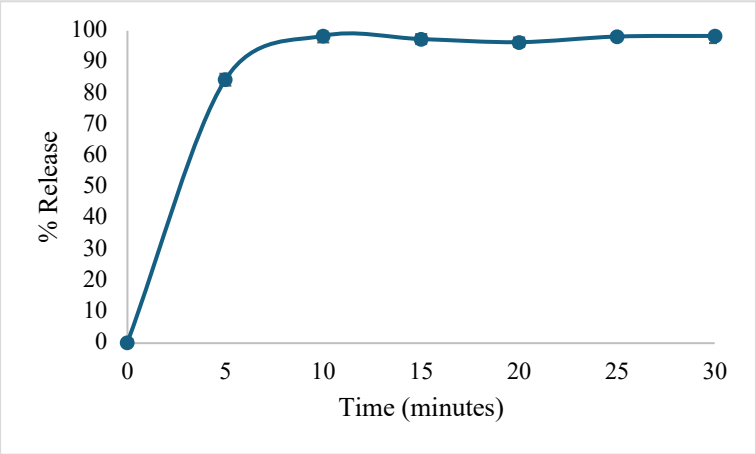

Evaluated parameters and *in vitro* dissolution profile:

ZP (Z-average): 342.4 nm

PS: -27.8 mV

PDI: 0.405

Comments: Formulation was moderately stable and a clear homogenous solution at 22℃.

RHODES UNIVERSITY, FACULTY OF PHARMACY

GRAHAMSTOWN, 6140, SOUTH AFRICA

AZI NANOSUSPENSION BATCH SUMMARY REPORT

Formulator:	**Sonal Bhana**
Product:	**AZI Nanosuspension**
Batch ID:	**AZI-NS 016**
Batch size:	**50 mL**
Date of manufacture:	**04 March 2025**

Formula:

Item	Material	Quantity	Unit	Batch Amount
1	AZI	0.02	%w/v	0.010 g
2	Ethanol	10	%v/v	5 mL
3	Tween®80	0.1	%w/v	0.050 g
4	PVP K30	0.125	%w/v	0.0625 g
5	Aqua	q.s. to 50	mL	45 mL

- **Solvent: Ethanol; Antisolvent: Aqua (solvent-antisolvent ratio is 1:9)**

Production equipment used:

Magnetic stirring: Precipitation was performed by dropwise addition of ethanolic AZI solution using a conical dropper into the antisolvent (water containing stabilisers) under magnetic stirring. Dropwise addition over 10 minutes with continuous stirring at 1500 rpm.

Probe sonication: The mixture was probe sonicated for 6 minutes post-precipitation to reduce particle size and ensure uniform dispersion.

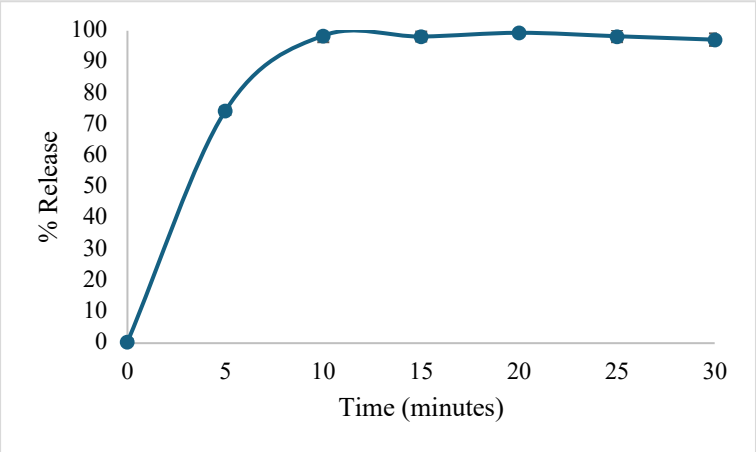

Evaluated parameters and *in vitro* dissolution profile:

ZP (Z-average): 371.9 nm

PS: -24.00 mV

PDI: 0.432

Comments: Formulation was moderately stable and a clear homogenous solution at 22℃.

RHODES UNIVERSITY, FACULTY OF PHARMACY

GRAHAMSTOWN, 6140, SOUTH AFRICA

AZI NANOSUSPENSION BATCH SUMMARY REPORT

Formulator:	**Sonal Bhana**
Product:	**AZI Nanosuspension**
Batch ID:	**AZI-NS 017**
Batch size:	**35 mL**
Date of manufacture:	**04 March 2025**

Formula:

Item	Material	Quantity	Unit	Batch Amount
1	AZI	0.0286	%w/v	0.010 g
2	Ethanol	14.29	%v/v	5 mL
3	Tween®80	0.1	%w/v	0.0350 g
4	PVP K30	0.125	%w/v	0.0437 g
5	Aqua	q.s. to 35	mL	30 mL

- **Solvent: Ethanol; Antisolvent: Aqua (solvent-antisolvent ratio is 1:6)**

Production equipment used:

Magnetic stirring: Precipitation was performed by dropwise addition of ethanolic AZI solution using a conical dropper into the antisolvent (water containing stabilisers) under magnetic stirring. Dropwise addition over 10 minutes with continuous stirring at 1500 rpm.

Probe sonication: The mixture was probe sonicated for 9 minutes post-precipitation to reduce particle size and ensure uniform dispersion.

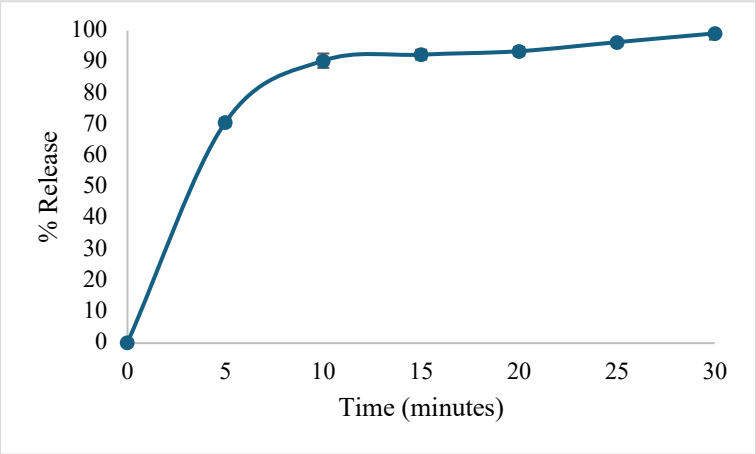

Evaluated parameters and *in vitro* dissolution profile:

ZP (Z-average): 401 nm

PS: -29.8 mV

PDI: 0.448

Comments: Formulation was highly stable and a clear homogenous solution at 22℃.

RHODES UNIVERSITY, FACULTY OF PHARMACY

GRAHAMSTOWN, 6140, SOUTH AFRICA

AZI NANOSUSPENSION BATCH SUMMARY REPORT

Formulator:	**Sonal Bhana**
Product:	**AZI Nanosuspension**
Batch ID:	**AZI-NS 018**
Batch size:	**50 mL**
Date of manufacture:	**04 March 2025**

Formula:

Item	Material	Quantity	Unit	Batch Amount
1	AZI	0.02	%w/v	0.010 g
2	Ethanol	10	%v/v	5 mL
3	Tween®80	0.1	%w/v	0.050 g
4	PVP K30	0.125	%w/v	0.0625 g
5	Aqua	q.s. to 50	mL	45 mL

- **Solvent: Ethanol; Antisolvent: Aqua (solvent-antisolvent ratio is 1:9)**

Production equipment used:

Magnetic stirring: Precipitation was performed by dropwise addition of ethanolic AZI solution using a conical dropper into the antisolvent (water containing stabilisers) under magnetic stirring. Dropwise addition over 10 minutes with continuous stirring at 1500 rpm.

Probe sonication: The mixture was probe sonicated for 3 minutes post-precipitation to reduce particle size and ensure uniform dispersion.

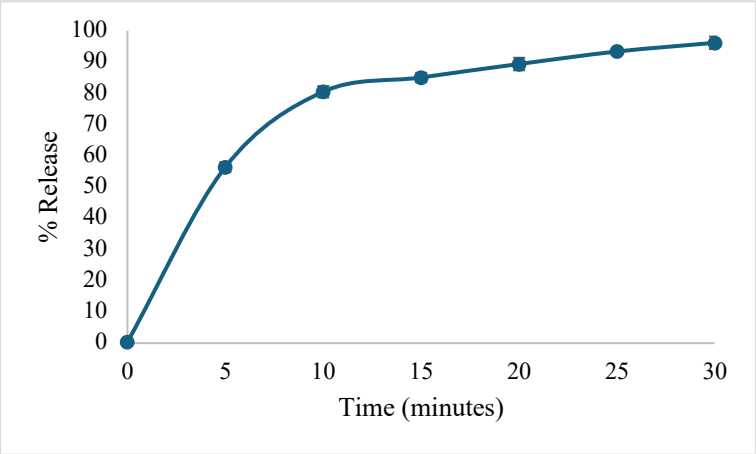

Evaluated parameters and *in vitro* dissolution profile:

ZP (Z-average): 456 nm

PS: -23.8 mV

PDI: 0.739

Comments: Formulation was moderately stable and a clear homogenous solution at 22℃.

RHODES UNIVERSITY, FACULTY OF PHARMACY

GRAHAMSTOWN, 6140, SOUTH AFRICA

AZI NANOSUSPENSION BATCH SUMMARY REPORT

Formulator: **Sonal Bhana**

Product: **AZI Nanosuspension**

Batch ID: **AZI-NS 019**

Batch size: **85 mL**

Date of manufacture: **04 March 2025**

Formula:

Item	Material	Quantity	Unit	Batch Amount
1	AZI	0.0118	%w/v	0.010 g
2	Ethanol	5.88	%v/v	5 mL
3	Tween®80	0.05	%w/v	0.0425 g
4	PVP K30	0.125	%w/v	0.1062 g
5	Aqua	q.s. to 85	mL	80 mL

- **Solvent: Ethanol; Antisolvent: Aqua (solvent-antisolvent ratio is 1:16)**

Production equipment used:

Magnetic stirring: Precipitation was performed by dropwise addition of ethanolic AZI solution using a conical dropper into the antisolvent (water containing stabilisers) under magnetic stirring. Dropwise addition over 10 minutes with continuous stirring at 1500 rpm.

Probe sonication: The mixture was probe sonicated for 3 minutes post-precipitation to reduce particle size and ensure uniform dispersion.

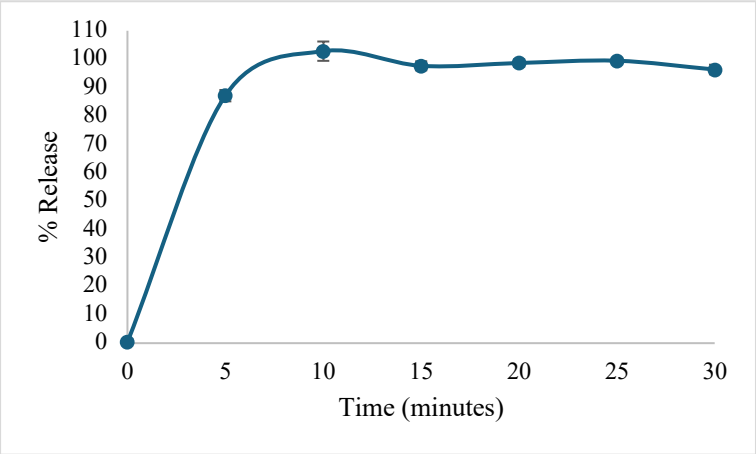

Evaluated parameters and *in vitro* dissolution profile:

ZP (Z-average): 2137 nm

PS: -26.4 mV

PDI: 1.000

Comments: Formulation was moderately stable and a clear homogenous solution at 22℃.

RHODES UNIVERSITY, FACULTY OF PHARMACY

GRAHAMSTOWN, 6140, SOUTH AFRICA

AZI NANOSUSPENSION BATCH SUMMARY REPORT

Formulator:	**Sonal Bhana**
Product:	**AZI Nanosuspension**
Batch ID:	**AZI-NS 020**
Batch size:	**50 mL**
Date of manufacture:	**04 March 2025**

Formula:

Item	Material	Quantity	Unit	Batch Amount
1	AZI	0.02	%w/v	0.010 g
2	Ethanol	10	%v/v	5 mL
3	Tween®80	0.1	%w/v	0.0500 g
4	PVP K30	0.05	%w/v	0.0250 g
5	Aqua	q.s. to 50	mL	45 mL

- **Solvent: Ethanol; Antisolvent: Aqua (solvent-antisolvent ratio is 1:9)**

Production equipment used:

Magnetic stirring: Precipitation was performed by dropwise addition of ethanolic AZI solution using a conical dropper into the antisolvent (water containing stabilisers) under magnetic stirring. Dropwise addition over 10 minutes with continuous stirring at 1500 rpm.

Probe sonication: The mixture was probe sonicated for 6 minutes post-precipitation to reduce particle size and ensure uniform dispersion.

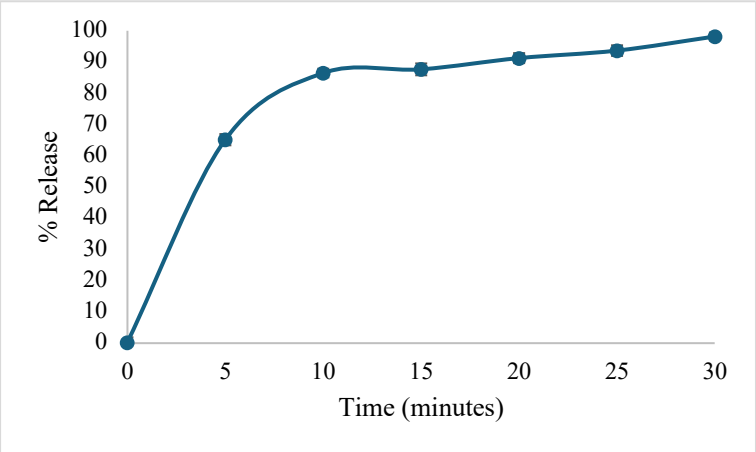

Evaluated parameters and *in vitro* dissolution profile:

ZP (Z-average): 315.9 nm

PS: -23.10 mV

PDI: 0.450

Comments: Formulation was moderately stable and a clear homogenous solution at 22℃.

RHODES UNIVERSITY, FACULTY OF PHARMACY

GRAHAMSTOWN, 6140, SOUTH AFRICA

AZI NANOSUSPENSION BATCH SUMMARY REPORT

Formulator:	**Sonal Bhana**
Product:	**AZI Nanosuspension**
Batch ID:	**AZI-NS 021**
Batch size:	**50 mL**
Date of manufacture:	**04 March 2025**

Formula:

Item	Material	Quantity	Unit	Batch Amount
1	AZI	0.02	%w/v	0.010 g
2	Ethanol	10	%v/v	5 mL
3	Tween®80	0.1	%w/v	0.0500 g
4	PVP K30	0.2	%w/v	0.1000 g
5	Aqua	q.s. to 50	mL	45 mL

- **Solvent: Ethanol; Antisolvent: Aqua (solvent-antisolvent ratio is 1:9)**

Production equipment used:

Magnetic stirring: Precipitation was performed by dropwise addition of ethanolic AZI solution using a conical dropper into the antisolvent (water containing stabilisers) under magnetic stirring. Dropwise addition over 10 minutes with continuous stirring at 1500 rpm.

Probe sonication: The mixture was probe sonicated for 9 minutes post-precipitation to reduce particle size and ensure uniform dispersion.

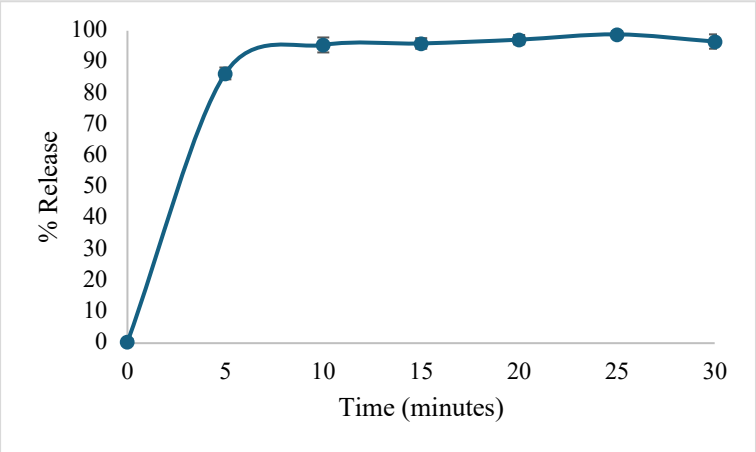

Evaluated parameters and *in vitro* dissolution profile:

ZP (Z-average): 101.3 nm

PS: -24.00 mV

PDI: 0.386

Comments: Formulation was moderately stable and a clear homogenous solution at 22℃.

RHODES UNIVERSITY, FACULTY OF PHARMACY

GRAHAMSTOWN, 6140, SOUTH AFRICA

AZI NANOSUSPENSION BATCH SUMMARY REPORT

Formulator:	**Sonal Bhana**
Product:	**AZI Nanosuspension**
Batch ID:	**AZI-NS 022**
Batch size:	**50 mL**
Date of manufacture:	**04 March 2025**

Formula:

Item	Material	Quantity	Unit	Batch Amount
1	AZI	0.02	%w/v	0.010 g
2	Ethanol	10	%v/v	5 mL
3	Tween®80	0.05	%w/v	0.0250 g
4	PVP K30	0.125	%w/v	0.0625 g
5	Aqua	q.s. to 50	mL	45 mL

- **Solvent: Ethanol; Antisolvent: Aqua (solvent-antisolvent ratio is 1:9)**

Production equipment used:

Magnetic stirring: Precipitation was performed by dropwise addition of ethanolic AZI solution using a conical dropper into the antisolvent (water containing stabilisers) under magnetic stirring. Dropwise addition over 10 minutes with continuous stirring at 1500 rpm.

Probe sonication: The mixture was probe sonicated for 9 minutes post-precipitation to reduce particle size and ensure uniform dispersion.

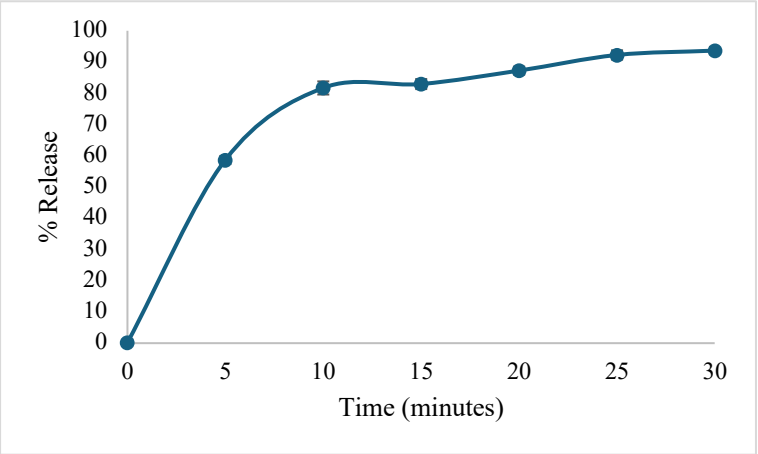

Evaluated parameters and *in vitro* dissolution profile:

ZP (Z-average): 2049 nm

PS: -20.40 mV

PDI: 1.000

Comments: Formulation was moderately stable and a clear homogenous solution at 22℃.

RHODES UNIVERSITY, FACULTY OF PHARMACY

GRAHAMSTOWN, 6140, SOUTH AFRICA

AZI NANOSUSPENSION BATCH SUMMARY REPORT

Formulator:	**Sonal Bhana**
Product:	**AZI Nanosuspension**
Batch ID:	**AZI-NS 023**
Batch size:	**50 mL**
Date of manufacture:	**04 March 2025**

Formula:

Item	Material	Quantity	Unit	Batch Amount
1	AZI	0.02	%w/v	0.010 g
2	Ethanol	10	%v/v	5 mL
3	Tween®80	0.15	%w/v	0.0750 g
4	PVP K30	0.2	%w/v	0.1000 g
5	Aqua	q.s. to 50	mL	45 mL

- **Solvent: Ethanol; Antisolvent: Aqua (solvent-antisolvent ratio is 1:9)**

Production equipment used:

Magnetic stirring: Precipitation was performed by dropwise addition of ethanolic AZI solution using a conical dropper into the antisolvent (water containing stabilisers) under magnetic stirring. Dropwise addition over 10 minutes with continuous stirring at 1500 rpm.

Probe sonication: The mixture was probe sonicated for 6 minutes post-precipitation to reduce particle size and ensure uniform dispersion.

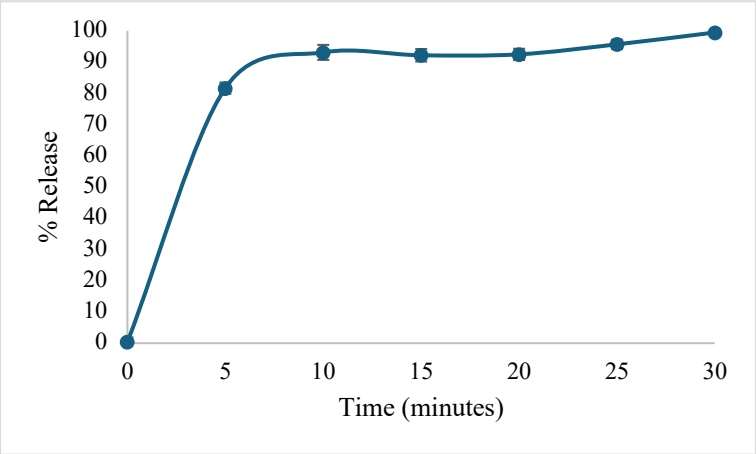

Evaluated parameters and *in vitro* dissolution profile:

ZP (Z-average): 470.5 nm

PS: -28.3 mV

PDI: 0.516

Comments: Formulation was highly stable and a clear homogenous solution at 22℃.

RHODES UNIVERSITY, FACULTY OF PHARMACY

GRAHAMSTOWN, 6140, SOUTH AFRICA

AZI NANOSUSPENSION BATCH SUMMARY REPORT

Formulator:	**Sonal Bhana**
Product:	**AZI Nanosuspension**
Batch ID:	**AZI-NS 024**
Batch size:	**35 mL**
Date of manufacture:	**04 March 2025**

Formula:

Item	Material	Quantity	Unit	Batch Amount
1	AZI	0.0286	%w/v	0.010 g
2	Ethanol	14.29	%v/v	5 mL
3	Tween®80	0.1	%w/v	0.0350 g
4	PVP K30	0.2	%w/v	0.0700 g
5	Aqua	q.s. to 35	mL	30 mL

- **Solvent: Ethanol; Antisolvent: Aqua (solvent-antisolvent ratio is 1:6)**

Production equipment used:

Magnetic stirring: Precipitation was performed by dropwise addition of ethanolic AZI solution using a conical dropper into the antisolvent (water containing stabilisers) under magnetic stirring. Dropwise addition over 10 minutes with continuous stirring at 1500 rpm.

Probe sonication: The mixture was probe sonicated for 3 minutes post-precipitation to reduce particle size and ensure uniform dispersion.

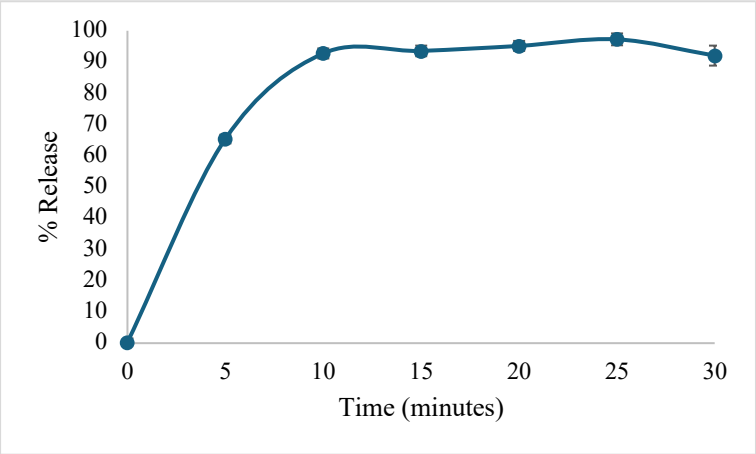

Evaluated parameters and *in vitro* dissolution profile:

ZP (Z-average): 735.4 nm

PS: -21.00 mV

PDI: 1.000

Comments: Formulation was moderately stable and a clear homogenous solution at 22℃.

RHODES UNIVERSITY, FACULTY OF PHARMACY

GRAHAMSTOWN, 6140, SOUTH AFRICA

AZI NANOSUSPENSION BATCH SUMMARY REPORT

Formulator:	**Sonal Bhana**
Product:	**AZI Nanosuspension**
Batch ID:	**AZI-NS 025**
Batch size:	**35 mL**
Date of manufacture:	**04 March 2025**

Formula:

Item	Material	Quantity	Unit	Batch Amount
1	AZI	0.0286	%w/v	0.010 g
2	Ethanol	14.29	%v/v	5 mL
3	Tween®80	0.05	%w/v	0.0175 g
4	PVP K30	0.2	%w/v	0.0700 g
5	Aqua	q.s. to 35	mL	30 mL

- **Solvent: Ethanol; Antisolvent: Aqua (solvent-antisolvent ratio is 1:6)**

Production equipment used:

Magnetic stirring: Precipitation was performed by dropwise addition of ethanolic AZI solution using a conical dropper into the antisolvent (water containing stabilisers) under magnetic stirring. Dropwise addition over 10 minutes with continuous stirring at 1500 rpm.

Probe sonication: The mixture was probe sonicated for 6 minutes post-precipitation to reduce particle size and ensure uniform dispersion.

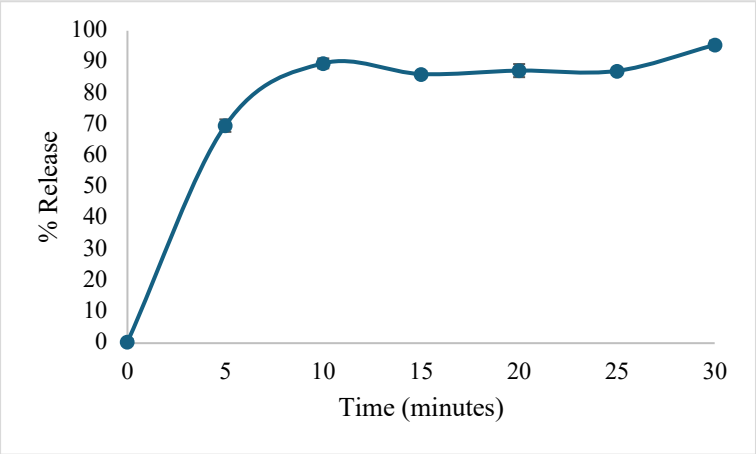

Evaluated parameters and *in vitro* dissolution profile:

ZP (Z-average): 336.2 nm

PS: -23.6 mV

PDI: 1.000

Comments: Formulation was moderately stable and a clear homogenous solution at 22℃.

RHODES UNIVERSITY, FACULTY OF PHARMACY

GRAHAMSTOWN, 6140, SOUTH AFRICA

AZI NANOSUSPENSION BATCH SUMMARY REPORT

Formulator:	**Sonal Bhana**
Product:	**AZI Nanosuspension**
Batch ID:	**AZI-NS 026**
Batch size:	**50 mL**
Date of manufacture:	**04 March 2025**

Formula:

Item	Material	Quantity	Unit	Batch Amount
1	AZI	0.02	%w/v	0.010 g
2	Ethanol	10	%v/v	5 mL
3	Tween®80	0.15	%w/v	0.0750 g
4	PVP K30	0.125	%w/v	0.0625 g
5	Aqua	q.s. to 50	mL	45 mL

- **Solvent: Ethanol; Antisolvent: Aqua (solvent-antisolvent ratio is 1:9)**

Production equipment used:

Magnetic stirring: Precipitation was performed by dropwise addition of ethanolic AZI solution using a conical dropper into the antisolvent (water containing stabilisers) under magnetic stirring. Dropwise addition over 10 minutes with continuous stirring at 1500 rpm.

Probe sonication: The mixture was probe sonicated for 6 minutes post-precipitation to reduce particle size and ensure uniform dispersion.

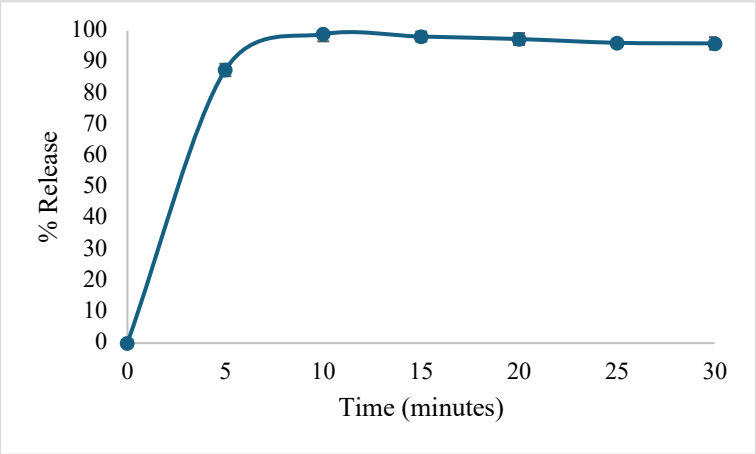

Evaluated parameters and *in vitro* dissolution profile:

ZP (Z-average): 99.37 nm

PS: -26.6 mV

PDI: 0.312

Comments: Formulation was moderately stable and a clear homogenous solution at 22℃.

RHODES UNIVERSITY, FACULTY OF PHARMACY

GRAHAMSTOWN, 6140, SOUTH AFRICA

AZI NANOSUSPENSION BATCH SUMMARY REPORT

Formulator:	**Sonal Bhana**
Product:	**AZI Nanosuspension**
Batch ID:	**AZI-NS 027**
Batch size:	**85 mL**
Date of manufacture:	**04 March 2025**

Formula:

Item	Material	Quantity	Unit	Batch Amount
1	AZI	0.0118	%w/v	0.010 g
2	Ethanol	5.88	%v/v	5 mL
3	Tween®80	0.1	%w/v	0.0850 g
4	PVP K30	0.2	%w/v	0.1700 g
5	Aqua	q.s. to 85	mL	80 mL

- **Solvent: Ethanol; Antisolvent: Aqua (solvent-antisolvent ratio is 1:16)**

Production equipment used:

Magnetic stirring: Precipitation was performed by dropwise addition of ethanolic AZI solution using a conical dropper into the antisolvent (water containing stabilisers) under magnetic stirring. Dropwise addition over 10 minutes with continuous stirring at 1500 rpm.

Probe sonication: The mixture was probe sonicated for 6 minutes post-precipitation to reduce particle size and ensure uniform dispersion.

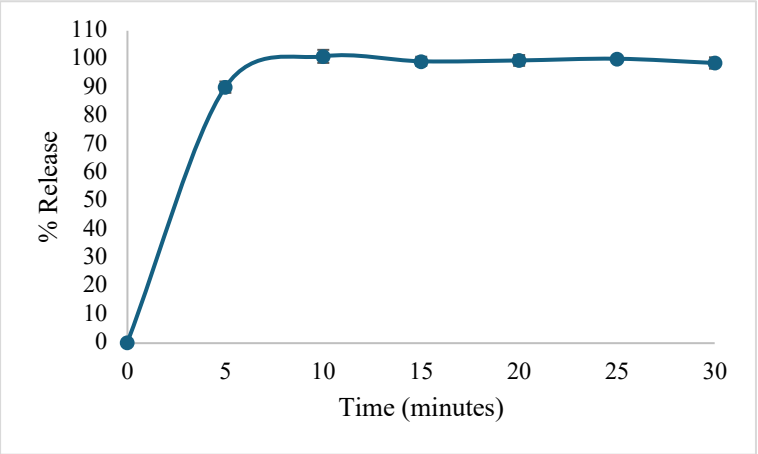

Evaluated parameters and *in vitro* dissolution profile:

ZP (Z-average): 321.2 nm

PS: -24.8 mV

PDI: 0.466

Comments: Formulation was moderately stable and a clear homogenous solution at 22℃.

RHODES UNIVERSITY, FACULTY OF PHARMACY

GRAHAMSTOWN, 6140, SOUTH AFRICA

AZI NANOSUSPENSION BATCH SUMMARY REPORT

Formulator:	**Sonal Bhana**
Product:	**AZI Nanosuspension**
Batch ID:	**AZI-NS 028**
Batch size:	**50 mL**
Date of manufacture:	**04 March 2025**

Formula:

Item	Material	Quantity	Unit	Batch Amount
1	AZI	0.02	%w/v	0.010 g
2	Ethanol	10	%v/v	5 mL
3	Tween®80	0.15	%w/v	0.050 g
4	PVP K30	0.05	%w/v	0.0625 g
5	Aqua	q.s. to 50	mL	45 mL

- **Solvent: Ethanol; Antisolvent: Aqua (solvent-antisolvent ratio is 1:9)**

Production equipment used:

Magnetic stirring: Precipitation was performed by dropwise addition of ethanolic AZI solution using a conical dropper into the antisolvent (water containing stabilisers) under magnetic stirring. Dropwise addition over 10 minutes with continuous stirring at 1500 rpm.

Probe sonication: The mixture was probe sonicated for 6 minutes post-precipitation to reduce particle size and ensure uniform dispersion.

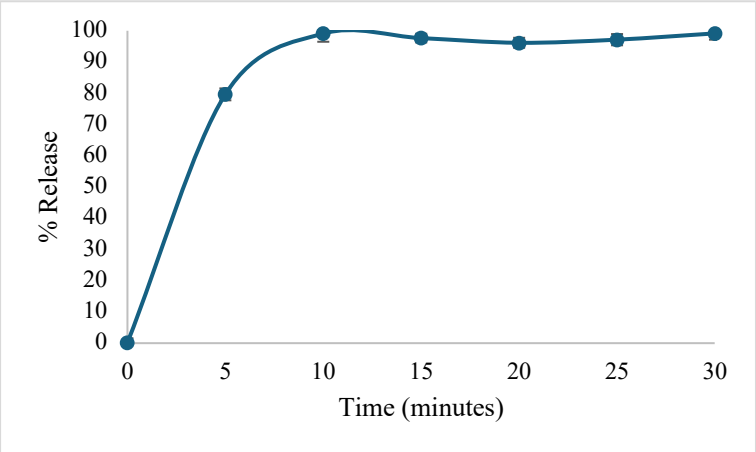

Evaluated parameters and *in vitro* dissolution profile:

ZP (Z-average): 651.8 nm

PS: -24.9 mV

PDI: 0.699

Comments: Formulation was moderately stable and a clear homogenous solution at 22℃.

RHODES UNIVERSITY, FACULTY OF PHARMACY

GRAHAMSTOWN, 6140, SOUTH AFRICA

AZI NANOSUSPENSION BATCH SUMMARY REPORT

Formulator:	**Sonal Bhana**
Product:	**AZI Nanosuspension**
Batch ID:	**AZI-NS 029**
Batch size:	**50 mL**
Date of manufacture:	**04 March 2025**

Formula:

Item	Material	Quantity	Unit	Batch Amount
1	AZI	0.02	%w/v	0.010 g
2	Ethanol	10	%v/v	5 mL
3	Tween®80	0.05	%w/v	0.050 g
4	PVP K30	0.125	%w/v	0.0625 g
5	Aqua	q.s. to 50	mL	45 mL

- **Solvent: Ethanol; Antisolvent: Aqua (solvent-antisolvent ratio is 1:9)**

Production equipment used:

Magnetic stirring: Precipitation was performed by dropwise addition of ethanolic AZI solution using a conical dropper into the antisolvent (water containing stabilisers) under magnetic stirring. Dropwise addition over 10 minutes with continuous stirring at 1500 rpm.

Probe sonication: The mixture was probe sonicated for 9 minutes post-precipitation to reduce particle size and ensure uniform dispersion.

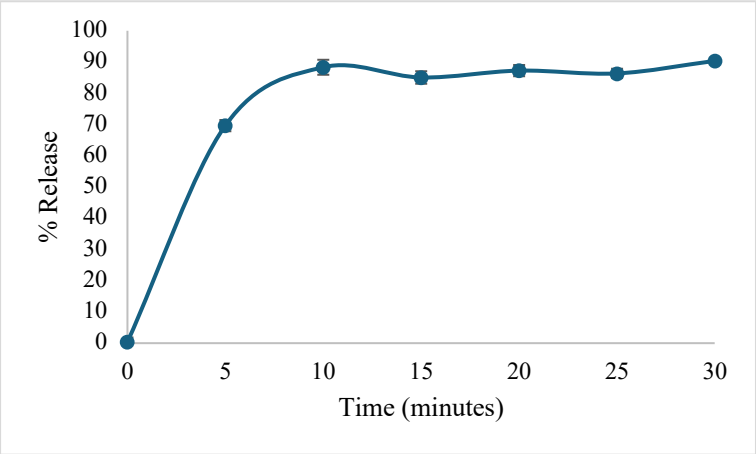

Evaluated parameters and *in vitro* dissolution profile:

ZP (Z-average): 400.8 nm

PS: -23.7 mV

PDI: 0.865

Comments: Formulation was moderately stable and a clear homogenous solution at 22℃.

REFERENCES

1. Hoepelman IM, Schneider MME. Azithromycin: the first of the tissue-selective azalides. International Journal of Antimicrobial Agents. 1995 May;5(3):145–67.

2. Ballow CH, Amsden GW. Azithromycin: The First Azalide Antibiotic. Ann Pharmacother. 1992 Oct;26(10):1253–61.

3. British Pharmacopoeia 2024 (Ph. Eur. 11.5 update) Online [Internet]. [cited 2024 Apr 10]. Available from: https://0-www.pharmacopoeia.com.wam.seals.ac.za/bp-2024/monographs/azithromycin.html?date=2024-07-01&text=azithromycin+monograph

4. United States Pharmacopeia 29th Edition. [Internet]. [cited 2024 Apr 10]. Available from: http://www.pharmacopeia.cn/v29240/usp29nf24s0_m6740.html

5. Japanese Pharmacopoeia 18th Edition. [Internet]. [cited 2024 Apr 10]. Available from: https://www.mhlw.go.jp/content/11120000/000904440.pdf

6. Raval M, Bagada H. Preparation, Solid-State Characterization, Phase Solubility and Dissolution Studies of Azithromycin/Hydroxypropyl-β- Cyclodextrin Host-Guest System. IJPI. 2019 Dec 16;9(4):174–9.

7. Arora SC, Sharma PK, Irchhaiya R, Khatkar A, Singh N, Gagoria J. Development, characterization and solubility study of solid dispersions of azithromycin dihydrate by solvent evaporation method. J Adv Pharm Technol Res. 2010;1(2):221–8.

8. Gandhi R, Pillai O, Thilagavathi R, Gopalakrishnan B, Kaul CL, Panchagnula R. Characterization of Azithromycin hydratesq. European Journal of Pharmaceutical Sciences. 2002;

9. McFarland JW, Berger CM, Froshauer SA, Hayashi SF, Hecker SJ, Jaynes BH, et al. Quantitative Structure−Activity Relationships among Macrolide Antibacterial Agents: In Vitro and in Vivo Potency against *Pasteurella multocida*. J Med Chem. 1997 Apr 1;40(9):1340–6.

10. Charman SA, Andreu A, Barker H, Blundell S, Campbell A, Campbell M, et al. An in vitro toolbox to accelerate anti-malarial drug discovery and development. Malar J. 2020 Dec;19(1):1.

11. Goldman RC, Fesik SW, Doran CC. Role of protonated and neutral forms of macrolides in binding to ribosomes from gram-positive and gram-negative bacteria. Antimicrob Agents Chemother. 1990 Mar;34(3):426–31.

12. Kong FYS, Horner P, Unemo M, Hocking JS. Pharmacokinetic considerations regarding the treatment of bacterial sexually transmitted infections with azithromycin: a review. Journal of Antimicrobial Chemotherapy. 2019 May 1;74(5):1157–66.

13. Mandić Z, Weitner Z, Ilijaš M. Electrochemical oxidation of azithromycin and its derivatives. Journal of Pharmaceutical and Biomedical Analysis. 2003 Nov;33(4):647–54.

14. Donovan SF, Pescatore MC. Method for measuring the logarithm of the octanol–water partition coefficient by using short octadecyl–poly(vinyl alcohol) high-performance liquid chromatography columns. Journal of Chromatography A. 2002 Apr;952(1–2):47–61.

15. Poole SK, Poole CF. Separation methods for estimating octanol–water partition coefficients. Journal of Chromatography B. 2003 Nov;797(1–2):3–19.

16. Chanteux H, Van Bambeke F, Mingeot-Leclercq MP, Tulkens PM. Accumulation and Oriented Transport of Ampicillin in Caco-2 Cells from Its Pivaloyloxymethylester Prodrug, Pivampicillin. Antimicrob Agents Chemother. 2005 Apr;49(4):1279–88.

17. Coates J. Interpretation of Infrared Spectra, A Practical Approach. In: Meyers RA, editor. Encyclopedia of Analytical Chemistry [Internet]. 1st ed. Wiley; 2000 [cited 2024 Apr 27]. Available from: https://onlinelibrary.wiley.com/doi/10.1002/9780470027318.a5606

18. Silverstein RM, Webster FX, Kiemle DJ. Spectrometric identification of organic compounds. 7th ed. Hoboken, NJ: John Wiley & Sons; 2005. 502 p.

19. Maddukuri S, Gv R. Formulation and Characterisation of Azithromycin Dihydrate Inclusion Complexes Using Derivatives of B-Cyclodextrins as Complexing Agents. Int Res J Pharm. 2019 Sep 6;10(8):77–85.

20. Timoumi S, Mangin D, Peczalski R, Zagrouba F, Andrieu J. Stability and thermophysical properties of azithromycin dihydrate. Arabian Journal of Chemistry. 2014 Apr;7(2):189–95.

21. Wu YJ. Highlights of Semi-synthetic Developments from Erythromycin A. CPD. 2000 Jan 1;6(2):181–223.

22. Mutak S. Azalides from Azithromycin to New Azalide Derivatives. J Antibiot. 2007 Feb;60(2):85–122.

23. Fiese EF, Steffen SH. Comparison of the acid stability of azithromycin and erythromycin A. Journal of Antimicrobial Chemotherapy. 1990 Jan 1;25(suppl A):39–47.

24. Davidson RJ. In vitro activity and pharmacodynamic/pharmacokinetic parameters of clarithromycin and azithromycin: why they matter in the treatment of respiratory tract infections. IDR. 2019 Mar;Volume 12:585–96.

25. Fiese EF, Steffen SH. Comparison of the acid stability of azithromycin and erythromycin A. Journal of Antimicrobial Chemotherapy. 1990 Jan 1;25(suppl A):39–47.

26. Pesachovich M, Isaacs S, Singer C, Saba K, Schwartz E. Degradation products of azithromycin, and methods for the indentification.

27. Mekasha YT, Chali BU, Feissa AB, Godena GH, Hassen HK, Wega SS. Quality evaluation of the Azithromycin tablets commonly marketed in Adama, and Modjo towns, Oromia Regional State, Ethiopia. PLoS One. 2023 Mar 2;18(3):e0282156.

28. Fohner AE, Sparreboom A, Altman RB, Klein TE. PharmGKB summary: Macrolide antibiotic pathway, pharmacokinetics/pharmacodynamics. Pharmacogenetics and Genomics. 2017 Apr;27(4):164–7.

29. Parnham MJ, Haber VE, Giamarellos-Bourboulis EJ, Perletti G, Verleden GM, Vos R. Azithromycin: Mechanisms of action and their relevance for clinical applications. Pharmacology & Therapeutics. 2014 Aug;143(2):225–45.

30. Heidary M, Ebrahimi Samangani A, Kargari A, Kiani Nejad A, Yashmi I, Motahar M, et al. Mechanism of action, resistance, synergism, and clinical implications of azithromycin. J Clin Lab Anal. 2022 Apr 21;36(6):e24427.

31. Amsden GW. Advanced-generation macrolides: tissue-directed antibiotics. International Journal of Antimicrobial Agents. 2001 Sep;18:11–5.

32. Amsden G. Erythromycin, clarithromycin, and azithromycin: are the differences real? Clinical Therapeutics. 1996 Feb;18(1):56–72.

33. Cunha BA. The atypical pneumonias: clinical diagnosis and importance. Clin Microbiol Infect. 2006 May;12 Suppl 3:12–24.

34. Qiu S, Zhong X. Macrolides: a promising pharmacologic therapy for chronic obstructive pulmonary disease. Ther Adv Respir Dis. 2017 Mar;11(3):147–55.

35. Yeo YH, Shiu SI, Ho HJ, Zou B, Lin JT, Wu MS, et al. First-line Helicobacter pylori eradication therapies in countries with high and low clarithromycin resistance: A systematic review and network meta-analysis. Gut. 2018;67(1):20–7.

36. Garau J. The clinical impact of macrolide resistance in pneumococcal respiratory infections. International Journal of Antimicrobial Agents. 2001 Sep;18:33–8.

37. Retsema J, Fu W. Macrolides: structures and microbial targets. International Journal of Antimicrobial Agents. 2001 Sep;18:3–10.

38. Bergman M, Huikko S, Huovinen P, Paakkari P, Seppälä H. Macrolide and Azithromycin Use Are Linked to Increased Macrolide Resistance in Streptococcus pneumoniae. Antimicrob Agents Chemother. 2006 Nov;50(11):3646–50.

39. Karlowsky JA, Lagacé-Wiens PRS, Low DE, Zhanel GG. Annual macrolide prescription rates and the emergence of macrolide resistance among Streptococcus pneumoniae in Canada from 1995 to 2005. International Journal of Antimicrobial Agents. 2009 Oct;34(4):375–9.

40. Munita JM, Arias CA. Mechanisms of Antibiotic Resistance. Microbiol Spectr. 2016 Apr;4(2):10.1128/microbiolspec.VMBF-0016–2015.

41. Marosevic D, Kaevska M, Jaglic Z. Resistance to the tetracyclines and macrolide-lincosamide-streptogramin group of antibiotics and its genetic linkage – a review. Ann Agric Environ Med. 2017 Jun 12;24(2):338–44.

42. Treadway G, Reisman A. Tolerability of 3-day, once-daily azithromycin suspension versus standard treatments for community-acquired paediatric infectious diseases. International Journal of Antimicrobial Agents. 2001 Nov;18(5):427–31.

43. Pacifico L, Chiesa C. Azithromycin in children: A critical review of the evidence. Current Therapeutic Research. 2002 Jan;63(1):54–76.

44. Zithromax product information. [Internet]. Pfizer Laboratories; [cited 2024 Apr 10]. Available from: https://labeling.pfizer.com/ShowLabeling.aspx?id=15258

45. Zithromax Suspension product information [Internet]. South African Health Products Regulatory Authority; [cited 2024 Apr 10]. Available from: https://www.sahpra.org.za/wp-content/uploads/2020/02/Zithromax-Suspension_PI_Pfizer_MCC-format-26-June-2015.pdf

46. Martindale. The complete drug reference 33rd Edition. Pharmaceutical Press (PhP), London. 2002, pp 153.

47. Amacher DE, Schomaker SJ, Retsema JA. Comparison of the effects of the new azalide antibiotic, azithromycin, and erythromycin estolate on rat liver cytochrome P-450 - PubMed. Antimicrobial Agents and Chemotherapy. 1991;35(6):1186–90.

48. Chave JP, Munafo A, Chatton JY, Dayer P, Glauser MP, Biollaz J. Once-a-week azithromycin in AIDS patients: tolerability, kinetics, and effects on zidovudine disposition. Antimicrob Agents Chemother. 1992 May;36(5):1013–8.

49. Choi Y, Lim HS, Chung D, Choi J gu, Yoon D. Risk Evaluation of Azithromycin-Induced QT Prolongation in Real-World Practice. Biomed Res Int. 2018 Oct 14;2018:1574806.

50. Ikeda AK, Prince AA, Chen JX, Lieu JEC, Shin JJ. Macrolide-associated sensorineural hearing loss: A systematic review. Laryngoscope. 2018 Jan;128(1):228–36.

51. Berger FA. Drug Induced QTC-Prolongation: Towards a better understanding of understanding potential risks. Colofon.

52. Keskin-Arslan E, Kaplan YC, Koren G. Use of azithromycin during pregnancy and breastfeeding: A coronavirus pan- demic (COVID-19) update.

53. Antonucci R, Cuzzolin L, Locci C, Dessole F, Capobianco G. Use of Azithromycin in Pregnancy: More Doubts than Certainties. Clin Drug Investig. 2022 Nov;42(11):921–35.

54. Drew RH, Gallis HA. Azithromycin--spectrum of activity, pharmacokinetics, and clinical applications. Pharmacotherapy. 1992;12(3):161–73.

55. Foulds G, Shepard RM, Johnson RB. The pharmacokinetics of azithromycin in human serum and tissues. J Antimicrob Chemother. 1990 Jan;25 Suppl A:73–82.

56. Rapp RP. Pharmacokinetics and pharmacodynamics of intravenous and oral azithromycin: enhanced tissue activity and minimal drug interactions. Ann Pharmacother. 1998;32(7–8):785–93.

57. Mennella JA, Spector AC, Reed DR, Coldwell SE. The Bad Taste of Medicines: Overview of Basic Research on Bitter Taste. Clinical Therapeutics. 2013 Aug 1;35(8):1225–46.

58. Neu HC. Clinical microbiology of azithromycin. Am J Med. 1991 Sep 12;91(3A):12S-18S.

59. Dunn CJ, Barradell LB. Azithromycin. A review of its pharmacological properties and use as 3-day therapy in respiratory tract infections. Drugs. 1996 Mar;51(3):483–505.

60. Di Paolo A, Barbara C, Chella A, Angeletti CA, Del Tacca M. Pharmacokinetics of azithromycin in lung tissue, bronchial washing, and plasma in patients given multiple oral doses of 500 and 1000 mg daily. Pharmacol Res. 2002 Dec;46(6):545–50.

61. Blandizzi C, Malizia T, Batoni G, Ghelardi E, Baschiera F, Bruschini P, et al. Distribution of Azithromycin in Plasma and Tonsil Tissue after Repeated Oral Administration of 10 or 20 Milligrams per Kilogram in Pediatric Patients. Antimicrob Agents Chemother. 2002 May;46(5):1594–6.

62. Stein GE, Schooley S. Comparative serum bactericidal activity of clarithromycin and azithromycin against macrolide-sensitive and resistant strains of Streptococcus pneumoniae. Diagn Microbiol Infect Dis. 2001 Mar;39(3):181–5.

63. Hunter RP, Koch DE, Coke RL, Goatley MA, Isaza R. Azithromycin metabolite identification in plasma, bile, and tissues of the ball python (Python regius). J Vet Pharmacol Ther. 2003 Apr;26(2):117–21.

64. Peters DH, Friedel HA, McTavish D. Azithromycin. A review of its antimicrobial activity, pharmacokinetic properties and clinical efficacy. Drugs. 1992 Nov;44(5):750–99.

65. Lalak NJ, Morris DL. Azithromycin clinical pharmacokinetics. Clin Pharmacokinet. 1993 Nov;25(5):370–4.

66. Abdu Hussen A. High-Performance Liquid Chromatography (HPLC): A review. Ann Adv Chem. 2022 Jun 20;6(1):010–20.

67. Sadaphal P, Dhamak K. Review article on High-Performance Liquid Chromatography (HPLC) Method Development and Validation. IJPSRR. 2022 Jun 15;23–9.

68. Sahu PK, Ramisetti NR, Cecchi T, Swain S, Patro CS, Panda J. An overview of experimental designs in HPLC method development and validation. Journal of Pharmaceutical and Biomedical Analysis. 2018 Jan;147:590–611.

69. Waghule SN, Jain NP, Patani CJ, Patani AC. Method development and validation of HPLC method for determination of azithromycin. 2013;

70. Patil PN. HPLC Method Development - a Review. JPRE. 2017;1(2):243–60.

71. Zubata P, Ceresole R, Rosasco MA, Pizzorno MT. A new HPLC method for azithromycin quantitation. Journal of Pharmaceutical and Biomedical Analysis. 2002 Feb;27(5):833–6.

72. Kamau FN, Chepkwony HK, Ngugi JK, Debremaeker D, Roets E, Hoogmartens J. Isocratic liquid chromatographic method for the analysis of azithromycin and its structurally related substances in bulk samples. J Chromatogr Sci. 2002 Oct;40(9):529–33.

73. Miguel L, Barbas C. LC determination of impurities in azithromycin tablets. J Pharm Biomed Anal. 2003 Sep 19;33(2):211–7.

74. Ghari T, Kobarfard F, Mortazavi SA. Development of a Simple RP-HPLC-UV Method for Determination of Azithromycin in Bulk and Pharmaceutical Dosage forms as an Alternative to the USP Method. Iran J Pharm Res. 2013;12(Suppl):57–63.

75. Al-Hakkani MF. A rapid, developed and validated RP-HPLC method for determination of azithromycin. SN Appl Sci. 2019 Feb 11;1(3):222.

76. Okaru AO, Abuga KO, Kamau FN, Ndwigah SN, Lachenmeier DW. A Robust Liquid Chromatographic Method for Confirmation of Drug Stability of Azithromycin in Bulk Samples, Tablets and Suspensions. Pharmaceutics. 2017 Feb 24;9(1):11.

77. Reem Abou A, Darwis Y. Development and validation of a stability-indicating RP-HPLC method for the detection and quantification of azithromycin in bulk, and self-emulsifying drug delivery system (SEDDs) formulation. J App Pharm Sci. 2017;7(9):20–9.

78. Al-Rimawi F, Kharoaf M. Analysis of Azithromycin and Its Related Compounds by RP-HPLC with UV Detection. Journal of Chromatographic Science. 2010 Feb 1;48(2):86–90.

79. Stojanović J, Krmar J, Protić A, Svrkota B, Đajić N, Otašević B. Experimental design in HPLC separation of pharmaceuticals. Arhiv za farmaciju. 2021;71(4):279–301.

80. Bezerra MA, Santelli RE, Oliveira EP, Villar LS, Escaleira LA. Response surface methodology (RSM) as a tool for optimization in analytical chemistry. Talanta. 2008 Sep 15;76(5):965–77.

81. Bhattacharya S. Central Composite Design for Response Surface Methodology and Its Application in Pharmacy. In: Response Surface Methodology in Engineering Science. IntechOpen; 2006.

82. Ferreira SLC, Bruns RE, Ferreira HS, Matos GD, David JM, Brandão GC, et al. Box-Behnken design: an alternative for the optimization of analytical methods. Anal Chim Acta. 2007 Aug 6;597(2):179–86.

83. Žuvela P, Skoczylas M, Jay Liu J, Bączek T, Kaliszan R, Wong MW, et al. Column Characterization and Selection Systems in Reversed-Phase High-Performance Liquid Chromatography. Chem Rev. 2019 Mar 27;119(6):3674–729.

84. Raines DA, Yusuf A, Jabak MH, Ahmed WS, Karcioglu ZA, El-Yazigi A. Simultaneous high-performance liquid chromatography analysis of azithromycin and two of its metabolites in human tears and plasma. Ther Drug Monit. 1998 Dec;20(6):680–4.

85. Rafferty JL, Siepmann JI, Schure MR. Molecular-Level Comparison of Alkylsilane and Polar-Embedded Reversed-Phase Liquid Chromatography Systems. Anal Chem. 2008 Aug 1;80(16):6214–21.

86. Ravisankar P, Anusha S, Supriya K, Kumar UA. Fundamental Chromatographic Parameters. (09).

87. Varma MM, Thulluru A, Kumar KTS, Kumar GS, Pavani K. HPLC method development and validation: a review. World Journal of Pharmaceutical Research.

88. FDA/CDER/"Beers D. Analytical Procedures and Methods Validation for Drugs and Biologics. 2015;

89. Singh AP, Chauhan I, Bhardwaj S, Gaur P, Kumar SS, J J. HPLC method development and validation for azithro-mycin in oral suspension. J App Pharm Sci Res. 2019 Apr 4;7–12.

90. L.C. Passos M, M.F.S. Saraiva ML. Detection in UV-visible spectrophotometry: Detectors, detection systems, and detection strategies. Measurement. 2019 Mar 1;135:896–904.

91. Kumar R, Reji M. Response surface methodology (RSM): An overview to analyze multivariate data. IJMR. 2023 Jan 28;9(4):241–8.

92. ICH Q2(R1): Validation of Analytical Procedures: Text and Methodology [Internet]. International Council for Harmonisation (ICH); 2005 [cited 2024 Dec 8]. Available from: https://www.ich.org/page/quality-guidelines

93. Blessy M, Patel RD, Prajapati PN, Agrawal YK. Development of forced degradation and stability indicating studies of drugs—A review. Journal of Pharmaceutical Analysis. 2014 Jun 1;4(3):159–65.

94. Chingunpituk J. Nanosuspension Technology for Drug Delivery. Walailak Journal of Science and Technology. 2007;4(2):139–53.

95. Patel VR, Agrawal YK. Nanosuspension: An approach to enhance solubility of drugs. Journal of Advanced Pharmaceutical Technology & Research. 2011 Jun;2(2):81.

96. Zhang D, Tan T, Gao L, Zhao W, Wang P. Preparation of azithromycin nanosuspensions by high pressure homogenization and its physicochemical characteristics studies. Drug development and industrial pharmacy. 2007;33(5):569–75.

97. Sattar A, Chen D, Jiang L, Pan Y, Tao Y, Huang L, et al. Preparation, characterization and pharmacokinetics of cyadox nanosuspension. Sci Rep. 2017 May 23;7(1):2289.

98. Maddukuri S, Srawanthi P, Metta S, Gv R, Ks MK. Screening of Stabilizers in Azithromycin Nanosuspensions. (15).

99. Mosby C. Colloids. Journal of Applied Pharmaceutical Science. 2023;1(1):2–26.

100. Flowers P, Theopold K, Richard L, William R. Chemistry 2e: Colloids. OpenStax. 2019;1(3).

101. Park H, Otte A, Park K. Evolution of Drug Delivery Systems: From 1950 to 2020 and Beyond. Journal of controlled release : official journal of the Controlled Release Society. 2021 Dec 29;342:53.

102. Ezike TC, Okpala US, Onoja UL, Nwike CP, Ezeako EC, Okpara OJ, et al. Advances in drug delivery systems, challenges and future directions. Heliyon. 2023 Jun 24;9(6):e17488.

103. Boyd BJ. Past and future evolution in colloidal drug delivery systems. Expert opinion on drug delivery. 2008;5(1):69–85.

104. Hoffman A. The origins and evolution of “controlled” drug delivery systems. Journal of controlled release : official journal of the Controlled Release Society. 2008;132(3):153–63.

105. Kaushik D, Kumar P, Sardana S. Design Development and Evaluation of Nanosuspension of Azithromycin. 2015;7(5).

106. Shariare MH, Mondal TK, Alothaid H. Azithromycin Nanosuspension Preparation using Evaporative Precipitation into the Aqueous Solution (EPAS) Method and its Comparative Dissolution Study. Current Pharmaceutical Analysis. 2021 Jan 10;17(9):1224–31.

107. Saddik MS, Elsayed MMA, El-Mokhtar MA, Sedky H, Abdel-Aleem JA, Abu-Dief AM, et al. Tailoring of Novel Azithromycin-Loaded Zinc Oxide Nanoparticles for Wound Healing. Pharmaceutics. 2022 Jan 5;14(1):111.

108. Jarvis M, Krishnan V, Mitragotri S. Nanocrystals: A perspective on translational research and clinical studies. Bioeng Transl Med. 2018 Dec 24;4(1):5–16.

109. Pardhi VP, Verma T, Flora SJS, Chandasana H, Shukla R. Nanocrystals: An Overview of Fabrication, Characterization and Therapeutic Applications in Drug Delivery. Curr Pharm Des. 2018;24(43):5129–46.

110. Alshawwa SZ, Kassem AA, Farid RM, Mostafa SK, Labib GS. Nanocarrier Drug Delivery Systems: Characterization, Limitations, Future Perspectives and Implementation of Artificial Intelligence. Pharmaceutics. 2022 Apr 18;14(4):883.

111. A. Witika B, E. Choonara Y, H. Demana P. A SWOT analysis of nano co-crystals in drug delivery: present outlook and future perspectives. RSC Advances. 2023;13(11):7339–51.

112. Lhaglham P, Jiramonai L, Jia Y, Huang B, Huang Y, Gao X, et al. Drug nanocrystals: Surface engineering and its applications in targeted delivery. iScience. 2024 Oct 16;27(11):111185.

113. Keck C, Muller R. Drug nanocrystals of poorly soluble drugs produced by high pressure homogenisation. European Journal of Pharmaceutics and Biopharmaceutics. 2006 Jan;62(1):3–16.

114. Kesisoglou F, Panmai S, Wu Y. Nanosizing — Oral formulation development and biopharmaceutical evaluation. Advanced Drug Delivery Reviews. 2007 Jul;59(7):631–44.

115. Müller R, Junghanns. Nanocrystal technology, drug delivery and clinical applications. IJN. 2008 Oct;295.

116. Pınar SG, Oktay AN, Karaküçük AE, Çelebi N. Formulation Strategies of Nanosuspensions for Various Administration Routes. Pharmaceutics. 2023 May 17;15(5):1520.

117. Joshi K, Chandra A, Jain K, Talegaonkar S. Nanocrystalization: An Emerging Technology to Enhance the Bioavailability of Poorly Soluble Drugs. Pharm Nanotechnol. 2019 Dec;7(4):259–78.

118. Vinchhi P, Patel JK, Patel MM. High-Pressure Homogenization Techniques for Nanoparticles. In: Patel JK, Pathak YV, editors. Emerging Technologies for Nanoparticle Manufacturing. 2021. p. 263–85.

119. Miniewicz A, Ślemp M, Pfleger J. Organic Nanocrystal Fabrication Using the Process of Resonant Second-Harmonic Generation of Light. ACS Omega. 2021 Apr 15;6(16):10547.

120. Alphandéry E. Ultrasound and nanomaterial: an efficient pair to fight cancer. Journal of Nanobiotechnology. 2022 Mar 18;20(1):139.

121. Gigliobianco MR, Casadidio C, Censi R, Di Martino P. Nanocrystals of Poorly Soluble Drugs: Drug Bioavailability and Physicochemical Stability. Journal of Pharmaceutical Sciences. 2018;3(10):134.

122. Li J, Wang Z, Zhang H, Gao J, Zheng A. Progress in the development of stabilization strategies for nanocrystal preparations. Drug Deliv. 28(1):19–36.

123. Chang TL, Zhan H, Liang D, Liang JF. Nanocrystal technology for drug formulation and delivery. Front Chem Sci Eng. 2015 Mar;9(1):1–14.

124. Masuda Y, editor. Nanocrystal. 1st ed. InTech; 2011. 504 p. (Colloidal Hybrid Nanocrystals: Synthesis, Properties, and Perspectives; vol. 1).

125. Neuville DR, Cornier L, Caurant D, Montagne L. From Glass to Crystal: Nucleation, Growth and Phase Separation: from Research to Applications. Les Ulis, FRANCE: EDP Sciences; 2017.

126. Erdemir D, Lee AY, Myerson AS. Nucleation of Crystals from Solution: Classical and Two-Step Models. Acc Chem Res. 2009 May 19;42(5):621–9.

127. Billot P, Couty M, Hosek P. Application of ATR-UV Spectroscopy for Monitoring the Crystallisation of UV Absorbing and Nonabsorbing Molecules. Org Process Res Dev. 2010 May 21;14(3):511–23.

128. Kotadiya N, Prajapati BG, Bhattacharya S. Atorvastatin Calcium nanoparticles using solvent-anti-solvent precipitation method. Journal of Science and Technology. 2016;11(4).

129. Zhang Hx, Wang Jx, Zhang Zb, Le Y, Shen Zg, Chen Jf. Micronization of atorvastatin calcium by antisolvent precipitation process. International journal of pharmaceutics. 2009;374(1–2):106–13.

130. Jakubowska E, Milanowski B, Lulek J. A Systematic Approach to the Development of Cilostazol Nanosuspension by Liquid Antisolvent Precipitation (LASP) and Its Combination with Ultrasound. Int J Mol Sci. 2021 Nov 17;22(22):12406.

131. Gupta L, Devnarayan D, Kumar R. Experimental Study of Particle Size Reduction of Albendazole by Antisolvent Precipitation Method. International Advances in Chemical Engineering. 2020 Feb 6;2(4).

132. Ji M, Chen X, Wai CM, Fulton JL. Synthesizing and Dispersing Silver Nanoparticles in a Water-in-Supercritical Carbon Dioxide Microemulsion. J Am Chem Soc. 1999 Mar 24;121(11):2631–2.

133. Misra SK, Pathak K. Supercritical fluid technology for solubilization of poorly water soluble drugs via micro- and naonosized particle generation. ADMET DMPK. 2020 Jun 29;8(4):355–74.

134. Le HV, Dulong V, Picton L, Le Cerf D. Lyophilization for Formulation Optimization of Drug-Loaded Thermoresponsive Polyelectrolyte Complex Nanogels from Functionalized Hyaluronic Acid. Pharmaceutics. 2023 Mar 13;15(3):929.

135. Li Y, Wang Y, Yue PF, Hu PY, Wu ZF, Yang M, et al. A novel high-pressure precipitation tandem homogenization technology for drug nanocrystals production - a case study with ursodeoxycholic acid. Pharm Dev Technol. 2014 Sep;19(6):662–70.

136. Shelar DB, Pawar SK, Vavia PR. Fabrication of isradipine nanosuspension by anti-solvent microprecipitation-high-pressure homogenization method for enhancing dissolution rate and oral bioavailability. Drug Deliv Transl Res. 2013 Oct;3(5):384–91.

137. Aldeeb MME, Wilar G, Suhandi C, Elamin KM, Wathoni N. Nanosuspension-Based Drug Delivery Systems for Topical Applications. Int J Nanomedicine. 2024 Jan 25;19:825–44.

138. Chogale MM, Ghodake VN, Patravale VB. Performance Parameters and Characterizations of Nanocrystals: A Brief Review. Pharmaceutics. 2016 Aug 30;8(3):26.

139. Mourdikoudis S, M. Pallares R, K. Thanh NT. Characterization techniques for nanoparticles: comparison and complementarity upon studying nanoparticle properties. Nanoscale. 2018;10(27):12871–934.

140. Dizaj SM, Vazifehasl Z, Salatin S, Adibkia K, Javadzadeh Y. Nanosizing of drugs: Effect on dissolution rate. Research in Pharmaceutical Sciences. 2015 Apr;10(2):95.

141. Shahrin N. Solubility and Dissolution of Drug Product: A Review. Int J Pharma Life Sci. 2013 May 30;2(1):33–41.

142. Danaei M, Dehghankhold M, Ataei S, Hasanzadeh Davarani F, Javanmard R, Dokhani A, et al. Impact of Particle Size and Polydispersity Index on the Clinical Applications of Lipidic Nanocarrier Systems. Pharmaceutics. 2018 May 18;10(2):57.

143. Stetefeld J, McKenna SA, Patel TR. Dynamic light scattering: a practical guide and applications in biomedical sciences. Biophys Rev. 2016 Oct 6;8(4):409–27.

144. Azhdarzadeh M, Lotfipour F, Zakeri-Milani P, Mohammadi G, Valizadeh H. Anti-bacterial performance of azithromycin nanoparticles as colloidal drug delivery system against different gram-negative and gram-positive bacteria. Adv Pharm Bull. 2012;2(1):17–24.

145. Yassin AE, Albekairy AM, Omer ME, Almutairi A, Alotaibi Y, Althuwaini S, et al. Chitosan-Coated Azithromycin/Ciprofloxacin-Loaded Polycaprolactone Nanoparticles: A Characterization and Potency Study. NSA. 2023 Dec 21;16:59–72.

146. Ohshima H. Henry's Function for Electrophoresis of a Cylindrical Colloidal Particle. Journal of Colloid and Interface Science. 1996 Jun 1;180(1):299–301.

147. Clogston JD, Patri AK. Zeta potential measurement. Methods Mol Biol. 2011;697:63–70.

148. Ahmad M, Gani A, Hassan I, Huang Q, Shabbir H. Production and characterization of starch nanoparticles by mild alkali hydrolysis and ultra-sonication process. Sci Rep. 2020 Feb 26;10(1):3533.

149. Lin PC, Lin S, Wang PC, Sridhar R. Techniques for physicochemical characterization of nanomaterials. Biotechnol Adv. 2014;32(4):711–26.

150. Mayerhöfer TG, Pipa AV, Popp J. Beer's Law-Why Integrated Absorbance Depends Linearly on Concentration. Chemphyschem. 2019 Nov 5;20(21):2748–53.

151. Muneer DRM. The calibration in %T has the drawbacks of being non- linear and readings decreasing with increasing concentration. Clinical Chemistry. (4).

152. Sarhan SR. Preparation of Chitosan Nanoparticles and Chitosan Nanoparticles Loaded with Azithromycin and the Study of Their Characterizations. IVJ. 2024 May 1;101(5):19–25.

153. Akartas I. Design of azithromycin loaded eudragit rl 100 nanoparticles with extended antibacterial effect. FARMACIA. 2023 Apr 27;71(2):345–58.

154. Gill P, Moghadam TT, Ranjbar B. Differential Scanning Calorimetry Techniques: Applications in Biology and Nanoscience. J Biomol Tech. 2010 Dec;21(4):167–93.

155. Mohammadi G, Valizadeh H, Barzegar-Jalali M, Lotfipour F, Adibkia K, Milani M, et al. Development of azithromycin-PLGA nanoparticles: physicochemical characterization and antibacterial effect against Salmonella typhi. Colloids Surf B Biointerfaces. 2010 Oct 1;80(1):34–9.

156. Titus D, James Jebaseelan Samuel E, Roopan SM. Nanoparticle characterization techniques. In: Green Synthesis, Characterization and Applications of Nanoparticles. Micro and Nano Technologies; 2019. p. 303–19.

157. Guimarães M, Somville P, Vertzoni M, Fotaki N. Investigating the Critical Variables of Azithromycin Oral Absorption Using In Vitro Tests and PBPK Modeling. J Pharm Sci. 2021 Dec;110(12):3874–88.

158. Zaid Alkilani A, Hamed R, Abdo H, Swellmeen L, Basheer HA, Wahdan W, et al. Formulation and Evaluation of Azithromycin-Loaded Niosomal Gel: Optimization, In Vitro Studies, Rheological Characterization, and Cytotoxicity Study. ACS Omega. 2022;7(44):39782–93.

159. Jones TM. Preformulation Studies. Royal Society of Chemistry. 2018;4(1):4–15.

160. Chaurasia G. A Review on Pharmaceutical Preformulation Studies in Formulation and Development of New Drug Molecules. International Journal of Pharmaceutical Sciences and Research. 7.

161. Wu CY, Wang W. Application of Antisolvent Precipitation Method for Formulating Excipient-Free Nanoparticles of Psychotropic Drugs. Pharmaceutics. 2022 Apr;14(4):819.

162. Ran Q, Wang M, Kuang W, Ouyang J, Han D, Gao Z, et al. Advances of Combinative Nanocrystal Preparation Technology for Improving the Insoluble Drug Solubility and Bioavailability. Crystals. 2022 Sep;12(9):1200.

163. Ye J, Li Z, Kubicki DJ, Zhang Y, Dai L, Otero-Martínez C, et al. Elucidating the Role of Antisolvents on the Surface Chemistry and Optoelectronic Properties of CsPbBrxI3-x Perovskite Nanocrystals. J Am Chem Soc. 2022 Jul 13;144(27):12102–15.

164. Ferguson P, Cross R, Schad G. Chapter 8 - Application of SFC for the characterization of formulated drug products. In: Hicks M, Ferguson P, editors. Separation Science and Technology. Academic Press; 2022. p. 221–55. (Practical Application of Supercritical Fluid Chromatography for Pharmaceutical Research and Development; vol. 14).

165. Ravichandran V, Lee M, Nguyen Cao TG, Shim MS. Polysorbate-Based Drug Formulations for Brain-Targeted Drug Delivery and Anticancer Therapy. Applied Sciences. 2021 Jan;11(19):9336.

166. Abedinoghli D, Charkhpour M, Osouli-Bostanabad K, Emami S, Barzegar-Jalali M, Adibkia K. Electrosprayed Nanosystems of Carbamazepine – PVP K30 for Enhancing Its Pharmacologic Effects. 2018;

167. Tekade BW, Jadhao UT, Thakre VM, Chaudhari KP, Meshram PR, Patil MP. Development and Invitro Evaluation of Azithromycin Microspheres by Solvent Evaporation Technique.

168. Edman P. Pharmaceutical Formulations— Suspensions and Solutions. Journal of Aerosol Medicine. 1994 Jan;7(s1):S-3-S-6.

169. Jacob S, Kather FS, Boddu SHS, Attimarad M, Nair AB. Nanosuspension Innovations: Expanding Horizons in Drug Delivery Techniques. Pharmaceutics. 2025 Jan 19;17(1):136.

170. Aldeeb MME, Wilar G, Suhandi C, Elamin KM, Wathoni N. Nanosuspension-Based Drug Delivery Systems for Topical Applications. IJN. 2024 Jan 25;19:825–44.

171. Thanh NTK, Maclean N, Mahiddine S. Mechanisms of Nucleation and Growth of Nanoparticles in Solution. Chem Rev. 2014 Aug 13;114(15):7610–30.

172. Kaushal Arora, Vishal Vets, Prabhakar Kumar Verma. A Review on Pharmaceutical Suspension and Its Advancement. Annals of Clinical Case Reports. 2022;7:2321.

173. Kumari K, Srinivasa Rao, Y. Nanosuspensions: A Review. Int J of Pharm. 2017 Jan 21;7(2):77–89.

174. Malgundkar HK, Pomaje MD, Nemade LS. Breaking Barriers with Nanosuspension: A Comprehensive Review. Biosciences Biotechnology Research Asia. 2024 Mar 30;21(1):57–68.

175. Leone F, Cavalli R. Drug nanosuspensions: a ZIP tool between traditional and innovative pharmaceutical formulations. Expert Opinion on Drug Delivery. 2015 Oct 3;12(10):1607–25.

176. Carissimi G, Montalbán MG, Víllora G, Barth A. Direct Quantification of Drug Loading Content in Polymeric Nanoparticles by Infrared Spectroscopy. Pharmaceutics. 2020 Sep 23;12(10):912.

177. Dash S, Murthy PN, Nath L, Chowdhury P. Kinetic modeling on drug release from controlled drug delivery systems. Acta Poloniae Pharmaceutica - Drug Research. 2010;67(3):217–23.

178. Rezigue M, Mashaqbeh H, Aljabali AAA, Mansour RS, Hamzeh I. Development and Evaluation of Azithromycin-Loaded Transethosomes for Enhanced Dermal Delivery and Antibacterial Efficacy. Pharmaceutics. 2025 Apr;17(4):400.

179. Montgomery DC. Design and Analysis of Experiments. Vol. 9. John Wiley & Sons; 2017. 749 p.

180. Honary S, Zahir F. Effect of Zeta Potential on the Properties of Nano-Drug Delivery Systems - A Review (Part 1). Trop J Pharm Res. 2013 May 9;12(2):255–64.

181. Mahajan A, Ramana E. Patents on Magnetoelectric Multiferroics and their Processing by Electrophoretic Deposition. MATS. 2014 Aug 31;7(2):109–30.

182. Bajaj S, Singla D, Sakhuja N. Stability Testing of Pharmaceutical Products. Journal of Applied Pharmaceutical Science.

183. Apmann K, Fulmer R, Soto A, Vafaei S. Thermal Conductivity and Viscosity: Review and Optimization of Effects of Nanoparticles. Materials (Basel). 2021 Mar 8;14(5):1291.

184. Hu X, Yin D, Chen X, Xiang G. Experimental investigation and mechanism analysis: Effect of nanoparticle size on viscosity of nanofluids. Journal of Molecular Liquids. 2020 Sep 15;314:113604.

185. Akotiya P, Bansal AK, Shete G. Stabilizers used in nano-crystal based drug delivery systems. Int Journal of Excipients and Food Chemicals. 2014 Dec 1;

186. Mahdavi M, Sharifpur M, Ahmadi MH, Meyer JP. Aggregation study of Brownian nanoparticles in convective phenomena. J Therm Anal Calorim. 2019 Jan;135(1):111–21.

187. Sanjay LR, Ashokbhai MK, Ghatole S, Roy S, Kashinath KP, Kaity S. Strategies for beating the bitter taste of pharmaceutical formulations towards better therapeutic outcomes. RSC Pharm. 2025;2(1):59–81.

188. Sohi H, Sultana Y, Khar RK. Taste Masking Technologies in Oral Pharmaceuticals: Recent Developments and Approaches. Drug Development and Industrial Pharmacy. 2004 Jan;30(5):429–48.

189. Pagar HB, Shinde UP, Agrawal YS, Barhate SD, Luhade TS, Sonawane RO. Taste Masking: A Review. Research Journal of Pharmacy and Technology. 2012 Feb 28;5(2):152–7.

190. Latha RS, Lakshmi PK. Electronic tongue: An analytical gustatory tool. J Adv Pharm Technol Res. 2012;3(1):3–8.

191. Chandrashekar J, Hoon MA, Ryba NJP, Zuker CS. The receptors and cells for mammalian taste. Nature. 2006 Nov 16;444(7117):288–94.

192. Kinnamon SC. Taste receptor signalling – from tongues to lungs. Acta Physiologica. 2012 Feb;204(2):158–68.

193. Roper SD. Taste buds as peripheral chemosensory processors. Seminars in Cell & Developmental Biology. 2013 Jan;24(1):71–9.

194. Beauchamp GK, Mennella JA. Early Flavor Learning and Its Impact on Later Feeding Behavior. J pediatr gastroenterol nutr. 2009 Mar;48(S1).

195. Breslin PAS. An Evolutionary Perspective on Food and Human Taste. Current Biology. 2013 May;23(9):R409–18.

196. Small DM, Prescott J. Odor/taste integration and the perception of flavor. Exp Brain Res. 2005 Oct;166(3–4):345–57.

197. Chaudhari N, Roper SD. The cell biology of taste. Journal of Cell Biology. 2010 Aug 9;190(3):285–96.

198. Taruno A, Vingtdeux V, Ohmoto M, Ma Z, Dvoryanchikov G, Li A, et al. CALHM1 ion channel mediates purinergic neurotransmission of sweet, bitter and umami tastes. Nature. 2013 Mar;495(7440):223–6.

199. Patel K. Advances in Taste-Masking Strategies for Pediatric Brain- Related Disease Treatments: Focus on Polymeric Coatings in Orally Disintegrating Tablets. Int J Sci R Tech. 2025;

200. Meyerhof W, Batram C, Kuhn C, Brockhoff A, Chudoba E, Bufe B, et al. The Molecular Receptive Ranges of Human TAS2R Bitter Taste Receptors. Chemical Senses. 2010 Feb;35(2):157–70.

201. Deepak S, Dinesh K, Mankaran S, Gurmeet S, Singh RM. Taste Masking Technologies: A Novel Approach for the Improvement of Organoleptic Property of Pharmaceutical Active Substance. 2012;

202. Mehnert W, Mäder K. Solid lipid nanoparticles: production, characterization and applications. Adv Drug Deliv Rev. 2001 Apr 25;47(2–3):165–96.

203. Müller RH, Mäder K, Gohla S. Solid lipid nanoparticles (SLN) for controlled drug delivery - a review of the state of the art. Eur J Pharm Biopharm. 2000 Jul;50(1):161–77.

204. Mozafari MR. Nanoliposomes: preparation and analysis. Methods Mol Biol. 2010;605:29–50.

205. Khan S, Kataria P, Nakhat P, Yeole P. Taste masking of ondansetron hydrochloride by polymer carrier system and formulation of rapid-disintegrating tablets. AAPS PharmSciTech. 2007 Jun;8(2):E127–33.

206. Leuner C, Dressman J. Improving drug solubility for oral delivery using solid dispersions. Eur J Pharm Biopharm. 2000 Jul;50(1):47–60.

207. Sharma DK. Solubility Enhancement Strategies for Poorly Water-Soluble Drugs in Solid Dispersions: A Review. Asian Journal of Pharmaceutics (AJP). 2007;1(1).

208. Rowe RC, Sheskey PJ, Quinn ME. Handbook of pharmaceutical excipients. 6th ed. London: Pharmaceutical press; 2009.

209. Stella VJ, Nti-Addae KW. Prodrug strategies to overcome poor water solubility. Adv Drug Deliv Rev. 2007 Jul 30;59(7):677–94.

210. Karaman R. Prodrugs for masking bitter taste of antibacterial drugs--a computational approach. J Mol Model. 2013 Jun;19(6):2399–412.

211. IARC Working Group on the Evaluation of Carcinogenic Risks to. Chloramphenicol. In: Pharmaceutical Drugs. International Agency for Research on Cancer; 1990. p. 50.

212. Stella VJ, He Q. Cyclodextrins. Toxicol Pathol. 2008 Jan;36(1):30–42.

213. Loftsson T, Duchêne D. Cyclodextrins and their pharmaceutical applications. Int J Pharm. 2007 Feb 1;329(1–2):1–11.

214. Rajesh AM, Bhatt SA, Brahmbhatt H, Anand PS, Popat KM. Taste masking of ciprofloxacin by ion-exchange resin and sustain release at gastric-intestinal through interpenetrating polymer network. Asian Journal of Pharmaceutical Sciences. 2015 Jul;10(4):331–40.

215. Meyerhof W, Batram C, Kuhn C, Brockhoff A, Chudoba E, Bufe B, et al. The molecular receptive ranges of human TAS2R bitter taste receptors. Chem Senses. 2010 Feb;35(2):157–70.

216. Cherian S, Lee BS, Tucker RM, Lee K, Smutzer G. Toward Improving Medication Adherence: The Suppression of Bitter Taste in Edible Taste Films. Adv Pharmacol Sci. 2018 Jun 25;2018:8043837.

217. Qin W, He Y, Guo Z, Zhang L, Wu L, Yin X, et al. Optimization of taste-masking on ibuprofen microspheres with selected structure features. Asian J Pharm Sci. 2019 Mar;14(2):174–82.

218. Uchida T. Taste Sensor Assessment of Bitterness in Medicines: Overview and Recent Topics. Sensors. 2024 Jan;24(15):4799.